Title
Image-Based Multiscale Modeling of Poroelastic Biological Materials with Application to Bones

Permalink
https://escholarship.org/uc/item/8gk9q5h4

Author
Yang, Judy

Publication Date
2012

Peer reviewed|Thesis/dissertation

UNIVERSITY OF CALIFORNIA

Los Angeles

Image-Based Multiscale Modeling of Poroelastic Biological Materials

with Application to Bones

A dissertation submitted in partial satisfaction of the

requirements for the degree Doctor of Philosophy

in Civil Engineering

by

Judy Ping Yang

2012

ABSTRACT OF THE DISSERTATION

Image-Based Multiscale Modeling of Poroelastic Biological Materials

with Application to Bones

by

Judy Ping Yang

Doctor of Philosophy in Civil Engineering

University of California, Los Angeles, 2012

Professor Jiun-Shyan Chen, Chair

Biot's theory has been widely used to construct the poroelasticity models for describing the mechanical behavior of biological materials. This phenomenological framework, however, does not take the explicit microstructural configuration and the corresponding solid-fluid coupling into consideration. This work investigates how the microstructural configuration and material properties of porous materials constitute the macroscopic poroelastic material behavior described

by the classical Biot's theory. We introduced an asymptotic based homogenization method to correlate the macro- and micro-mechanical behaviors of poroelastic materials, where an elastic solid and Newtonian fluid of low viscosity are considered. Through this homogenization process, the generalized Darcy's law, homogenized macroscopic continuity equation, and homogenized macroscopic equilibrium equation were obtained, where the homogenized macroscopic continuity and equilibrium equations reassemble the governing equations in Biot's theory.

For an effective modeling of microstructures, a numerical solution for PDEs based on a strong form collocation that employs image pixels as the discretization points is proposed. To achieve this objective, a gradient reproducing kernel collocation method (G-RKCM) formulated based on the partition of nullity and gradient reproducing conditions was developed. This approach reduces the order of differentiation to the first order when solving second order PDEs with strong form collocation. We showed that the same number of collocation points and source points can be used in G-RKCM for optimal convergence, unlike other strong form collocation methods. In addition, same order of convergence rate in the solution and its first order derivative are achieved, owing to the imposition of gradient reproducing conditions. The computational complexity of G-RKCM is also shown to be an enhancement over other strong form collocation methods, such as the reproducing kernel collocation method (RKCM).

In this work, we introduced the active contour model based on variational level set formulation for interface identification and boundary segmentation for the discretization of microstructures based on medical images. Using pixel point discretization, we introduced the RKCM and G-RKCM to solve the level set equation. In particular, the G-RKCM has been shown be effective since the second derivatives of the level set function involved in the regularization term are

approximated by the first order differentiations of the gradient RK shape functions. We further showed that a B-spline kernel function with lower continuity can be preferably used to avoid the oscillation of level set functions in the two-color images.

The image based G-RKCM was applied to model trabecular bone microstructures with complex geometry for both solid and fluid phases. The corresponding numerical issues such as interface discretization and kernel function support size selection have been addressed. The investigation on the proper choice of unit cell dimension and image resolution has been performed, which provides guidance in the image-based trabecular bone modeling. The validation of the proposed image based multiscale modeling framework has been carried out by comparing the numerical prediction of effective material properties with experimental data of trabecular bone in the literature and solving a macroscopic trabecular bone problem using the homogenized material constants.

The dissertation of Judy Ping Yang is approved.

Jiann-Wen Ju

Ertugrul Taciroglu

William Klug

Jiun-Shyan Chen, Committee Chair

University of California, Los Angeles

2012

To My Family

TABLE OF CONTENTS

LIST OF FIGURES

xiii

LIST OF TABLES

ACKNOWLEDGEMENTS

First of all, I would like to express my deepest gratitude and sincerest appreciation to my advisor, Professor Jiun-Shyan Chen, for his patience in guiding me, supporting me, and encouraging me throughout my graduate study at UCLA. In particular, his profound knowledge in computational mechanics assists me in accomplishing this research. His hard working attitude and deliberate thinking towards research really inspire me. Indeed, Professor Chen is a good model for young researchers to develop their ability and habit in the research area. I will keep in mind what he has taught and advised me in the past years in order to become a good researcher.

Secondly, I would like to convey my great thankfulness to my committee members, Professor Jiann-Wen Ju, Professor Ertugrul Taciroglu, and Professor William Klug. Their valuable advice and useful comments based on their professional research experience in different disciplines help me improve the contents and quality of this dissertation. During my study at UCLA, it has been a great experience for me to join the bio-related project in collaboration with Dr. John Hodgson and Professor V. R. Edgerton from School of Medicine at UCLA, and Professor Shantanu Sinha from School of Medicine at UCSD. From this project, I have learned a lot about muscle physiology. Also, I would like to thank Professor H.Y. Hu from Mathematics Department at Tunghai University, Taiwan, for sharing with me her knowledge on mathematical analysis in developing the numerical methods used in this study.

Thirdly, I would like to express my special thanks to Dr. Sheng-Wei Chi for assisting me in numerical analysis, discussing the project contents, and providing suggestions to overcome the

difficulties encountered. Thanks should also go to Ms. Janice Chen, who worked with me as an undergraduate student during summer 2011 in retrieving and dealing with the medical images. All the former and current members of the computational mechanics group at UCLA also deserve my appreciation, including Professor Pai-Chen Guan, Professor Xiaodan Ren, Dr. Chung-Hao Lee, Dr. Marcus Rüter, Mr. Shih-Po Lin, Mr. Mike Hillman, Ms. Camille Marodon, and so on. Their valuable discussions have helped me in different ways to finish this research.

Last but not least, I would like to convey my whole-hearted appreciation to my beloved family, especially my dad, my mom, my brother, my sister, my brother-in-law, and the newborn baby. I know that there are endless love and spiritual power supporting me and waiting for me, no matter when I need and where I go. They deserve the credit of every effort and success I have made in pursuing this doctoral degree. All credit goes to the ones whom I love!

VITA

April 18, 1982   Born in Ithaca, New York, U.S.A.

2000-2004   B.S., Department of Civil Engineering,

National Taiwan University, Taipei 10617, Taiwan

2004-2006   M.S., Division of Structural Engineering,

Department of Civil Engineering,

National Taiwan University, Taipei 10617, Taiwan

2008-2012   Research Assistant, Division of Structural Mechanics,

Department of Civil and Environmental Engineering,

University of California, Los Angeles, CA 90095, U.S.A.

2009-2011   Teaching Assistant / Teaching Associate

Department of Civil and Environmental Engineering,

University of California, Los Angeles, CA 90095, U.S.A.

PUBLICATIONS AND PRESENTATIONS

Chi SW, Chen JS, Hu HY, **Yang JP**. A Gradient Reproducing Kernel Collocation Method for Boundary Value Problems. Internat. J. Numer. Methods Engrg. Under revision, 2012.

Hodgson JA, Chi SW, **Yang JP**, Chen JS, Edgerton VR, Sinha S. Finite Element Modeling of Passive Material Influence on the Deformation and Force Output of Skeletal Muscle. J. Mech. Behav. Biomed. Mater. 2012; 9: 163-183.

Yang, J.P., and Chen, J.S., "Multiscale Modeling of Poroelastic Biological Materials with Application to Bones," 3rd International Symposium on Computational Mechanics in conjunction with 2nd symposium on Computational Structural Engineering (ISCM III - CSE II), Taipei, Taiwan, December 5-7, 2011.

Yang, J.P., and Chen, J.S., "Multiscale Modeling of Poroelastic Biological Materials with Application to Bones," 11th U.S. National Congress on Computational Mechanics (USNCCM-11), Minneapolis, MN, July 25-28, 2011.

Yang, J.P., and Chen, J.S., "Multiscale Modeling of Poroelastic Biological Materials," 11th U.S. National Congress on Computational Mechanics (USNCCM-11), Minneapolis, MN, July 25-28, 2011. (poster)

Chapter 1 Introduction

1.1 Motivation of the Proposed Work

The biological materials, such as those in bones existing in all living creatures, are structures with heterogeneous material properties and complex microstructural topology. For instance, the human skeleton consisting of bones roughly comprises one fifth of an individual body weight. The main functions of bones are to support and protect organs, perform exercises and make movements, and produce the blood cells, etc. As far as the macroscopic composition of bones is concerned, the bones can be classified as cortical bone (also known as the compact bone) and trabecular bone (also called the cancellous bone or spongy bone). With reference to Figure 1-1 (a) for a femur long bone, the cortical bone constitutes about 80% of the human skeleton mass and forms an outer layer of bones, while the trabecular bone fills the interior with a porous and cancellous structure, as can be observed in the corresponding microstructure of the femur long bone in Figure 1-2 (b). In general, the cortical bone is stiffer, harder, and denser than the trabecular bone so that it has the ability to protect organs, support the body for movement, and transmit chemical components. In contrast, the trabecular bone has a larger surface area and lower density and stiffness than those of the cortical bone, and it has higher porosity as exemplified by the fact that the value of porosity is usually greater than 30%. Owning to the porous nature of the trabecular bone, there exists room for the blood vessels and bone marrow to flow inside the spongy structure, as can be seen from the CT scan of the trabecular bone microstructure in Figure 1-2. As such, the bone materials can be characterized as porous media

of solid skeleton with the pores filled by fluid. The fluid saturated porous material has been introduced to describe the constitutive behavior of biomaterials.
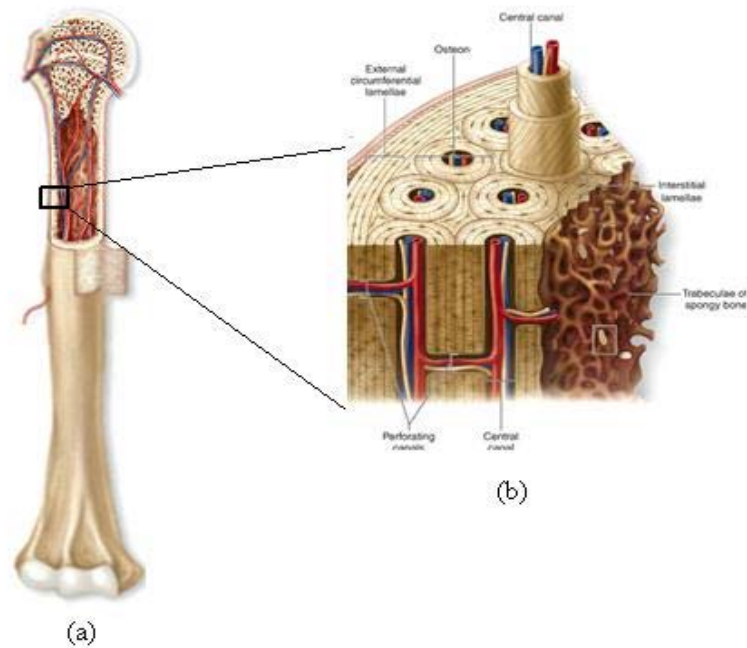
Figure 1-1 Macrostructure of bone: (a) A femur long bone; (b) Cortical and trabecular bones (adapted from http://academic.kellogg.edu/herbrandsonc/bio201_mckinley/skele tal.htm)
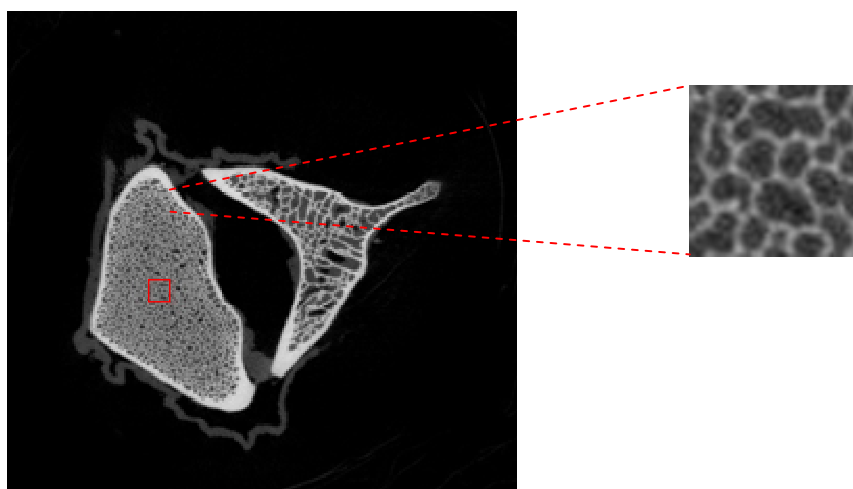
Figure 1-2 Microstructure of bone (adopted from http://www.scanco.ch/)

Recently, much attention has been drawn to investigate how the morphology of biological materials influences the deformation pattern of tissues. To study how the microscopic material properties in the solid skeleton and fluid affect the macroscopic mechanical properties, an asymptotic expansion based homogenization method has been introduced to provide a systematic analysis paradigm for multiscale homogenization of poroelastic materials. It is noteworthy that the homogenization yields macroscopic results that resemble the Biot's theory, but with embedded microscopic response. Nevertheless, the finite element based numerical investigation of the biological materials is ineffective for creation of the geometric representation of biological materials and the associated microstructures. For biological materials, the macroscopic topology and microscopic geometry are typically obtained from medical images. The transformation from image data to geometry representation by computer aided engineering (CAE) to a finite element mesh is extremely cumbersome. More specifically, the topological change through the cross sections of the biological materials has been the major bottleneck in mesh generation. A computational framework that can effectively model biological materials with complex geometric configuration, heterogeneity, and material incompressibility is of an urgent need for advancement of bioscience.

1.2 Objective and Scope

The main objectives of this research are two-fold: (1) derivation of a multiscale constitutive formulation for poroelastic biological materials, and (2) development of a computational framework based on the strong form with direct collocation for modeling the microscopic

structures and analyzing the multiscale behavior of poroelastic biological materials with application to bones. The specific achievements of this research are summarized as follows:

(1) Mathematical homogenization of poroelastic materials

Biological materials are typically poroelastic in nature with complicated microstructural configurations and high degree of material heterogeneity. As such, a multiscale homogenization method with asymptotic expansion is introduced to characterize the macro- and micro-mechanical behaviors of poroelastic materials, where the Stokes equation, continuity equation, and equilibrium equation are considered. Through the homogenization process, the generalized Darcy's law, homogenized macroscopic continuity equation, and homogenized macroscopic equilibrium equation were derived. In particular, the coarse-scale solid displacement and fluid pressure are shown to be independent of the microscopic coordinates, whereas the coarse-scale fluid velocity is related to the microscopic coordinates. The characteristic functions are used in calculating the homogenized poroelastic material parameters in the generalized Darcy's law, macroscopic equilibrium and continuity equations.

(2) A gradient reproducing kernel collocation method (G-RKCM) formulation for solving boundary value problems

A gradient approximation is introduced in the reproducing kernel collocation method (RKCM) for solving the second order PDEs. Based on the partition of nullity and derivative reproducing conditions, a gradient reproduction kernel approximation was proposed to reduce the order of differentiation of the PDEs to the first order for solution by RKCM with

strong form. We also showed that the same number of collocation points and source points can be used, which is different from the typical strong form collocation method for optimal convergence. The complexity analysis and convergence study have been investigated. The numerical examples are given to verify the analytical prediction.

(3) Level set formulation based on strong form collocation for interface and boundary identification

The reproducing kernel collocation method has been introduced to solve the level set equation based on the point discretization. It was demonstrated that the medical image obtained from CT scan with blurry objects can be segmented successfully by using the collocation method to solve the level set equation. For images with two color data, an investigation on the continuity of the kernel function showed that a B-spline kernel function with lower continuity can be preferably used to avoid the oscillation of level set functions.

(4) Gradient reproducing kernel collocation method (G-RKCM) for solving level set equation

The gradient reproducing kernel collocation method has been introduced to solve the level set equation efficiently due to the fact that the second derivatives in the regularization term are approximated by the first order differentiations and a determined system can be used instead of an overdetermined system.

(5) Simplified strong form collocation method for solving level set equation

When using the reproducing kernel collocation method to solve the level set equation in the image process, the consistency condition in construction of the RK shape function can be

released such that the kernel function is used directly in the approximation for computational efficiency. For images presented by two colors, the direct collocation method is introduced to solve the degenerated level set equation with no regularization term, in which the transformation matrix is no longer needed, thereby making the numerical algorithm very efficient.

(6) Strong form collocation method for solving unit cell problems

Inspired by the point discretization of medical images obtained from CT scan or MRI, the strong form collocation method was introduced to solve the unit cell problems, where the microstructure models were constructed directly on the basis of image segmentation preprocessed by the level set method. In this manner, no mesh is needed to construct the complex topology of the microstructure.

(7) Verification and validation of microstructural modeling and trabecular bone analysis

Solving unit cell problems by G-RKCM was verified by comparing the numerical results with analytical solutions. For modeling microstructures with complex geometry, the corresponding numerical issues including interface approximation, unit cell size effect, and image resolution for image-based strong form methods were investigated. Furthermore, a parametric study comparing the numerically predicted trabecular bone material properties with experimental data and a macroscopic modeling of trabecular bone using homogenized material constants were conducted to demonstrate the developed computational framework in multiscale modeling of trabecular bones.

This remaining part of the dissertation is organized as follows. Chapter 2 gives a literature review of the theories of poroelasticity, associated multiscale homogenization of poroelastic materials, and advanced numerical methods applicable to bone mechanics. Chapter 3 presents the theory of poroelasticity based on Biot's theory. Chapter 4 introduces the asymptotic based homogenization for poroelastic materials along with the homogenized material parameters, the latter are computed in terms of the characteristic functions defined for the unit cells. In Chapter 5, the gradient reproducing kernel collocation method (G-RKCM) is proposed for solving the boundary value problems. In Chapter 6, the specific active contour model in the level set method is first introduced. Then, the strong form collocation methods including RKCM, G-RKCM, simplified collocation method, and direct collocation method are introduced for solving the level set equation computationally more efficiently. Chapter 7 demonstrates the proposed image-based computational framework by solving microstructural problems with heterogeneous feature and comparing the numerical results with experimental data. Chapter 8 concludes this research conducted in this dissertation with future work highlighted.

Chapter 2 Literature Review

2.1 Poroelasticity

A porous medium has biphasic nature due to the composition of the solid skeleton and fluid. When the poroelastic material is subjected to external loads, the solid skeleton and fluid in the pores interact with each other. There are two well-known theories of poroelasticity, i.e., theory of porous media (TPM) (de Boer, 1988; Schanz and Diebels, 2003) and Biot's theory (Terzaghi, 1925; Biot, 1941; Biot, 1955; Biot, 1956; Biot, 1961), both providing a coupled description of the system interaction. It is noted that both theories have been initiated in geomechanics. Due to different subjects of multiphase continuum mechanics, the two theories have been developed and used to date.

The pioneering work on porous media should be attributed to Fillunger (1913). In 1913, Fillunger tried to solve the buoyancy problem of barrages and developed a formula to calculate the uplift in fluid-saturated porous solids. Starting from his work, the theory of porous media, known as TPM, has been developed based on the continuum and thermodynamic theories of mixtures. In 1976, Bowen extended the mixture theory by the concept of volume fractions which distributes the mass of the solid skeleton and the mass of the fluid in the total control space. It is noted that the distribution relies on the porosity which serves as a constraint to fix the volume ratios of constituents to the control space, under the assumption that the pores are statically distributed over the control space. The concept of volume fractions leads to a smeared continuum which can be treated with the mixture theory.

Another important theory on the behavior of porous media is based on the work by Terzaghi, which is known as the one-dimensional soil consolidation theory (Terzaghi, 1925). In this theory, the grains or particles of soil constitute a porous medium represented by a unit cubic element. By using the phenomenological approach, Biot extended Terzaghi's theory to a three-dimensional theory and gave a theoretical description of isotropic poroelastic materials saturated with fluid (Biot, 1941), known as the quasi-static Biot's theory. The generalization of the theory is applicable to anisotropic porous solids and poroelastodynamics, where acoustic propagation in the poroelastic solid skeleton with viscous fluid is considered (Biot, 1955; Biot, 1956; Biot 1962). In particular, the inclusion of inertia effect leads to the dynamic version of Biot's theory. One contribution of the dynamic theory was the identification of three different types of waves, i.e., two compressive waves and one shear wave, in a three-dimensional continuum. Both the quasi-static and dynamic versions of Biot's theory are applicable to compressible and incompressible constituents, while the dynamic formulation of TPM is only established for incompressible constituents as pointed out by Schanz (2009). Because of this reason, Biot's theory will be adopted in this study.

Recently, much attention has been paid to the modeling of porous media, as evidenced by the fact that its application has been extended from geomechanics to material science and biomechanics, such as composite materials, foam materials, and biological tissues, etc. It is noteworthy that biological tissues are viewed as fluid-saturated porous materials, where fluid plays an important role. Simon et al. (1996) derived a poroelastic finite element formulation to include transport and swelling in soft tissues. Huyghe and Janssen (1997) computed the quasi-static finite deformation of swelling incompressible porous media by the mixture theory and showed that their result is consistent with Biot's theory in the limiting case.

2.2 Multiscale Homogenization Method

One of the major driving forces of research in homogenization is due to the composite material technology invented in the 1950s. The main objective is to find the effective mechanical properties of the overall composite materials and determine their dependency on microscopic components, where the local structures are defined by the representative volume element (RVE). The methodology called homogenization was introduced by Babuska (1976), in which the asymptotic behavior of the structural system is characterized by a scale parameter λ taken as the representative size of the microstructures. Here, the microstructures are considered as relatively small compared to the dimensions of the overall system such that they can be assumed to be periodically arranged. The mathematical formulations for heterogeneous media based on the asymptotic expansion can be found in a series of publications by Benssousan et al. (1978), Sanchez-Palencia (1980), Lions (1981), Bakhvalov and Panasenko (1989), Guedes and Kikuchi (1990), among others. The basic feature of multiscale homogenization lies in that the microscopic characteristics are implied in the macroscopic behavior with material heterogeneity taken into consideration.

The homogenization method has been applied to a variety of mechanics problems for composite materials. In this study, we shall focus our attention on multiscale homogenization of poroelastic materials based on Biot's theory. It was known that the behavior of a Stokes flow in porous media is governed by Darcy's law, a characterization of the influence of microstructural configuration on fluid flow at the microscopic level. Based on the constitutive relation used, the specific scaling of parameters in the asymptotic expansion leads to different homogenization results (Hornung, 1997; Terada et al., 1998; Rohan et al., 2006). The extension of multiscale

homogenization to composite materials with large deformation and nonlinear composite materials has been dealt with the updated Lagrangian formulation (Takano et al., 2000; Rohan et al., 2006). A total Lagrangian formulation for homogenization of composite materials was given by Zhang et al. (2006), though intended for polycrystalline materials. Recently, the multiscale homogenization of porous materials has been introduced to biological tissues. Rohan and Lukes (2004) have applied this approach to simulating arterial walls, where the solid skeleton is modeled by the neo-Hookean material. Rohan (2006) and Rohan et al. (2006) have utilized the specific scaling of the hydraulic permeability tensor to account for the viscoelastic behavior observed as the hereditary creep at macroscopic scale by parallel computing. It is noteworthy that most of the aforementioned works have been carried out using the weak form based finite element method. For complicated structural systems with complex microstructures such as biological tissues, mesh construction becomes a critical issue.

2.3 Reproducing Kernel Collocation Method

In the past few decades, meshfree methods have been developed as a mature tool for solving the partial differential equations (PDEs) based on the Galerkin weak form formulation. The approximation functions with a compact support, such as the moving least-squares (MLS) and reproducing kernel (RK) shape functions, have been commonly adopted in the weak form formulation. In particular, the local feature in the approximation leads to a well-conditioned discrete system and the monomial basis gives the algebraic convergence property. Nonetheless,

the background mesh in the domain integration with quadrature rules and Dirichlet boundary imposition is a complex process of the weak form meshfree methods.

On the other hand, the strong form based meshfree methods with direct collocation have been introduced to solve PDEs recently. The collocation method relies on the point discretization, which not only eliminates the quadrature integration in the domain but also simplifies the imposition of boundary conditions. One distinguishable feature of the method is that the number of collocation points enforcing zero residuals is larger than the number of source points to ensure accuracy of the solution, as pointed out by Zhang et al. (2001) and Hu et al. (2007). The resulting over-determined system is generally solved by the least-squares method. Furthermore, as pointed out by Chen and his co-workers (Hu et al., 2007), the standard collocation method shows large solution errors near the boundaries. The unbalanced residuals in the least-squares functional associated with domain and boundary can be better improved when the boundary collocation equations are properly weighted.

There are two approximation functions widely used under the strong form framework, the radial basis functions (RBFs) and the reproducing kernel (RK) shape functions. The former global functions offer exponential convergence, while their nonlocal character yields a full and ill-conditioned discrete system. The latter local functions mitigate the aforementioned drawback besides having algebraic convergence. In the reproducing kernel (RK) approximation, the locality and smoothness of shape function are defined in the kernel function with a compact support, while the correction function is composed of basis functions with certain order of completeness. Although the RK approximation yields algebraic convergence, it leads to a well-conditioned system that is as stable as the finite element method (FEM). A detailed investigation

of the convergence and stability of the RK approximation was given by Hu et al. (2011), which indicates that the degree of monomial bases used in the RK approximation needs to be larger than one for convergence.

2.4 Level Set Method for Image Segmentation and Boundary Identification

The level set method originally devised by Osher and Sethian (1988) is a widely adopted numerical technique for tracking the topological changes, such as merging and breaking. It has been extensively applied in many practical research areas. A review of the method was given by Osher and Fedkiw (2001), in which the application of the method can be found in computer graphics, image processing, optimization, and computational fluid dynamics.

Methods based on energy minimization and variational principle have been devoted to image segmentation and boundary identification vigorously since the late 1980s. The classical active contour models (snakes) invented by Kass et al. (1988) utilizes the evolution of a parameterized curve subjected to constraints from a given image, in which the internal energy and external constraints with respect to contour smoothness and edge-detection stopping criteria are considered. However, the snakes methods have the drawback of being sensitive to initial conditions. Osher and Sethian (1988) initiated the curvature-dependent algorithm for the level set method, in which the formation of sharp cusps in the moving fronts associated with the topological changes are captured accurately, providing that the boundaries of the objects are defined by the gradient on a fixed rectangular grid. As for objects whose boundaries are not

defined by the gradient of the image, Chan and Vese (1999, 2001) proposed an active contour model on the basis of the Mumford-Shah functional for image segmentation with a level set formulation. With this model, the minimization of the energy functional leads to the evolution of the active contour, which will stop on the desired boundary of a particular segmentation of the image. That is, the deviation of the image information inside and outside the curve of the object governs the evolving interface, and the minimum condition is reached when the boundary of the object is detected. Chan and his co-workers extended the model to deal with vector-valued images, where the objects having some missing parts can still be detected successfully (Chan et al., 2000). The novel technique with active contours for image segmentation and boundary identification has been recognized as the Chan-Vese model in the past decade with the following notable features: The model can detect objects with and without gradients; it can automatically detect the interior contours of an object without noise removal and stops at the place without an edge-function; and the initial curve can be placed anywhere in the image regardless of whether it touches the object or not. Later, Vese and Chan (2002) extended the active contour model to multi-level set formulation to segment images and denoise signal with more than two phases. The application to dealing with medical images having more than two segments was presented by Chan and Vese (2002).

The level set method has been extensively adopted to capture the interfacial evolution since its inception. However, one major drawback with this method is that it embeds the interface as the zero level set of a function which is one dimension higher, and thus results in expensive computational cost. As such, many efforts have been made to improve the efficiency. Adalsteinsson and Sethian (1995) proposed a technique to adapt the mesh close to the propagating interface, while performing computation only on these points at each step. Peng et al.

14

(1999) developed a fast local level set method by using the information from the level set function and dismissing the need to find explicit location of the interface in space, in which the computational effort has been reduced by one order of magnitude. Song and Chan (2002) approached the Chan-Vese model directly by checking if the energy decreases at each point when changing a point inside the level set to outside and vice versa. In this way, a PDE is not required to be solved and the gradient of the functional is not needed. Recently, Gibou and Fedkiw (2005) made a connection between the Chan-Vese model and k-Means clustering type partitioning, in which the interface evolution processes until no changes of mean image intensity occurring inside and outside the level set function. The k-Means and nonlinear diffusion preprocessor controlling interface smoothness constitute the hybrid k-Means level set algorithm for image segmentation. Using these two methods, the sign of the level set function is considered rather than its value, and this reduces the computational cost.

2.5 Multiscale Modeling of Porous Bone Materials

Trabecular bone is a hierarchical structure with complicated morphology and material heterogeneity due to its porous nature. In the past decades, it has become a subject widely studied in the area of orthopedics and dentistry including bone remodeling and adaptation, age-related bone fracture, and bone implant design, etc. In particular, the mechanical properties of trabecular bones, such as elastic stiffness and strength, have been recognized to vary according to the sampling site, age, and density of the bone selected. The microscopic investigation of trabecular microstructures as a kind of porous composition by considering the variation of solid

15

skeleton and pores provides opportunities for accurately predicting the macroscopic behavior of trabecular bones. Concerning the microstructure of trabecular bones, the scale of pore size is typically about 1 mm, and the scale of solid skeleton (trabecula) is about one order less than that of the pore. The associated microstructural organization leads to the anisotropic material property of trabecular bones, in which the largest elastic stiffness and strength occur in the principal directions. Some recent reviews of bone poroelasticity and trabecular bone mechanics can be found in Cowin (1998) and Keaveny et al. (2001).

Owning to complex topology of the trabecular bone microstructure, previous attempts to simulate the multiscale response from the microstructures have been made on the basis of simplified and idealized models (Williams and Lewis, 1982; Gibson, 1985; Hollister et al., 1991). Although these microstructural models originated from trabecular deformation, they did not predict the experimental results consistently. In particular, the predicted stiffness of trabecular bones was reported to be greater than that of the experimental data (Hollister et al., 1991; Hollister et al., 1994). On the other hand, it has been generally accepted that the microstructural organization affects the strength and stiffness of trabecular bones. This indicates that the trabecular bone stiffness may be overestimated due to reasons such as the simplification in trabecular microstructures and the associated assumptions made in the idealized models. Therefore, a realistic microstructural model considering the variation of solid skeleton and pores should provide a more rational way for simulating the mechanics of trabecular bones.

In the past decades, high resolution digital imaging techniques such as micro-computed tomography (micro-CT) and micro-magnetic resonance imaging (micro-MRI) have evolved to the point where the microstructures of trabecular bones can be surveyed more precisely,

generating the trabecular bone images necessary for a detailed investigation of the associated mechanical properties. One of the major challenges in the unit cell modeling of porous bone materials is the numerical defects introduced by using the finite element method (FEM). For instance, the image-based finite element method converts the pixels into elements in construction of the topology for microstructures, where the jagged interface and sharp corner between different phases may lead to the localized responses, such as stress concentration and solution oscillation on the boundary (Hollister and Riemer, 1993; Hollister and Kikuchi, 1994). When the finite element model is constructed based on the input geometry of images, mesh reconstruction is always required to avoid highly distorted elements and to achieve a smooth mesh, which is commonly done by a mesh decimation method (Hoppe et al., 1993; Podshivalov et al., 2009; Podshivalov et al., 2011) or interpolation between nodes (Ulrich et al., 1998). Furthermore, when reconstructing microstructural models from high-resolution medical images, the images generally come with background noise and fuzzy objects which increase difficulty in the reconstruction process. If the reconstructed models appear to lack representative information, the resulting analysis may lose reliability, thereby leading to incorrect predictions and diagnoses. This points out another critical issue, thresholding in image segmentation, to convert the pixel density from images to the material points for model reconstruction (Hollister and Riemer, 1993; Hollister and Kikuchi, 1994; Podshivalov et al., 2011). Consequently, mesh reconstruction, smoothing solutions, and thresholding techniques are usually unavoidable in the finite element modeling owning to the complexity in geometry encountered. Smoothing procedures such as the Gaussian filter technique (Hollister and Riemer, 1993) and post-processing filtration method (Charras and Guldberg, 2000) have been used to reduce local solution errors in the finite element procedure. The thresholding technique based on the pixel density was given by Kuhn et al.

(1990). An investigation on threshold selection suggested that it is important for the mechanical

properties to be accurately predicted (Hara et al., 2002).

Chapter 3 Mechanics of Poroelasticity

3.1 Introduction

There are two branches of theories of poroelasticity, the theory of porous media (TPM) and Biot's theory. TPM is based on the axioms of continuum theories of mixtures, whereas Biot's theory describes the poroelastic response based on stress equilibrium and mass conservation. The quasi-static Biot's theory will be adopted as the poroelasticity framework in this thesis, and it will be reviewed and discussed in the following sections.

3.2 Quasi-Static Biot's Theory

In the quasi-static Biot's theory, several assumptions have been made. The fluid-saturated porous medium is composed of the solid skeleton and fluid as shown in Figure 3-1, in which the interconnected pores are assumed to be fully saturated with fluid, and the sealed pores are regarded as part of the solid skeleton. Both the solid skeleton and fluid in the pores are assumed to be uniformly distributed. A unit cubic element is introduced to represent the porous medium, which is large enough compared to the size of pores so that the element can be viewed as homogeneous. In the meanwhile, the size of the element is considered to be small enough compared to the scale of macroscopic phenomena so that the element can be treated as infinitesimal in the mathematical formulation (Biot, 1941).
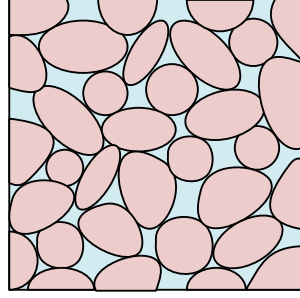
Figure 3-1 Microscopic cubic element of porous materials

Considering Hooke's law for a body made of isotropic elastic materials with Young's modulus E and Poisson's ratio ν, the stress-strain relation is described by

$$\varepsilon_{ij} = \frac{1+\nu}{E}\sigma_{ij} - \frac{\nu}{E}\sigma_{kk}\delta_{ij} \tag{3.1}$$

Let the strain in the porous medium and the variation in fluid content be denoted by ε_{ij} and ξ, respectively. By adopting the assumption of small strain and fluid variation, the stress-strain relation of the porous medium can be taken as linear. Further, by using the fluid pressure p to represent the fluid effect, the strain ε_{ij} in the porous medium can be expressed as

$$\varepsilon_{ij} = \frac{1+\nu}{E}\sigma_{ij} - \frac{\nu}{E}\sigma_{kk}\delta_{ij} + \frac{p}{3H}\delta_{ij} \tag{3.2}$$

where H is a material constant similar to the bulk modulus, which is related to a measure of compressibility of the porous medium and will be described in more detail later on. An essential property of the fluid pressure in (3.2) is that it contributes only to the normal strain components

(ε_{11}, ε_{22}, and ε_{33}) of the porous medium. In a similar way, the general form of the variation in fluid content can be written as

$$\xi = \frac{1}{3H_1}\left(\sigma_{11} + \sigma_{22} + \sigma_{33}\right) + \frac{p}{R} = \frac{1}{3H_1}\sigma_{kk} + \frac{p}{R} \tag{3.3}$$

where H_1 and R are material constants having similar function as the bulk modulus, as will be interpreted later. Assuming that there exists a potential energy density function, and the work done to bring the porous medium to its final state is independent of the path. In this conservative field, the potential energy density function can be expressed as

$$U = \frac{1}{2}\left(\sigma_{ij}\varepsilon_{ij} + p\xi\right) \tag{3.4}$$

Considering (3.2) and (3.3) and taking derivatives of U with respect to σ_{ij} and p separately lead to

$$\frac{\partial U}{\partial \sigma_{ij}} = \varepsilon_{ij}$$
$$\frac{\partial U}{\partial p} = \xi \tag{3.5}$$

Furthermore, differentiating ε_{ij} with respect to p and differentiating ξ with respect to σ_{ij} yield

$$\frac{\partial \varepsilon_{ij}}{\partial p} = \frac{1}{3H}\delta_{ij}$$
$$\frac{\partial \xi}{\partial \sigma_{ij}} = \frac{1}{3H_1}\delta_{ij} \tag{3.6}$$

21

From (3.5) and (3.6), it is observed that $\dfrac{\partial^2 U}{\partial \sigma_{ij}\partial p} = \dfrac{\partial^2 U}{\partial p \partial \sigma_{ij}}$. This gives rise to

$$H = H_1 \tag{3.7}$$

as was pointed out by Biot (1941). Through the use of (3.7), (3.3) can be rewritten as

$$\xi = \frac{1}{3H}\sigma_{kk} + \frac{p}{R} \tag{3.8}$$

By the use of (3.2) and (3.8), one can derive the stress σ_{ij} in the porous medium and the variation in fluid content ξ in terms of the strain ε_{ij} and fluid pressure p as

$$\sigma_{ij} = 2G\varepsilon_{ij} + 2G\frac{v\varepsilon_{kk}}{1-2v}\delta_{ij} - \alpha p \delta_{ij} \tag{3.9}$$

$$\xi = \alpha\varepsilon_{ii} + \frac{p}{M} \tag{3.10}$$

where G is the shear modulus, and the remaining material parameters are defined as

$$\alpha = \frac{2(1+v)}{3(1-2v)}\frac{G}{H} \tag{3.11}$$

$$\frac{1}{M} = \frac{1}{R} - \frac{\alpha}{H} \tag{3.12}$$

in which α is interpreted as the ratio of fluid volume variation to the volume change of the porous medium; $1/M$ is a measure of the amount of fluid that can be forced into the porous medium under pressure, while the volume of the porous medium is kept constant. To interpret the material constants R and H, let us consider a porous medium enclosed in a thin rubber bag

such that the stress applied to the porous medium is zero. Then, the fluid will be drained from the porous medium, and a negative pressure $(-p)$ is applied to the sample. Under this condition, the variation in fluid content (3.8) becomes

$$\xi = -\frac{p}{R} \tag{3.13}$$

where $1/R$ is a measure of the change in fluid content under a given change in fluid pressure. The corresponding volume change of the porous medium in (3.2) reduces to

$$\varepsilon_{kk} = -\frac{p}{H} \tag{3.14}$$

where $1/H$ is a measure of compressibility of the porous medium under a change in fluid pressure. The interpretations of the material constants such as $1/M$, $1/R$, and $1/H$ were given by Biot (1941). From (3.12), (3.13), and (3.14), $1/M$ can be better interpreted as a combination of the compressibility of the porous medium and the compressibility of fluid as a consequence.

3.3 Terzaghi's Effective Stress

The total stress of the porous medium consists of the stresses from two constituents. One is caused by the effective stress in the porous medium, and the other is caused by the hydrostatic pressure of the fluid filling the pores. By defining the total stress of the porous medium as

$$\sigma_{ij}^{t} = 2G\varepsilon_{ij} + 2G\frac{v\varepsilon_{kk}}{1-2v}\delta_{ij} \tag{3.15}$$

One can obtain from (3.9) the effective stress of the porous medium as

$$\sigma_{ij}^{eff} = \sigma_{ij}^{t} - \alpha p \delta_{ij} \tag{3.16}$$

where σ_{ij}^{t} is defined as positive for tension, while the fluid pressure p in the pores is defined as positive for compression, and α is the effective stress coefficient defined in (3.11). By considering the drained and undrained responses of the porous medium and adopting the micromechanical approach, Detournay and Cheng (1993) derived the effective stress coefficient α and $1/M$ in terms of the bulk moduli of materials. The effective stress coefficient is given by

$$\alpha = 1 - \frac{K}{K_s} \tag{3.17}$$

where K and K_s are the bulk moduli of the drained porous medium and the solid skeleton, respectively. Rewriting (3.10) in terms of the displacement field u_i of the porous medium yields

$$\xi = \alpha u_{i,i} + \frac{1}{M} p \tag{3.18}$$

where

$$\frac{1}{M} = \frac{K}{K_s}\left(\frac{1}{K} - \frac{1}{K_s}\right) + \phi\left(\frac{1}{K_f} - \frac{1}{K_s}\right) \tag{3.19}$$

in which K_f is the bulk modulus of the fluid, and ϕ is the porosity defined as the volume of the fluid in the interconnected pores per unit bulk volume. It is worth noting that the case of $K/K_s \leq 1$ accounts for the incompressible solid skeleton and the case of $K/K_f \leq 1$ accounts for

the incompressible fluid, respectively. If both constituents are incompressible, it can be shown that incompressible solid skeleton and fluid gives rise to $\alpha = 1$ and $1/M = 0$ based on (3.17) and (3.19), which are consistent with the results presented by Biot (1961). As a consequence, the effective stress in the porous medium has the following form:

$$\sigma_{ij}^{eff} = \sigma_{ij}^{t} - p\delta_{ij} \tag{3.20}$$

and the variation in fluid content (3.18) reduces to

$$\xi = u_{i,i} \tag{3.21}$$

3.4 Governing Equations in Poroelasticity

3.4.1 Equilibrium Equation of a Porous Medium

To describe the transient phenomenon of a porous medium, the effective stress in the porous medium must satisfy the equilibrium equation given by

$$\sigma_{ij,j}^{eff} = 0 \tag{3.22}$$

where the effective stress is defined in (3.16). Substituting (3.16) into (3.22) leads to

$$\sigma_{ij,j}^{t} - \alpha p_{,i} = 0 \tag{3.23}$$

which is the equilibrium equation of the porous medium. In poroelasticity, the porous medium is assumed to be composed of a linear elastic material with the constitutive law described by

$$\sigma_{ij}^t = C_{ijkl}\varepsilon_{kl} = C_{ijkl}u_{(k,l)} \tag{3.24}$$

where C_{ijkl} is the elasticity tensor.

From (3.23), it is observed that there are three equilibrium equations with four unknown variables u_1, u_2, u_3, and p. Apparently, one more equation that relates fluid pressure p to the fluid motion is needed to describe the system of poroelasticity.

3.4.2 Darcy's Law for a Porous Medium

In a porous medium, the behavior of fluid is described by Darcy's law that governs the flow of fluid. The quasi-static Darcy's law is derived herein. Consider the equation of motion for the fluid:

$$\sigma_{ij,j}^F + \rho b_i = \rho\frac{dv_i}{dt} \tag{3.25}$$

where ρ is the density; b_i and v_i are the body force and velocity of fluid, respectively. For the purpose of describing the fluid motion, we define the stress σ_{ij}^F for a Newtonian fluid as

$$\sigma_{ij}^F = -p\delta_{ij} + f\left(D_{ij}\right) \tag{3.26}$$

where p is the hydrostatic pressure and $f\left(D_{ij}\right)$ is the deviatoric viscous stress defined by the rate of deformation D_{ij} expressed as

$$D_{ij} = \frac{1}{2}\left(\frac{\partial v_i}{\partial x_j} + \frac{\partial v_j}{\partial x_i}\right) \qquad (3.27)$$

The general form of the stress for the Newtonian fluid is given by

$$\sigma_{ij}^{F} = -p\delta_{ij} + 2\mu D_{ij} + \lambda D_{kk}\delta_{ij} \qquad (3.28)$$

where λ is a viscous coefficient and μ is the dynamic viscosity. Substituting (3.28) into (3.25) leads to the generalized Navier-Stokes equation of motion for fluid

$$-p_{,i} + (\lambda + \mu)v_{k,ki} + \mu v_{i,kk} + \rho b_i - \rho \frac{dv_i}{dt} = 0 \qquad (3.29)$$

In (3.29), the first term represents the pressure gradient force, the second and third terms represent the viscous resisting forces, the forth term is the body force, and the last term denotes the inertia force, respectively. If the fluid is assumed to be incompressible (i.e., $v_{k,k} = 0$), (3.29) can be simplified to

$$-p_{,i} + \mu v_{i,kk} + \rho b_i = \rho \frac{dv_i}{dt} \qquad (3.30)$$

which is the Navier-Stokes equation of motion for an incompressible fluid. Further, by assuming stationary flow, the Navier-Stokes equation (3.30) gives rise to the Stokes equation

$$-p_{,i} + \mu v_{i,kk} + \rho b_i = 0 \qquad (3.31)$$

Let the body force be denoted by the gravity g_i. Rewrite (3.31) as

$$-p_{,i} + \mu v_{i,kk} + \rho g_i = 0 \tag{3.32}$$

Recall that the second term in (3.32) is the viscous resisting force, which is assumed to be proportional to the velocity and opposite in direction, as given by

$$\mu v_{i,kk} = -\frac{\mu}{k}\phi v_i \tag{3.33}$$

where ϕ is the porosity and k is the absolute permeability for isotropic materials. Substituting (3.33) into (3.32) leads to Darcy's law as follows:

$$q_i = -\frac{k}{\mu}\left(p_{,i} - \rho g_i\right) \tag{3.34}$$

where q_i is the flux (also called the rate of flow or filtration velocity) defined as $q_i = \phi v_i$ with unit (m/s). Based on (3.34), by neglecting the gravity, the quasi-static Darcy's law for anisotropic materials can be expressed as

$$q_i = -K_{ij} p_{,j} \tag{3.35}$$

where K_{ij} is the hydraulic permeability tensor defined as

$$K_{ij} = \frac{k_{ij}}{\mu} \tag{3.36}$$

where k_{ij} is the absolute permeability tensor. It is noteworthy that Darcy's law is valid for slow and viscous flow, in which the fluid behavior is described as steady flow, and the fluid flux is caused by the pressure gradient. The next step is to relate the fluid pressure gradient to the

deformation of the porous medium via mass conservation (continuity), which will be described in the next section.

3.4.3 Continuity Equation of a Porous Medium

To connect the behaviors of the two phases of the solid skeleton and fluid in a porous medium, the continuity condition on the boundary of a representative cubic element as shown in Figure 3-2 is considered. The derivation of the continuity equation is based on the conservation of mass (Malvern, 1969).
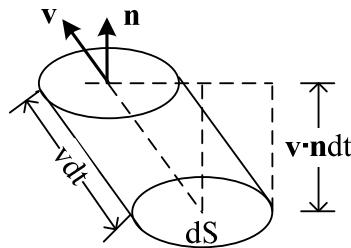
Figure 3-2 Flux across a surface

As shown in Figure 3-2, a flux crossing a surface with an outward normal $\mathbf{n}$ is assumed to be in the positive direction. The volume of fluid flowing through the infinitesimal surface area dS in time dt is equal to the volume of the cylinder with base dS and slant height vdt parallel to the fluid velocity $\mathbf{v}$. The height of the cylinder is $\mathbf{v} \cdot \mathbf{n}dt$ and the volume of fluid is $\mathbf{v} \cdot \mathbf{n}dtdS$. The volume of the flux is defined as

$$\int_S \mathbf{v} \cdot \mathbf{n}dS = \int_S v_i n_i dS \tag{3.37}$$

29

which represents the volume per unit time flowing through dS. The mass flux (rate of mass outflow) is obtained by multiplying the fluid density ρ given by

$$\int_S \rho v_i n_i dS \tag{3.38}$$

For a continuous medium of density ρ filling the volume V in space at time t, the total mass is $M = \int_V \rho dV$. The rate of increase of the total mass in the volume is defined as

$$\frac{\partial M}{\partial t} = \int_V \frac{\partial \rho}{\partial t} dV \tag{3.39}$$

If there is no mass created or diminished in V, the rate of mass increment must equal the rate of mass inflow through the surface. By using the divergence theorem, (3.38) can be rewritten as

$$-\int_S \rho v_i n_i dS = -\int_V (\rho v_i)_{,i} dV \tag{3.40}$$

Applying the rule of conservation of mass and equating (3.39) to (3.40) lead to

$$\int_V \left[\frac{\partial \rho}{\partial t} + (\rho v_i)_{,i} \right] dV = 0 \tag{3.41}$$

which gives rise to the continuity equation as follows:

$$\frac{\partial \rho}{\partial t} + (\rho v_i)_{,i} = 0 \tag{3.42}$$

In a similar way, the continuity equation for a porous medium can be derived. Let ρ denote the fluid density and recall the variation in fluid content ξ (a non-dimensional parameter). The total

mass of fluid in a porous medium is $M = \int_V \rho \xi dV$. The rate of increase of fluid mass is expressed as

$$\frac{\partial M}{\partial t} = \int_V \frac{\partial (\rho \xi)}{\partial t} dV \tag{3.43}$$

The rate of mass inflow can be defined by the flux as

$$-\int_V (\rho q_i)_{,i} dV \tag{3.44}$$

By the conservation of mass, one can equate (3.43) to (3.44), leading to

$$\int_V \left[\frac{\partial (\rho \xi)}{\partial t} + (\rho q_i)_{,i} \right] dV = 0 \tag{3.45}$$

which implies

$$\frac{\partial (\rho \xi)}{\partial t} + (\rho q_i)_{,i} = 0 \tag{3.46}$$

For constant fluid density, the continuity equation is given by

$$\frac{\partial \xi}{\partial t} + q_{i,i} = 0 \tag{3.47}$$

which states that the rate of fluid content must equal the volume of fluid entering the surface of the unit cubic element per second. Substituting the expressions for variation in fluid content in (3.18) and Darcy's law in (3.35) into (3.47) yields

31

$$\left(K_{ij}p_{,j}\right)_{,i} - \alpha\frac{\partial u_{i,i}}{\partial t} - \frac{1}{M}\frac{\partial p}{\partial t} = 0 \qquad (3.48)$$

which is the general form of the continuity equation of a porous medium. This equation relates fluid pressure to the deformation of the porous medium, and thus provides additional equation in addition to the equilibrium equations (3.23) to solve for the complete field and state variables u_1, u_2, u_3, and p in a porous medium.

3.5 Poroelasticity Boundary Value Problem
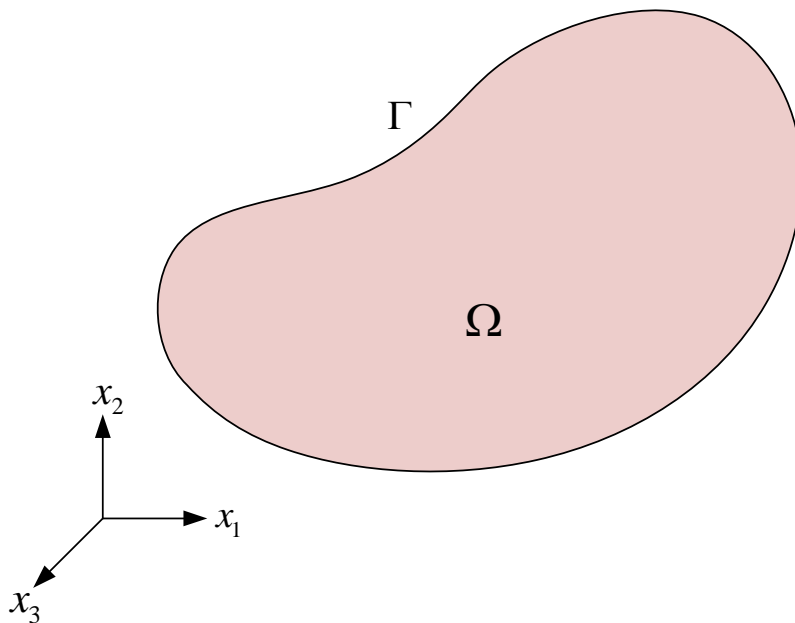
Figure 3-3 A porous medium with domain Ω and boundary Γ

In the quasi-static Biot's theory, a poroelastic medium has been depicted as a homogeneous medium in Figure 3-3, in which Ω and Γ represent the total domain and boundary of the medium, respectively. It is noted that no assumption has been made on the compressibility of the constituents. The general governing equations of porous materials and the associated solid and fluid boundary conditions are summarized in this section.

The equilibrium equation is based on the effective stress of the porous medium in equilibrium, which can be expressed in terms of the total stress and the fluid pressure as

$$\sigma_{ij,j}^t - \alpha p_{,i} = 0 \text{ in } \Omega \tag{3.49}$$

Assuming that the flow is at sufficiently low velocity and the gravity is negligible, Darcy's law can be deduced from the Navier-Stokes equation. Considering Darcy's law and continuity condition of the medium, the continuity equation is given by

$$\left(K_{ij} p_{,j} \right)_{,i} - \alpha \frac{\partial u_{i,i}}{\partial t} - \frac{1}{M} \frac{\partial p}{\partial t} = 0 \text{ in } \Omega \tag{3.50}$$

For the equilibrium equation, the displacement field boundary conditions are

$$\begin{aligned} u_i &= \overline{u}_i & \text{on } \Gamma_u \\ \sigma_{ij}^{eff} n_j &= \overline{t}_i & \text{on } \Gamma_t \end{aligned} \tag{3.51}$$

where Γ_u and Γ_t denote the prescribed displacement and traction boundaries, respectively. Forthe continuity equation, the pressure field boundary conditions are

$$\begin{aligned} p &= -\overline{p} & \text{on } \Gamma_p \\ -K_{ij} p_{,j} &= \overline{q}_i & \text{on } \Gamma_q \end{aligned} \tag{3.52}$$

33

in which Γ_p and Γ_q denote the prescribed fluid pressure and flux boundaries, respectively. The whole boundary is denoted by Γ and the following relation applies

$$\Gamma_t \cap \Gamma_u = \varnothing, \ \Gamma_p \cap \Gamma_q = \varnothing$$
$$\Gamma_t \cup \Gamma_u = \Gamma, \ \Gamma_p \cup \Gamma_q = \Gamma$$

(3.53)

The initial conditions for the transient problem of the porous medium are given by

$$u_i(t=0) = \bar{u}_{0i} \quad \text{in } \Omega$$
$$p(t=0) = \bar{p}_0 \quad \text{in } \Omega$$

(3.54)

Chapter 4 Multiscale Homogenization of Poroelastic Materials

4.1 Introduction

The mathematical theory of homogenization offers an effective and rigorous way to describe media having high degree of material heterogeneity. For the fluid-saturated poroelastic materials composed of solid skeleton and fluid in the pores, the homogenization can be achieved by considering the explicit field equations of each constituent and the associated geometric details. The theory of homogenization was popularized in the 1970s where the applications of composite materials with consideration of microstructural effects began to gain attention. Specifically, the main interest is to determine the effective mechanical properties of composite materials by linking the local features of microstructures to the macroscopic responses. The asymptotic expansion theory was termed the homogenization method and investigated from the aspect of computation by Babuska (1976). Bensoussan and his co-workers (1978) introduced the periodic structures, the so-called unit cells, to the asymptotic analysis. Sanchez-Palencia (1980) applied the mathematical framework to many physics-related problems. Lions (1981) investigated homogenization analysis from the viewpoint of mathematical convergence. Guedes and Kikuchi (1990) introduced weak form formulation to the homogenization method for numerical analysis.

The homogenization method was first applied to composites in solid mechanics. Extension was made to porous materials leading to the generalized Darcy's law that describes the behavior of a

flux flowing through a porous medium. In the homogenization of porous media, fluid viscosity is the key component affecting the interaction between the solid and fluid in the microstructures and their scaling to the macroscopic poroelastic behavior. Different choices of the scaling parameters in the asymptotic homogenization method have been discussed by Sanchez-Palencia (1980) and Hornung (1997) in the literature.

The method of asymptotic expansion relates the microscopic characteristics to the macroscopic behavior of the poroelastic media, and yields leading order equations at different length scales. The procedure of asymptotic expansion based homogenization for the quasi-static deformation of a poroelastic medium with fluid of low viscosity will be detailed in the following sections. The boundary value problem governing the coupled solid and fluid phases in the microstructure is discussed in Section 4.2. The procedure for multiscale homogenization of a poroelastic medium is presented in Section 4.3. A summary of the homogenization results is given in Section 4.4.

4.2 Microscale Poroelasticity

4.2.1 Constitutive Relation in Poroelastic Materials

Consider a porous medium composed of a linearly elastic solid and Newtonian fluid. In particular, the medium is assumed to have interconnected canals filled with incompressible fluid of low viscosity. For a linear elastic material in the solid phase, the stress in the solid is given by

$$\sigma_{ij}^{S} = C_{ijkl}\varepsilon_{kl} = C_{ijkl}u_{(k,l)} \tag{4.1}$$

where u_i is the displacement of the solid skeleton. Recall the general form of the stress for the Newtonian fluid defined in Chapter 3 as

$$\sigma_{ij}^F = -p\delta_{ij} + 2\mu D_{ij} + \lambda D_{kk}\delta_{ij} \qquad (4.2)$$

where p is the fluid pressure; λ and μ are used herein to denote the bulk viscosity and dynamic viscosity, respectively; and D_{ij} is the rate of deformation defined in terms of fluid velocity v_i given as

$$D_{ij} = \frac{1}{2}\left(\frac{\partial v_i}{\partial x_j} + \frac{\partial v_j}{\partial x_i}\right) \equiv v_{(i,j)} \qquad (4.3)$$

Assuming that the fluid is incompressible, the stress in fluid reduces to

$$\sigma_{ij}^F = -p\delta_{ij} + 2\mu v_{(i,j)} \qquad (4.4)$$

4.2.2 Governing Equations in Microscale Poroelasticity

To describe a two-phase poroelastic medium, we consider the following boundary value problem with reference to Figure 4-1:

$$
\begin{aligned}
\sigma_{ij,j}^S + \rho^S b_i^S = 0 & \quad \text{in } \Omega_S \\
u_i = \overline{u}_i & \quad \text{on } \Gamma_{Su} \\
\sigma_{ij}^S n_j^S = \overline{t}_i^{\,S} & \quad \text{on } \Gamma_{St}
\end{aligned}
\qquad (4.5)
$$

which is the equilibrium equation for the solid phase.

$$
\begin{aligned}
&\sigma_{ij,j}^{F} + \rho^{F} b_{i}^{F} = 0 && \text{in } \Omega_{F} \\
&v_{i,i} = 0 && \text{in } \Omega_{F} \\
&v_{i} = \overline{v}_{i} && \text{on } \Gamma_{Fv} \\
&\sigma_{ij}^{F} n_{j}^{F} = \overline{t}_{i}^{F} && \text{on } \Gamma_{Ft}
\end{aligned}
\tag{4.6}
$$

which are the steady-state Stokes equation and continuity equation for the incompressible fluid phase.

Let Γ_{I} denote the solid-fluid interface, the corresponding interface equilibrium condition can be expressed as

$$
\begin{aligned}
&v_{i} = \frac{\partial u_{i}}{\partial t} && \text{on } \Gamma_{I} \\
&\sigma_{ij}^{F} n_{j}^{F} = \sigma_{ij}^{S} n_{j}^{S} && \text{on } \Gamma_{I}
\end{aligned}
\tag{4.7}
$$

where $n_{j}^{F} = -n_{j}^{S}$ on Γ_{I}. With superposed "S" denoting the solid phase and superposed "F" denoting the fluid phase, the parameters used in (4.5)-(4.7) are defined as follows: σ_{ij}^{S} and σ_{ij}^{F} are the stress tensors, ρ^{S} and ρ^{F} denote the density, $\rho^{S} b_{i}^{S}$ and $\rho^{F} b_{i}^{F}$ represent the body force vectors, u_{i} is the solid displacement with the prescribed displacement $\overline{u}_{i}$ on Γ_{Su}, v_{i} is the fluid velocity with the prescribed velocity $\overline{v}_{i}$ on Γ_{Fv}, $\overline{t}_{i}^{S}$ and $\overline{t}_{i}^{F}$ are the surface tractions on Γ_{St} and Γ_{Ft}, respectively, and n_{j}^{S} and n_{j}^{F} are the unit normals on the boundaries.
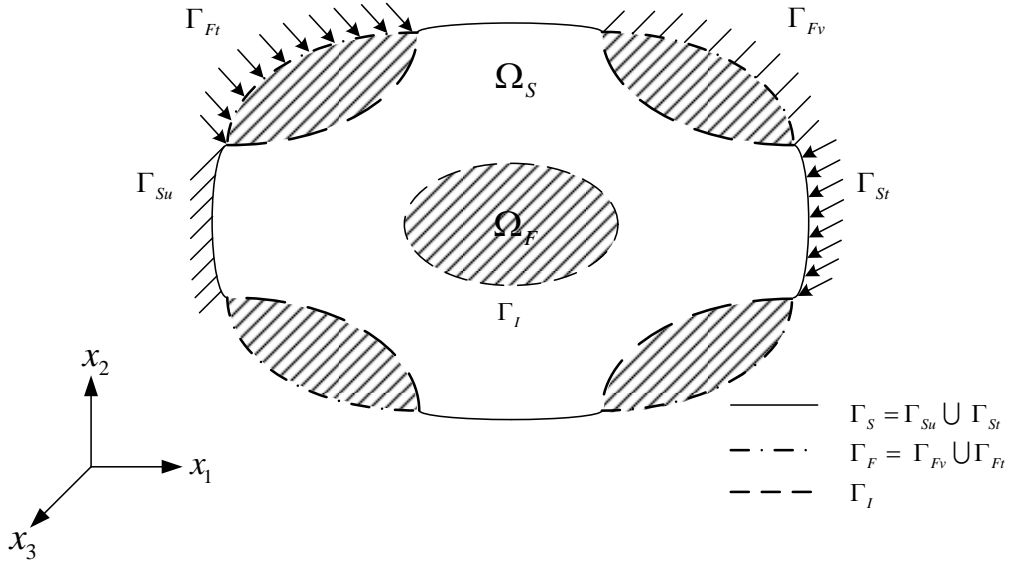
Figure 4-1 A two phase porous medium with boundary and interface conditions

4.2.3 Weak Form Formulation for Poroelastic Materials

The following is a formulation of the weak form expression for the porous medium.

Given the prescribed surface traction $\bar{t}_i^{\,S}$ on Γ_{St} and $\bar{t}_i^{\,F}$ on Γ_{Ft}, the prescribed solid displacement $\bar{u}_i$ on Γ_{Su}, the prescribed fluid velocity $\bar{v}_i$ on Γ_{Fv}, the elastic tensor C_{ijkl} for the solid skeleton, and the dynamic viscosity μ for the fluid, find $u_i \in H^1$, $u_i = \bar{u}_i$ on Γ_{Su}, $v_i \in H^1$, $v_i = \bar{v}_i$ on Γ_{Fv}, $p \in H^0$, for all $w_i \in H^0$, $\varpi_i = 0$ on Γ_{Su} and $w_i = 0$ on Γ_{Fv}, and $\omega \in H^1$, such that

$$-\int_{\Omega_F} p w_{i,i} d\Omega + \int_{\Omega_F} 2\mu v_{(i,j)} w_{i,j} d\Omega = \int_{\Omega_F} \rho^F b_i^F w_i d\Omega + \int_{\Gamma_{Ft}} \bar{t}_i^{\,F} w_i d\Gamma + \int_{\Gamma_I} \sigma_{ij}^S n_j^S w_i d\Gamma \qquad (4.8)$$

$$\int_{\Omega_F} v_{i,i} \omega d\Omega = 0 \qquad (4.9)$$

39

$$\int_{\Omega_S} C_{ijkl} u_{(k,l)} \varpi_{(i,j)} d\Omega = \int_{\Omega_S} \rho^S b_i^S \varpi_i d\Omega + \int_{\Gamma_{St}} \bar{t}_i^S \varpi_i d\Gamma + \int_{\Gamma_I} \sigma_{ij}^F n_j^F \varpi_i d\Gamma \qquad (4.10)$$

where $u_{(i,j)} \equiv \left(u_{i,j} + u_{j,i}\right)/2$. The coupling effect between the solid and fluid phases has been introduced on the interface Γ_I as in (4.8) and (4.10).

4.3 Multiscale Homogenization of a Poroelastic Medium

In the followings, the heterogeneous medium is assumed to be assembled from spatially repeated microstructures as shown in Figure 4-2, where Y denotes the microscopic cell of the porous medium. The macroscopic coordinate $\mathbf{x}$ and the microscopic coordinate $\mathbf{y}$ are related by a scale parameter λ as

$$\mathbf{x} = \lambda \mathbf{y} \qquad (4.11)$$

To present the heterogeneous system, we shall use Ω^λ to denote the total domain of the medium considering heterogeneity and the field variables with superscript λ to denote the total scale of the fields. Rewrite the weak forms in (4.8)-(4.10) with heterogeneity considered as

$$-\int_{\Omega_F^\lambda} p^\lambda w_{i,i} d\Omega + \int_{\Omega_F^\lambda} 2\mu v_{(i,j)}^\lambda w_{i,j} d\Omega = \int_{\Omega_F^\lambda} \rho^F b_i^F w_i d\Omega + \int_{\Gamma_{Ft}} \bar{t}_i^F w_i d\Gamma + \int_{\Gamma_I} \sigma_{ij}^S n_j^S w_i d\Gamma \qquad (4.12)$$

$$\int_{\Omega_F^\lambda} v_{i,i}^\lambda \omega d\Omega = 0 \qquad (4.13)$$

$$\int_{\Omega_S^\lambda} C_{ijkl} u_{(k,l)}^\lambda \varpi_{(i,j)} d\Omega = \int_{\Omega_S^\lambda} \rho^S b_i^S \varpi_i d\Omega + \int_{\Gamma_{St}} \bar{t}_i^S \varpi_i d\Gamma + \int_{\Gamma_I} \sigma_{ij}^F n_j^F \varpi_i d\Gamma \qquad (4.14)$$
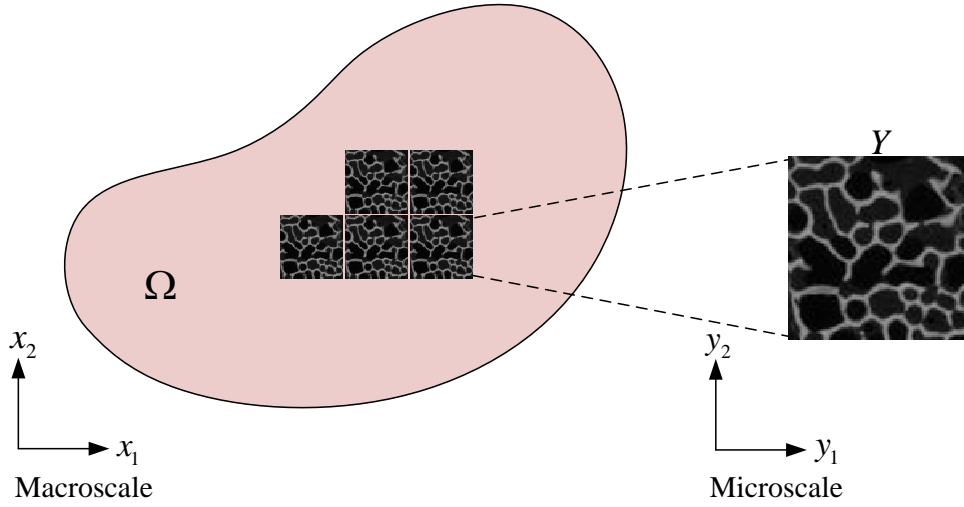
Figure 4-2 Macroscopic and microscopic coordinate systems

4.3.1 Asymptotic Expansion

Based on the assumption of Y-periodicity in a heterogeneous medium, the fields of variables can be expressed as functions of multiple spatial scales to account for the existence of microstructures. By the concept of two-scale decomposition, the unknown variables can be expressed in an asymptotic form as:

$$u_i^{\lambda}(\mathbf{x},t) = u_i^0(\mathbf{x},\mathbf{y},t) + \lambda u_i^1(\mathbf{x},\mathbf{y},t) \tag{4.15}$$

$$v_i^{\lambda}(\mathbf{x},t) = v_i^0(\mathbf{x},\mathbf{y},t) + \lambda v_i^1(\mathbf{x},\mathbf{y},t) \tag{4.16}$$

$$p^{\lambda}(\mathbf{x},t) = p^0(\mathbf{x},\mathbf{y},t) + \lambda p^1(\mathbf{x},\mathbf{y},t) \tag{4.17}$$

where each expanding term is assumed to be a periodic function with respect to the microscopic coordinate $\mathbf{y}$. Without loss of generality, it is assumed that at a fixed point $\mathbf{x}$ at the macroscale,

the composition of microstructures varies in a periodic way. Variables with superscript "0" and "1" are coarse and fine scale components of the variable with superscript " λ ", respectively.

4.3.2 Multiscale Decomposition of Equilibrium Equation

Due to low viscosity assumption, we have $\sigma_{ij}^{S} n_{j}^{S} = p \delta_{ij} n_{j}^{F}$ on the interface. Therefore, the interface traction in (4.14) can be written as $\int_{\Gamma_I} p^{\lambda} n_{i}^{F} \varpi_{i} d\Gamma$. Rewriting (4.14) yields

$$\int_{\Omega_{S}^{\lambda}} C_{ijkl} u_{(k,l)}^{\lambda} \varpi_{(i,j)} d\Omega = \int_{\Omega_{S}^{\lambda}} \rho^{S} b_{i}^{S} \varpi_{i} d\Omega + \int_{\Gamma_{St}} \bar{t}_{i}^{S} \varpi_{i} d\Gamma + \int_{\Gamma_I} p^{\lambda} n_{i}^{F} \varpi_{i} d\Gamma \tag{4.18}$$

By applying the asymptotic expansion given in (4.15), one can derive from (4.18) the following:

$$\int_{\Omega_{S}^{\lambda}} C_{ijkl} \left(u_{(k,l)}^{0} + \lambda u_{(k,l)}^{1} \right) \left(\varpi_{(i,j)}^{0} + \lambda \varpi_{(i,j)}^{1} \right) d\Omega$$
$$= \int_{\Omega_{S}^{\lambda}} \rho^{S} b_{i}^{S} \left(\varpi_{i}^{0} + \lambda \varpi_{i}^{1} \right) d\Omega + \int_{\Gamma_{St}} \bar{t}_{i}^{S} \left(\varpi_{i}^{0} + \lambda \varpi_{i}^{1} \right) d\Gamma + \int_{\Gamma_I} \left(p^{0} + \lambda p^{1} \right) n_{i}^{F} \left(\varpi_{i}^{0} + \lambda \varpi_{i}^{1} \right) d\Gamma \tag{4.19}$$

Under the multiscale framework, the spatial derivative of a function can be derived by the chain rule as follows:

$$\frac{\partial}{\partial x_i} \left(\Phi(\mathbf{x}, \mathbf{y}) \right) = \frac{\partial \Phi}{\partial x_i} + \frac{1}{\lambda} \frac{\partial \Phi}{\partial y_i} \tag{4.20}$$

Applying the multiscale decomposition in (4.20) to (4.19) leads to

$$\int_{\Omega_S^\lambda} C_{ijkl} \left(\frac{\partial u_k^0}{\partial x_l} + \frac{1}{\lambda} \frac{\partial u_k^0}{\partial y_l} + \lambda \frac{\partial u_k^1}{\partial x_l} + \frac{\partial u_k^1}{\partial y_l} \right) \left(\frac{\partial \varpi_i^0}{\partial x_j} + \frac{1}{\lambda} \frac{\partial \varpi_i^0}{\partial y_j} + \lambda \frac{\partial \varpi_i^1}{\partial x_j} + \frac{\partial \varpi_i^1}{\partial y_j} \right) d\Omega$$

$$= \int_{\Omega_S^\lambda} \rho^S b_i^S \left(\varpi_i^0 + \lambda \varpi_i^1 \right) d\Omega + \int_{\Gamma_{St}} \bar{t}_i^S \left(\varpi_i^0 + \lambda \varpi_i^1 \right) d\Gamma + \int_{\Gamma_I} \left(p^0 + \lambda p^1 \right) n_i^F \left(\varpi_i^0 + \lambda \varpi_i^1 \right) d\Gamma \qquad (4.21)$$

The first term in (4.21) can be expanded as the following:

$$\int_{\Omega_S^\lambda} C_{ijkl} \left[\frac{1}{\lambda^2} \frac{\partial u_k^0}{\partial y_l} \frac{\partial \varpi_i^0}{\partial y_j} + \frac{1}{\lambda} \left(\frac{\partial u_k^0}{\partial x_l} \frac{\partial \varpi_i^0}{\partial y_j} + \frac{\partial u_k^1}{\partial y_l} \frac{\partial \varpi_i^0}{\partial y_j} + \frac{\partial u_k^0}{\partial y_l} \frac{\partial \varpi_i^0}{\partial x_j} + \frac{\partial u_k^0}{\partial y_l} \frac{\partial \varpi_i^1}{\partial y_j} \right) \right.$$

$$+ \left(\frac{\partial u_k^1}{\partial x_l} \frac{\partial \varpi_i^0}{\partial y_j} + \frac{\partial u_k^0}{\partial x_l} \frac{\partial \varpi_i^0}{\partial x_j} + \frac{\partial u_k^1}{\partial y_l} \frac{\partial \varpi_i^0}{\partial x_j} + \frac{\partial u_k^0}{\partial y_l} \frac{\partial \varpi_i^1}{\partial x_j} + \frac{\partial u_k^0}{\partial x_l} \frac{\partial \varpi_i^1}{\partial y_j} + \frac{\partial u_k^1}{\partial y_l} \frac{\partial \varpi_i^1}{\partial y_j} \right)$$

$$\left. + \lambda \left(\frac{\partial u_k^1}{\partial x_l} \frac{\partial \varpi_i^0}{\partial x_j} + \frac{\partial u_k^0}{\partial x_l} \frac{\partial \varpi_i^1}{\partial x_j} + \frac{\partial u_k^1}{\partial y_l} \frac{\partial \varpi_i^1}{\partial x_j} + \frac{\partial u_k^1}{\partial x_l} \frac{\partial \varpi_i^1}{\partial y_j} \right) + \lambda^2 \frac{\partial u_k^1}{\partial x_l} \frac{\partial \varpi_i^1}{\partial x_j} \right] d\Omega \qquad (4.22)$$

For a Y-periodic function $\Psi(y)$, it is assumed that the volume average of $\Psi(y)$ is extended to all the volume covered by the unit cell, as described by the following:

$$\lim_{\lambda \to 0^+} \int_{\Omega^\lambda} \Psi \left(\frac{x}{\lambda} \right) d\Omega \to \int_\Omega \frac{1}{|Y|} \int_Y \Psi(y) dY \, d\Omega \qquad (4.23)$$

$$\lim_{\lambda \to 0^+} \lambda \int_{\Gamma^\lambda} \Psi \left(\frac{x}{\lambda} \right) d\Gamma \to \int_\Omega \frac{1}{|Y|} \int_{\partial Y} \Psi(y) d\Gamma \, d\Omega \qquad (4.24)$$

where Γ^λ is the union of the surface of voids; $|Y|$ is the unit cell volume; Y denote the unit cell domain and ∂Y denotes the union of the surface of voids in a unit cell, respectively.

Applying the averaging process over the unit cell (4.24) to the last term on the right hand side of (4.21) yields

43

$$\int_{\Gamma_I} p^0 n_i^F \left(\varpi_i^0 + \lambda \varpi_i^1 \right) d\Gamma = \frac{1}{\lambda} \int_\Omega \frac{1}{|Y|} \int_{\partial Y_I} p^0 n_i^F \varpi_i^0 d\Gamma d\Omega + \int_\Omega \frac{1}{|Y|} \int_{\partial Y_I} p^0 n_i^F \varpi_i^1 d\Gamma d\Omega \qquad (4.25)$$

$$\int_{\Gamma_I} \lambda p^1 n_i^F \left(\varpi_i^0 + \lambda \varpi_i^1 \right) d\Gamma = \int_\Omega \frac{1}{|Y|} \int_{\partial Y_I} p^1 n_i^F \varpi_i^0 d\Gamma d\Omega + \lambda \int_\Omega \frac{1}{|Y|} \int_{\partial Y_I} p^1 n_i^F \varpi_i^1 d\Gamma d\Omega \qquad (4.26)$$

To ensure that the first term on the right hand side of (4.25) is finite, the admissible space for ϖ_i^0 needs to be divergence free in Y. Based on periodicity and divergence theorem, it can be shown that $p^1 = 0$ from (4.26) (Sanchez-Palencia, 1980; Terada et al., 1998).

By substituting $p^1 = 0$, (4.22), and (4.25) into (4.21), collecting terms with the same order λ together and treating u_i^0, u_i^1, and p^0 as independent variables, one can rearrange (4.21) as

$$\int_{\Omega_S^\lambda} C_{ijkl} \left[\frac{1}{\lambda^2} \frac{\partial u_k^0}{\partial y_l} \frac{\partial \varpi_i^0}{\partial y_j} + \frac{1}{\lambda} \left(\frac{\partial u_k^0}{\partial x_l} \frac{\partial \varpi_i^0}{\partial y_j} + \frac{\partial u_k^1}{\partial y_l} \frac{\partial \varpi_i^0}{\partial y_j} + \frac{\partial u_k^0}{\partial y_l} \frac{\partial \varpi_i^0}{\partial x_j} + \frac{\partial u_k^0}{\partial y_l} \frac{\partial \varpi_i^1}{\partial y_j} \right) \right.$$
$$+ \left(\frac{\partial u_k^1}{\partial x_l} \frac{\partial \varpi_i^0}{\partial y_j} + \frac{\partial u_k^0}{\partial x_l} \frac{\partial \varpi_i^0}{\partial x_j} + \frac{\partial u_k^1}{\partial y_l} \frac{\partial \varpi_i^0}{\partial x_j} + \frac{\partial u_k^0}{\partial y_l} \frac{\partial \varpi_i^1}{\partial x_j} + \frac{\partial u_k^0}{\partial x_l} \frac{\partial \varpi_i^1}{\partial y_j} + \frac{\partial u_k^1}{\partial y_l} \frac{\partial \varpi_i^1}{\partial y_j} \right)$$
$$\left. + \lambda \left(\frac{\partial u_k^1}{\partial x_l} \frac{\partial \varpi_i^0}{\partial x_j} + \frac{\partial u_k^0}{\partial x_l} \frac{\partial \varpi_i^1}{\partial x_j} + \frac{\partial u_k^1}{\partial y_l} \frac{\partial \varpi_i^1}{\partial x_j} + \frac{\partial u_k^1}{\partial x_l} \frac{\partial \varpi_i^1}{\partial y_j} \right) + \lambda^2 \frac{\partial u_k^1}{\partial x_l} \frac{\partial \varpi_i^1}{\partial x_j} \right] d\Omega$$
$$= \int_{\Omega_S^\lambda} \rho^S b_i^S \left(\varpi_i^0 + \lambda \varpi_i^1 \right) d\Omega + \int_{\Gamma_{St}} \bar{t}_i^S \left(\varpi_i^0 + \lambda \varpi_i^1 \right) d\Gamma - \int_\Omega \frac{1}{|Y|} \int_{Y_S} p^0 \frac{\partial \varpi_i^1}{\partial y_i} dY d\Omega \qquad (4.27)$$

By taking the limit as $\lambda \to 0^+$ in (4.27), this equation can be decomposed into three sub-equations at different length scales as follows:

$$\frac{1}{\lambda^2} \int_{\Omega_S^\lambda} C_{ijkl} \frac{\partial u_k^0}{\partial y_l} \frac{\partial \varpi_i^0}{\partial y_j} d\Omega = 0 \qquad (4.28)$$

which is known to be the microscale equation.

44

$$\frac{1}{\lambda}\int_{\Omega_S^\lambda} C_{ijkl}\left(\frac{\partial u_k^0}{\partial x_l}\frac{\partial \varpi_i^0}{\partial y_j}+\frac{\partial u_k^1}{\partial y_l}\frac{\partial \varpi_i^0}{\partial y_j}+\frac{\partial u_k^0}{\partial y_l}\frac{\partial \varpi_i^0}{\partial x_j}+\frac{\partial u_k^0}{\partial y_l}\frac{\partial \varpi_i^1}{\partial y_j}\right)d\Omega=0 \tag{4.29}$$

which is the scale-coupling equation.

$$\int_{\Omega_S^\lambda} C_{ijkl}\left(\frac{\partial u_k^1}{\partial x_l}\frac{\partial \varpi_i^0}{\partial y_j}+\frac{\partial u_k^0}{\partial x_l}\frac{\partial \varpi_i^0}{\partial x_j}+\frac{\partial u_k^1}{\partial y_l}\frac{\partial \varpi_i^0}{\partial x_j}+\frac{\partial u_k^0}{\partial y_l}\frac{\partial \varpi_i^1}{\partial x_j}+\frac{\partial u_k^0}{\partial x_l}\frac{\partial \varpi_i^1}{\partial y_j}+\frac{\partial u_k^1}{\partial y_l}\frac{\partial \varpi_i^1}{\partial y_j}\right)d\Omega$$
$$=\int_{\Omega_S^\lambda}\rho^S b_i^S \varpi_i^0 d\Omega+\int_{\Gamma_{St}}\overline{t}_i^S \varpi_i^0 d\Gamma-\int_\Omega \frac{1}{|Y|}\int_{Y_S} p^0 \frac{\partial \varpi_i^1}{\partial y_i}dYd\Omega \tag{4.30}$$

which is the macroscale equation.

By introducing (4.23) to average over the unit cell in (4.28), the microscale equation (4.28) becomes

$$\int_\Omega \frac{1}{|Y|}\int_{Y_S} C_{ijkl}\frac{\partial u_k^0}{\partial y_l}\frac{\partial \varpi_i^0}{\partial y_j}dYd\Omega=0 \quad \forall \varpi_i^0 \in V_{\Omega\times Y_s} \tag{4.31}$$

where Y_S denotes the unit cell domain in solid phase. Since ϖ_i^0 is arbitrary, we can let $\varpi_i^0=\varpi_i^0(\mathbf{y},t)$. Then,

$$\frac{1}{|Y|}\int_{Y_S} C_{ijkl}\frac{\partial u_k^0}{\partial y_l}\frac{\partial \varpi_i^0}{\partial y_j}dY=0 \quad \forall \varpi_i^0 \in V_Y \tag{4.32}$$

which yields

$$u_i^0=u_i^0(\mathbf{x},t) \tag{4.33}$$

By using $u_i^0 = u_i^0(\mathbf{x},t)$ and applying the averaging process (4.23) to (4.29), the scale-coupling equation (4.29) becomes

$$\int_\Omega \frac{1}{|Y|} \int_{Y_S} C_{ijkl} \left(\frac{\partial u_k^0}{\partial x_l} \frac{\partial \varpi_i^0}{\partial y_j} + \frac{\partial u_k^1}{\partial y_l} \frac{\partial \varpi_i^0}{\partial y_j} \right) dYd\Omega = 0 \qquad (4.34)$$

where $\varpi_i^0 = \varpi_i^0(\mathbf{x},t)$ is satisfied.

The averaging process (4.23) together with the fact $u_i^0 = u_i^0(\mathbf{x},t)$ and (4.25) for the interfacial traction enable us to express the macroscale equation (4.30) as

$$\int_\Omega \frac{1}{|Y|} \int_{Y_S} C_{ijkl} \left(\frac{\partial u_k^1}{\partial x_l} \frac{\partial \varpi_i^0}{\partial y_j} + \frac{\partial u_k^0}{\partial x_l} \frac{\partial \varpi_i^0}{\partial x_j} + \frac{\partial u_k^1}{\partial y_l} \frac{\partial \varpi_i^0}{\partial x_j} + \frac{\partial u_k^0}{\partial x_l} \frac{\partial \varpi_i^1}{\partial y_j} + \frac{\partial u_k^1}{\partial y_l} \frac{\partial \varpi_i^1}{\partial y_j} \right) dYd\Omega$$
$$= \int_\Omega \frac{1}{|Y|} \int_{Y_S} \rho^S b_i^S \varpi_i^0 dYd\Omega + \int_{\Gamma_{St}} \bar{t}_i^S \varpi_i^0 d\Gamma - \int_\Omega \frac{1}{|Y|} \int_{Y_S} p^0 \frac{\partial \varpi_i^1}{\partial y_i} dYd\Omega \qquad (4.35)$$

Letting $\varpi_i^0 = \varpi_i^0(\mathbf{x})$, one can write

$$\int_\Omega \frac{1}{|Y|} \int_{Y_S} C_{ijkl} \left(\frac{\partial u_k^0}{\partial x_l} \frac{\partial \varpi_i^0}{\partial x_j} + \frac{\partial u_k^1}{\partial y_l} \frac{\partial \varpi_i^0}{\partial x_j} + \frac{\partial u_k^0}{\partial x_l} \frac{\partial \varpi_i^1}{\partial y_j} + \frac{\partial u_k^1}{\partial y_l} \frac{\partial \varpi_i^1}{\partial y_j} \right) dYd\Omega$$
$$= \int_\Omega \frac{1}{|Y|} \int_{Y_S} \rho^S b_i^S \varpi_i^0 dYd\Omega + \int_{\Gamma_{St}} \bar{t}_i^S \varpi_i^0 d\Gamma - \int_\Omega \frac{1}{|Y|} \int_{Y_S} p^0 \frac{\partial \varpi_i^1}{\partial y_i} dYd\Omega \qquad (4.36)$$

The macroscopic and microscopic equations can be separated from (4.36) as

$$\int_\Omega \frac{1}{|Y|} \int_{Y_S} C_{ijkl} \left(\frac{\partial u_k^0}{\partial x_l} + \frac{\partial u_k^1}{\partial y_l} \right) \frac{\partial \varpi_i^0}{\partial x_j} dYd\Omega = \int_\Omega \frac{1}{|Y|} \int_{Y_S} \rho^S b_i^S \varpi_i^0 dYd\Omega + \int_{\Gamma_{St}} \bar{t}_i^S \varpi_i^0 d\Gamma \qquad (4.37)$$

and

$$\int_\Omega \frac{1}{|Y|} \int_{Y_s} C_{ijkl} \left(\frac{\partial u_k^0}{\partial x_l} + \frac{\partial u_k^1}{\partial y_l} \right) \frac{\partial \varpi_i^1}{\partial y_j} dY d\Omega = -\int_\Omega \frac{1}{|Y|} \int_{Y_s} p^0 \frac{\partial \varpi_i^1}{\partial y_i} dY d\Omega \qquad (4.38)$$

4.3.3 Characteristic Functions and Unit Cell Problems

To relate the coarse-scale and fine-scale variables, the characteristic functions are introduced to describe the coupling response of the deformation at different length scales. Due to the linearity of the problem in (4.38), the solution u_i^1 can be related to the macroscopic variables as (Hornung, 1997; Terada et al., 1998):

$$u_i^1 (\mathbf{x}, \mathbf{y}, t) = -\chi_i^{kl} (\mathbf{y}) \frac{\partial u_k^0 (\mathbf{x}, t)}{\partial x_l} - \eta_i (\mathbf{y}) p^0 (\mathbf{x}, t) \qquad (4.39)$$

where $\chi_i^{kl} (\mathbf{y})$ and $\eta_i (\mathbf{y})$ are the characteristic functions, namely, the scale-coupling functions. Introducing (4.39) to the microscopic equation (4.38) leads to

$$\int_\Omega \frac{1}{|Y|} \int_{Y_s} \left[C_{ijkl} \left(\frac{\partial u_k^0}{\partial x_l} - \frac{\partial \chi_k^{rs}}{\partial y_l} \frac{\partial u_r^0}{\partial x_s} - \frac{\partial \eta_k}{\partial y_l} p^0 \right) + p^0 \delta_{ij} \right] \frac{\partial \varpi_i^1}{\partial y_j} dY d\Omega = 0 \qquad (4.40)$$

which can be arranged as

$$\int_\Omega \frac{1}{|Y|} \left[\int_{Y_s} \left(C_{ijkl} - C_{ijmn} \frac{\partial \chi_m^{kl}}{\partial y_n} \right) \frac{\partial \varpi_i^1}{\partial y_j} dY \frac{\partial u_k^0}{\partial x_l} - \int_{Y_s} \left(C_{ijkl} \frac{\partial \eta_k}{\partial y_l} - \delta_{ij} \right) \frac{\partial \varpi_i^1}{\partial y_j} dY p^0 \right] d\Omega = 0 \qquad (4.41)$$

By collecting all the terms with the same unknown variables u_k^0 and p^0 together, (4.41) can be decomposed into two unit cell problems for the scale-coupling functions as follows:

47

$$\int_{Y_S} C_{ijmn} \frac{\partial \chi_m^{kl}}{\partial y_n} \frac{\partial \varpi_i^1}{\partial y_j} dY = \int_{Y_S} C_{ijkl} \frac{\partial \varpi_i^1}{\partial y_j} dY \tag{4.42}$$

$$\int_{Y_S} C_{ijkl} \frac{\partial \eta_k}{\partial y_l} \frac{\partial \varpi_i^1}{\partial y_j} dY = \int_{Y_S} \delta_{ij} \frac{\partial \varpi_i^1}{\partial y_j} dY \tag{4.43}$$

in which the domain of the solid phase within a unit cell is denoted by Y_S.

Substituting (4.39) into the macroscopic equation in (4.37) gives rise to

$$\int_\Omega \frac{1}{|Y|} \int_{Y_S} \left(C_{ijkl} - C_{ijmn} \frac{\partial \chi_m^{kl}}{\partial y_n} \right) dY \frac{\partial u_k^0}{\partial x_l} \frac{\partial \varpi_i^0}{\partial x_j} d\Omega - \int_\Omega \frac{1}{|Y|} \int_{Y_S} C_{ijkl} \frac{\partial \eta_k}{\partial y_l} dY p^0 \frac{\partial \varpi_i^0}{\partial x_j} d\Omega$$
$$= \int_\Omega \frac{1}{|Y|} \int_{Y_S} \rho^S b_i^S \varpi_i^0 dY d\Omega + \int_{\Gamma_{St}} \bar{t}_i^S \varpi_i^0 d\Gamma \tag{4.44}$$

Based on (4.44), define the homogenized elasticity tensor $\bar{C}_{ijkl}$, the homogenized effective stress

tensor $\bar{\alpha}_{ij}$, and the average body force of the solid phase $\bar{f}_i^S$ are defined as follows:

$$\bar{C}_{ijkl} = \frac{1}{|Y|} \int_{Y_S} \left(C_{ijkl} - C_{ijmn} \frac{\partial \chi_m^{kl}(\mathbf{y})}{\partial y_n} \right) dY \tag{4.45}$$

$$\bar{\alpha}_{ij} = \frac{1}{|Y|} \int_{Y_S} C_{ijkl} \frac{\partial \eta_k(\mathbf{y})}{\partial y_l} dY \tag{4.46}$$

$$\bar{f}_i^S = \frac{1}{|Y|} \int_{Y_S} \rho^S b_i^S dY = \frac{|Y_s|}{|Y|} \rho^S b_i^S \tag{4.47}$$

With the definitions of the homogenized material parameters in (4.45)-(4.47), the homogenized

macroscopic equilibrium equation (4.44) can be recast in its final form as

$$\int_\Omega \bar{C}_{ijkl} \frac{\partial u_k^0}{\partial x_l} \frac{\partial \varpi_i^0}{\partial x_j} d\Omega - \int_\Omega \bar{\alpha}_{ij} p^0 \frac{\partial \varpi_i^0}{\partial x_j} d\Omega = \int_\Omega \bar{f}_i^S \varpi_i^0 d\Omega + \int_{\Gamma_{St}} \bar{t}_i^S \varpi_i^0 d\Gamma \qquad (4.48)$$

4.3.4 Multiscale Decomposition of Stokes Equation

To establish scale decomposition of the stokes equation, we substitute (4.16) and (4.17) into (4.12) to give

$$-\int_{\Omega_F^\lambda} \left(p^0 + \lambda p^1 \right) \left(w_{i,i}^0 + \lambda w_{i,i}^1 \right) d\Omega + \lambda^2 \int_{\Omega_F^\lambda} 2\mu \left(v_{(i,j)}^0 + \lambda v_{(i,j)}^1 \right) \left(w_{(i,j)}^0 + \lambda w_{(i,j)}^1 \right) d\Omega$$
$$= \int_{\Omega_F^\lambda} \rho^F b_i^F \left(w_i^0 + \lambda w_i^1 \right) d\Omega + \int_{\Gamma_{Ft}} \bar{t}_i^F \left(w_i^0 + \lambda w_i^1 \right) d\Gamma + \int_{\Gamma_I} K_S \left(u_{k,k}^0 + \lambda u_{k,k}^1 \right) n_i^S \left(w_i^0 + \lambda w_i^1 \right) d\Gamma \qquad (4.49)$$

For fluid with low viscosity, the scale factor λ^2 for the fluid viscosity μ to account for the viscous effect in comparison with the inertia effect has been introduced (Sanchez-Palencia, 1980; Hornung, 1997; Terada et al., 1998). In addition, it is assumed that the fluid shear stress is negligible due to low viscosity when imposing equilibrium with the solid traction on the interface.

Introducing the multiscale decomposition in (4.20) to (4.49) yields

$$-\int_{\Omega_F^\lambda} \left(p^0 + \lambda p^1 \right) \left(\frac{\partial w_i^0}{\partial x_i} + \frac{1}{\lambda} \frac{\partial w_i^0}{\partial y_i} + \lambda \frac{\partial w_i^1}{\partial x_i} + \frac{\partial w_i^1}{\partial y_i} \right) d\Omega$$
$$+ \lambda^2 \int_{\Omega_F^\lambda} 2\mu \left(\frac{\partial v_i^0}{\partial x_j} + \frac{1}{\lambda} \frac{\partial v_i^0}{\partial y_j} + \lambda \frac{\partial v_i^1}{\partial x_j} + \frac{\partial v_i^1}{\partial y_j} \right) \left(\frac{\partial w_i^0}{\partial x_j} + \frac{1}{\lambda} \frac{\partial w_i^0}{\partial y_j} + \lambda \frac{\partial w_i^1}{\partial x_j} + \frac{\partial w_i^1}{\partial y_j} \right) d\Omega$$
$$= \int_{\Omega_F^\lambda} \rho^F b_i^F \left(w_i^0 + \lambda w_i^1 \right) d\Omega + \int_{\Gamma_{Ft}} \bar{t}_i^F \left(w_i^0 + \lambda w_i^1 \right) d\Gamma$$
$$+ \int_{\Gamma_I} C_{ijkl} \left(\frac{\partial u_k^0}{\partial x_l} + \frac{1}{\lambda} \frac{\partial u_k^0}{\partial y_l} + \lambda \frac{\partial u_k^1}{\partial x_l} + \frac{\partial u_k^1}{\partial y_l} \right) n_j^S \left(w_i^0 + \lambda w_i^1 \right) d\Gamma \qquad (4.50)$$

49

Expanding the second term in (4.50) gives

$$
\begin{aligned}
\int_{\Omega_F^\lambda} 2\mu &\left[\frac{\partial v_i^0}{\partial y_j}\frac{\partial w_i^0}{\partial y_j} + \lambda\left(\frac{\partial v_i^0}{\partial y_j}\frac{\partial w_i^0}{\partial x_j} + \frac{\partial v_i^0}{\partial x_j}\frac{\partial w_i^0}{\partial y_j} + \frac{\partial v_i^1}{\partial y_j}\frac{\partial w_i^0}{\partial y_j} + \frac{\partial v_i^0}{\partial y_j}\frac{\partial w_i^1}{\partial y_j} \right) \right. \\
&+ \lambda^2 \left(\frac{\partial v_i^0}{\partial x_j}\frac{\partial w_i^0}{\partial x_j} + \frac{\partial v_i^1}{\partial y_j}\frac{\partial w_i^0}{\partial x_j} + \frac{\partial v_i^1}{\partial x_j}\frac{\partial w_i^0}{\partial y_j} + \frac{\partial v_i^0}{\partial y_j}\frac{\partial w_i^1}{\partial x_j} + \frac{\partial v_i^0}{\partial x_j}\frac{\partial w_i^1}{\partial y_j} + \frac{\partial v_i^1}{\partial y_j}\frac{\partial w_i^1}{\partial y_j} \right) \\
&\left. + \lambda^3 \left(\frac{\partial v_i^0}{\partial x_j}\frac{\partial w_i^1}{\partial x_j} + \frac{\partial v_i^1}{\partial y_j}\frac{\partial w_i^1}{\partial x_j} + \frac{\partial v_i^1}{\partial x_j}\frac{\partial w_i^0}{\partial x_j} + \frac{\partial v_i^1}{\partial x_j}\frac{\partial w_i^1}{\partial y_j} \right) + \lambda^4 \frac{\partial v_i^1}{\partial x_j}\frac{\partial w_i^1}{\partial x_j} \right] d\Omega
\end{aligned}
\tag{4.51}
$$

Substituting (4.51) back into (4.50) leads to

$$
\begin{aligned}
\int_{\Omega_F^\lambda} &\left\{ -\frac{1}{\lambda} p^0 \frac{\partial w_i^0}{\partial y_i} - \left(p^0 \frac{\partial w_i^0}{\partial x_i} + p^0 \frac{\partial w_i^1}{\partial y_i} + p^1 \frac{\partial w_i^0}{\partial y_i} \right) - \lambda\left(p^0 \frac{\partial w_i^1}{\partial x_i} + p^1 \frac{\partial w_i^0}{\partial x_i} + p^1 \frac{\partial w_i^1}{\partial y_i} \right) \right. \\
&- \lambda^2 p^1 \frac{\partial w_i^1}{\partial x_i} + 2\mu\left[\frac{\partial v_i^0}{\partial y_j}\frac{\partial w_i^0}{\partial y_j} + \lambda\left(\frac{\partial v_i^0}{\partial y_j}\frac{\partial w_i^0}{\partial x_j} + \frac{\partial v_i^0}{\partial x_j}\frac{\partial w_i^0}{\partial y_j} + \frac{\partial v_i^1}{\partial y_j}\frac{\partial w_i^0}{\partial y_j} + \frac{\partial v_i^0}{\partial y_j}\frac{\partial w_i^1}{\partial y_j} \right) \right. \\
&+ \lambda^2 \left(\frac{\partial v_i^0}{\partial x_j}\frac{\partial w_i^0}{\partial x_j} + \frac{\partial v_i^1}{\partial y_j}\frac{\partial w_i^0}{\partial x_j} + \frac{\partial v_i^1}{\partial x_j}\frac{\partial w_i^0}{\partial y_j} + \frac{\partial v_i^0}{\partial y_j}\frac{\partial w_i^1}{\partial x_j} + \frac{\partial v_i^0}{\partial x_j}\frac{\partial w_i^1}{\partial y_j} + \frac{\partial v_i^1}{\partial y_j}\frac{\partial w_i^1}{\partial y_j} \right) \\
&\left.\left. + \lambda^3 \left(\frac{\partial v_i^0}{\partial x_j}\frac{\partial w_i^1}{\partial x_j} + \frac{\partial v_i^1}{\partial y_j}\frac{\partial w_i^1}{\partial x_j} + \frac{\partial v_i^1}{\partial x_j}\frac{\partial w_i^0}{\partial x_j} + \frac{\partial v_i^1}{\partial x_j}\frac{\partial w_i^1}{\partial y_j} \right) + \lambda^4 \frac{\partial v_i^1}{\partial x_j}\frac{\partial w_i^1}{\partial x_j} \right] \right\} d\Omega \\
&= \int_{\Omega_F^\lambda} \rho^F b_i^F \left(w_i^0 + \lambda w_i^1 \right) d\Omega + \int_{\Gamma_{Ft}} \overline{t}_i^F \left(w_i^0 + \lambda w_i^1 \right) d\Gamma \\
&+ \int_{\Gamma_I} C_{ijkl}\left(\frac{\partial u_k^0}{\partial x_l} + \frac{1}{\lambda}\frac{\partial u_k^0}{\partial y_l} + \lambda\frac{\partial u_k^1}{\partial x_l} + \frac{\partial u_k^1}{\partial y_l} \right) n_j^S \left(w_i^0 + \lambda w_i^1 \right) d\Gamma
\end{aligned}
\tag{4.52}
$$

Applying the averaging process over the unit cell (4.24) to the last term in (4.52) gives

$$
\begin{aligned}
\int_{\Gamma_I} C_{ijkl} \frac{\partial u_k^0}{\partial x_l} n_j^S \left(w_i^0 + \lambda w_i^1 \right) d\Gamma &= \frac{1}{\lambda}\int_\Omega \frac{1}{|Y|}\int_{\partial Y_I} C_{ijkl} \frac{\partial u_k^0}{\partial x_l} n_j^S w_i^0 \, d\Gamma d\Omega \\
&+ \int_\Omega \frac{1}{|Y|}\int_{\partial Y_I} C_{ijkl} \frac{\partial u_k^0}{\partial x_l} n_j^S w_i^1 \, d\Gamma d\Omega
\end{aligned}
\tag{4.53}
$$

$$\frac{1}{\lambda}\int_{\Gamma_I} C_{ijkl}\frac{\partial u_k^0}{\partial y_l}n_j^S\left(w_i^0+\lambda w_i^1\right)d\Gamma = \frac{1}{\lambda^2}\int_\Omega \frac{1}{|Y|}\int_{\partial Y_I} C_{ijkl}\frac{\partial u_k^0}{\partial y_l}n_j^S w_i^0 d\Gamma d\Omega$$

$$+\frac{1}{\lambda}\int_\Omega \frac{1}{|Y|}\int_{\partial Y_I} C_{ijkl}\frac{\partial u_k^0}{\partial y_l}n_j^S w_i^1 d\Gamma d\Omega \qquad (4.54)$$

$$\lambda\int_{\Gamma_I} C_{ijkl}\frac{\partial u_k^1}{\partial x_l}n_j^S\left(w_i^0+\lambda w_i^1\right)d\Gamma = \int_\Omega \frac{1}{|Y|}\int_{\partial Y_I} C_{ijkl}\frac{\partial u_k^1}{\partial x_l}n_j^S w_i^0 d\Gamma d\Omega$$

$$+\lambda\int_\Omega \frac{1}{|Y|}\int_{\partial Y_I} C_{ijkl}\frac{\partial u_k^1}{\partial x_l}n_j^S w_i^1 d\Gamma d\Omega \qquad (4.55)$$

$$\int_{\Gamma_I} C_{ijkl}\frac{\partial u_k^1}{\partial y_l}n_j^S\left(w_i^0+\lambda w_i^1\right)d\Gamma = \frac{1}{\lambda}\int_\Omega \frac{1}{|Y|}\int_{\partial Y_I} C_{ijkl}\frac{\partial u_k^1}{\partial y_l}n_j^S w_i^0 d\Gamma d\Omega$$

$$+\int_\Omega \frac{1}{|Y|}\int_{\partial Y_I} C_{ijkl}\frac{\partial u_k^1}{\partial y_l}n_j^S w_i^1 d\Gamma d\Omega \qquad (4.56)$$

To ensure that the first terms in (4.53), (4.54), and (4.56) be finite, the admissible space for w_i^0 needs to be divergence free in Y.

Substituting (4.53)-(4.56) into (4.52), collecting terms with the same order λ together, and treating v_i^0, p^0 and p^1 as independent variables render the following equation:

$$\int_{\Omega_F^\lambda}\left\{-\frac{1}{\lambda}p^0\frac{\partial w_i^0}{\partial y_i}-\left(p^0\frac{\partial w_i^0}{\partial x_i}+p^0\frac{\partial w_i^1}{\partial y_i}+p^1\frac{\partial w_i^0}{\partial y_i}\right)-\lambda\left(p^0\frac{\partial w_i^1}{\partial x_i}+p^1\frac{\partial w_i^0}{\partial x_i}+p^1\frac{\partial w_i^1}{\partial y_i}\right)\right.$$

$$-\lambda^2p^1\frac{\partial w_i^1}{\partial x_i}+2\mu\left[\frac{\partial v_i^0}{\partial y_j}\frac{\partial w_i^0}{\partial y_j}+\lambda\left(\frac{\partial v_i^0}{\partial y_j}\frac{\partial w_i^0}{\partial x_j}+\frac{\partial v_i^0}{\partial x_j}\frac{\partial w_i^0}{\partial y_j}+\frac{\partial v_i^1}{\partial y_j}\frac{\partial w_i^0}{\partial y_j}+\frac{\partial v_i^0}{\partial y_j}\frac{\partial w_i^1}{\partial y_j}\right)\right.$$

$$+\lambda^2\left(\frac{\partial v_i^0}{\partial x_j}\frac{\partial w_i^0}{\partial x_j}+\frac{\partial v_i^1}{\partial y_j}\frac{\partial w_i^0}{\partial x_j}+\frac{\partial v_i^1}{\partial x_j}\frac{\partial w_i^0}{\partial y_j}+\frac{\partial v_i^0}{\partial y_j}\frac{\partial w_i^1}{\partial x_j}+\frac{\partial v_i^0}{\partial x_j}\frac{\partial w_i^1}{\partial y_j}+\frac{\partial v_i^1}{\partial y_j}\frac{\partial w_i^1}{\partial y_j}\right)$$

$$\left.+\lambda^3\left(\frac{\partial v_i^0}{\partial x_j}\frac{\partial w_i^1}{\partial x_j}+\frac{\partial v_i^1}{\partial y_j}\frac{\partial w_i^1}{\partial x_j}+\frac{\partial v_i^1}{\partial x_j}\frac{\partial w_i^0}{\partial x_j}+\frac{\partial v_i^1}{\partial x_j}\frac{\partial w_i^1}{\partial y_j}\right)+\lambda^4\frac{\partial v_i^1}{\partial x_j}\frac{\partial w_i^1}{\partial x_j}\right]\bigg\}d\Omega$$

$$=\int_{\Omega_F^\lambda}\rho^F b_i^F\left(w_i^0+\lambda w_i^1\right)d\Omega+\int_{\Gamma_{Ft}}\bar{t}_i^F\left(w_i^0+\lambda w_i^1\right)d\Gamma+\int_\Omega\frac{1}{|Y|}\int_{\partial Y_I}C_{ijkl}\frac{\partial u_k^0}{\partial x_l}n_j^S w_i^1 d\Gamma d\Omega$$

$$+\frac{1}{\lambda}\int_\Omega\frac{1}{|Y|}\int_{\partial Y_I}C_{ijkl}\frac{\partial u_k^0}{\partial y_l}n_j^S w_i^1 d\Gamma d\Omega+\int_\Omega\frac{1}{|Y|}\int_{\partial Y_I}C_{ijkl}\frac{\partial u_k^1}{\partial x_l}n_j^S w_i^0 d\Gamma d\Omega$$

$$+\lambda\int_\Omega\frac{1}{|Y|}\int_{\partial Y_I}C_{ijkl}\frac{\partial u_k^1}{\partial x_l}n_j^S w_i^1 d\Gamma d\Omega+\int_\Omega\frac{1}{|Y|}\int_{\partial Y_I}C_{ijkl}\frac{\partial u_k^1}{\partial y_l}n_j^S w_i^1 d\Gamma d\Omega \tag{4.57}$$

Assuming that the functions in (4.57) are smooth enough so that the terms with the same order of λ are removed as $\lambda\to0^+$.

$$\int_{\Omega_F^\lambda}\left[-\frac{1}{\lambda}p^0\frac{\partial w_i^0}{\partial y_i}-\left(p^0\frac{\partial w_i^0}{\partial x_i}+p^0\frac{\partial w_i^1}{\partial y_i}+p^1\frac{\partial w_i^0}{\partial y_i}\right)+2\mu\frac{\partial v_i^0}{\partial y_j}\frac{\partial w_i^0}{\partial y_j}\right]d\Omega$$

$$=\int_{\Omega_F^\lambda}\rho^F b_i^F w_i^0 d\Omega+\int_{\Gamma_{Ft}}\bar{t}_i^F w_i^0 d\Gamma$$

$$+\int_\Omega\frac{1}{|Y|}\int_{\partial Y_I}C_{ijkl}\frac{\partial u_k^0}{\partial x_l}n_j^S w_i^1 d\Gamma d\Omega+\frac{1}{\lambda}\int_\Omega\frac{1}{|Y|}\int_{\partial Y_I}C_{ijkl}\frac{\partial u_k^0}{\partial y_l}n_j^S w_i^1 d\Gamma d\Omega$$

$$+\int_\Omega\frac{1}{|Y|}\int_{\partial Y_I}C_{ijkl}\frac{\partial u_k^1}{\partial x_l}n_j^S w_i^0 d\Gamma d\Omega+\int_\Omega\frac{1}{|Y|}\int_{\partial Y_I}C_{ijkl}\frac{\partial u_k^1}{\partial y_l}n_j^S w_i^1 d\Gamma d\Omega \tag{4.58}$$

Therefore, (4.58) can be decomposed into equations at different length scales as follows:

$$-\int_{\Omega_F^\lambda}p^0\frac{\partial w_i^0}{\partial y_i}d\Omega=\int_\Omega\frac{1}{|Y|}\int_{\partial Y_I}C_{ijkl}\frac{\partial u_k^0}{\partial y_l}n_j^S w_i^1 d\Gamma d\Omega \tag{4.59}$$

52

$$\int_{\Omega_F^\lambda} \left[-\left(p^0 \frac{\partial w_i^0}{\partial x_i} + p^0 \frac{\partial w_i^1}{\partial y_i} + p^1 \frac{\partial w_i^0}{\partial y_i} \right) + 2\mu \frac{\partial v_i^0}{\partial y_j} \frac{\partial w_i^0}{\partial y_j} \right] d\Omega$$

$$= \int_{\Omega_F^\lambda} \rho^F b_i^F w_i^0 d\Omega + \int_{\Gamma_{F_t}} \bar{t}_i^F w_i^0 d\Gamma + \int_\Omega \frac{1}{|Y|} \int_{\partial Y_I} C_{ijkl} \frac{\partial u_k^0}{\partial x_l} n_j^S w_i^1 d\Gamma d\Omega \qquad (4.60)$$

$$+ \int_\Omega \frac{1}{|Y|} \int_{\partial Y_I} C_{ijkl} \frac{\partial u_k^1}{\partial x_l} n_j^S w_i^0 d\Gamma d\Omega + \int_\Omega \frac{1}{|Y|} \int_{\partial Y_I} C_{ijkl} \frac{\partial u_k^1}{\partial y_l} n_j^S w_i^1 d\Gamma d\Omega$$

Applying the averaging process over the unit cell to (4.59) yields

$$-\int_\Omega \frac{1}{|Y|} \int_{Y_F} \frac{\partial p^0}{\partial y_i} w_i^0 dY d\Omega = \int_\Omega \frac{1}{|Y|} \int_{\partial Y_I} C_{ijkl} \frac{\partial u_k^0}{\partial y_l} n_j^S w_i^1 d\Gamma d\Omega \qquad (4.61)$$

where Y_F is the domain of the fluid phase within a unit cell. Using the fact $u_i^0 = u_i^0(\mathbf{x}, t)$ in (4.33),

(4.61) implies

$$p^0 = p^0(\mathbf{x}, t) \qquad (4.62)$$

Substituting $p^1 = 0$ into (4.60) yields

$$\int_{\Omega_F^\lambda} \left[-\left(p^0 \frac{\partial w_i^0}{\partial x_i} + p^0 \frac{\partial w_i^1}{\partial y_i} \right) + 2\mu \frac{\partial v_i^0}{\partial y_j} \frac{\partial w_i^0}{\partial y_j} \right] d\Omega$$

$$= \int_{\Omega_F^\lambda} \rho^F b_i^F w_i^0 d\Omega + \int_{\Gamma_{F_t}} \bar{t}_i^F w_i^0 d\Gamma + \int_\Omega \frac{1}{|Y|} \int_{\partial Y_I} C_{ijkl} \frac{\partial u_k^0}{\partial x_l} n_j^S w_i^1 d\Gamma d\Omega \qquad (4.63)$$

$$+ \int_\Omega \frac{1}{|Y|} \int_{\partial Y_I} C_{ijkl} \frac{\partial u_k^1}{\partial x_l} n_j^S w_i^0 d\Gamma d\Omega + \int_\Omega \frac{1}{|Y|} \int_{\partial Y_I} C_{ijkl} \frac{\partial u_k^1}{\partial y_l} n_j^S w_i^1 d\Gamma d\Omega$$

which can be separated by the following macroscopic and microscopic equations:

53

$$\int_{\Omega_F^\lambda}\left(-p^0\frac{\partial w_i^0}{\partial x_i}+2\mu\frac{\partial v_i^0}{\partial y_j}\frac{\partial w_i^0}{\partial y_j}\right)d\Omega$$

$$=\int_{\Omega_F^\lambda}\rho^F b_i^F w_i^0 d\Omega+\int_{\Gamma_{Ft}}\bar{t}_i^F w_i^0 d\Gamma+\int_\Omega\frac{1}{|Y|}\int_{\partial Y_I}C_{ijkl}\frac{\partial u_k^1}{\partial x_l}n_j^S w_i^0 d\Gamma d\Omega \qquad (4.64)$$

and

$$-\int_{\Omega_F^\lambda}p^0\frac{\partial w_i^1}{\partial y_i}d\Omega=\int_\Omega\frac{1}{|Y|}\int_{\partial Y_I}C_{ijkl}\frac{\partial u_k^0}{\partial x_l}n_j^S w_i^1 d\Gamma d\Omega+\int_\Omega\frac{1}{|Y|}\int_{\partial Y_I}C_{ijkl}\frac{\partial u_k^1}{\partial y_l}n_j^S w_i^1 d\Gamma d\Omega \qquad (4.65)$$

Applying the averaging process over the unit cell to (4.64) yields

$$\int_\Omega\frac{1}{|Y|}\int_{Y_F}\left(-p^0\frac{\partial w_i^0}{\partial x_i}+2\mu\frac{\partial v_i^0}{\partial y_j}\frac{\partial w_i^0}{\partial y_j}\right)dY d\Omega$$

$$=\int_\Omega\frac{1}{|Y|}\int_{Y_F}\rho^F b_i^F w_i^0 dY d\Omega+\int_\Omega\frac{1}{|Y|}\int_{\partial Y_I}C_{ijkl}\frac{\partial u_k^1}{\partial x_l}n_j^S w_i^0 d\Gamma d\Omega \qquad (4.66)$$

where the far field traction prescribed on the heterogeneous medium vanishes in the unit cell. Let $w_i^0=w_i^0(\mathbf{y})$, (4.66) becomes

$$\int_\Omega\frac{1}{|Y|}\int_{Y_F}2\mu\frac{\partial v_i^0}{\partial y_j}\frac{\partial w_i^0}{\partial y_j}dY d\Omega$$

$$=\int_\Omega\frac{1}{|Y|}\int_{Y_F}\rho^F b_i^F w_i^0 dY d\Omega+\int_\Omega\frac{1}{|Y|}\int_{\partial Y_I}C_{ijkl}\frac{\partial u_k^1}{\partial x_l}n_j^S w_i^0 d\Gamma d\Omega \qquad (4.67)$$

Applying the divergence theorem to the last term in (4.67) yields

$$\int_\Omega\frac{1}{|Y|}\int_{Y_F}2\mu\frac{\partial v_i^0}{\partial y_j}\frac{\partial w_i^0}{\partial y_j}dY d\Omega$$

$$=\int_\Omega\frac{1}{|Y|}\int_{Y_F}\rho^F b_i^F w_i^0 dY d\Omega-\int_\Omega\frac{1}{|Y|}\int_{Y_F}C_{ijkl}\frac{\partial u_k^1}{\partial y_j\partial x_l}w_i^0 d\Gamma d\Omega \qquad (4.68)$$

54

where w_i^0 satisfies the divergence free condition in Y_F. Substituting the expression for u_k^1 in (4.39) into (4.68) gives

$$\int_\Omega \frac{1}{|Y|} \int_{Y_F} 2\mu \frac{\partial v_i^0}{\partial y_j} \frac{\partial w_i^0}{\partial y_j} dY d\Omega$$
$$= \int_\Omega \frac{1}{|Y|} \int_{Y_F} \rho^F b_i^F w_i^0 dY d\Omega + \int_\Omega \frac{1}{|Y|} \int_{Y_F} C_{ijkl} \left(\frac{\partial \chi_k^{mn}(\mathbf{y})}{\partial y_j} \frac{\partial u_m^0}{\partial x_n \partial x_l} + \frac{\partial \eta_k(\mathbf{y})}{\partial y_j} \frac{\partial p^0}{\partial x_l} \right) w_i^0 d\Gamma d\Omega$$

(4.69)

where we assume that the last force term in (4.69) can be mainly attributed to the pressure gradient in the fluid domain. Therefore, the linearity of the problem in (4.69) implies a solution of the following form (Terada et al., 1998):

$$v_i^0(\mathbf{x},\mathbf{y},t) = \frac{\partial u_i^0(\mathbf{x},t)}{\partial t} + \left(\rho^F b_j^F - \frac{\partial p^0}{\partial x_j} \right) \kappa_{ij}(\mathbf{y})$$

(4.70)

where $\kappa_{ij}(\mathbf{y})$ is the characteristic function related to the hydraulic permeability. Recall the interface condition $v_i = \partial u_i / \partial t$ in (4.7), the second term on the right hand side of (4.70) can be viewed as the relative velocity of fluid with respect to the solid phase, which is zero on the interface and in solid. Substituting (4.70) into (4.69) leads to

$$2\mu \frac{\partial \kappa_{ij}(\mathbf{y})}{\partial y_k \partial y_k} + \delta_{ij} = 0 \quad \text{in } Y_F$$
$$\kappa_{ij}(\mathbf{y}) = 0 \quad \text{on } \partial Y$$

(4.71)

which is the unit cell problem, and $\kappa_{ij}(\mathbf{y})$ is a function characterizing the steady-state Stokes flow within the cell, which is Y-periodic and divergence free.

By averaging over the unit cell on the relative velocity in (4.70), the homogenized macroscopic velocity is given by the generalized Darcy's law

$$\overline{v}_i = \frac{\partial u_i^0(\mathbf{x},t)}{\partial t} - \overline{K}_{ij}\frac{\partial \overline{P}}{\partial x_j} \tag{4.72}$$

where the macroscopic permeability tensor $\overline{K}_{ij}$ and the generalized pressure gradient $\partial \overline{P}/\partial x_j$ are defined as follows:

$$\overline{K}_{ij} = \frac{1}{|Y|}\int_{Y_F} \kappa_{ij}(\mathbf{y})\,dY \tag{4.73}$$

$$\frac{\partial \overline{P}}{\partial x_j} = -\left(\rho_F b_j^F - \frac{\partial p^0(\mathbf{x})}{\partial x_j}\right) \tag{4.74}$$

4.3.5 Multiscale Decomposition of Continuity Equation

Introducing the asymptotic expansion of the fluid velocity in (4.16) and the multiscale decomposition in (4.20) to (4.13) yields

$$\int_{\Omega_F^\lambda}\left(\frac{\partial v_i^0}{\partial x_i} + \frac{1}{\lambda}\frac{\partial v_i^0}{\partial y_i} + \lambda\frac{\partial v_i^1}{\partial x_i} + \frac{\partial v_i^1}{\partial y_i}\right)\omega\,d\Omega = 0 \tag{4.75}$$

Taking the limit as $\lambda \to 0^+$ and substituting v_i^0 in (4.70) into (4.75) gives the macroscopic continuity equation:

$$\int_{\Omega_F^\lambda} \frac{\partial}{\partial x_i}\left(\frac{\partial u_i^0(\mathbf{x},t)}{\partial t}\right)\omega d\Omega + \int_{\Omega_F^\lambda} \frac{\partial}{\partial x_i}\left[\left(\rho_F b_j^F - \frac{\partial p^0(\mathbf{x})}{\partial x_j}\right)\kappa_{ij}(\mathbf{y})\right]\omega d\Omega + \int_{\Omega_F^\lambda}\frac{\partial v_i^1}{\partial y_i}\omega d\Omega = 0 \qquad (4.76)$$

Applying average over the unit cell and assuming $\omega = \omega(\mathbf{x})$ lead to

$$\int_{\Omega} \frac{\partial}{\partial x_i}\left(\frac{\partial u_i^0(\mathbf{x},t)}{\partial t}\right)\omega d\Omega + \int_{\Omega}\frac{1}{|Y|}\int_{Y_F}\frac{\partial}{\partial x_i}\left(\rho^F b_j^F - \frac{\partial p^0(\mathbf{x})}{\partial x_j}\right)\kappa_{ij}(\mathbf{y})dY\omega d\Omega = 0 \qquad (4.77)$$

where the last term in (4.76) can be shown to be zero by periodicity. Based on the definitions of

the permeability tensor $\bar{K}_{ij}$ and the generalized pressure gradient $\partial \bar{P}/\partial x_j$ in (4.73) and (4.74),

respectively, the final form of the homogenized macroscopic continuity equation (4.77) is

$$\int_{\Omega} \frac{\partial}{\partial x_i}\left(\frac{\partial u_i^0(\mathbf{x},t)}{\partial t}\right)\omega d\Omega - \int_{\Omega}\frac{\partial}{\partial x_i}\left(\frac{\partial \bar{P}}{\partial x_j}\right)\bar{K}_{ij}\omega d\Omega = 0 \qquad (4.78)$$

4.3.6 Homogenized Macroscopic Stress

From the homogenized macroscopic equilibrium equation in (4.48), the corresponding strong

form of the homogenized macroscopic equilibrium equation can be derived as

$$\begin{aligned}
\left(\bar{C}_{ijkl}u_{(k,l)}^0 - \bar{\alpha}_{ij}p^0\right)_{,j} + \bar{f}_i^S &= 0 \quad \text{in } \Omega \\
u_i^0 &= \bar{u}_i^0 \qquad\qquad \text{on } \Gamma_u \qquad\qquad (4.79)\\
\left(\bar{C}_{ijkl}u_{(k,l)}^0 - \bar{\alpha}_{ij}p^0\right)n_j &= \bar{t}_i^S \qquad \text{on } \Gamma_t
\end{aligned}$$

from which the homogenized macroscopic stress for the porous medium is given by

$$\bar{\sigma}_{ij} = \bar{C}_{ijkl} u^0_{(k,l)} - \bar{\alpha}_{ij} p^0 \tag{4.80}$$

It is noteworthy that the form of the homogenized macroscopic stress in (4.80) resembles the concept of the effective stress in Biot's theory (Chapter 3).

4.4 Summary of Multiscale Homogenization of Poroelastic Materials

A poroelastic medium composed of an elastic solid and Newtonian fluid of low viscosity has been analyzed by the two-scale asymptotic expansion method. The concept of homogenization provides the homogenized macroscopic equations for describing the behavior of the overall structure, in which the micromechanical response of the interaction between the solid and fluid is considered. In particular, the viscous fluid flow within the microstructure is described by Stokes equation, and the homogenization of Stokes equation leads to the generalized Darcy's law. The homogenized governing equations of poroelastic materials are summarized as follows:

The generalized Darcy's law is given by

$$\bar{v}_i = \frac{\partial u^0_i(\mathbf{x},t)}{\partial t} - \bar{K}_{ij} \frac{\partial \bar{P}}{\partial x_j} \tag{4.81}$$

The homogenized macroscopic continuity equation is

$$\int_\Omega \frac{\partial}{\partial x_i} \left(\frac{\partial u^0_i(\mathbf{x},t)}{\partial t} \right) \omega d\Omega + \int_\Omega \frac{\partial}{\partial x_i} \left(\rho^F b^F_j - \frac{\partial p^0(\mathbf{x})}{\partial x_j} \right) \bar{K}_{ij} \omega d\Omega = 0 \tag{4.82}$$

and the homogenized macroscopic equilibrium equation is

$$\int_\Omega \bar{C}_{ijkl} \frac{\partial u_k^0}{\partial x_l} \frac{\partial \varpi_i^0}{\partial x_j} d\Omega - \int_\Omega \bar{\alpha}_{ij} p^0 \frac{\partial \varpi_i^0}{\partial x_j} d\Omega = \int_\Omega \bar{f}_i^S \varpi_i^0 d\Omega + \int_{\Gamma_{St}} \bar{t}_i^S \varpi_i^0 d\Gamma \qquad (4.83)$$

As shown in (4.81)-(4.83), the macroscopic behavior of a poroelastic medium is governed by the generalized Darcy's law and macroscopic equilibrium equation together with the macroscopic continuity equation, in which an incompressible medium is taken into consideration. Furthermore, (4.81)-(4.83) have a form similar to that of the governing equations in Biot's theory, as discussed in Chapter 3.

The corresponding homogenized material parameters are defined in the following way:

$$\bar{K}_{ij} = \frac{1}{|Y|} \int_{Y_F} \kappa_{ij}(\mathbf{y}) dY \qquad (4.84)$$

$$\frac{\partial \bar{P}}{\partial x_j} = -\left(\rho^F b_j^F - \frac{\partial p^0(\mathbf{x})}{\partial x_j} \right) \qquad (4.85)$$

$$\bar{C}_{ijkl} = \frac{1}{|Y|} \int_{Y_S} \left(C_{ijkl} - C_{ijmn} \frac{\partial \chi_m^{kl}(\mathbf{y})}{\partial y_n} \right) dY \qquad (4.86)$$

$$\bar{\alpha}_{ij} = \frac{1}{|Y|} \int_{Y_S} C_{ijkl} \frac{\partial \eta_k(\mathbf{y})}{\partial y_l} dY \qquad (4.87)$$

$$\bar{f}_i^S = \frac{|Y_S|}{|Y|} \rho^S b_i^S \qquad (4.88)$$

Here $\bar{K}_{ij}$ is the macroscopic permeability tensor, $\partial \bar{P}/\partial x_j$ is the generalized pressure gradient, $\bar{C}_{ijkl}$ the homogenized elasticity tensor, $\bar{\alpha}_{ij}$ the homogenized effective stress tensor, and $\bar{f}_i^S$ the average body force of the solid phase.

Chapter 5 A Gradient Reproducing Kernel Collocation Method for Boundary Value Problems

5.1 Introduction

In the past two decades, significant advancement has been achieved in the development of meshfree methods for solving partial differential equations (PDEs) based on the Galerkin weak formulation. The approximation functions with compact support such as moving least-squares (MLS) (Lancuster and Salkauskas, 1981; Belytschko et al., 1996, 1994) and reproducing kernel (RK) (Liu et al., 1995; Chen et al., 1996) functions are commonly adopted in Galerkin meshfree methods. With monomial reproducing properties in compactly supported MLS and RK, algebraic convergence rates are obtained (Babuska and Melenk, 1997; Han and Meng, 2001) and the discrete systems are well-conditioned. Nonetheless, domain integration of the weak equation adds substantial difficulties and complexities to the Galerkin meshfree methods (Beissel and Belytschko, 1996; Bonet and Kulasegaram, 2000; Chen et al., 2009; Puso et al., 2008; Babuska et al., 2009).

On the other hand, meshfree methods formulated based on the strong form with direct collocation have also been proposed (Kansa, 1992a, 1992b; Onate et al., 1996; Aluru, 2000; Kim and Kim, 2003; Zhang et al., 2001; Hu et al., 2007). This approach reduces the complexities associated with domain integration and the imposition of boundary conditions. The radial basis functions (RBFs) (Hardy, 1971, 1990; Franke, 1982; Madych, 1992) are commonly used in the

strong form collocation method (Kansa, 1992a, 1992b; Hu et al., 2007), generally called the radial basis collocation method (RBCM). While the nonlocal RBFs with certain regularity offer exponential convergence in RBCM (Madych, 1992; Franke and Schaback, 1998; Wendland, 1999), the linear system of RBCM is typically ill-conditioned (Hon and Schaback, 2001; Kansa and Hon, 2000). An alternative approach is the employment of smooth approximation with compact support such as the MLS or RK approximation in the strong form collocation method (Aluru, 2000; Onate et al., 1996; Kim and Kim, 2003; Hu et al., 2011; Hu and Lai, 2009). The reproducing kernel collocation method (RKCM) offers a much better-conditioned discrete system than that of RBCM; nevertheless it converges algebraically (Hu et al., 2011; Hu and Lai, 2009). The work in (Chen et al., 2008) shows that one can construct a localized RBF using a partition of unity function, such as the reproducing kernel enhanced radial basis function, to yield a local approximation while maintaining the exponential convergence in RBCM. This localized RBF, combined with the subdomain collocation method, has been applied to problems with local features, such as problems with heterogeneity (Chen et al., 2009) or cracks (Wang et al., 2010) that are difficult to be solved by RBCM.

It is noteworthy that higher order derivatives of the approximation functions are needed in the strong form collocation method compared to the Galerkin method. While approximation functions such as RK and MLS can be arbitrarily smooth, taking derivatives of these functions is computationally costly, making RKCM less efficient. In particular, the high complexity in RKCM is caused by taking derivatives of the moment matrix inversion in the multi-dimensional RK shape functions, see the detailed complexity and error analysis of RKCM in (Hu and Lai, 2009) and (Hu et al., 2011), respectively. Further, for optimal convergence in RBCM and RKCM, using the number of collocation points much larger than the number of source points is

needed, and this adds additional computational effort (Hu et al., 2007; Hu et al., 2011). Motivated by the above mentioned disadvantages in RKCM, a gradient RK approximation is introduced in solving second order PDEs with strong form collocation, termed the gradient reproducing kernel collocation method (G-RKCM). The gradient RK approximation is formulated based on partition of nullity and derivative reproducing conditions, where similar construction has been introduced in synchronized reproducing kernel approximation (Li and Liu, 1998) and the implicit gradient approximation for localization problems (Chen et al., 2004). Different from (Chen et al., 2004; Li and Liu, 1998) where the gradient RK approximation is used as the enrichment of the standard RK approximation under Galerkin weak formulation, the present approach introduces gradient RK as the "assumed strain" field directly in the strong form. The convergence properties of this G-RKCM approach will be derived, and the complexity of this method in comparison with RKCM will also be analyzed in this chapter.

The chapter is organized as follows. Section 5.2 reviews the basic equations and the fundamental properties of RK approximation and RKCM. In Section 5.3, the gradient RK approximation is introduced, and it application to the strong form to construct G-RKCM discrete equations is presented in Section 5.4. The error analysis of G-RKCM and the choice of collocation points are given in Section 5.5. The complexities of G-RKCM and RKCM are compared in Section 5.6. The numerical examples are given in Section 5.7 to demonstrate the effectiveness of the proposed method. The conclusion remarks of the proposed G-RKCM are presented in Section 5.8.

5.2 Review of Reproducing Kernel Collocation Method

Consider the following boundary value problem:

$$
\begin{aligned}
\mathbf{L}\mathbf{u} &= \mathbf{f} &&\text{in } \Omega \\
\mathbf{B}_h\mathbf{u} &= \mathbf{h} &&\text{on } \partial\Omega_h \\
\mathbf{B}_g\mathbf{u} &= \mathbf{g} &&\text{on } \partial\Omega_g
\end{aligned}
\tag{5.1}
$$

where Ω is the problem domain, $\partial\Omega_h$ is the Neumann boundary, $\partial\Omega_g$ is the Dirichlet boundary, $\partial\Omega = \partial\Omega_h \cup \partial\Omega_g$, $\mathbf{L}$ is the differential operator in Ω, and $\mathbf{B}_h$ and $\mathbf{B}_g$ are the boundary operators on $\partial\Omega_h$ and $\partial\Omega_g$, respectively. To solve (5.1) by strong form collocation, the reproducing kernel approximation of $\mathbf{u}$, denoted by $\mathbf{v}$, is expressed as

$$
\mathbf{u}(\mathbf{x}) \approx \mathbf{v}(\mathbf{x}) = \sum_{I=1}^{N_s} \Psi_I(\mathbf{x}) \mathbf{a}_I
\tag{5.2}
$$

where N_s is the number of source points, and $\Psi_I(\mathbf{x})$ is the reproducing kernel (RK) shape function expressed as

$$
\Psi_I(\mathbf{x}) = C(\mathbf{x}; \mathbf{x} - \mathbf{x}_I) \varphi_a(\mathbf{x} - \mathbf{x}_I)
\tag{5.3}
$$

where $\varphi_a(\mathbf{x} - \mathbf{x}_I)$ is the kernel function, and $C(\mathbf{x}; \mathbf{x} - \mathbf{x}_I)$ is the correction function:

$$
\begin{aligned}
C(\mathbf{x}; \mathbf{x} - \mathbf{x}_I) &= \sum_{|\alpha|=0}^{p} b_\alpha(\mathbf{x})(\mathbf{x} - \mathbf{x}_I)^\alpha, \quad p \geq 0 \\
&=: \mathbf{H}^{\mathrm{T}}(\mathbf{x} - \mathbf{x}_I)\mathbf{b}(\mathbf{x})
\end{aligned}
\tag{5.4}
$$

Here we introduce the multi index notation in d-dimension $\alpha = (\alpha_1, \alpha_2, \ldots, \alpha_d)$, with the length of

α defined as $|\alpha| = \sum_{i=1}^{d} \alpha_i$, $\mathbf{x}^\alpha \equiv x_1^{\alpha_1} \cdot x_2^{\alpha_2} \cdots x_d^{\alpha_d}$, $\mathbf{x}^\alpha_I \equiv x_{1I}^{\alpha_1} \cdot x_{2I}^{\alpha_2} \cdots x_{dI}^{\alpha_d}$,

$(\mathbf{x} - \mathbf{x}_I)^\alpha \equiv (x_1 - x_{1I})^{\alpha_1} (x_2 - x_{2I})^{\alpha_2} \cdots (x_d - x_{dI})^{\alpha_d}$, and $b_\alpha \equiv b_{\alpha_1, \alpha_2, \ldots, \alpha_d}$. The vectors $\mathbf{H}^{\mathrm{T}}(\mathbf{x} - \mathbf{x}_I)$ and

$\mathbf{b}^{\mathrm{T}}(\mathbf{x})$ are the corresponding row vectors of $\{(\mathbf{x} - \mathbf{x}_I)^\alpha\}_{|\alpha| \le p}$ and $\{b_\alpha(\mathbf{x})\}_{|\alpha| \le p}$, respectively. The

shape functions are required to satisfy p-th order reproducing conditions given as follows:

$$\sum_I \Psi_I(\mathbf{x}) \mathbf{x}^\alpha_I = \mathbf{x}^\alpha, \quad |\alpha| \le p \tag{5.5}$$

The coefficients $\mathbf{b}(\mathbf{x})$ are obtained by satisfying (5.5), and it yields the following RK shape

function:

$$\Psi_I(\mathbf{x}) = \mathbf{H}^{\mathrm{T}}(\mathbf{0}) \mathbf{M}^{-1}(\mathbf{x}) \mathbf{H}(\mathbf{x} - \mathbf{x}_I) \varphi_a(\mathbf{x} - \mathbf{x}_I) \tag{5.6}$$

and

$$\mathbf{M}(\mathbf{x}) = \sum_{I=1}^{N_s} \mathbf{H}(\mathbf{x} - \mathbf{x}_I) \mathbf{H}^{\mathrm{T}}(\mathbf{x} - \mathbf{x}_I) \varphi_a(\mathbf{x} - \mathbf{x}_I) \tag{5.7}$$

Introducing RK approximation of $\mathbf{u}$ in (5.2) to the strong form in (5.1), and evaluating the

differential equation and boundary conditions at the collocation points $\mathbf{p}_\ell \in \Omega$, $\mathbf{q}_\ell \in \partial\Omega_h$, and

$\mathbf{r}_\ell \in \partial\Omega_g$, we have the following collocation equations:

$$\mathbf{Lv}(\mathbf{p}_\ell) = \mathbf{f}(\mathbf{p}_\ell) \quad \forall \, \mathbf{p}_\ell \in \Omega, \qquad \ell = 1, \cdots, N_p$$
$$\mathbf{B}_h \mathbf{v}(\mathbf{q}_\ell) = \mathbf{h}(\mathbf{q}_\ell) \quad \forall \, \mathbf{q}_\ell \in \partial\Omega_h, \quad \ell = 1, \cdots, N_q \qquad (5.8)$$
$$\mathbf{B}_g \mathbf{v}(\mathbf{r}_\ell) = \mathbf{g}(\mathbf{r}_\ell) \quad \forall \, \mathbf{r}_\ell \in \partial\Omega_g, \quad \ell = 1, \cdots, N_r$$

Collection of the collocation equations yields the following linear system:

$$\mathbf{Aa} = \mathbf{b} \qquad (5.9)$$

where $\mathbf{A} = \mathbf{A}\left((\mathbf{L\Psi})_{\mathbf{p}_\ell}, (\mathbf{B}_h\mathbf{\Psi})_{\mathbf{q}_\ell}, (\mathbf{B}_g\mathbf{\Psi})_{\mathbf{r}_\ell} \right)$ and $\mathbf{b} = \mathbf{b}\left((\mathbf{f})_{\mathbf{p}_\ell}, (\mathbf{h})_{\mathbf{q}_\ell}, (\mathbf{g})_{\mathbf{r}_\ell} \right)$ $\forall \, \mathbf{p}_\ell \in \Omega$, $\mathbf{q}_\ell \in \partial\Omega_h$,

and $\mathbf{r}_\ell \in \partial\Omega_g$. Note that the total number of collocation points $N_p + N_q + N_r$ is typically much

larger than the number of source points N_s for optimal convergence, and hence yields an over-

determined system in (5.9).

Remake 5.1

The collocation equations in (5.8) can be shown to be equivalent to the minimization of the

following least-squares functional with quadrature (Hu et al., 2007), that is, to seek solution

$\mathbf{u}^r \in V = span\{\Psi_1, \cdots, \Psi_{N_s}\}$, *such that*

$$E(\mathbf{u}^r) = \inf_{\mathbf{v} \in V} E(\mathbf{v}) \qquad (5.10)$$

where

$$E(\mathbf{v}) = \frac{1}{2}\int_\Omega (\mathbf{Lv} - \mathbf{f})^{\mathrm{T}}(\mathbf{Lv} - \mathbf{f})d\Omega + \frac{1}{2}\int_{\partial\Omega_h}(\mathbf{B}_h\mathbf{v} - \mathbf{h})^{\mathrm{T}}(\mathbf{B}_h\mathbf{v} - \mathbf{h})d\Gamma$$
$$+ \frac{1}{2}\int_{\partial\Omega_g}(\mathbf{B}_g\mathbf{v} - \mathbf{g})^{\mathrm{T}}(\mathbf{B}_g\mathbf{v} - \mathbf{g})d\Gamma \qquad (5.11)$$

By choosing the quadrature points in (5.11) the same as the collocation points in (5.8) in solving (5.9) by a weighted least-squares method, the equivalence between the solution by minimization of (5.11) and the solution of (5.9) can be established; see (Hu et al., 2007) for details.

Remake 5.2

To keep the balance of errors in the domain and boundary terms in the least-squares functional, a weighted least-squares functional has been proposed (Hu et al., 2007; Hu et al., 2011):

$$E(\mathbf{v}) = \frac{1}{2} \int_{\Omega} (\mathbf{Lv} - \mathbf{f})^{\mathrm{T}} (\mathbf{Lv} - \mathbf{f}) d\Omega + \frac{\alpha_h}{2} \int_{\partial \Omega_h} (\mathbf{B}_h \mathbf{v} - \mathbf{h})^{\mathrm{T}} (\mathbf{B}_h \mathbf{v} - \mathbf{h}) d\Gamma$$
$$+ \frac{\alpha_g}{2} \int_{\partial \Omega_g} (\mathbf{B}_g \mathbf{v} - \mathbf{g})^{\mathrm{T}} (\mathbf{B}_g \mathbf{v} - \mathbf{g}) d\Gamma$$

$$(5.12)$$

where the weights $\sqrt{\alpha_h} = 1$ *,* $\sqrt{\alpha_g} = \kappa N_s$ *, with* $\kappa = 1$ *for Poisson problem and* $\kappa = \max\{\lambda, \mu\}$ *for elasticity for optimal convergence have been proposed. A set of equivalent collocation equations can be obtained:*

$$\mathbf{Lv}(\mathbf{p}_\ell) = \mathbf{f}(\mathbf{p}_\ell) \qquad \forall \, \mathbf{p}_\ell \in \Omega, \qquad \ell = 1, \cdots, N_p$$
$$\alpha_h \mathbf{B}_h \mathbf{v}(\mathbf{q}_\ell) = \alpha_h \mathbf{h}(\mathbf{q}_\ell) \quad \forall \, \mathbf{q}_\ell \in \partial \Omega_h, \quad \ell = 1, \cdots, N_q$$
$$\alpha_g \mathbf{B}_g \mathbf{v}(\mathbf{r}_\ell) = \alpha_g \mathbf{g}(\mathbf{r}_\ell) \quad \forall \, \mathbf{r}_\ell \in \partial \Omega_g, \quad \ell = 1, \cdots, N_r$$

$$(5.13)$$

This RKCM converges in the following norm (Hu et al., 2011):

$$\left\| \mathbf{u} - \mathbf{u}^r \right\| \le C \left\{ \left\| \mathbf{u} - \mathbf{v} \right\|_{2,\Omega} + \left\| (\mathbf{u} - \mathbf{v})_n \right\|_{0,\partial \Omega_h} + \left\| \mathbf{u} - \mathbf{v} \right\|_{0,\partial \Omega_g} \right\}$$
$$\le C \kappa a^{p-1} \left| \mathbf{u} \right|_{p+1,\Omega}$$

$$(5.14)$$

where C is a genetic constant and κ *is the overlapping number.*

This result indicates that for RKCM to converge, the RK approximation of degree $p \ge 2$ *needs to be used.*

5.3 Gradient Reproducing Kernel Approximation

Strong form collocation for second order differential equations requires taking second order differentiation on the RK shape functions of (5.6), which is time consuming, especially in calculating higher order derivatives of $\mathbf{M}^{-1}(\mathbf{x})$ at every evaluation point x. In this work, we consider the approximation of $\mathbf{u}_{,\beta}$ as follows:

$$\mathbf{u}_{,\beta} \approx \mathbf{w}_{\beta} = \sum_{I=1}^{N_s} \Psi_I^{\beta}(\mathbf{x}) \mathbf{a}_I \tag{5.15}$$

where

$$\Psi_I^{\beta}(\mathbf{x}) = C^{\beta}(\mathbf{x}; \mathbf{x} - \mathbf{x}_I) \varphi_a(\mathbf{x} - \mathbf{x}_I) \tag{5.16}$$

and $\beta = (\beta_1, \beta_2, \ldots, \beta_d)$, $|\beta| = \sum_{i=1}^{d} \beta_i \le k$ for $\Psi_I^{\beta} \in C^k$.

Here the correction functions in (5.16) are constructed with monomial bases of degree q:

$$
\begin{aligned}
C^{\beta}(\mathbf{x}; \mathbf{x} - \mathbf{x}_I) &= \sum_{|\alpha|=0}^{q} b_{\alpha}^{\beta}(\mathbf{x})(\mathbf{x} - \mathbf{x}_I)^{\alpha}, \quad q \ge 0 \\
&=: \mathbf{H}^{\mathrm{T}}(\mathbf{x} - \mathbf{x}_I) \mathbf{b}^{\beta}(\mathbf{x})
\end{aligned}
\tag{5.17}
$$

The coefficients b_{α}^{β} are obtained from the following gradient reproducing conditions:

$$\sum_{I=1}^{N_s} \Psi_I^{\beta} \mathbf{x}_I^{\alpha} = D^{\beta} \mathbf{x}^{\alpha}, \quad 0 \le |\alpha| \le q \tag{5.18}$$

where $D^\beta \equiv \partial^{\beta_1} / \partial^{\beta_1} x_1 \cdot \partial^{\beta_2} / \partial^{\beta_2} x_2 \ldots \partial^{\beta_d} / \partial^{\beta_d} x_d$. As shown in (Liu et al., 1997), (5.18) is

equivalent to

$$\sum_{I=1}^{N_s} \Psi_I^\beta \left(\mathbf{x} - \mathbf{x}_I\right)^\alpha = \left(-1\right)^{|\beta|} D^\beta \mathbf{H}\left(\mathbf{0}\right) \tag{5.19}$$

where

$$D^\beta \mathbf{H}\left(\mathbf{x}\right) = \frac{\alpha!}{\left(\alpha - \beta\right)!} \mathbf{x}^{\alpha - \beta} \tag{5.20}$$

and

$$D^\beta \mathbf{H}\left(\mathbf{0}\right) = \alpha! \delta_{\beta\alpha} \tag{5.21}$$

Substituting (5.17) into (5.19) gives rise to

$$\mathbf{M}\left(\mathbf{x}\right)\mathbf{b}^\beta\left(\mathbf{x}\right) = \left(-1\right)^{|\beta|} D^\beta \mathbf{H}\left(\mathbf{0}\right) \tag{5.22}$$

where $\mathbf{M}\left(\mathbf{x}\right)$ is the moment matrix given in (5.7). Consequently the gradient RK shape functions

are obtained as

$$\Psi_I^\beta\left(\mathbf{x}\right) = \left(-1\right)^{|\beta|} D^\beta \mathbf{H}^T\left(\mathbf{0}\right) \mathbf{M}^{-1}\left(\mathbf{x}\right) \mathbf{H}\left(\mathbf{x} - \mathbf{x}_I\right) \varphi_a\left(\mathbf{x} - \mathbf{x}_I\right) \tag{5.23}$$

It is noted that $\mathbf{M}\left(\mathbf{x}\right)$ is the Gram matrix of basis functions $\mathbf{H}\left(\mathbf{x} - \mathbf{x}_I\right)$ with respect to

$\varphi_a\left(\mathbf{x} - \mathbf{x}_I\right)$. The positivity of the kernel function $\varphi_a\left(\mathbf{x} - \mathbf{x}_I\right)$ ensures the positive definiteness of

$\mathbf{M}\left(\mathbf{x}\right)$. In this work, $\varphi_a\left(\mathbf{x} - \mathbf{x}_I\right)$ is chosen to be the quintic B-spline kernel function:

$$\varphi_a\left(s\right)=\begin{cases}\dfrac{11}{20}-\dfrac{9s^2}{2}+\dfrac{81s^4}{4}-\dfrac{81s^5}{4}, & 0\le s<\dfrac{1}{3},\\[3mm]\dfrac{17}{40}+\dfrac{15s}{8}-\dfrac{63s^2}{4}+\dfrac{135s^3}{4}-\dfrac{243s^4}{8}+\dfrac{81s^5}{8}, & \dfrac{1}{3}\le s<\dfrac{2}{3},\\[3mm]\dfrac{81}{40}-\dfrac{81s}{8}+\dfrac{81s^2}{4}-\dfrac{81s^3}{4}+\dfrac{81s^4}{8}-\dfrac{81s^5}{40}, & \dfrac{2}{3}\le s<1,\\[3mm]0, & s\ge 1,\end{cases}\qquad s=\dfrac{\left\|\mathbf{x}-\mathbf{x}_I\right\|}{a}\qquad(5.24)$$

where s is the normalized nodal distance.

If equal order bases are used in the approximation of $\mathbf{u}$ and $\mathbf{u}_{,\beta}$, the term $\mathbf{M}^{-1}\left(\mathbf{x}\right)$ is identical in all shape functions Ψ_I and Ψ_I^{β}. Furthermore, by comparing the shape function for $\mathbf{u}$ in (5.6) and the shape functions for $\mathbf{u}_{,\beta}$ in (5.23), it appears that $\mathbf{H}^{\mathrm{T}}\left(\mathbf{0}\right)$ in (5.6) is replaced by $\left(-1\right)^{|\beta|}D^{\beta}\mathbf{H}^{T}\left(\mathbf{0}\right)$ in (5.23), leading to a significant time saving in computing Ψ_I^{β} compared to a direct differentiation of Ψ_I.

For sake of simplicity but without loss of generality, we consider two-dimensional problems in this study. The approximation of $\mathbf{u}_{,x}$ and $\mathbf{u}_{,y}$ denoted as follows will be used in the following sections and the simplified derivation of Ψ_I^x and Ψ_I^y is given in Appendix A.

$$\begin{aligned}\mathbf{u}_{,x}&\approx\mathbf{w}_x=\sum_{I=1}^{N_s}\Psi_I^x\left(\mathbf{x}\right)\mathbf{a}_I\\\mathbf{u}_{,y}&\approx\mathbf{w}_y=\sum_{I=1}^{N_s}\Psi_I^y\left(\mathbf{x}\right)\mathbf{a}_I\end{aligned}\qquad(5.25)$$

Hence, the second order derivatives of $\mathbf{u}$ is obtained by taking direct derivatives of $\mathbf{w}_x$ and $\mathbf{w}_y$, i.e.,

$$\mathbf{u}_{,xx} \approx \mathbf{w}_{x,x} = \sum_{I=1}^{N_s} \Psi_{I,x}^x(\mathbf{x}) \mathbf{a}_I$$

$$\mathbf{u}_{,yy} \approx \mathbf{w}_{y,y} = \sum_{I=1}^{N_s} \Psi_{I,y}^y(\mathbf{x}) \mathbf{a}_I$$

(5.26)

5.4 Gradient Reproducing Kernel Collocation Method (G-RKCM)

To introduce gradient RK approximation in the discretization of strong form, consider the following boundary value problem:

$$\begin{aligned}
\mathbf{L}^1\mathbf{u}_{,x} + \mathbf{L}^2\mathbf{u}_{,y} &= \mathbf{f} & \text{in } \Omega \\
\mathbf{B}_h^1\mathbf{u}_{,x} + \mathbf{B}_h^2\mathbf{u}_{,y} &= \mathbf{h} & \text{on } \partial\Omega_h \\
\mathbf{B}_g\mathbf{u} &= \mathbf{g} & \text{on } \partial\Omega_g
\end{aligned}$$

(5.27)

where $\mathbf{L}^1$ and $\mathbf{L}^2$ are the differential operators in Ω, $\mathbf{B}_h^1$ and $\mathbf{B}_h^2$ are the boundary operators on $\partial\Omega_h$, and $\mathbf{B}_g$ is the boundary operator on $\partial\Omega_g$. The explicit forms of the operators and vectors for Poisson and elasticity problems in two-dimension are given in Table 5-1. The approximations of $\mathbf{u}$, $\mathbf{u}_{,x}$ and $\mathbf{u}_{,y}$ are given as:

$$\begin{aligned}
\mathbf{u} &\approx \mathbf{v} = \mathbf{\Psi}^{\mathrm{T}}\mathbf{a} \\
\mathbf{u}_{,x} &\approx \mathbf{w}_x = \mathbf{\Psi}^{x^{\mathrm{T}}}\mathbf{a} \\
\mathbf{u}_{,y} &\approx \mathbf{w}_y = \mathbf{\Psi}^{y^{\mathrm{T}}}\mathbf{a}
\end{aligned}$$

(5.28)

where $\mathbf{\Psi}$, $\mathbf{\Psi}^x$, $\mathbf{\Psi}^y$, and $\mathbf{a}$ are the vector forms of $\{\Psi_I\}_{I=1}^{N_s}$, $\{\Psi_I^x\}_{I=1}^{N_s}$, $\{\Psi_I^y\}_{I=1}^{N_s}$ and $\mathbf{a}_I$, respectively.

70

Table 5-1 Explicit forms of operators for Poisson and elasticity problems in two-dimension

Operator	Poisson's Problem	Elasticity Problem
L^1	$\dfrac{\partial}{\partial x}$	$\begin{bmatrix} (\lambda+2\mu)\dfrac{\partial}{\partial x} & \mu\dfrac{\partial}{\partial y} \\ \lambda\dfrac{\partial}{\partial y} & \mu\dfrac{\partial}{\partial x} \end{bmatrix}$
L^2	$\dfrac{\partial}{\partial y}$	$\begin{bmatrix} \mu\dfrac{\partial}{\partial y} & \lambda\dfrac{\partial}{\partial x} \\ \mu\dfrac{\partial}{\partial x} & (\lambda+2\mu)\dfrac{\partial}{\partial y} \end{bmatrix}$
B_h^1	n_x	$\begin{bmatrix} (\lambda+2\mu)n_x & \mu n_y \\ \lambda n_y & \mu n_x \end{bmatrix}$
B_h^2	n_y	$\begin{bmatrix} \mu n_y & \lambda n_x \\ \mu n_x & (\lambda+2\mu)n_y \end{bmatrix}$
B_g	1	$\begin{bmatrix} 1 & 0 \\ 0 & 1 \end{bmatrix}$

We define a least-squares functional associated with the boundary value problem in (5.27) with approximations $\mathbf{u} \approx \mathbf{v}, \mathbf{u}_{,x} \approx \mathbf{w}_x, \mathbf{u}_{,y} \approx \mathbf{w}_y$ as:

$$
\begin{aligned}
E\left(\mathbf{v}, \mathbf{w}_x, \mathbf{w}_y\right) = {} & \frac{1}{2}\int_\Omega \left(\mathbf{L}^1\mathbf{w}_x + \mathbf{L}^2\mathbf{w}_y - \mathbf{f}\right)^{\mathrm{T}} \left(\mathbf{L}^1\mathbf{w}_x + \mathbf{L}^2\mathbf{w}_y - \mathbf{f}\right) d\Omega \\
& + \frac{\alpha_h}{2}\int_{\partial\Omega_h} \left(\mathbf{B}_h^1\mathbf{w}_x + \mathbf{B}_h^2\mathbf{w}_y - \mathbf{h}\right)^{\mathrm{T}} \left(\mathbf{B}_h^1\mathbf{w}_x + \mathbf{B}_h^2\mathbf{w}_y - \mathbf{h}\right) d\Gamma \\
& + \frac{\alpha_g}{2}\int_{\partial\Omega_g} \left(\mathbf{B}_g\mathbf{u} - \mathbf{g}\right)^{\mathrm{T}} \left(\mathbf{B}_g\mathbf{u} - \mathbf{g}\right) d\Gamma
\end{aligned}
\tag{5.29}
$$

Here the first term accounts for the least-squares residual of the differential equation in the domain, and the second and third terms account for the least-squares residuals of the Neumann and Dirichlet boundary conditions, respectively. Weights α_h and α_g are considered in the least-

squares residual for the boundary constraints. Substituting (5.28) into (5.29) and considering the stationary condition lead to the variational discrete equation:

$$\delta E = \delta \mathbf{a}^{\mathrm{T}} \int_{\Omega} \mathbf{L}^1 \mathbf{\Psi}^x \left(\mathbf{L}^1 \mathbf{\Psi}^{x^{\mathrm{T}}} \mathbf{a} + \mathbf{L}^2 \mathbf{\Psi}^{y^{\mathrm{T}}} \mathbf{a} - \mathbf{f} \right) d\Omega + \delta \mathbf{a}^{\mathrm{T}} \int_{\Omega} \mathbf{L}^2 \mathbf{\Psi}^y \left(\mathbf{L}^1 \mathbf{\Psi}^{x^{\mathrm{T}}} \mathbf{a} + \mathbf{L}^2 \mathbf{\Psi}^{y^{\mathrm{T}}} \mathbf{a} - \mathbf{f} \right) d\Omega$$

$$+ \alpha_h \delta \mathbf{a}^{\mathrm{T}} \int_{\partial \Omega_h} \mathbf{B}_h^1 \mathbf{\Psi}^x \left(\mathbf{B}_h^1 \mathbf{\Psi}^{x^{\mathrm{T}}} \mathbf{a} + \mathbf{B}_h^2 \mathbf{\Psi}^{y^{\mathrm{T}}} \mathbf{a} - \mathbf{h} \right) d\Gamma \qquad (5.30)$$

$$+ \alpha_h \delta \mathbf{a}^{\mathrm{T}} \int_{\partial \Omega_h} \mathbf{B}_h^2 \mathbf{\Psi}^y \left(\mathbf{B}_h^1 \mathbf{\Psi}^{x^{\mathrm{T}}} \mathbf{a} + \mathbf{B}_h^2 \mathbf{\Psi}^{y^{\mathrm{T}}} \mathbf{a} - \mathbf{h} \right) d\Gamma + \alpha_g \delta \mathbf{a}^{\mathrm{T}} \int_{\partial \Omega_g} \mathbf{B}_g \mathbf{\Psi} \left(\mathbf{B}_g \mathbf{\Psi}^{T} \mathbf{a} - \mathbf{g} \right) d\Gamma$$

Performing quadrature rules at the collocation points yields

$$\delta E = \delta \mathbf{a}^{\mathrm{T}} \sum_{\ell=1}^{N_p} \left[\mathbf{L}^1 \left(\mathbf{\Psi}^{x^{\mathrm{T}}} (\mathbf{p}_\ell) \right)^{\mathrm{T}} \left(\mathbf{L}^1 \mathbf{\Psi}^{x^{\mathrm{T}}} (\mathbf{p}_\ell) \mathbf{a} + \mathbf{L}^2 \mathbf{\Psi}^{y^{\mathrm{T}}} (\mathbf{p}_\ell) \mathbf{a} - \mathbf{f}(\mathbf{p}_\ell) \right) \right.$$

$$\left. + \mathbf{L}^2 \left(\mathbf{\Psi}^{y^{\mathrm{T}}} (\mathbf{p}_\ell) \right)^{\mathrm{T}} \left(\mathbf{L}^1 \mathbf{\Psi}^{x^{\mathrm{T}}} (\mathbf{p}_\ell) \mathbf{a} + \mathbf{L}^2 \mathbf{\Psi}^{y^{\mathrm{T}}} (\mathbf{p}_\ell) \mathbf{a} - \mathbf{f}(\mathbf{p}_\ell) \right) \right] w_\ell^1$$

$$+ \delta \mathbf{a}^{\mathrm{T}} \alpha_h \sum_{\ell=1}^{N_q} \left[\mathbf{B}_h^1 \left(\mathbf{\Psi}^{x^{\mathrm{T}}} (\mathbf{q}_\ell) \right)^{\mathrm{T}} \left(\mathbf{B}_h^1 \mathbf{\Psi}^{x^{\mathrm{T}}} (\mathbf{q}_\ell) \mathbf{a} + \mathbf{B}_h^2 \mathbf{\Psi}^{y^{\mathrm{T}}} (\mathbf{q}_\ell) \mathbf{a} - \mathbf{h}(\mathbf{q}_\ell) \right) \right. \qquad (5.31)$$

$$\left. + \mathbf{B}_h^2 \left(\mathbf{\Psi}^{y^{\mathrm{T}}} (\mathbf{q}_\ell) \right)^{\mathrm{T}} \left(\mathbf{B}_h^1 \mathbf{\Psi}^{x^{\mathrm{T}}} (\mathbf{q}_\ell) \mathbf{a} + \mathbf{B}_h^2 \mathbf{\Psi}^{y^{\mathrm{T}}} (\mathbf{q}_\ell) \mathbf{a} - \mathbf{h}(\mathbf{q}_\ell) \right) \right] w_\ell^2$$

$$+ \delta \mathbf{a}^{\mathrm{T}} \alpha_g \sum_{\ell=1}^{N_r} \left[\mathbf{B}_g \left(\mathbf{\Psi}^{T} (\mathbf{q}_\ell) \right)^{\mathrm{T}} \left(\mathbf{B}_g \mathbf{\Psi}^{T} (\mathbf{q}_\ell) \mathbf{a} - \mathbf{g}(\mathbf{q}_\ell) \right) \right] w_\ell^3 = 0$$

where $\left\{ \mathbf{p}_\ell, w_\ell^1 \right\}_{\ell=1}^{N_p}$, $\left\{ \mathbf{q}_\ell, w_\ell^2 \right\}_{\ell=1}^{N_q}$, and $\left\{ \mathbf{r}_\ell, w_\ell^3 \right\}_{\ell=1}^{N_r}$ are the pairs of quadrature points and weights in Ω and on $\partial \Omega_h$ and $\partial \Omega_g$, respectively.

We can rewrite (5.31) as:

$$\delta E = \delta \mathbf{a}^{\mathrm{T}} \left[\mathbf{A}^{1^{\mathrm{T}}} \mathbf{W}^1 \left(\mathbf{A}^2 \mathbf{a} + \mathbf{A}^1 \mathbf{a} - \mathbf{b}^1 \right) + \mathbf{A}^{2^{\mathrm{T}}} \mathbf{W}^1 \left(\mathbf{A}^1 \mathbf{a} + \mathbf{A}^2 \mathbf{a} - \mathbf{b}^1 \right) \right.$$

$$\left. + \alpha_h \mathbf{A}^{3^{\mathrm{T}}} \mathbf{W}^2 \left(\mathbf{A}^3 \mathbf{a} + \mathbf{A}^4 \mathbf{a} - \mathbf{b}^2 \right) + \alpha_h \mathbf{A}^{4^{\mathrm{T}}} \mathbf{W}^2 \left(\mathbf{A}^3 \mathbf{a} + \mathbf{A}^4 \mathbf{a} - \mathbf{b}^2 \right) + \alpha_g \mathbf{A}^{5^{\mathrm{T}}} \mathbf{W}^3 \left(\mathbf{A}^5 \mathbf{a} - \mathbf{b}^3 \right) \right]$$

$$= \delta \mathbf{a}^{\mathrm{T}} \left[\mathbf{A}^{\mathrm{T}} \mathbf{W} \left(\mathbf{A} \mathbf{a} - \mathbf{b} \right) \right] = 0$$

$$(5.32)$$

where

$$\mathbf{A} = \begin{pmatrix} \mathbf{A}^1 + \mathbf{A}^2 \\ \sqrt{\alpha_h}\left(\mathbf{A}^3 + \mathbf{A}^4\right) \\ \sqrt{\alpha_g}\mathbf{A}^5 \end{pmatrix}, \quad \mathbf{b} = \begin{pmatrix} \mathbf{b}^1 \\ \sqrt{\alpha_h}\mathbf{b}^2 \\ \sqrt{\alpha_g}\mathbf{b}^3 \end{pmatrix}, \quad \mathbf{W} = \begin{pmatrix} \mathbf{W}^1 & & \\ & \mathbf{W}^2 & \\ & & \mathbf{W}^3 \end{pmatrix} \tag{5.33}$$

$$\mathbf{A}^1 = \begin{pmatrix} \mathbf{L}^1 \mathbf{\Psi}^{x^{\mathrm{T}}}\left(\mathbf{p}_1\right) \\ \mathbf{L}^1 \mathbf{\Psi}^{x^{\mathrm{T}}}\left(\mathbf{p}_2\right) \\ \vdots \\ \mathbf{L}^1 \mathbf{\Psi}^{x^{\mathrm{T}}}\left(\mathbf{p}_{N_p}\right) \end{pmatrix}, \quad \mathbf{A}^2 = \begin{pmatrix} \mathbf{L}^2 \mathbf{\Psi}^{y^{\mathrm{T}}}\left(\mathbf{p}_1\right) \\ \mathbf{L}^2 \mathbf{\Psi}^{y^{\mathrm{T}}}\left(\mathbf{p}_2\right) \\ \vdots \\ \mathbf{L}^2 \mathbf{\Psi}^{y^{\mathrm{T}}}\left(\mathbf{p}_{N_p}\right) \end{pmatrix} \tag{5.34}$$

$$\mathbf{A}^3 = \begin{pmatrix} \mathbf{B}_h^1 \mathbf{\Psi}^{x^{\mathrm{T}}}\left(\mathbf{q}_1\right) \\ \mathbf{B}_h^1 \mathbf{\Psi}^{x^{\mathrm{T}}}\left(\mathbf{q}_2\right) \\ \vdots \\ \mathbf{B}_h^1 \mathbf{\Psi}^{x^{\mathrm{T}}}\left(\mathbf{q}_{N_q}\right) \end{pmatrix}, \quad \mathbf{A}^4 = \begin{pmatrix} \mathbf{B}_h^2 \mathbf{\Psi}^{y^{\mathrm{T}}}\left(\mathbf{q}_1\right) \\ \mathbf{B}_h^2 \mathbf{\Psi}^{y^{\mathrm{T}}}\left(\mathbf{q}_2\right) \\ \vdots \\ \mathbf{B}_h^2 \mathbf{\Psi}^{y^{\mathrm{T}}}\left(\mathbf{q}_{N_q}\right) \end{pmatrix}, \quad \mathbf{A}^5 = \begin{pmatrix} \mathbf{B}_g \mathbf{\Psi}^{\mathrm{T}}\left(\mathbf{r}_1\right) \\ \mathbf{B}_g \mathbf{\Psi}^{\mathrm{T}}\left(\mathbf{r}_2\right) \\ \vdots \\ \mathbf{B}_g \mathbf{\Psi}^{\mathrm{T}}\left(\mathbf{r}_{N_r}\right) \end{pmatrix} \tag{5.35}$$

$$\mathbf{b}^1 = \begin{pmatrix} \mathbf{f}\left(\mathbf{p}_1\right) \\ \mathbf{f}\left(\mathbf{p}_2\right) \\ \vdots \\ \mathbf{f}\left(\mathbf{p}_{N_p}\right) \end{pmatrix}, \quad \mathbf{b}^2 = \begin{pmatrix} \mathbf{h}\left(\mathbf{q}_1\right) \\ \mathbf{h}\left(\mathbf{q}_2\right) \\ \vdots \\ \mathbf{h}\left(\mathbf{q}_{N_q}\right) \end{pmatrix}, \quad \mathbf{b}^3 = \begin{pmatrix} \mathbf{g}\left(\mathbf{r}_1\right) \\ \mathbf{g}\left(\mathbf{r}_2\right) \\ \vdots \\ \mathbf{g}\left(\mathbf{r}_{N_r}\right) \end{pmatrix},$$

$$\mathbf{W}^1 = \begin{pmatrix} w_1^1 & & \\ & \ddots & \\ & & w_{N_p}^1 \end{pmatrix}, \quad \mathbf{W}^2 = \begin{pmatrix} w_1^2 & & \\ & \ddots & \\ & & w_{N_q}^2 \end{pmatrix}, \quad \mathbf{W}^3 = \begin{pmatrix} w_1^3 & & \\ & \ddots & \\ & & w_{N_r}^3 \end{pmatrix} \tag{5.36}$$

From (5.32), the discrete weighted least-squares equation has the following form:

$$\mathbf{A}^{\mathrm{T}}\mathbf{W}\mathbf{A}\mathbf{y} = \mathbf{A}^{\mathrm{T}}\mathbf{W}\mathbf{b} \tag{5.37}$$

Eq. (5.37) is the weighted least-squares approximation of the linear system $\mathbf{A}\mathbf{y} = \mathbf{b}$, that is

$$
\underbrace{\begin{pmatrix} \mathbf{A}^1 + \mathbf{A}^2 \\ \sqrt{\alpha_h}\left(\mathbf{A}^3 + \mathbf{A}^4\right) \\ \sqrt{\alpha_g}\,\mathbf{A}^5 \end{pmatrix}}_{\mathbf{A}} \mathbf{a} = \underbrace{\begin{pmatrix} \mathbf{b}^1 \\ \sqrt{\alpha_h}\,\mathbf{b}^2 \\ \sqrt{\alpha_g}\,\mathbf{b}^3 \end{pmatrix}}_{\mathbf{b}}
\tag{5.38}
$$

The sub-matrices in matrix $\mathbf{A}$, and the vectors $\mathbf{a}$ and $\mathbf{b}$ for Poisson and elasticity problems are

summarized in

Table 5-2.

Table 5-2 Sub-matrices in discrete equations for Poisson and elasticity problems

Sub-matrix	Poisson's Problem	Elasticity Problem
$\mathbf{A}^1_{IJ}$	$\left[\Psi^x_{J,x}(\mathbf{p}_I)\right]$	$\begin{bmatrix} (\lambda+2\mu)\,\Psi^x_{J,x}(\mathbf{p}_I) & \mu\Psi^x_{J,y}(\mathbf{p}_I) \\ \lambda\Psi^x_{J,y}(\mathbf{p}_I) & \mu\Psi^x_{J,x}(\mathbf{p}_I) \end{bmatrix}$
$\mathbf{A}^2_{IJ}$	$\left[\Psi^y_{J,y}(\mathbf{p}_I)\right]$	$\begin{bmatrix} \mu\Psi^y_{J,y}(\mathbf{p}_I) & \lambda\Psi^y_{J,x}(\mathbf{p}_I) \\ \mu\Psi^y_{J,x}(\mathbf{p}_I) & (\lambda+2\mu)\,\Psi^y_{J,y}(\mathbf{p}_I) \end{bmatrix}$
$\mathbf{A}^3_{IJ}$	$\left[\Psi^x_J(\mathbf{q}_I)n_x\right]$	$\begin{bmatrix} (\lambda+2\mu)\,\Psi^x_J(\mathbf{q}_I)n_x & \mu\Psi^x_J(\mathbf{q}_I)n_y \\ \lambda\Psi^x_J(\mathbf{q}_I)n_y & \mu\Psi^x_J(\mathbf{q}_I)n_x \end{bmatrix}$
$\mathbf{A}^4_{IJ}$	$\left[\Psi^y_J(\mathbf{q}_I)n_y\right]$	$\begin{bmatrix} \mu\Psi^y_J(\mathbf{q}_I)n_y & \lambda\Psi^y_J(\mathbf{q}_I)n_x \\ \mu\Psi^y_J(\mathbf{q}_I)n_x & (\lambda+2\mu)\,\Psi^y_J(\mathbf{q}_I)n_y \end{bmatrix}$
$\mathbf{A}^5_{IJ}$	$\left[\Psi_J(\mathbf{r}_I)\right]$	$\begin{bmatrix} \Psi_J(\mathbf{r}_I) & 0 \\ 0 & \Psi_J(\mathbf{r}_I) \end{bmatrix}$

5.5 Convergence Study

We first consider a two-dimensional Poisson boundary value problem (BVP) as a model problem:

$$
\begin{aligned}
u_{,xx} + u_{,yy} &= f \quad in \quad \Omega \\
u &= g \quad on \quad \partial\Omega_g \\
\nabla u \cdot \mathbf{n} \equiv u_n &= h \quad on \quad \partial\Omega_h
\end{aligned}
\tag{5.39}
$$

As discussed in Section 5.4, the strong form collocation can be related to the least-squares functional with quadrature. Based on the least-squares functional in (5.29) and considering the BVP in (5.39), E-norm is defined as follow:

$$
\left\| v, w_x, w_y \right\|_E = \left\{ \left\| w_{x,x} + w_{y,y} \right\|^2_{0,\Omega} + \alpha_h \left\| w_n \right\|^2_{0,\partial\Omega_h} + \alpha_g \left\| v \right\|^2_{0,\partial\Omega_g} \right\}^{1/2}
\tag{5.40}
$$

where $w_n = w_x n_1 + w_y n_1$, and

$$
\begin{aligned}
v &= \sum_{I=1}^{N_s} \Psi_I a_I, \quad v \in V = span\left\{ \Psi_1, \Psi_2, \cdots \Psi_{N_S} \right\} \\
w_x &= \sum_{I=1}^{N_s} \Psi_I^x a_I, \quad w_x \in W_x = span\left\{ \Psi_1^x, \Psi_1^x, \cdots \Psi_{N_S}^x \right\} \\
w_y &= \sum_{I=1}^{N_s} \Psi_I^y a_I \quad w_y \in W_y = span\left\{ \Psi_1^y, \Psi_1^y, \cdots \Psi_{N_S}^y \right\}
\end{aligned}
\tag{5.41}
$$

Thus, we have:

$$\left\| u-v, u_{,x}-w_x, u_{,y}-w_y \right\|_E = \left\{ \left\| w_{x,x}+w_{y,y}-f \right\|_{0,\Omega}^2 + \alpha_h \left\| w_n-h \right\|_{0,\partial\Omega_h}^2 + \alpha_g \left\| v-g \right\|_{0,\partial\Omega_g}^2 \right\}^{1/2}$$

$$\leq \left\| w_{x,x}+w_{y,y}-f \right\|_{0,\Omega} + \sqrt{\alpha_h} \left\| w_n-h \right\|_{0,\partial\Omega_h} + \sqrt{\alpha_g} \left\| v-g \right\|_{0,\partial\Omega_g} \qquad (5.42)$$

$$\equiv E_1 + E_2 + E_3$$

Here E_1 is the error from domain, E_2 is the error from the Neumann boundary, and E_3 is the error from Dirichlet boundary. The individual error norms are estimated as follows:

$$E_1 = \left\| w_{x,x}+w_{y,y}-f \right\|_{0,\Omega}$$

$$= \left\| w_{x,x}+w_{y,y}-u_{,xx}-u_{,yy} \right\|_{0,\Omega}$$

$$\leq \left\| w_{x,x}-u_{,xx} \right\|_{0,\Omega} + \left\| w_{y,y}-u_{,yy} \right\|_{0,\Omega} \qquad (5.43)$$

$$\leq \left\| w_x-u_{,x} \right\|_{1,\Omega} + \left\| w_y-u_{,y} \right\|_{1,\Omega}$$

$$\leq C_1 a^{-1} \left\| w_x-u_{,x} \right\|_{0,\Omega} + C_2 a^{-1} \left\| w_y-u_{,y} \right\|_{0,\Omega}$$

$$E_2 = \sqrt{\alpha_h} \left\| w_n-h \right\|_{0,\partial\Omega_h}$$

$$= \sqrt{\alpha_h} \left\| w_n-u_n \right\|_{0,\partial\Omega_h}$$

$$\leq \bar{C}_3 \sqrt{\alpha_h} \left\| w_x-u_{,x} \right\|_{1,\Omega} + \bar{C}_4 \sqrt{\alpha_h} \left\| w_y-u_{,y} \right\|_{1,\Omega} \qquad (5.44)$$

$$\leq C_3 a^{-1} \sqrt{\alpha_h} \left\| w_x-u_{,x} \right\|_{0,\Omega} + C_4 a^{-1} \sqrt{\alpha_h} \left\| w_y-u_{,y} \right\|_{0,\Omega}$$

$$E_3 = \sqrt{\alpha_g} \left\| v-g \right\|_{0,\partial\Omega_g}$$

$$= \sqrt{\alpha_g} \left\| v-u \right\|_{0,\partial\Omega_g}$$

$$\leq \bar{C}_5 \sqrt{\alpha_g} \left\| v-u \right\|_{1,\Omega} \qquad (5.45)$$

$$\leq C_5 a^{-1} \sqrt{\alpha_g} \left\| v-u \right\|_{0,\Omega}$$

We further introduce the following properties of the reproducing kernel approximation of degree p in (5.5) and the gradient reproducing kernel approximation of degree q in (5.18):

$$\|u - v\|_{0,\Omega} \leq C a^{p+1} |u|_{p+1,\Omega}$$
$$\|u_{,x} - w_x\|_{0,\Omega} \leq C a^q |u|_{q+1,\Omega} \qquad (5.46)$$
$$\|u_{,y} - w_y\|_{0,\Omega} \leq C a^q |u|_{q+1,\Omega}$$

As can be seen, E_1 and E_2 are associated with the gradient reproducing kernel approximation (w_x and w_y) of the differential equation and the Neumann boundary condition, respectively. It appears that the errors E_1 and E_2 are in balance without the weight in E_2, thus the weight α_h is unnecessary. The error term E_3 is associated with the reproducing kernel approximation (v), and its balance with the errors E_1 and E_2 requires the properties in (5.46). As such, the weights for imposition of boundary conditions in G-RKCM are selected as shown below

$$\sqrt{\alpha_h} \approx O(1), \quad \sqrt{\alpha_g} \approx O\left(a^{q-p-1}\right) \qquad (5.47)$$

Combining the properties in (5.46) and the weights in (5.47), we have

$$\left\|u - v, u_{,x} - w_x, u_{,y} - w_y\right\|_E \leq a^{q-1}\left(C_9 |u|_{q+1,\Omega} + C_{10} |u|_{p+1,\Omega}\right) \qquad (5.48)$$

Assuming the discrete bilinear form associated with the minimization of E-norm in (5.42) is bounded and coercive, by Lax-Milgram and Cea's Lemmas, there exists an optimal estimate

$$\left\|u - u^h, u_{,x} - u^h_{,x}, u_{,y} - u^h_{,y}\right\|_E \leq \bar{C} \inf_{\substack{v \in V \\ w_x \in W_x \\ w_y \in W_y}} \left\|u - v, u_{,x} - w_x, u_{,y} - w_y\right\|_E$$
$$\leq a^{q-1}\left(C_{11} |u|_{q+1,\Omega} + C_{12} |u|_{p+1,\Omega}\right) \qquad (5.49)$$

Further, considering the balance of errors in the E-norm, and the error properties in (5.43)-(5.45), we have:

77

$$\left\| u - u^h \right\|_{1,\Omega} \approx O(a^{q-1}), \quad \left\| u_{,x} - u^h_{,x} \right\|_{1,\Omega} + \left\| u_{,y} - u^h_{,y} \right\|_{1,\Omega} \approx O(a^{q-1}) \tag{5.50}$$

$$\left\| u - u^h \right\|_{0,\Omega} \approx O(a^{q}), \quad \left\| u_{,x} - u^h_{,x} \right\|_{0,\Omega} + \left\| u_{,y} - u^h_{,y} \right\|_{0,\Omega} \approx O(a^{q}) \tag{5.51}$$

For elasticity, similar procedures are followed to obtain:

$$
\begin{aligned}
E_1 &\leq C_1 \kappa a^{-1} \left\| w_x - u_{,x} \right\|_{0,\Omega} + C_2 \kappa a^{-1} \left\| w_y - u_{,y} \right\|_{0,\Omega} \\
E_2 &\leq C_3 \kappa a^{-1} \sqrt{\alpha_h} \left\| w_x - u_{,x} \right\|_{0,\Omega} + C_4 \kappa a^{-1} \sqrt{\alpha_h} \left\| w_y - u_{,y} \right\|_{0,\Omega} \\
E_3 &\leq C_5 a^{-1} \sqrt{\alpha_g} \left\| v - u \right\|_{0,\Omega}
\end{aligned}
\tag{5.52}
$$

where $\kappa = \max\{\lambda, \mu\}$. For balance of errors between E_1, E_2, and E_3, the following weights are selected:

$$\sqrt{\alpha_h} \approx O(1), \quad \sqrt{\alpha_g} \approx O\left(\kappa a^{q-p-1}\right) \tag{5.53}$$

Similar convergence properties to the Poisson problem as given in (5.48)-(5.51) can be obtained for elasticity problems.

Remark 5.3

The results in (5.49) indicate that the convergence of this method is only dependent on the polynomial degree q in the approximation of $\mathbf{u}_{,x}$ and $\mathbf{u}_{,y}$, and is independent of the polynomial degree p in the approximation of $\mathbf{u}$. Further, $q \geq 2$ is needed for convergence.

Remark 5.4

The collocation points in the strong form collocation method plays a similar role as the

78

quadrature points in the least-squares method as discussed in Section 5.3. For strong form collocation method based on approximation for u, such as the reproducing kernel collocation method (RKCM) (Chen et al. 2008; HU et al., 2011; Hu et al., 2009), it requires second order differentiation of the approximation functions.

Typically, higher order differentiation in the approximation function requires higher order quadrature rule for sufficient accuracy in the solution process. Taking RKCM for a Poisson problem for example, we have:

$$\left| \int_{\Omega} \Delta v d\Omega - \overset{\wedge}{\int_{\Omega}} \Delta v d\Omega \right| \leq C h_c^{r+1} N_s^{r+3} \|v\|_{1,\Omega}^2 \tag{5.54}$$

In the above, $\overset{\wedge}{\int}$ denotes numerical integration, $h_c = 1 / N_c$, N_c and N_s are the numbers of collocation points and source points in one-dimension, respectively, and r is the parameter related to the accuracy of numerical integration method, for example, $r = 1$ for Trapezoidal rule. Here, $\Delta v = \nabla \cdot \nabla v$ involves second order differentiation of the approximation in v. For the proposed GRKCM, Δv is replaced by $\nabla \cdot [w_x, w_y]$ which requires only first order differentiation of w_x and w_y, and we have:

$$\left| \int_{\Omega} \nabla \cdot [w_x, w_y] d\Omega - \overset{\wedge}{\int_{\Omega}} \nabla \cdot [w_x, w_y] d\Omega \right| \leq C h_c^{r+1} N_s^{r+1} \|w_n\|_{1,\Omega}^2 \tag{5.55}$$

where $w_n = w_x n_1 + w_y n_2$.

For RKCM, it requires $h_c^{r+1} N_s^{r+3} = N_c^{-(r+1)} N_s^{r+3} \approx o(1)$ for integration error to be under control, and thus necessitates the use of more collocation points N_c than source points N_s in the collocation method, and that leads to an over-determined system in its collocation equations. For the proposed GRKCM, we need $h_c^{r+1} N_s^{r+1} = N_c^{-(r+1)} N_s^{r+1} \approx o(1)$, and thus allows the use of

$N_c = N_s$ *for sufficient accuracy as will be shown in the numerical examples.*

5.6 Complexity Analysis

In this section, we analyze the complexity of RKCM and the proposed G-RKCM method. For complexity comparison of RKCM and G-RKCM, consider the solution of the following Poisson problem:

$$
\begin{aligned}
-\Delta u &= f \quad in\ \Omega \\
u &= g \quad on\ \partial\Omega_g \\
u_n &= h \quad on\ \partial\Omega_h
\end{aligned}
\tag{5.56}
$$

where $\Delta = \nabla \cdot \nabla$ and $u_{,n} = \nabla u \cdot \mathbf{n}$. We consider the follow two formulations in the approximations

$$
RKCM: \quad u \approx v = \sum_{I=1}^{N_s} \Psi_I(\mathbf{x}) a_I, \quad u_{,\alpha} \approx v_{,\alpha} = \sum_{I=1}^{N_s} \Psi_{I,\alpha}(\mathbf{x}) a_I, \quad u_{,\alpha\alpha} \approx v_{,\alpha\alpha} = \sum_{I=1}^{N_s} \Psi_{I,\alpha\alpha}(\mathbf{x}) a_I \tag{5.57}
$$

$$
G-RKCM: \quad u \approx v = \sum_{I=1}^{N_s} \Psi_I(\mathbf{x}) a_I, \quad u_{,\alpha} \approx w_\alpha = \sum_{I=1}^{N_s} \Psi_I^\alpha(\mathbf{x}) a_I, \quad u_{,\alpha\alpha} \approx w_{\alpha,\alpha} = \sum_{I=1}^{N_s} \Psi_{I,\alpha}^\alpha(\mathbf{x}) a_I \tag{5.58}
$$

where $\alpha = 1, 2$, $\Psi_I(\mathbf{x})$ is the RK shape function of degree p, and Ψ_I^α is the gradient RK shape function with degree q. Consider a set of collocation points:

$$
\square = \left\{ \left\{ \mathbf{p}_\ell \right\}_{\ell=1}^{N_p}, \left\{ \mathbf{q}_\ell \right\}_{\ell=1}^{N_q}, \left\{ \mathbf{r}_\ell \right\}_{\ell=1}^{N_r} \right\}, \quad \mathbf{p}_\ell \in \Omega, \mathbf{q}_\ell \in \partial\Omega_g, \mathbf{r}_\ell \in \partial\Omega_h \tag{5.59}
$$

Introducing RK approximation in (5.57) into the strong form (5.56), and enforcing the residual to be zero at the collocation points to yield:

$$-\sum_{I=1}^{N_s} \Delta\Psi_I\left(\mathbf{p}_\ell\right) a_I = f\left(\mathbf{p}_\ell\right), \quad \mathbf{p}_\ell \in \Omega, \quad \ell = 1,\cdots,N_p$$

$$\sqrt{\alpha_g} \sum_{I=1}^{N_s} \Delta\Psi_I\left(\mathbf{q}_\ell\right) a_I = \sqrt{\alpha_g}\, g\left(\mathbf{q}_\ell\right), \quad \mathbf{q}_\ell \in \partial\Omega_g, \quad \ell = 1,\cdots,N_q \qquad (5.60)(a),\,(b),\,(c)$$

$$\sqrt{\alpha_h} \sum_{I=1}^{N_s} \left(\nabla\Psi_I\left(\mathbf{r}_\ell\right)\cdot\mathbf{n}\left(\mathbf{r}_\ell\right)\right) a_I = \sqrt{\alpha_h}\, h\left(\mathbf{r}_\ell\right), \quad \mathbf{r}_\ell \in \partial\Omega_h, \quad \ell = 1,\cdots,N_r$$

Note that for RKCM, the second order derivation on the shape function $\Delta\Psi_I = \Psi_{I,xx} + \Psi_{I,yy}$ is needed in (5.60)(a), while for G-RKCM, this term is replaced by $\Delta\Psi_I = \Psi_{I,x}^x + \Psi_{I,y}^y$. Similarly in (5.60)(c), $\nabla\Psi_I = [\Psi_{I,x}, \Psi_{I,y}]$ for RKCM, while $\nabla\Psi_I = [\Psi_I^x, \Psi_I^y]$ for G-RKCM. It is therefore imperative to analyze the operating counts of Ψ_I, $\Psi_{I,\alpha}$, and Ψ_I^α, $\alpha = 1,2$ as in the followings. We denote multiplication and division operations by M/D, and the addition and subtraction operations by A/S. For RKCM, operation counts following (Hu et al., 2011) are:

$$\Psi_I \begin{cases} M/D: & S^3 + \left(2k+1\right)S^2 + S + 1 \\ A/S: & S^3 + \left(k-2\right)S^2 + S - 1 \end{cases} \qquad (5.61)$$

$$\Psi_{I,\alpha} \begin{cases} M/D: & 3S^3 + \left(8k+4\right)S^2 + 3S + 2 \\ A/S: & 3S^3 + \left(4k-5\right)S^2 + S + 1 \end{cases} \qquad (5.62)$$

$$\Psi_{I,\alpha\alpha} \begin{cases} M/D: & 6S^3 + \left(20k+12\right)S^2 + 6S + 4 \\ A/S: & 6S^3 + \left(10k-11\right)S^2 + S + 12 \end{cases} \qquad (5.63)$$

where $S = (p+d)!/(p!d!)$, p is the reproducing degree of RK approximation, d is the space dimension, and k is the kernel support overlapping number. For G-RKCM, the operating count for Ψ_I is the same as (5.61), and the operating counts for Ψ_I^α and $\Psi_{I,\alpha}^\alpha$ are

$$\Psi_I^\alpha \begin{cases} M/D: & \bar{S}^3 + (2k+1)\bar{S}^2 + \bar{S} + 1 \\ A/S: & \bar{S}^3 + (k-2)\bar{S}^2 + \bar{S} - 1 \end{cases} \tag{5.64}$$

$$\Psi_{I,\alpha}^\alpha \begin{cases} M/D: & 3\bar{S}^3 + (8k+4)\bar{S}^2 + 3\bar{S} + 2 \\ A/S: & 3\bar{S}^3 + (4k-5)\bar{S}^2 + \bar{S} + 1 \end{cases} \tag{5.65}$$

where $\bar{S} = (q+d)!/(q!d!)$, and q is the reproducing degree of gradient RK approximation. Note that the complexity of Ψ_I^α is the same as that for Ψ_I, and the complexity of $\Psi_{I,\alpha}^\alpha$ is the same as that for $\Psi_{I,\alpha}$, with p in S replaced by q in $\bar{S}$. The computational complexities of these shape functions in two-dimension for $p = q = 2$ are shown in Table 5-3 and Table 5-4, respectively. The kernel support overlapping number is based on normaliized kernel support of $k = 4S$ in two-dimension.

Table 5-3 Complexity comparison of shape function calculation in RKCM and G-RKCM in two-dimension

RKCM		$p = 2$	G-RKCM		$p = q = 2$
Ψ_I	M/D	1987	Ψ_I	M/D	1987
	A/S	1013		A/S	1013
$\Psi_{I,\alpha}$	M/D	7724	Ψ_I^α	M/D	1987
	A/S	3931		A/S	1013
$\Psi_{I,\alpha\alpha}$	M/D	19048	$\Psi_{I,\alpha}^\alpha$	M/D	7724
	A/S	9558		A/S	3991

Table 5-4 Complexity comparison of shape function calculation in RKCM and G-RKCM in three-dimension

RKCM		$p = 2$	G-RKCM		$p = q = 2$
Ψ_I	M/D A/S	17111 8809	Ψ_I	M/D A/S	17111 8809
$\Psi_{I,\alpha}$	M/D A/S	67432 34511	Ψ_I^{α}	M/D A/S	17111 8809
$\Psi_{I,\alpha\alpha}$	M/D A/S	167264 84922	$\Psi_{I,\alpha}^{\alpha}$	M/D A/S	67432 34511

The collocation equations in (5.60) leads to a linear system

$$\mathbf{Aa} = \mathbf{b} \qquad (5.66)$$

In (5.66), the matrix A is with dimension $N_c \times N_s$, where $N_c = N_p + N_q + N_r$ is the total number of collocation points, N_s is the number of source points, $N_c \geq N_s$ for RKCM, while $N_c = N_s$ for G-RKCM. Thus, the solution time for solving the linear system (5.66) also favors G-RKCM in addition to its simplicity in shape function calculations as discussed above. Further, the computation time in constructing the linear system in G-RKCM is also considerably less than that in RKCM. For example, let $\bar{N}_p$, $\bar{N}_q$, and $\bar{N}_r$ be the counter parts of N_p, N_q, and N_r in G-RKCM, and $\bar{N}_c = \bar{N}_p + \bar{N}_q + \bar{N}_r = N_s$. It can be shown that the construction times for the linear system of (5.66) are:

$$\text{RKCM: } N_s \left(38096 N_p + 1987 N_q + 7724 N_r \right) \qquad (5.67)$$

$$\text{G-RKCM: } N_s \left(15548 \bar{N}_p + 1987 \bar{N}_q + 1987 \bar{N}_r \right) \qquad (5.68)$$

By considering that fact that $N_p + N_q + N_r \geq \bar{N}_p + \bar{N}_q + \bar{N}_r$ as discussed above, the CPU advantage in G-RKCM is trivial.

5.7 Numerical Examples

In the following numerical examples, both RK shape functions and gradient RK shape functions are constructed with the quintic B-spline kernel function. For comparison, the solutions of the proposed G-RKCM method are compared with analytical solutions and RKCM solutions. In the solution of BVPs, the boundary weights of $\sqrt{\alpha_h} = 1$, $\sqrt{\alpha_g} = \kappa N_s$ are used for RKCM following (Hu et al., 2007), while $\sqrt{\alpha_h} = 1$, $\sqrt{\alpha_g} = \kappa a^{q-p-1}$ are used for G-RKCM, with $\kappa = 1$ for Poisson problem and $\kappa = \max\{\lambda, \mu\}$ for elasticity as discussed in Section 5.5.

5.7.1 Approximation of a Sine Function

The RK shape functions and gradient RK (GRK) shape functions are employed to approximate $\sin(\pi x)\sin(\pi y)$ and the associated derivative in the domain $[0,1] \times [0,1]$, respectively. The L2 error norms of the function approximation by RK shape function with $p = 1$ and $p = 2$ are shown in Figure 5-1 (a) while the L2 error norms of the approximation of sine function derivative with $q = 1$ and $q = 2$ are shown in Figure 5-1 (b). The same number of collocation

points as that of source points is used in this study. The convergence rates are in agreement with the theoretical values.

(a)   (b)
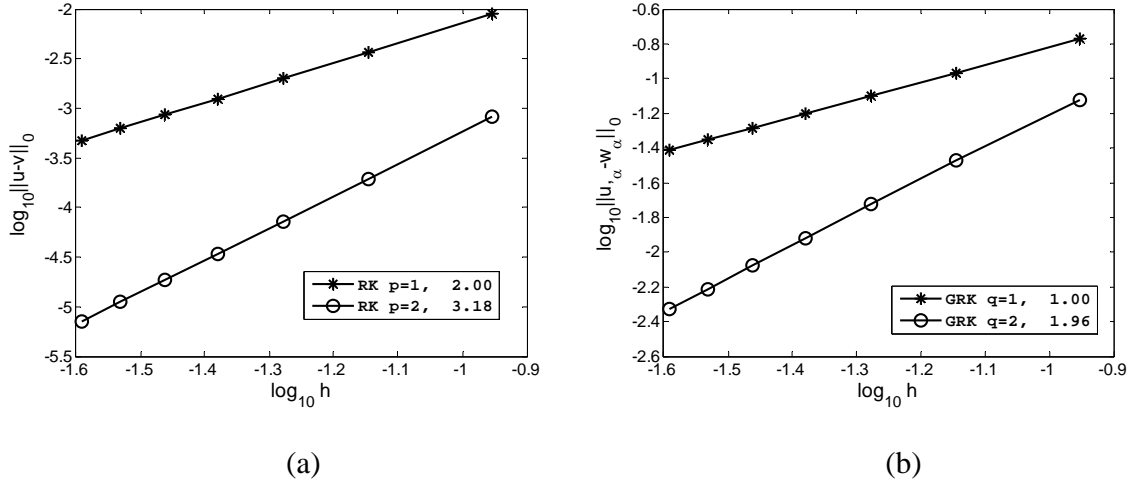
Figure 5-1 Convergence of L2 norms in approximation a sine function and its derivative

5.7.2 Two Dimensional Poisson Problem

Consider a two-dimensional Poisson problem as follows:

$$\Delta u\left(x, y\right) = \left(x^2 + y^2\right)e^{xy} \quad \text{in } \Omega = \left(0,1\right)\times\left(0,1\right)$$
$$u\left(x, y\right) = e^{xy} \quad \text{on } \partial\Omega$$

(5.69)

The numbers of source points and collocation points employed for RKCM in the convergence study are $\left\{10\times10, 15\times15, 20\times20, 25\times25, 30\times30\right\}$ and $\left\{19\times19, 29\times29, 39\times39, 49\times49, 59\times59\right\}$, respectively, and the number of collocation points are the same as the number of source points $\left\{10\times10, 15\times15, 20\times20, 25\times25, 30\times30\right\}$ for G-RKCM. Figure 5-2 compares L2 norms of u and $u_{,\alpha}$ obtained by the proposed G-RKCM with various degrees of bases, as well as RKCM with

85

$p = 2$. As predicted by the theory in Section 5.4, G-RKCM requires at least second order bases in the gradient RK approximation for convergence, similar to the convergence requirement for RKCM (Hu et al., 2011). The results also show that the rate of convergence in G-RKCM is determined by the degree of bases in the gradient RK approximation (q), although higher degree of bases in the RK approximation (p) improves the solution accuracy in u. The CPU comparison for RKCM and G-RKCM shown in Figure 5-3 demonstrates the effectiveness of the proposed G-RKCM.
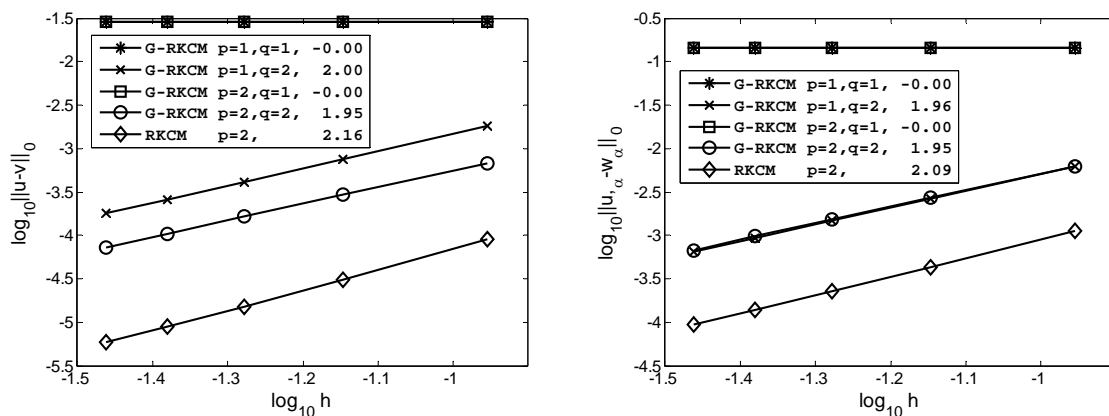
Figure 5-2 Convergence of L2 norms of u and $u_{,\alpha}$ in two-dimensional Poisson problem
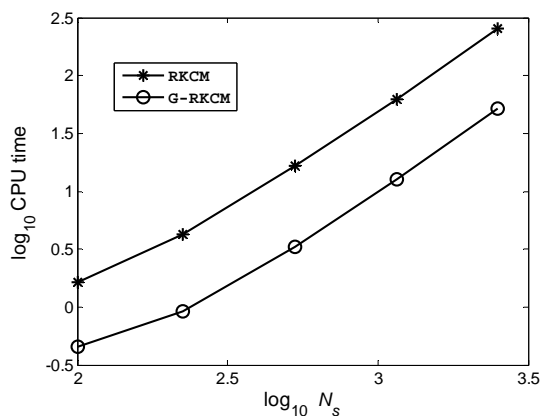
Figure 5-3 CPU comparison of RKCM and G-RKCM

5.7.3 Infinite Long Cylinder under Internal Pressure

Inner radius: 4
Outer radius: 10
P=100
Young's modulus E=3×10^7
Poisson's ratio v=0.25
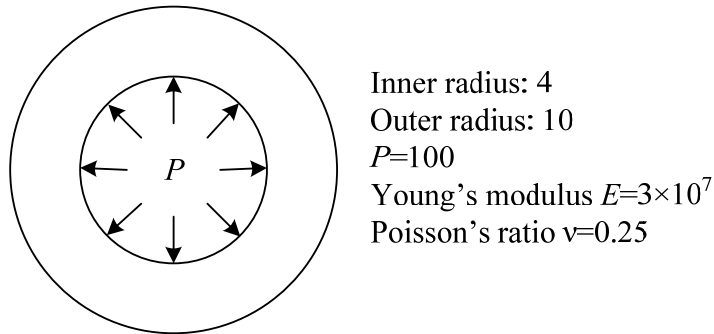
Figure 5-4 An infinite long cylinder subjected to an internal pressure

(a)   (b)

Figure 5-5 (a) Quarter model and (b) distribution of source points and collocation points for RKCM

An infinite long elastic cylinder subjected to an internal pressure is depicted in Figure 5-4 , where a plane strain condition in the out of plane direction is assumed. Due to symmetry, only a quarter of the domain is modeled by G-RKCM as shown in Figure 5-5 (a). The corresponding boundary value problem is

$$\sigma_{ij,j} = 0 \quad \text{in } \Omega \tag{5.70}$$

$$
\begin{aligned}
&h_i = -Pn_i \quad \text{on } \Gamma_1 \\
&u_2 = 0, \quad h_1 = 0 \quad \text{on } \Gamma_2 \\
&h_i = 0 \quad \text{on } \Gamma_3 \\
&u_1 = 0, \quad h_2 = 0 \quad \text{on } \Gamma_4
\end{aligned}
\tag{5.71}
$$

where $\sigma_{ij} = C_{ijkl} u_{(k,l)}$ and $h_i = \sigma_{ij} n_j$. The analytical solutions to this problem are given by

$$
\begin{aligned}
u_r(r) &= \frac{Pa^2 r}{E(b^2 - a^2)} \left[(1+v)(1-2v) + \frac{b^2}{r^2}(1+v) \right] \\
\sigma_{rr}(r) &= \frac{Pa^2}{b^2 - a^2} \left(1 - \frac{b^2}{r^2} \right) \\
\sigma_{\theta\theta}(r) &= \frac{Pa^2}{b^2 - a^2} \left(1 + \frac{b^2}{r^2} \right)
\end{aligned}
\tag{5.72}
$$

where P is the internal pressure, b and a are the outer and inner radii of the cylinder, respectively. The distribution of source points and collocation points for RKCM is shown in Figure 5-5 (b). Five levels of discretization with source points $\{66, 222, 469, 808, 1238\}$ are employed in the convergence study. The number of collocation points is approximately four times the source points for the RKCM whereas the collocation points are the same as the source points for G-RKCM. As shown in Figure 5-6, disregarding the degree of basis p, the G-RKCM with quadratic basis $q=2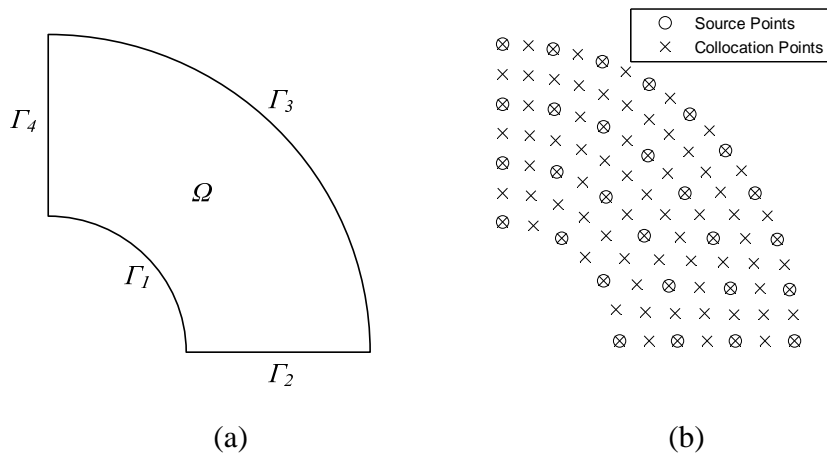$ achieves the similar rate of convergence as the RKCM with quadratic basis while it yields better accuracy than RKCM in this problem. The errors in the G-RKCM with $q=2$ along the radial direction are also compared with those in the RKCM in Figure 5-7. In general, the stress results obtained by G-RKCM are less oscillatory in comparison with those by RKCM. The results also show that for G-RKCM, the solution is predominated by the order of

basis functions (*q*) in the gradient RK shape functions, and is nearly independent to the order of

basis functions (*p*) in the RK shape functions.

(a)   (b)
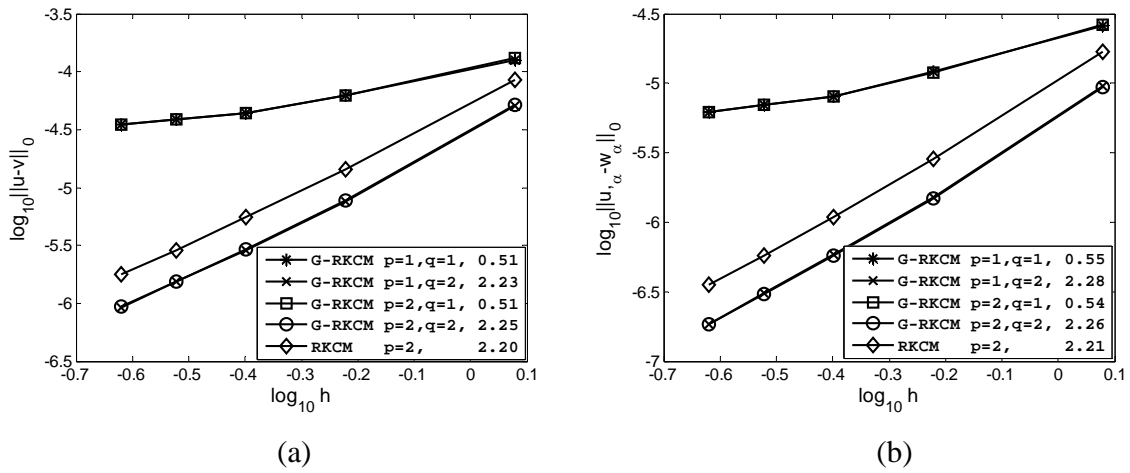
Figure 5-6 Convergence of L2 norms of *u* and $u_{,\alpha}$ in the cylinder problem
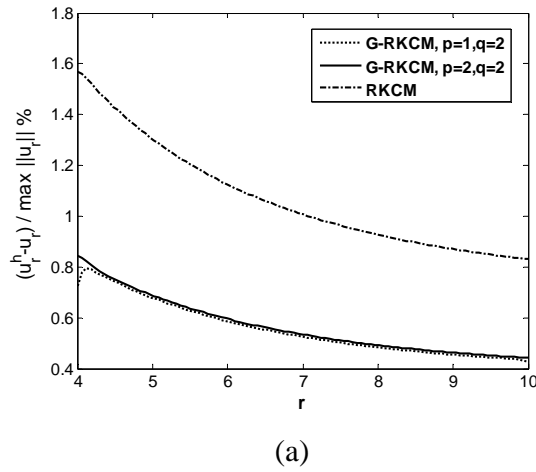
(a)
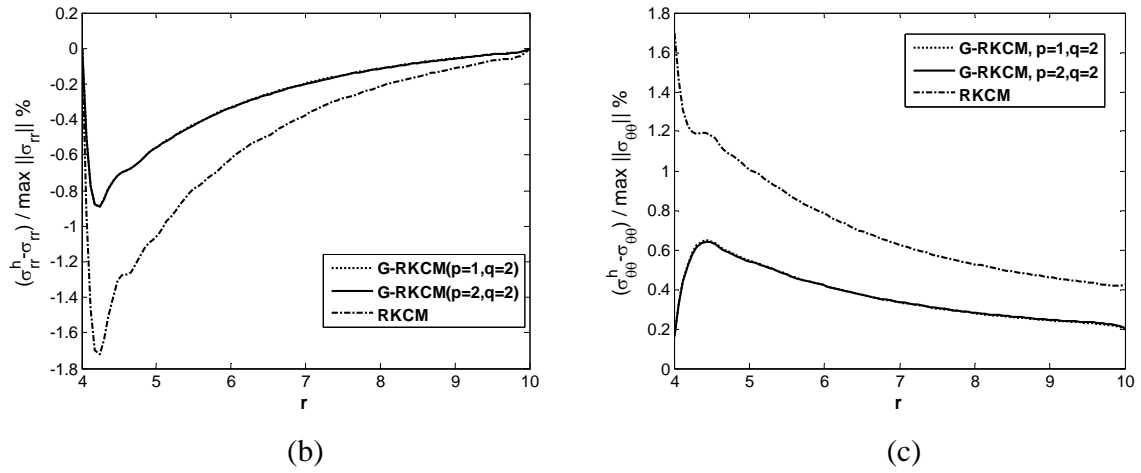
Figure 5-7 Displacement and stresses along radial direction of the cylinder

5.7.4 Beam Under Shear Load

$$h_2 = \frac{6P}{D^3}\left(\frac{D^2}{4} - y^2\right)$$

L=8 m
D=2 m
P=100 N/m
Young's modulus E=3×10⁷Pa
Poisson ratio ν=0.25
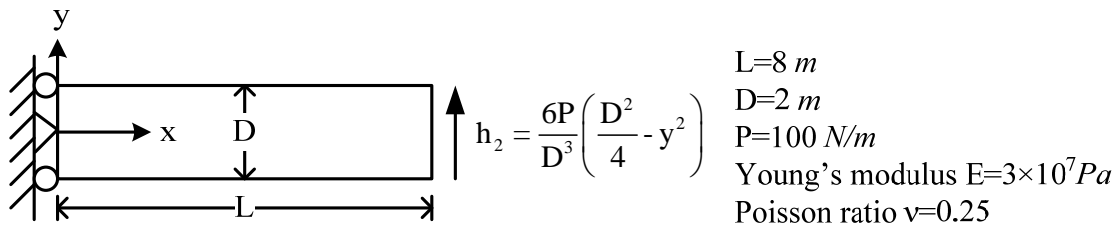
Figure 5-8 Cantilever problem statement

Consider a plane-strain elastic cantilever beam subjected to a tip shear traction, *P*, shown in Figure 5-8. The corresponding boundary value problem and boundary conditions are given as

$$\sigma_{ij,j} = 0, \quad 0 < x < L, \quad -D/2 < y < D/2 \tag{5.73}$$

(1) at $x = 0$, $\quad y = 0$, $\quad u_1 = u_2 = 0$

(2) at $x = 0$, $\quad y = \pm D/2$, $\quad u_1 = 0$, $\quad h_2 = 0$

(3) on $x = L$, $\quad -D/2 \le y \le D/2$, $\quad h_1 = 0$, $\quad h_2 = \dfrac{6P}{D^3}\left(\dfrac{D^2}{4} - y^2\right)$ $\qquad$ (5.74)

(4) on $x = 0$, $\quad -D/2 < y < 0$, $\quad 0 < y < D/2$, $\quad h_1 = \dfrac{12PL}{D^3}y$, $\quad h_2 = -\dfrac{6P}{D^3}\left(\dfrac{D^2}{4} - y^2\right)$

(5) on $0 < x < L$, $\quad y = \pm D/2$, $\quad h_1 = h_2 = 0$

The analytical solutions to the problem are

$$u_1(x,y) = -\frac{Py}{6\bar{E}I}\left[(6L - 3x)x + (2 + \bar{v})\left(y^2 - \frac{D^2}{4}\right)\right]$$

$$u_2(x,y) = \frac{P}{6\bar{E}I}\left[(3L - x)x^2 + 3\bar{v}y^2(L - x) + (4 + 5\bar{v})\frac{D^2x}{4}\right]$$

$\qquad$ (5.75)

where $I = D^3/12$, $\bar{E} = E/(1 - v^2)$, and $\bar{v} = v/(1 - v)$.

Six discretizations are performed in the convergence study with source points $\{17 \times 5, 25 \times 7, 33 \times 9, 41 \times 11, 49 \times 13, 57 \times 15\}$ and collocation points in both G-RKCM and RKCM are the same as the source points in this problem. The L2 norms of u and $u_{,\alpha}$ obtained by the proposed G-RKCM with various degrees of bases are compared with those obtained by RKCM ($p = 2$) in Figure 5-9. Again, almost independent of the degree of basis p, the G-RKCM with quadratic basis $q=2$ achieves the similar rate of convergence as the RKCM with quadratic basis. The comparison of shear stress solutions along $x = L/2$ obtained by G-RKCM with $q=2$ and RKCM with $p = 2$ is shown in Figure 5-10, where $N_s = 25 \times 7$ is used. The results of shear stress obtained by G-RKCM are less oscillatory compared to that obtained by RKCM.

91
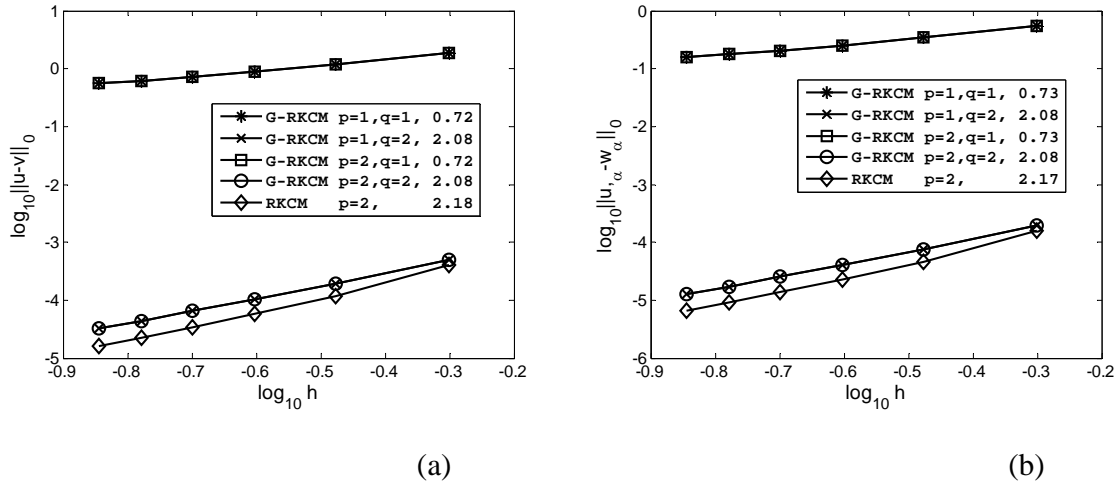
Figure 5-9 Convergence of L2 norms of u and $u_{,\alpha}$ in cantilever problem
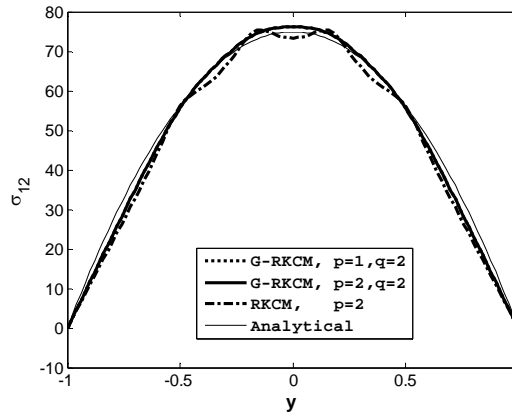
Figure 5-10 Comparison of shear stress along $x = L/2$ in cantilever problem

5.8 Summary

While RKCM using direct RK approximation of strong form has shown an enhanced
conditioning and sparsity in its discrete system compared to RBCM using radial basis

approximation of strong form, and it also resolved the domain integration issues in the weak form based Galerkin meshfree method, the method suffers from the high level of complexity involved in computing the second order derivatives of RK shape functions and the need of using the number of collocation points much larger than the number of source points for optimal convergence. To resolve these issues, in this work we propose a gradient reproducing kernel collocation method (G-RKCM) by formulating the derivatives of RK shape functions directly based on the partition of nullity and discrete derivative reproducing conditions to eliminate the need of taking second derivatives of the Gram matrix involved in RKCM for solving second order PDEs.

We also showed that in the proposed G-RKCM the number of collocation points needs not to be greater than that of source points required in RKCM. The error analysis showed that the rate of convergence in G-RKCM is determined by the polynomial degree in the gradient RK approximation, and is independent to the polynomial degree in the RK approximation. Further, G-RKCM yields the same convergence rates in L2 norms of u and $u_{,\alpha}$. The complexity analysis provided precious operating counts of both RKCM and G-RKCM and clearly demonstrated the significant computational efficiency of G-RKCM over RKCM. The numerical results confirmed with the analytical predictions, and showed that the proposed G-RKCM yields similar convergence property as the RKCM in both L2 norms of u and $u_{,\alpha}$, yet it is roughly 10 times computationally more efficient than RKCM.

Chapter 6 Strong Form Collocation Method for Active Contour Model

6.1 Introduction

The level set method originally devised by Osher and Sethian (1988) was intended to track the topological changes such as merging and breaking. The level set technique has been extensively applied in many practical research areas such as computer graphics, image processing, optimization, and computational fluid dynamics. By this method, the front propagation of a physical quantity is described by an auxiliary function, which is known as the level set function.

The essential idea of the level set method is to track the evolution of a surface in $N-1$ dimensions presented by the level set function with N dimensions in space. Consequently, the motion of boundary, is governed by the evolution of the level set function. One advantage of the level set method is the implicit representation of the curve through the geometric parameters, which facilitates the control of the moving interfaces with changing topology effectively in the process of evolution.

A curvature-dependent algorithm for the level set method was initiated by Osher and Sethian (1988). With this method, the functional contains constraint terms, which depend on the gradient of the image and are effective for images with sharp gradient. As for objects whose boundaries are not defined by the gradient of the image, Chan and Vese (1999, 2001) proposed an active

contour model for image segmentation based on the Mumford-Shah functional with a level set formulation. The minimization of the energy functional leads to the evolution of interface, and the boundary of the object is detected when the deviation of the image information inside and outside the contour of the object reaches the minimum. This novel technique for image segmentation and interface identification was known as the Chan-Vese model, which has the following notable features: The model can detect objects with and without gradients, such as objects with smooth boundaries or discontinuous boundaries; it can automatically detect the interior contours of an object with background noise and stop even if there is no edge-function; and the initial trial interface can be placed anywhere in the image no matter it touches the object or not.

The level set equation in the active contour model is usually solved by the finite difference methods (FDM), where the inputs of the image, known as pixels, are discretized uniformly on the grid points. Nevertheless, for problems of objects whose boundaries evolve in response to the physical process, such as contact and penetration problems, a numerical algorithm based on a Lagrangian grid is needed to avoid the background mesh. Chi (2009) introduced a strong form collocation method, the Reproducing Kernel Collocation Method (RKCM), to discrete the level set equation, and it has been shown that the regularization term becomes less important. Further, to solve the level set equation efficiently without taking the second order derivative of the reproducing kernel shape functions in RKCM, the Gradient Reproducing Kernel Collocation Method (G-RKCM) has been introduced in Chapter 5 to carry out the numerical simulation. To further enhance the computational efficiency of the procedure in this research, a modified RKCM is introduced to the active contour model based on partition of unity. In addition, we

95

introduce the direct collocation method to solve the level set equation without regularization terms.

The outline of this chapter is arranged as follows. The level set function and the associated implicit geometric representation are reviewed in Section 6.2. The Chan-Vese model, active contours without edges, is presented in Section 6.3. The strong form collocation method for solving the level set equation is introduced in Section 6.4, where the image segmentation can be reached directly by the Reproducing Kernel Collocation Method (RKCM) on a Lagrangian grid. To deal with the regularization terms efficiently in the level set equation, the Gradient Reproducing Kernel Collocation Method (G-RKCM) is proposed in Section 6.5 to avoid taking the second order derivatives of the RK shape functions. The modified RKCM without reproducing conditions for level set equation is introduced in Section 6.6. To further speed up the procedure in solving the level set equation with no regularization term, a direct collocation method is adopted in Section 6.7. A summary of the study is given in Section 6.8.

6.2 Implicit Level Set Function
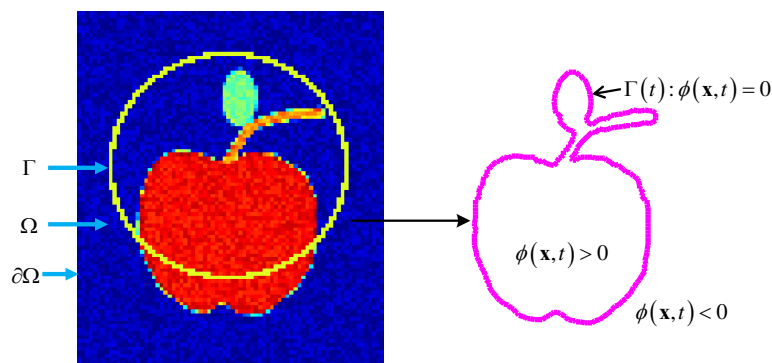
Figure 6-1 Level set function

Consider a closed moving interface $\Gamma(t)$ enclosed by an open region Ω with the boundary $\partial\Omega$

in R^n. Let the region Ω be associated with an auxiliary function $\phi(\mathbf{x},t)$, known as the level set

function, which is Lipschitz continuous and satisfies the following conditions:

$$\begin{cases} \phi(\mathbf{x},t)>0 & \text{if } \mathbf{x} \text{ is inside } \Gamma(t) \\ \phi(\mathbf{x},t)=0 & \text{if } \mathbf{x} \text{ is on } \Gamma(t) \\ \phi(\mathbf{x},t)<0 & \text{if } \mathbf{x} \text{ is outside } \Gamma(t) \end{cases} \tag{6.1}$$

where $\mathbf{x} \in R^n$ as shown in Figure 6-1. The geometric representation of the interface $\Gamma(t)$

includes the unit outward normal $\mathbf{n}$, the mean curvature κ, the area A^+ inside $\Gamma(t)$, the area A^-

outside $\Gamma(t)$, and the length of $\Gamma(t)$, which can be expressed in terms of $\phi(\mathbf{x},t)$ as follows:

$$\mathbf{n} = -\frac{\nabla\phi}{|\nabla\phi|} \tag{6.2}$$

$$\kappa = \nabla\cdot\mathbf{n} = -\nabla\cdot\frac{\nabla\phi}{|\nabla\phi|} \tag{6.3}$$

$$A^+ = \int_\Omega H\left(\phi(\mathbf{x},t)\right)d\mathbf{x} \tag{6.4}$$

$$A^- = \int_\Omega \left(1 - H\left(\phi(\mathbf{x},t)\right)\right)d\mathbf{x} \tag{6.5}$$

$$Length(\Gamma) = \int_\Omega \delta\left(\phi(\mathbf{x},t)\right)\left|\nabla\phi(\mathbf{x},t)\right|d\mathbf{x} \tag{6.6}$$

where the one-dimensional Heaviside function $H(\cdot)$ and Delta function $\delta(\cdot)$ are defined as

$$H(z) = \begin{cases} 1, & z \geq 0 \\ 0, & z < 0 \end{cases} \tag{6.7}$$

97

$$\delta(z) = \frac{dH(z)}{dz} \tag{6.8}$$

Let the level set function $\phi(\mathbf{x},t)$ be a signed distance function to the interface $\Gamma(t)$. We define

$$\phi(\mathbf{x},t) = \begin{cases} +d & \text{if } \mathbf{x} \text{ is inside } \Gamma(t) \\ 0 & \text{if } \mathbf{x} \text{ is on } \Gamma(t) \\ -d & \text{if } \mathbf{x} \text{ is outside } \Gamma(t) \end{cases} \tag{6.9}$$

where

$$d = \min|\mathbf{x}-\mathbf{y}| \quad \text{for all } \mathbf{y} \in \Gamma(t) \tag{6.10}$$

The evolution of the moving interface $\Gamma(t)$ presented by the zero level set, i.e, $\phi(\mathbf{x},t)=0$, is related to the velocity field $\mathbf{v}$ which governs the physical law as

$$\phi_t + \mathbf{v}\cdot\nabla\phi = 0 \tag{6.11}$$

which is the general equation of the level set evolution. It is noted that the level set function $\phi(\mathbf{x},t)$ is updated by the time integration in (6.11). During the updating process, the level set function may deviate from a signed distance function, which may lead to numerical instability and inaccurate interface tracking. To prevent the aforementioned deviation of the level set function in (6.11) from becoming too flat or steep, the reinitialization of the level set function to an approximately signed distance function is considered so that the level set function can reach a steady state with accuracy. The equation of reinitialization with associated initial condition is given as follows (Sussman et al., 1994):

$$\frac{\partial \psi(\mathbf{x},t)}{\partial t} = sign(\phi(\mathbf{x},\tau))(1-|\nabla \psi(\mathbf{x},t)|)$$
$$\psi(\mathbf{x},0) = \phi(\mathbf{x},\tau)$$

<div align="right">(6.12)</div>

where $\phi(\mathbf{x},\tau)$ is the solution at time τ, and $\psi(\mathbf{x},t)$ is the reinitialized $\phi(\mathbf{x},\tau)$ such that $\psi(\mathbf{x},t)$ has the same zero level set as $\phi(\mathbf{x},\tau)$. Away from the interface, $\psi(\mathbf{x},t)$ will converge to $|\nabla \psi(\mathbf{x},t)| = 1$. The detailed derivation of the numerical algorithm for the reinitialization for evolving (6.12) to a steady state is summarized in Appendix A, with reference to the work by Sussman et al. (1994).

6.3 Active Contour Model

<div align="center">(a)   (b)</div>
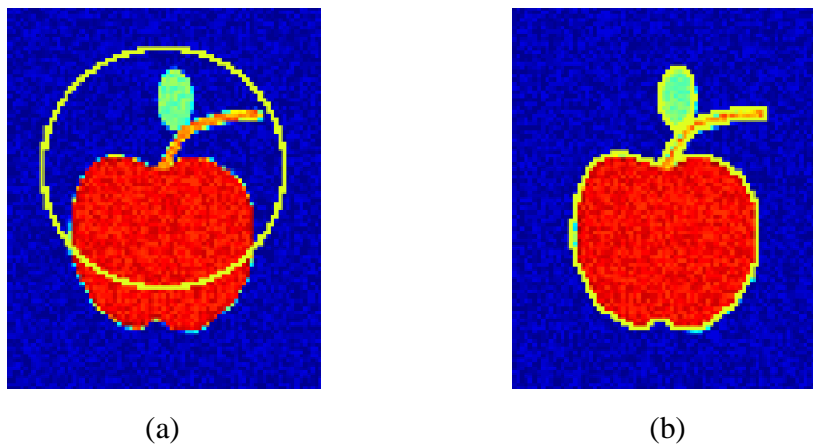
Figure 6-2 Active contour model for image segmentation

Consider a closed evolving interface Γ in Ω and a given image presented by an image color code $C(\mathbf{x})$ in Ω as illustrated in Figure 6-2 (a). Assume that the color code $C(\mathbf{x})$ contains two regions, i.e., the object to be detected and the remaining region outside the object in the image. The object, an apple, is represented by Ω^i and the rest area of the image is represented by Ω^o, a functional considering the inside and outside parts of the object can be defined as

$$\Pi(\Gamma) = \int_{inside\ \Gamma} \left(C(\mathbf{x}) - \overline{c}_1\right)^2 d\mathbf{x} + \int_{outside\ \Gamma} \left(C(\mathbf{x}) - \overline{c}_2\right)^2 d\mathbf{x} \qquad (6.13)$$

where Γ is the trial boundary of the object, and constants $\overline{c}_1$ and $\overline{c}_2$ are the averages of $C(\mathbf{x})$ inside and outside Γ, respectively. For a given initial trial boundary Γ^0, the minimization of (6.13) drives Γ^0 toward the true boundary of the object $\partial\Omega^i$.

Based on the Mumford-Shah functional for image segmentation (Mumford and Shah, 1989), two terms, called the regularization terms, including the length of Γ and the area inside Γ, have been added to (6.13) to yield the following energy functional $\Pi(\overline{c}_1, \overline{c}_2, \Gamma)$ (Chan and Vese, 1999, 2001):

$$\begin{aligned}\Pi(\overline{c}_1, \overline{c}_2, \Gamma) = {} & \mu \cdot Length(\Gamma) + \nu \cdot Area(inside\ \Gamma) \\ & + \lambda_1 \int_{inside\ \Gamma} \left(C(\mathbf{x}) - \overline{c}_1\right)^2 d\mathbf{x} + \lambda_2 \int_{outside\ \Gamma} \left(C(\mathbf{x}) - \overline{c}_2\right)^2 d\mathbf{x}\end{aligned} \qquad (6.14)$$

where $\mu \geq 0$, $\nu \geq 0$, and $\lambda_1, \lambda_2 > 0$ are constant coefficients. The first two regularization terms control the smoothness of the detected boundary while the last two constraints drive the trial interface toward the true boundary of the object. As suggested by Chan and Vese (2001) and Osher and Fedkiw (2002), the values $\nu = 0$ and $\lambda_1 = \lambda_2 = \lambda$ are adopted in this study. Moreover,

100

a scale factor defined as μ/λ controls the resolution of the image segmentation. In general, only large objects are to be detected when μ/λ is large. For example, if the object is formed by scattering data, only the large object, not the small pieces, is of interest, and a large μ/λ is required. The initial trial interface breaks into pieces, for which small objects are to be detected, when μ/λ is small.

To implicitly represent the moving interface $\Gamma(t)$, introducing the level set function $\phi(\mathbf{x},t)$ to (6.1) and the associated geometric representation in (6.4)-(6.6) to the functional $\Pi(\overline{c}_1,\overline{c}_2,\Gamma)$ in (6.14) gives rise to

$$
\begin{aligned}
\Pi(\overline{c}_1,\overline{c}_2,\Gamma) = {}& \mu\int_\Omega \delta(\phi)|\nabla\phi|\,d\mathbf{x} + v\int_\Omega H(\phi)\,d\mathbf{x} \\
& + \lambda_1\int_\Omega \left(C(\mathbf{x})-\overline{c}_1\right)^2 H(\phi)\,d\mathbf{x} + \lambda_2\int_\Omega \left(C(\mathbf{x})-\overline{c}_2\right)^2 \left(1-H(\phi)\right)\,d\mathbf{x}
\end{aligned}
\tag{6.15}
$$

where H is the heaviside function, and

$$
\begin{aligned}
\overline{c}_1 &= \frac{\int_\Omega C(\mathbf{x})H(\phi)\,d\mathbf{x}}{\int_\Omega H(\phi)\,d\mathbf{x}} \\
\overline{c}_2 &= \frac{\int_\Omega C(\mathbf{x})\left(1-H(\phi)\right)\,d\mathbf{x}}{\int_\Omega \left(1-H(\phi)\right)\,d\mathbf{x}}
\end{aligned}
\tag{6.16}
$$

The stationary of functional $\Pi(\overline{c}_1,\overline{c}_2,\Gamma)$ yields

$$\frac{\partial \phi}{\partial t} = \delta(\phi) \left[\mu \nabla \cdot \left(\frac{\nabla \phi}{|\nabla \phi|} \right) - v - \lambda_1 \left(C(\mathbf{x}) - \bar{c}_1 \right)^2 + \lambda_2 \left(C(\mathbf{x}) - \bar{c}_2 \right)^2 \right] \quad \text{in } \Omega$$

$$\phi(\mathbf{x},0) = \phi_0(\mathbf{x}) \quad \text{in } \Omega \qquad (6.17)$$

$$\delta(\phi) \frac{\nabla \phi}{|\nabla \phi|} \cdot \mathbf{n} = 0 \quad \text{on } \partial\Omega$$

where $\mathbf{n}$ is the outward normal to the boundary $\partial\Omega$ and ϕ is the steady state solution of (6.17).

A regularization function H_ε is introduced to the Heaviside function $H(\cdot)$ with the following form:

$$H_\varepsilon(z) = \frac{1}{2}\left(1 + \frac{2}{\pi}\arctan\left(\frac{z}{\varepsilon}\right)\right) \qquad (6.18)$$

where ε is a positive parameter. The corresponding Delta function $\delta(\cdot)$ defined in (6.8) becomes

$$\delta_\varepsilon(z) = \frac{1}{\pi\varepsilon}\left(1 + \left(\frac{z}{\varepsilon}\right)^2\right)^{-1} \qquad (6.19)$$

The finite difference method (FDM) is usually employed to solve (6.17) numerically for image segmentation. An implicit finite difference scheme is given as follows:

$$\phi_{i,j}^{n+1} = \phi_{i,j}^{n} + \Delta t \cdot \delta_{\varepsilon}\left(\phi_{i,j}^{n}\right) \cdot \frac{\mu}{h^2} \cdot$$

$$
\left(
\frac{\phi_{i+1,j}^{n+1} - \phi_{i,j}^{n+1}}{\sqrt{\dfrac{\left(\phi_{i+1,j}^{n} - \phi_{i,j}^{n}\right)^2}{h^2} + \dfrac{\left(\phi_{i,j+1}^{n} - \phi_{i,j-1}^{n}\right)^2}{(2h)^2}}}
-
\frac{\phi_{i,j}^{n+1} - \phi_{i-1,j}^{n+1}}{\sqrt{\dfrac{\left(\phi_{i,j}^{n} - \phi_{i-1,j}^{n}\right)^2}{h^2} + \dfrac{\left(\phi_{i-1,j+1}^{n} - \phi_{i-1,j-1}^{n}\right)^2}{(2h)^2}}}
\right.
$$

$$
\left.
+ \frac{\phi_{i,j+1}^{n+1} - \phi_{i,j}^{n+1}}{\sqrt{\dfrac{\left(\phi_{i+1,j}^{n} - \phi_{i-1,j}^{n}\right)^2}{(2h)^2} + \dfrac{\left(\phi_{i,j+1}^{n} - \phi_{i,j}^{n}\right)^2}{h^2}}}
-
\frac{\phi_{i,j}^{n+1} - \phi_{i,j-1}^{n+1}}{\sqrt{\dfrac{\left(\phi_{i+1,j-1}^{n} - \phi_{i-1,j-1}^{n}\right)^2}{(2h)^2} + \dfrac{\left(\phi_{i,j}^{n} - \phi_{i,j-1}^{n}\right)^2}{h^2}}}
\right)
\tag{6.20}
$$

$$
+ \Delta t \cdot \delta_{\varepsilon}\left(\phi_{i,j}^{n}\right)\left[-\nu - \lambda_1 \left(C_{i,j} - c_1\left(\phi^n\right)\right)^2 + \lambda_2 \left(C_{i,j} - c_2\left(\phi^n\right)\right)^2 \right]
$$

where h is the nodal distance, and the superscript n and the subscript j denote the time step and space step, respectively.

6.3.1 Numerical Examples

In this section, two examples will be presented using the active contour model. The finite difference scheme is employed to solve the level set equation in (6.17), in which one level set function is used in each example. The numerical test demonstrates that the level set method presented is able to segment the image into two phases and detect the boundary effectively.

6.3.1.1 Boundary Identification
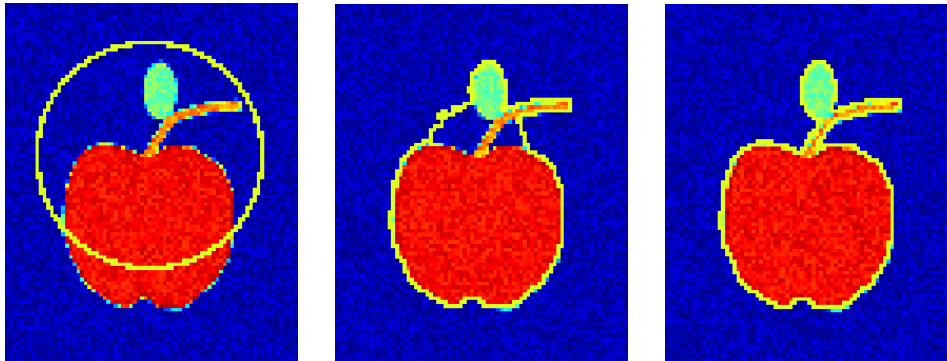
(a) Initial (b) 30 steps (c) 120 steps

Figure 6-3 Boundary identification of an object with different colors

The image presented in Figure 6-3 (a) contains a colorful object with random background noise. The parameters used in solving the level set equation are selected as follows: $\mu = 20$, $v = 0$, $\varepsilon = 0.5$, and $\lambda_1 = \lambda_2 = 1$. A steady state solution is obtained after 120 steps with the time step size $dt = 0.01$, and there is no reinitialization involved in this example. The boundary evolution process is shown in Figure 6-3 (a)-(c). Interestingly, as the ratio μ/λ decreases, the number of time steps required to retrieve the real boundary of the object decreases as well, where $\mu = 20$ and $dt = 0.01$ are set as the reference. Table 6-1 shows the comparison of the scale factor μ/λ versus the number of time steps.

Table 6-1 μ/λ vs. the number of time steps (based on $\mu = 20$ and $dt = 0.01$)

μ/λ	1	10	20
steps	11	60	120

6.3.1.2 Image Segmentation

(a) Initial	(b) 10 steps	(c) 30 steps
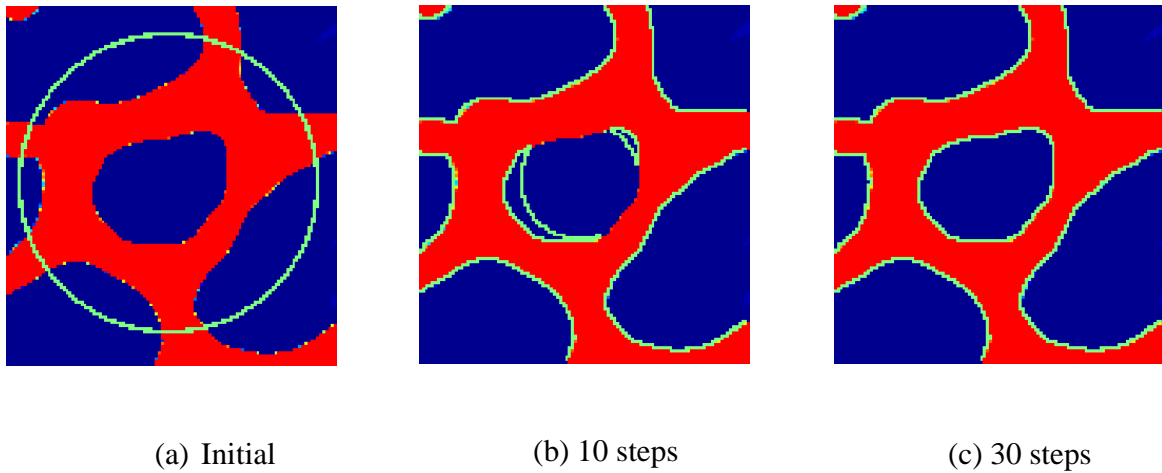
Figure 6-4 Segmentation of image with complex geometry

Figure 6-4 (a) shows a simplified geometry for a unit cell of the bone tissue, in which two phases, the solid skeleton depicted in red and the fluid in the pores depicted in blue, need to be segmented apart. The parameters $\mu = 100$, $v = 0$, $\varepsilon = 0.5$, and $\lambda_1 = \lambda_2 = 20$ are used in solving the level set equation. A time step size $dt = 0.01$ with total 30 steps gives the steady state solution, where the dissimilar phases are segmented completely. No reinitialization is required in this example. The process of interfacial evolution is given in Figure 6-4 (a)-(c).

6.4 Strong Form Collocation Method for Active Contour Model

Inspired by the image pixels such as the microstructures of biological bone materials given on uniformly distributed grid, we introduce the strong form collocation method to deal with images directly based on point discretization. However, the original level set equation (6.17) is generally solved by the FDMs as expressed in (6.20).

When the interface evolution is a consequence of the physical process, i.e., the object to be detected is changing as a function of time, a background Eulerian grid is required to project the material points onto the nearest grid points (Chi, 2009). Therefore, the parameter μ associated with the regularization term in the level set equation needs to be large to retrieve interface with enough smoothness, and the time step size needs to be small so that the Courant-Friedrichs-Lewy (CFL) condition is satisfied, which make the finite difference scheme time-consuming. As such, the strong form collocation method is introduced to formulate the level set equation on a Lagrangian grid, in which the influence of the interface regularity becomes less important and the parameter associated with the regularization term becomes small as well. Based on the collocation formulation, the biological microstructures with complex geometry can be constructed directly and easily.

6.4.1 Strong Form Collocation Method

Consider the general strong form of the level set equation as follows:

$$\frac{\partial \phi}{\partial t} = L\phi + f \qquad \text{in } \Omega$$

$$\phi(\mathbf{x},0) = \phi_0(\mathbf{x}) \quad \text{in } \Omega \qquad\qquad (6.21)$$

$$B\phi = h \qquad\qquad \text{on } \partial\Omega$$

where L and B are the differential operators in the domain Ω and on the boundary $\partial\Omega$, respectively. f and h are the source term in Ω and the prescribed boundary condition on $\partial\Omega$, respectively, and ϕ_0 is the initial condition. In the process of image segmentation for boundary and interface identification, the main purpose is to identify the boundary and interface of the object represented by the zero level set function $\phi = 0$ rather than to find ϕ exactly. As a consequence, the real boundary condition on $\partial\Omega$ has insignificant influence on the solution ϕ close to $\phi = 0$, and it can be neglected in the numerical scheme for computational efficiency.

By introducing the strong form collocation method to solve the level set equation in (6.21), the level set function ϕ is approximated by ϕ^h as

$$\phi \approx \phi^h = \sum_{I=1}^{N_s} \Psi_I(\mathbf{x}) \mathbf{a}_I(t) =: \Psi^{\mathrm{T}}(\mathbf{x}) \mathbf{a}(t), \quad \forall \mathbf{x} \in \Omega \qquad\qquad (6.22)$$

and

$$\Psi^{\mathrm{T}} = \left[\Psi_1, \cdots, \Psi_{N_s} \right], \quad \mathbf{a}^{\mathrm{T}} = \left[a_1, \cdots, a_{N_s} \right] \qquad\qquad (6.23)$$

where N_s is the number of source points, $\Psi_I(\mathbf{x})$ is the shape function, and a_I is the generalized coefficient. It is noted that in the reproducing kernel collocation method (RKCM), $\Psi_I(\mathbf{x})$ is the reproducing kernel (RK) shape function as presented in Chapter 5.

107

By substituting the approximation of the level set function in (6.22) into the level set equation in (6.21), and evaluating the differential equation and initial condition at the collocation points $\mathbf{p}_\ell \in \Omega$ with $\ell = 1, 2, \ldots, N_c$, the semi-discrete collocation system is derived as follows:

$$\mathbf{N}\dot{\mathbf{a}}(t) = \mathbf{L} + \mathbf{f}$$
$$\mathbf{N}\mathbf{a}(0) = \boldsymbol{\varphi}_0 \qquad (6.24)$$
$$\mathbf{B}\mathbf{a}(\mathbf{x}) = \mathbf{h}$$

where

$$\mathbf{L} = \left[L\phi^h(\mathbf{p}_1), L\phi^h(\mathbf{p}_2), \ldots, L\phi^h(\mathbf{p}_{N_c}) \right]^{\mathrm{T}}$$
$$\mathbf{f} = \left[f(\mathbf{p}_1), f(\mathbf{p}_2), \ldots, f(\mathbf{p}_{N_c}) \right]^{\mathrm{T}}$$
$$\mathbf{N} = \left[\boldsymbol{\Psi}(\mathbf{p}_1), \boldsymbol{\Psi}(\mathbf{p}_2), \ldots, \boldsymbol{\Psi}(\mathbf{p}_{N_c}) \right]^{\mathrm{T}}$$
$$\boldsymbol{\varphi}_0 = \left[\phi_0(\mathbf{p}_1), \phi_0(\mathbf{p}_2), \ldots, \phi_0(\mathbf{p}_{N_c}) \right]^{\mathrm{T}} \qquad (6.25)$$
$$\mathbf{B} = \left[B\phi^h(\mathbf{p}_1), B\phi^h(\mathbf{p}_2), \ldots, B\phi^h(\mathbf{p}_{N_c}) \right]^{\mathrm{T}}$$
$$\mathbf{h} = \left[h(\mathbf{p}_1), h(\mathbf{p}_2), \ldots, h(\mathbf{p}_{N_c}) \right]^{\mathrm{T}}$$

Denote the level set function evaluated at the collocation point $\mathbf{p}_I$ by $\phi_I^h = \boldsymbol{\Psi}^T(\mathbf{p}_I)\mathbf{a}$, the explicit form of the component L_I in matrix $\mathbf{L}$ is given by

$$L_I = \delta_\varepsilon\left(\phi_I^h\right)\left[\mu\boldsymbol{\Xi}\left(\phi_I^h\right) - \nu - \lambda_1\left(C(\mathbf{p}_I) - \bar{c}_1\right)^2 + \lambda_2\left(C(\mathbf{p}_I) - \bar{c}_2\right)^2 \right] \qquad (6.26)$$

where

$$\Xi\left(\phi_I^h\right) = \left(\phi_{I,xx}^h + \phi_{I,yy}^h + \phi_{I,zz}^h\right)\left(\phi_{I,x}^h\phi_{I,x}^h + \phi_{I,y}^h\phi_{I,y}^h + \phi_{I,z}^h\phi_{I,z}^h\right)^{-\frac{1}{2}}$$

$$-\left(\phi_{I,x}^h\phi_{I,x}^h + \phi_{I,y}^h\phi_{I,y}^h + \phi_{I,z}^h\phi_{I,z}^h\right)^{-\frac{3}{2}}\left(\phi_{I,xx}^h\phi_{I,x}^h\phi_{I,x}^h + \phi_{I,yy}^h\phi_{I,y}^h\phi_{I,y}^h + \phi_{I,zz}^h\phi_{I,z}^h\phi_{I,z}^h\right.$$

$$\left. +2\phi_{I,xy}^h\phi_{I,x}^h\phi_{I,y}^h + 2\phi_{I,yz}^h\phi_{I,y}^h\phi_{I,z}^h + 2\phi_{I,zx}^h\phi_{I,z}^h\phi_{I,x}^h\right) \tag{6.27}$$

and

$$\overline{c}_1 = \frac{\sum_{I=1}^{N_c} C\left(\mathbf{p}_I\right) H_\varepsilon\left(\phi_I^h\right) dA_I}{\sum_{I=1}^{N_c} H_\varepsilon\left(\phi_I^h\right) dA_I} \tag{6.28}$$

$$\overline{c}_2 = \frac{\sum_{I=1}^{N_c} C\left(\mathbf{p}_I\right)\left(1 - H_\varepsilon\left(\phi_I^h\right)\right) dA_I}{\sum_{I=1}^{N_c} \left(1 - H_\varepsilon\left(\phi_I^h\right)\right) dA_I} \tag{6.29}$$

where dA_I is the weight in the integration presented by the area of a Voronoi cell with respect to the collocation point $\mathbf{p}_I$. In the level set based image segmentation, a unit area for dA_I is adopted herein.

By employing the forward Euler's method, the collocation equations in (6.24) become

$$\begin{aligned} \mathbf{N}\left(\mathbf{a}^{n+1} - \mathbf{a}^n\right) &= \Delta t\mathbf{L}^n \\ \mathbf{N}\mathbf{a}^0 &= \boldsymbol{\varphi}_0 \end{aligned} \tag{6.30}$$

in which the superscript denotes the n-th time step and Δt is the time step size. In the collocation method, the number of collocation points with zero residuals enforced is usually taken to be larger than the number of source points to form an overdetermined system, while ensuring the solution accuracy, as pointed out by Zhang et al. (2001) and Hu et al. (2007).

However, the overdetermined system may make the level set method become computationally inefficient especially for images of high resolution. Therefore, it is recommended that the same number of collocation points and source points be used. The unknown $\mathbf{a}^{n+1}$ can be obtained by the following incremental formulation at $t = n+1$:

$$\mathbf{a}^{n+1} = \mathbf{a}^n + \Delta t \mathbf{N}^{-1} \mathbf{L}^n \qquad (6.31)$$

$$\mathbf{a}^0 = \mathbf{N}^{-1} \boldsymbol{\varphi}_0 \qquad (6.32)$$

Based on the direct strong form collocation, the numerical algorithm for solving the level set equation in the active contour model is given as follows:

(1) Compute the shape functions Ψ_I from a set of source points and evaluate Ψ_I at the collocation points to form the transformation matrix $\mathbf{N}$ and its inverse $\mathbf{N}^{-1}$.

(2) Form an initial trial level set function $\boldsymbol{\varphi}_0$ and calculate $\mathbf{a}^0$ by using (6.32).

(3) Compute $\overline{c}_1$, $\overline{c}_2$, and $\mathbf{L}^n$ at $t = n$.

(4) Calculate $\mathbf{a}^{n+1}$ at $t = n+1$ by using (6.31).

(5) If $\left(\left| \overline{c}_1^{n+1} - \overline{c}_1^n \right| + \left| \overline{c}_2^{n+1} - \overline{c}_2^n \right| \right) \Big/ \left(\overline{c}_1^1 + \overline{c}_2^1 \right) < tolerance$, stop the procedure. Otherwise, go to step (1) and continue.

Here we modify the residual as $\left(\left| \overline{c}_1^{n+1} - \overline{c}_1^n \right| + \left| \overline{c}_2^{n+1} - \overline{c}_2^n \right| \right) \Big/ \left(\overline{c}_1^1 + \overline{c}_2^1 \right)$.

6.4.2 Numerical Examples

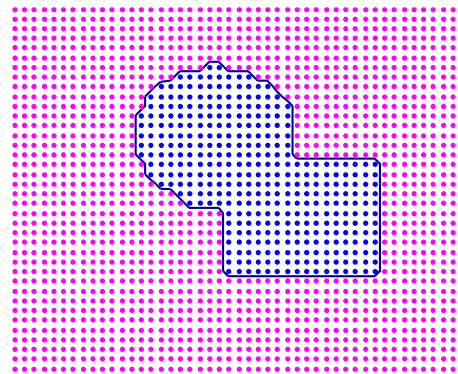### 6.4.2.1 Investigation of the RK Properties on Image Segmentation

In this example, we shall investigate the influences of different orders of RK bases and kernel functions on the RK support size in the image segmentation based on RKCM. The image simulated by a set of 47×38 discrete points with two different colors is shown in Figure 6-5, where each point occupies a single pixel in the image. For computational efficiency in detecting the boundary of the object, the collocation points N_c are chosen to be the same as the source points N_s in RKCM. The parameters for solving the level set equation are selected as follows: $\mu = 1$, $v = 0$, $\lambda_1 = \lambda_2 = 1$, $dt = 0.01$, the residual is set as 10^{-3} and ε equals twice the RK support size a. A quintic B-spline kernel function and a quadratic B-spline kernel function with two different order bases, the linear basis and the quadratic basis, used in constructing the RK shape functions will be investigated.

When a high order kernel function such as the quintic B-spline kernel function is used in RKCM to approximate a discontinuous image color code, a very large support size is needed even for a linear basis in the RK shape function, in order to avoid the oscillation of the level set function. In contrast, the use of a low order kernel function like the quadratic B-spline kernel function can resolve the oscillation of the level set function with a "proper" support size with respect to the order of basis in the RK shape function. In Table 6-2, the corresponding RK support sizes a with respect to the order of RK bases and kernel functions are summarized. The steady state solutions obtained by the quintic B-spline and quadratic B-spline kernel functions with different

111

bases are shown in Figure 6-5 (a)-(b) and (c)-(d), respectively; the corresponding residuals and

total time steps are summerized in Table 6-3.
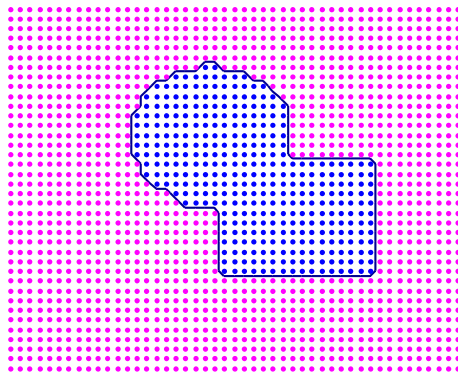
(a) Linear basis with $a = 3.8$ (c) Linear basis with $a = 2.4$
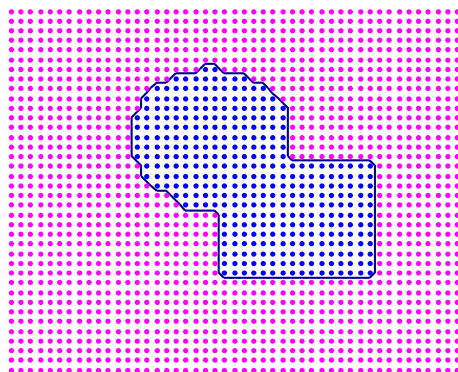
(b) Quadratic basis with $a = 4.0$ (d) Quadratic basis with $a = 2.4$

Figure 6-5 Boundary identification of an object obtained by using different kernel functions and bases; Quintic B-spline kernel function with (a) Linear basis and (b) Quadratic basis; Quadratic B-spline kernel function with (c) Linear basis and (d) Quadratic basis

Table 6-2 RK support sizes vs. RK bases and kernel functions for $\mu \neq 0$

Kernel / Basis	Quintic B-spline	Quadratic B-spline
Linear	3.8	2.4
Quadratic	4.0	2.4

Table 6-3 Comparison of residuals and total time steps

Kernel	Quintic B-spline		Quadratic B-spline	
Basis	Linear	Quadratic	Linear	Quadratic
Residual	9.8309e-004	9.8121e-004	9.7932e-004	9.7928e-004
Total Steps	60	62	46	46

6.4.2.2 Interface Identification of a Microstructure

A three-dimensional image of sheep vertebrae shown in Figure 6-6 is adopted from the website of SCANCO Medical, in which the trabecular bone image is obtained by Xtreme-CT with nominal resolution of 41 µm. Specifically, the Xtreme-CT is designed to perform a three-dimen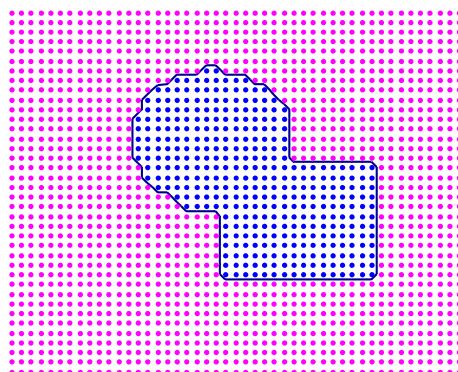sional peripheral quantitative-computed tomography (pQCT), which measures both the bone density and bone structure, and yields cross-sectional images of the bones in vivo with high-resolution. As shown in Figure 6-7 (a), one slice of the trabecular bone image is composed of 1024×973 pixels with a maximum scan size $126\text{mm} \times 150\text{mm}$ in the plane. The corresponding microstructural image of a unit cell with 75×75 pixels is given in Figure 6-7 (b), where the unit cell location is specified in Figure 6-7 (a).
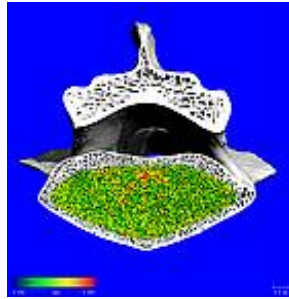
Figure 6-6 Three-dimensional image of sheep vertebrae (adopted from SCANCO Medical)
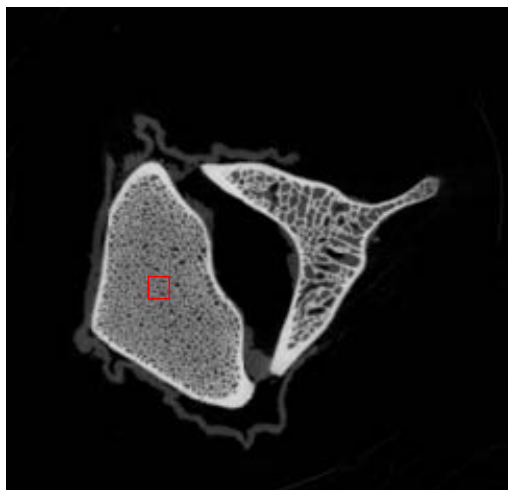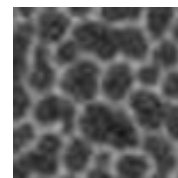
<div align="center">(a)   (b)</div>

Figure 6-7 Trabecular bone image of sheep vertebrae (adopted from SCANCO Medical)

For medical images obtained from CT or MRI, the images are in general presented in grayscale with background noise such as the one shown in Figure 6-7 (a) and (b). To retrieve a smooth interface of a microstructure, a large μ is preferred. The corresponding parameters in the level set equation are $\mu = 1000$, $\nu = 0$, $\lambda_1 = \lambda_2 = 3500$, $dt = 0.1$, $\varepsilon = 2a$, and the residual is set to be

5×10^{-6}. The collocation points are chosen to be the same as the source points ($N_c = N_s$). A quadratic basis and a quadratic B-spline kernel function are adopted in the construction of RK shape functions, and the support size of RK shape function is 2.4. For the image shown in Figure 6-7 (b), the initial trial interface and final evolved interface are presented in Figure 6-8 (a) and (b), respectively. The steady state solution is reached after 55 steps with the residual 4.4537e-006.

(a) Initial   (b) 55 steps

Figure 6-8 Interface identification of a microstructure by RKCM; (a) Initial trial interface; (b) Final evolved interface

6.4.2.3 Two-Phase Segmentation

Consider a microstructure presented by two colors as shown in Figure 6-9 (a) with 50×50 pixels, the parameters for solving the level set equation are $\mu = v = 0$, $\lambda_1 = \lambda_2 = 1$, $dt = 0.1$, $\varepsilon = 2a$, and residual 5×10^{-4}. The collocation points are selected the same as the source points, and the RK shape functions are constructed by a constant basis and a linear spline kernel function. The support size of RK shape function is chosen as $a = 0.51$. The interface evolution process is shown in Figure 6-9 (b) and (c), the solid phase and fluid phase are segmented after 18 steps, where the pink points denote the solid skeleton while the blue points denote the fluid phase. It is noted that when $\mu = 0$, the level set equation degenerates to an ordinary differential equation

115

(ODE), which can be solved easily by function approximation, providing that the image does not have background noise.

(a) Initial   (b) 2 steps   (c) 18 steps
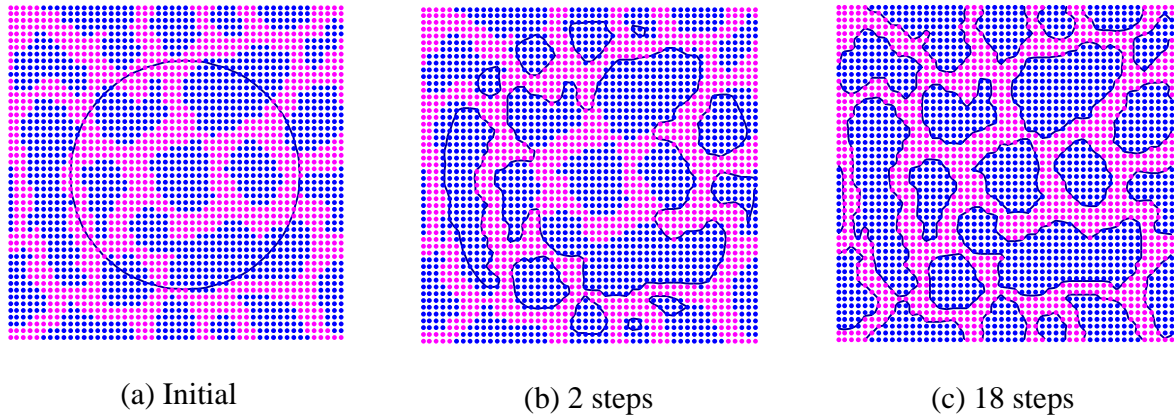
Figure 6-9 Interface identification in the microstructure with two phases by RKCM

6.5 Gradient Reproducing Kernel Collocation Method for Active Contour Model

In Chapter 5, we proposed the gradient reproducing kernel collocation method (G-RKCM) for solving the boundary value problems, which has been demonstrated to be less computationally expensive owing to the gradient approximation introduced to avoid taking the second derivatives of reproducing kernel (RK) shape functions. Based on this concept, the proposed G-RKCM is introduced to solve the level set equation in the active contour model, where nonzero μ is considered herein to detect a smooth boundary of the object.

6.5.1 Gradient Reproducing Kernel Approximation

In the gradient reproducing kernel approximation, the derivatives of the level set function ϕ are approximated by the shape functions directly as follows:

$$\phi_{,x} \approx \phi^x = \sum_{I=1}^{N_s} \Psi_I^x(\mathbf{x}) a_I(t) =: \Psi^{x^{\mathrm{T}}}(\mathbf{x}) \mathbf{a}(t)$$

$$\phi_{,y} \approx \phi^y = \sum_{I=1}^{N_s} \Psi_I^y(\mathbf{x}) a_I(t) =: \Psi^{y^{\mathrm{T}}}(\mathbf{x}) \mathbf{a}(t), \quad \forall \mathbf{x} \in \Omega \qquad (6.33)$$

$$\phi_{,z} \approx \phi^z = \sum_{I=1}^{N_s} \Psi_I^z(\mathbf{x}) a_I(t) =: \Psi^{z^{\mathrm{T}}}(\mathbf{x}) \mathbf{a}(t)$$

and

$$\Psi^{x^{\mathrm{T}}} = \begin{bmatrix} \Psi_1^x & \Psi_2^x & \dots & \Psi_{N_s}^x \end{bmatrix}, \quad \Psi^{y^{\mathrm{T}}} = \begin{bmatrix} \Psi_1^y & \Psi_2^y & \dots & \Psi_{N_s}^y \end{bmatrix},$$
$$\Psi^{z^{\mathrm{T}}} = \begin{bmatrix} \Psi_1^z & \Psi_2^z & \dots & \Psi_{N_s}^z \end{bmatrix}, \quad \mathbf{a}^{\mathrm{T}} = \begin{bmatrix} a_1, \cdots, a_{N_s} \end{bmatrix} \qquad (6.34)$$

where $\Psi_I^m(\mathbf{x})$ is the gradient RK shape function in G-RKCM, which satisfies the gradient reproducing kernel conditions presented in Chapter 5.

Introducing the approximation of ϕ in (6.22) and the corresponding gradient approximation in (6.33) to the level set equation in (6.21), and evaluating the governing equations at the collocation points $\mathbf{p}_\ell \in \Omega \ (\ell = 1, 2, ..., N_c)$ lead to the semi-discrete collocation system in (6.24). The explicit expression for the component B_I in matrix $\mathbf{B}$ has been given in (6.26), while the operator Ξ in G-RKCM has the following form:

$$\Xi\left(\phi_I^x,\phi_I^y,\phi_I^z\right)=\left(\phi_{I,x}^x+\phi_{I,y}^y+\phi_{I,z}^z\right)\left(\phi_I^x\phi_I^x+\phi_I^y\phi_I^y+\phi_I^z\phi_I^z\right)^{-\frac{1}{2}}$$

$$-\left(\phi_I^x\phi_I^x+\phi_I^y\phi_I^y+\phi_I^z\phi_I^z\right)^{-\frac{3}{2}}\left(\phi_{I,x}^x\phi_I^x\phi_I^x+\phi_{I,y}^y\phi_I^y\phi_I^y+\phi_{I,z}^z\phi_I^z\phi_I^z\right. \tag{6.35}$$

$$\left.+\phi_{I,y}^x\phi_I^x\phi_I^y+\phi_{I,x}^y\phi_I^x\phi_I^y+\phi_{I,z}^y\phi_I^y\phi_I^z+\phi_{I,y}^z\phi_I^y\phi_I^z+\phi_{I,x}^z\phi_I^x\phi_I^z+\phi_{I,z}^x\phi_I^x\phi_I^z\right)$$

6.5.2 Numerical Examples

6.5.2.1 Interface Identification of a Microstructure

To investigate the computational efficiency of the proposed gradient reproducing kernel collocation method in the interface and boundary identification process, we consider the same microstructure shown in Figure 6-7 (b), which is presented by 75×75 pixels in Figure 6-10 (a). The corresponding parameters for solving the level set equation are given as follows: $\mu=1000$, $\nu=0$, $\lambda_1=\lambda_2=3500$, $dt=0.1$, and ε is set to be twice the RK support size a. The same numbers of collocation points and source points ($N_c=N_s$) are adopted, and the residual is set to be 5×10^{-6}.

Without loss of generality, the standard RKCM with a quadratic basis RK shape function ($p=2$) is compared with the G-RKCM with equal-order quadratic bases ($p=q=2$), in which the level set function ϕ is approximated by the p-th order basis RK shape function while the derivative $\nabla\phi$ is approximated by the q-th order basis in the gradient RK shape function. The RK support size is chosen as 2.4, and a quadratic B-spline kernel function is adopted in construction of both the RK and gradient RK shape functions. The interface detected by G-RKCM is shown in Figure 6-10 (b), and the related residual and CPU time are summarized in Table 6-4, in which the

118

detected interface by RKCM can be referred to section 6.4.2.2. As can be observed from Figure 6-10 (b), G-RKCM with equal-order quadratic bases ($p = q = 2$) can detect the interface with representative contours clearly. By examining the quadratic basis ($p = 2$) in RKCM and G-RKCM with equal-order quadratic bases ($p = q = 2$), G-RKCM is computationally more efficient than RKCM ($p = 2$), in that the CPU time is reduced by about 16%.

(a) Initial   (b) 55 steps
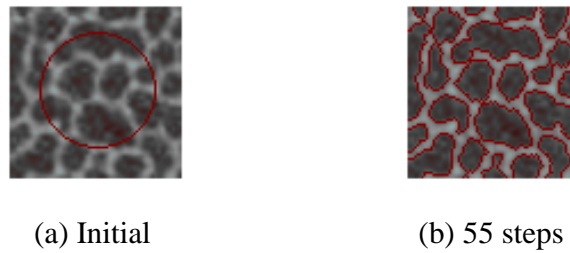
Figure 6-10 Interface identification of a microstructure by G-RKCM: (a) Initial trial interface; (b) Final evolved interface

Table 6-4 Comparison of residuals and total steps with different collocation methods

Method	RKCM $p = 2$	G-RKCM $p = q = 2$
Residual	4.4537e-006	4.4725e-006
Total Steps	55	55
Time (sec.)	244.0059	205.1419
CPU saving (%)	-	15.9275

Note: Time is calculated on the basis of constructing shape functions

6.5.2.2 Investigation of G-RKCM on Image Segmentation

Consider the same microstructure shown in Figure 6-7 (b), it is presented by 50×50 pixels in

Figure 6-11 (a) with two colors. The parameters $\mu = 1000$, $v = 0$, $\lambda_1 = \lambda_2 = 3500$, $dt = 0.1$, and

$\varepsilon = 2a$ are adopted in the level set equation, and the residual is 10^{-5}. The collocation points are

adopted to be the same as the source points ($N_c = N_s$). Two cases with a quadratic B-spline

kernel function are considered: standard RKCM with a quadratic basis shape function ($p = 2$),

and G-RKCM with equal-order quadratic bases ($p = q = 2$). The RK support size $a = 2.4$ is

adopted in the construction of both RK and gradient RK shape functions.

The detected interfaces of the microstructures are shown in

Figure 6-11 (b) and (c). Table 6-5 compares the residuals obtained after 43 steps and the

corresponding CPU time. Similarly, both methods with quadratic basis ($p = 2$) evolve and can

identify the interfaces in the same trend, while G-RKCM with equal-order quadratic bases

($p = q = 2$) is computationally less expensive by saving CPU time about 17.40%, in comparison

with RKCM ($p = 2$).

Table 6-5 Comparison of residuals and CPU time with different collocation methods

Method	RKCM $p = 2$	G-RKCM $p = q = 2$
Residual	9.7555e-006	9.7538e-006
Total Steps	47	47
CPU Time (sec.)	45.9816	37.9808
CPU Saving (%)	-	17.40

Note: Time is calculated on the basis of constructing shape functions
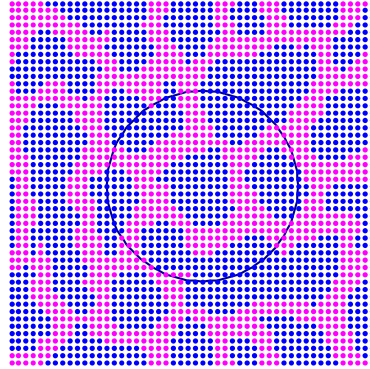
(a) Initial
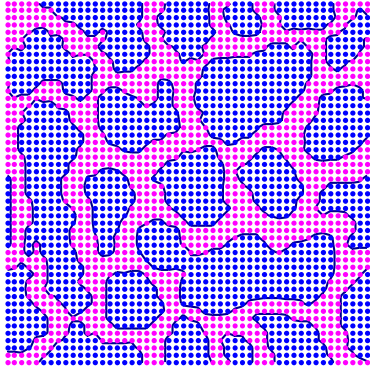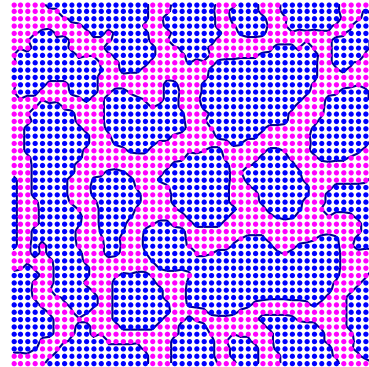
(b) RKCM $p = 2$ (c) G-RKCM $p = q = 2$

Figure 6-11 Interface identification in the microstructure with two phases by RKCM and G-RKCM: (a) Initial trial interface; (b) Interface detected by RKCM ($p = 2$); (c) Interface detected by G-RKCM ($p = q = 2$)

6.6 Modified Reproducing Kernel Collocation Method for Active Contour Model

When solving a PDE by RKCM and G-RKCM, one requires the shape functions to satisfy the 2nd order consistency to ensure convergence, in which the basis function requires to achieve the associated order of completeness. However, in the image process of boundary and interface

identification, the constraints, controlling the difference of average color codes inside and outside the contour, play the major role in driving the moving interface toward the true boundary of the object, which make the regularization terms less important. As a consequence, the consistency condition in constructing the RK shape function can be further loosened to solve the level set equation computationally efficiently. In the following section, the kernel function is directly employed as the shape function in the strong form collocation method to solve the level set equation and identify the boundary. A quadratic B-spline kernel function is given below:

$$\varphi_a(s) = \begin{cases} \dfrac{3}{4} - \dfrac{9}{4}s^2, & 0 \le s < \dfrac{1}{3}, \\[2mm] \dfrac{9}{8} - \dfrac{9}{4}s + \dfrac{9}{8}s^2, & \dfrac{1}{3} \le s < 1, \quad s = \dfrac{\|\mathbf{x} - \mathbf{x}_I\|}{a} \\[2mm] 0, & s \ge 1, \end{cases} \qquad (6.36)$$

6.6.1 Numerical Examples

6.6.1.1 Interface Identification of a Microstructure

Consider the microstructure presented by 75×75 pixels in Figure 6-12 (a). The parameters for solving the level set equation are given as follows: $\mu = 1000$, $\nu = 0$, $\lambda_1 = \lambda_2 = 3500$, $dt = 0.1$, and ε is set to be twice the RK support size a. The collocation points are adopted the same as the source points ($N_c = N_s$), and the residual is set to be 5×10^{-6}. A quadratic kernel function is used, and the support size is 1.2. The steady state solution is obtained at 52 steps with residual 2.8656e-006 as shown in Figure 6-12 (b).

122

(a) Initial   (b) 52 steps
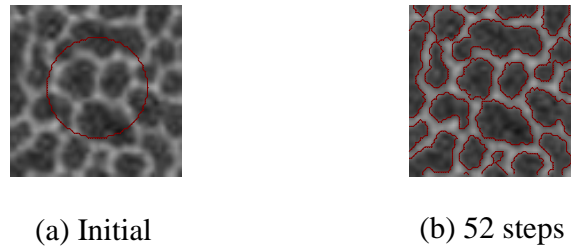
Figure 6-12 Interface identification of a microstructure by modified RKCM: (a) Initial trial interface; (b) Final detected interface

6.7 Direct Collocation Method for Solving Ordinary Differential Level Set Equation

As illustrated in previous sections, when the image has background noise, the parameter μ in the regularization term needs to be large in order to detect a smooth interface and boundary, especially for those images obtained from CT scan and MRI. Nevertheless, when dealing with microstructures composed of two phases, the solid skeleton and pores, the microstructural images available for numerical investigation may be presented in two colors. In this case, the influence of the interface regularity becomes less important and the parameter associated with the regularization term can be small as well. When the regularization is set to be zero, the level set equation degenerates to an ordinary differential equation (ODE), and can be solved with a larger time step. In this section, we introduce the direct collocation method to further solve the level set equation computationally more efficiently, in which the level set function is approximated at each collocation point. In this way, the transformation matrix composed of the shape functions is no longer needed in the strong form collocation method, and the calculation of

123

the inverse of the transformation matrix in each time step can be avoided, which makes the incremental level set algorithm simpler and more efficient.

6.7.1 Direct Collocation Method

In the case when the parameter μ is set to be zero, the level set equation degenerates to an ODE:

$$\frac{\partial \phi}{\partial t} = \delta(\phi)\left[-v - \lambda_1\left(C(\mathbf{x}) - \overline{c}_1\right)^2 + \lambda_2\left(C(\mathbf{x}) - \overline{c}_2\right)^2\right] \quad \text{in } \Omega$$
$$\phi(\mathbf{x},0) = \phi_0(\mathbf{x}) \quad \text{in } \Omega$$

(6.37)

which can be written in the general strong form as follows:

$$\frac{\partial \phi}{\partial t} = f(\phi) \quad \text{in } \Omega$$
$$\phi(\mathbf{x},0) = \phi_0(\mathbf{x}) \quad \text{in } \Omega$$

(6.38)

where f is a function of the level set function ϕ in the domain Ω, and ϕ_0 is the initial condition.

Introducing the direct collocation method to the general level set equations in (6.38), and evaluating the differential equation and initial condition at collocation points $\mathbf{x}_J \in \Omega$ with $J = 1, 2, \ldots, N_c$, yield the semi-discrete collocation equations:

$$\dot{\mathbf{a}}(t) = \mathbf{L}$$
$$\mathbf{a}(0) = \boldsymbol{\varphi}_0$$

(6.39)

where

$$\mathbf{L} = \left[f\left(\phi^h\left(\mathbf{x}_1\right)\right), f\left(\phi^h\left(\mathbf{x}_2\right)\right), \ldots\ldots, f\left(\phi^h\left(\mathbf{x}_{N_c}\right)\right) \right]^{\mathrm{T}}$$

$$\boldsymbol{\varphi}_0 = \left[\phi_0\left(\mathbf{x}_1\right), \phi_0\left(\mathbf{x}_2\right), \ldots\ldots, \phi_0\left(\mathbf{x}_{N_c}\right) \right]^{\mathrm{T}}$$

(6.40)

Denote the level set function evaluated at collocation point $\mathbf{x}_J$ by $\phi_J^h = a_J(t)$, the explicit expression of the component L_J in the matrix $\mathbf{L}$ is

$$L_J = \delta_\varepsilon\left(\phi_J^h\right)\left[-\nu - \lambda_1\left(C\left(\mathbf{x}_J\right) - \overline{c}_1\right)^2 + \lambda_2\left(C\left(\mathbf{x}_J\right) - \overline{c}_2\right)^2 \right]$$

(6.41)

and

$$\overline{c}_1 = \frac{\displaystyle\sum_{J=1}^{N_c} C\left(\mathbf{x}_J\right) H_\varepsilon\left(\phi_J^h\right) dA_J}{\displaystyle\sum_{J=1}^{N_c} H_\varepsilon\left(\phi_J^h\right) dA_J}$$

$$\overline{c}_2 = \frac{\displaystyle\sum_{J=1}^{N_c} C\left(\mathbf{x}_J\right)\left(1 - H_\varepsilon\left(\phi_J^h\right)\right) dA_J}{\displaystyle\sum_{J=1}^{N_c}\left(1 - H_\varepsilon\left(\phi_J^h\right)\right) dA_J}$$

(6.42)

where the weight of integration dA_J is the area of a Voronoi cell with respect to the collocation point $\mathbf{x}_J$, which is set to be unity in the collocation method herein.

Introducing the forward Euler's method to the semi-discrete collocation system in (6.39) leads to

$$\mathbf{a}^{n+1} - \mathbf{a}^n = \Delta t \mathbf{L}^n$$

$$\mathbf{a}^0 = \boldsymbol{\varphi}_0$$

(6.43)

in which the superscript n and Δt are the time step number and its size, respectively. As a consequence, the incremental algorithm for calculating the unknown $\mathbf{a}^{n+1}$ at $t = n+1$ with initial condition is given by

$$
\begin{aligned}
\mathbf{a}^{n+1} &= \mathbf{a}^n + \Delta t \mathbf{L}^n \\
\mathbf{a}^0 &= \boldsymbol{\varphi}_0
\end{aligned}
\tag{6.44}
$$

where the proposed incremental formula in (6.44) is neat and efficient. Moreover, unlike the one in (6.31) and (6.32), there is no need to calculate the transformation matrix and its inverse at each time step. The detailed incremental algorithm was given in Section 6.4.

6.7.2 Numerical Examples

6.7.2.1 Boundary Identification of an Object on a Lagrangian Grid
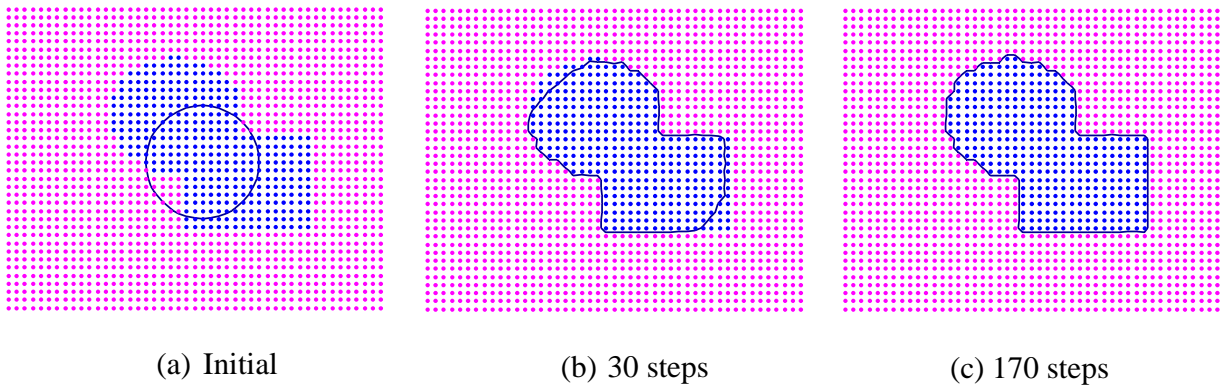

(a) Initial   (b) 30 steps   (c) 170 steps

Figure 6-13 Boundary identification of an object by direct collocation method; (a) Initial trial interface; (b) and (c) are the evolving interface at 30 steps and 170 steps, respectively

126

Consider the image with 47×38 pixels shown in Figure 6-13 (a). To solve the ordinary differential level set equation in (6.37), the parameters are chosen as $v = 0$, $\lambda_1 = \lambda_2 = 1$, $dt = 0.001$, $\varepsilon = 0.5$, and the residual is set to be 5×10^{-5}. The boundary evolution of the object is shown in Figure 6-13 (b)-(c), where the object is detected with 170 steps and the residual is 4.9875e-005. Although more time steps are needed for desired accuracy in this approach compared to that based on RKCM, the fact that no solution of a linear system is needed results in a significant time saving.

6.7.2.2 Two-Phase Segmentation

| (a) Initial | (b) 2 steps | (c) 70 steps |
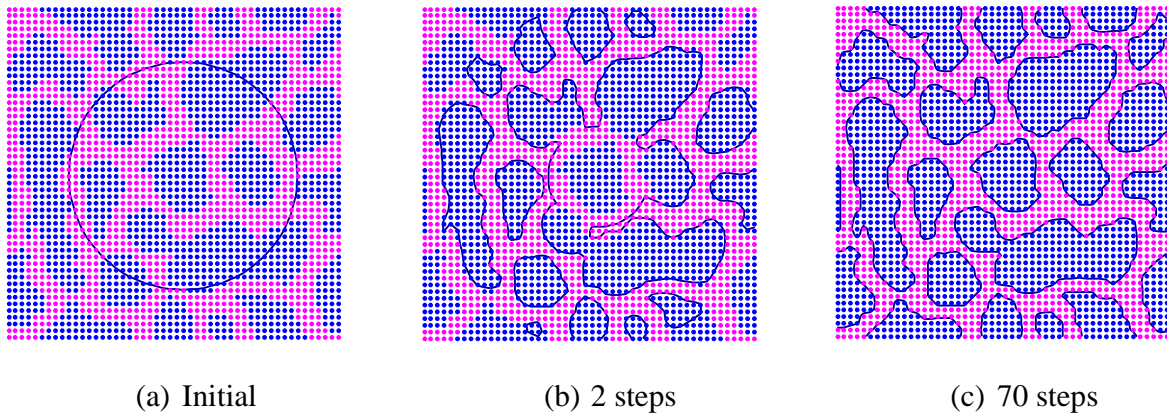
Figure 6-14 Interface identification of a microstructure by direct collocation method; (a) Initial trial interface; (b) and (c) are the evolving interface at 2 steps and 70 steps, respectively

The microstructure shown in Figure 6-14 (a) is discretized by 50×50 pixels. The following parameters are adopted to solve the ordinary differential level set equation: $v = 0$, $\lambda_1 = \lambda_2 = 1$, $dt = 0.1$, $\varepsilon = 0.5$, and the residual is set as 10^{-4}. The evolution of the interface is shown in

Figure 6-14 (b) and (c), and the detected interface is obtained at 70 steps when the residual reaches 9.9688e-005.

6.8 Summary

Based on the variational formulation of the level set functional, the active contour model has been applied to the processing of images, in particular, the boundary identification and image segmentation of images with background noise and complex geometry. Inspired by the image data presented by the pixels, we introduce the strong form collocation method to directly deal with images obtained from CT scan or MRI, which are discretized uniformly on grid points.

With the RKCM, an investigation of the RK parameters in solving the level set equation has been carried out to give some insights into the choice of parameters with respect to different orders of bases and kernel functions. On the other hand, when using the strong form collocation method to solve the level set equation, the regularization term with parameter $\mu \neq 0$ makes the numerical algorithm cumbersome and less efficient. In this regard, we introduced the proposed G-RKCM described in Chapter 5 to avoid taking the second derivatives of the approximation function. The proposed G-RKCM has been demonstrated to be an efficient means for solving the level set equation with the regularization terms in the collocation method. Since the influence of regularization term is less than the constraints for interface marching, the consistency condition in the RK shape function can be further released to enhance the computational efficiency. A modified RKCM for active contour model is investigated. For image with two color data, we proposed a direct collocation method to solve the degenerated level set equation (when the

parameter $\mu = 0$), which is an ODE with no regularization terms. In this method, the transformation matrix and the inverse of the matrix at each time step is no longer needed, which make the incremental algorithm much more efficient than the conventional strong form collocation method.

Chapter 7 Image-Based Strong Form Collocation Method for Multiscale Modeling of Porous Bone Materials

7.1 Introduction

Trabecular bone is a hierarchical structure with complicated morphology and heterogeneity, and it has been widely studied in the area of orthopedics and dentistry in the past decades. Due to its porous composition, the investigation of trabecular microstructures by considering the variation of solid skeleton and pores provides opportunities to accurately predict the macroscopic behavior of trabecular bones, since the bone microstructures and the associated macroscopic mechanical properties alter in different sampling sites, ages, and density. Specifically, the macroscopic material properties of trabecular bones have been recognized as orthotropy or transverse isotropy with the largest elastic stiffness and strength occurring in the principal directions.

Some idealized models with simplified geometry have been applied to simulating microstructural responses (Williams and Lewis, 1982; Gibson, 1985; Hollister et al., 1991). However, the predicted stiffness of trabecular bones was reported to overestimate the experimental data (Hollister et al., 1991; Hollister et al., 1994). Since it has been generally accepted that the microstructural organization affects the strength and stiffness of trabecular bones, a realistic

microstructural model considering the biphasic variation should provide a rational way to investigate the mechanics of trabecular bones.

As high resolution digital imaging techniques emerge, such as the advancement of micro-scale tomography (micro-CT) and micro-magnetic resonance imaging (micro-MRI), the investigation of trabecular bone mechanical properties can be estimated more precisely. In the unit cell modeling of bone materials, major challenges related to numerical defects introduced by using the finite element method (FEM) exist. To model the microstructural topology by converting the image pixels into elements, the jagged interface and sharp corner due to the piecewise approximation in the C^0 FEM may lead to artificial localized responses such as stress concentration and solution oscillation on the boundary (Hollister and Riemer, 1993; Hollister and Kikuchi, 1994). When the finite element model is constructed from the input geometry of images, mesh reconstruction is always needed to avoid highly distorted elements and to achieve desired mesh topology (Hoppe et al., 1993; Ulrich et al., 1998; Podshivalov et al., 2009; Podshivalov et al., 2011). Another issue arises from the model reconstruction process based on high-resolution medical images is the background noise and blurred objects, where the numerical analysis may lead to incorrect predictions and diagnoses if the reconstructed models lack representative information to convert the pixel density from images to the material points (Kuhn et al., 1990; Hollister and Riemer, 1993; Hollister and Kikuchi, 1994; Charras and Guldberg, 2000; Hara et al., 2002; Podshivalov et al., 2011). Consequently, the aforementioned drawbacks including mesh reconstruction, smoothing solutions, and thresholding techniques make the finite element simulation complicated and time-consuming owning to the complex microstructural geometry encountered.

To investigate the influence of microstructural topology and material properties on the effective material parameters and the load transmission in bone at tissue level, the reliability of the homogenized material parameters in the multiscale bone modeling remain challenging. Many factors such as sampling position of unit cells, sampling size of unit cells, and resolution of microstructural images contribute to the accuracy of the homogenized macroscopic material behavior and associated structural response predictions.

In the proposed image-based strong form collocation numerical method presented in Chapter 5 in conjunction with the mathematical homogenization framework discussed in Chapter 4, one critical feature for an effective numerical prediction is the ability to effectively identify microstructural material interface and segment phases based on images with jagged edges and blurry boundaries, in which the level set method in Chapter 6 has been introduced. This framework allows effective microstructural modeling directly based on images without thresholding techniques for phase segmentation. In addition, the strong form collocation method enables us to solve problems with complex geometry based on point discretization without complexities resulting from mesh reconstruction and smoothing solutions. The proposed numerical framework will be employed to simulate the trabecular bone microstructures and calculate the associated macroscopic mechanical properties aiming to a seamless integration of imaging technology and patient specific computer aided diagnosis for osteoporosis applications.

The arrangement of this chapter is as follows: Section 7.2 describes the image based modeling of solving unit cell problems by the strong form collocation method. The numerical issues for G-RKCM image based modeling are discussed in Section 7.3. The investigation of unit cell size and image resolution on mechanical properties and the validation of the proposed method are

given in Section 7.4. The summary of the proposed image based computational framework for modeling porous bone materials is provided in Section 7.5.

7.2 Multiscale Poroelasticity Modeling

7.2.1 Unit Cell Problems in Strong Form

Based on the framework of multiscale homogenization with the two-scale asymptotic expansion introduced in Chapter 4, we have formulated the unit cell problems for poroelastic materials composed of an elastic solid and Newtonian fluid of low viscosity, in which the microstructural response is embedded in the characteristic functions. To solve the unit cell problems directly by the image-based strong form collocation method, the corresponding unit cell problems are revisited in strong form herein. The strong form of the unit cell problem for the Y-periodic characteristic function χ in the solid domain is

$$\left(C_{ijmn} \frac{\partial \chi_m^{kl}}{\partial y_n} \right)_{,j} = 0 \quad \text{in } Y_S \tag{7.1}$$

$$\left(C_{ijmn} \frac{\partial \chi_m^{kl}}{\partial y_n} - C_{ijkl} \right) n_j^S = 0 \quad \text{on } \partial Y_{\mathrm{S}} \tag{7.2}$$

where C_{ijkl} is the elastic tensor of the solid skeleton and n_j^S is the unit normal on the inner boundary of the cell. The strong form of the unit cell problem for the Y-periodic characteristic function η in the solid domain is

$$\left(C_{ijkl} \frac{\partial \eta_k}{\partial y_l} \right)_{,j} = 0 \quad \text{in } Y_S \tag{7.3}$$

$$\left(C_{ijkl} \frac{\partial \eta_k}{\partial y_l} - \delta_{ij} \right) n_j^S = 0 \quad \text{on } \partial Y_S \tag{7.4}$$

The strong form of the unit cell problem for the Y-periodic and divergence free $\boldsymbol{\kappa}$ in the fluid domain is

$$2\mu_v \frac{\partial^2 \kappa_{ij}}{\partial y_k \partial y_k} + \delta_{ij} = 0 \quad \text{in } Y_F \tag{7.5}$$

$$\kappa_{ij} = 0 \quad \text{on } \partial Y_F \tag{7.6}$$

where μ_v is the fluid viscosity. The inner boundary conditions of unit cells on ∂Y_S and ∂Y_F are stated in (7.2), (7.4) and (7.6), respectively, while the periodic boundary conditions are imposed on the outer boundaries of unit cells.

After obtaining the characteristic functions, the following homogenized material parameters can be determined to represent the material properties of the overall macrostructure, which are

$$\bar{C}_{ijkl} = \frac{1}{|Y|} \int_{Y_S} \left(C_{ijkl} - C_{ijmn} \frac{\partial \chi_m^{kl}(\mathbf{y})}{\partial y_n} \right) dY \tag{7.7}$$

$$\bar{\alpha}_{ij} = \frac{1}{|Y|} \int_{Y_S} C_{ijkl} \frac{\partial \eta_k(\mathbf{y})}{\partial y_l} dY \tag{7.8}$$

$$\bar{K}_{ij} = \frac{1}{|Y|} \int_{Y_F} \kappa_{ij}(\mathbf{y}) dY \tag{7.9}$$

in which $\overline{C}_{ijkl}$ is the homogenized elasticity tensor, $\overline{\alpha}_{ij}$ is the homogenized effective stress tensor, and $\overline{K}_{ij}$ is the homogenized permeability tensor, respectively. In addition, the upper and lower bounds for $\overline{\alpha}_{ii}$ are $0 \leq \overline{\alpha}_{ii} \leq 2(1-\phi)$, which are presented in Appendix C by modifying the work of Lydzba and Shao (2000).

7.2.2 G-RKCM for Solving Unit Cell Problems

Recall the general weighted strong form collocation equations of boundary value problems introduced in Chapter 5:

$$\mathbf{Aa} = \begin{bmatrix} \mathbf{A}^1 + \mathbf{A}^2 \\ \sqrt{\alpha_h} \left(\mathbf{A}^3 + \mathbf{A}^4 \right) \\ \sqrt{\alpha_g} \mathbf{A}^5 \end{bmatrix} \mathbf{a} = \begin{bmatrix} \mathbf{b}^1 \\ \sqrt{\alpha_h} \mathbf{b}^2 \\ \sqrt{\alpha_g} \mathbf{b}^3 \end{bmatrix} = \mathbf{b} \tag{7.10}$$

where $\mathbf{A}$ constitutes matrices associated with the differential operators and $\mathbf{b}$ constitutes vectors related to the source terms, respectively, and $\sqrt{\alpha_h}$ is the weight on $\partial\Omega^h$ and $\sqrt{\alpha_g}$ is the weight on $\partial\Omega^g$.

For the χ-unit cell problem given in (7.1)-(7.2), the gradient RK approximation χ in two-dimension are introduced as

$$\chi = \sum_{I=1}^{N_s} \Psi_I \mathbf{a}_I \tag{7.11}$$

$$\chi_{,x} = \sum_{I=1}^{N_s} \Psi_I^x \mathbf{a}_I$$

$$\chi_{,y} = \sum_{I=1}^{N_s} \Psi_I^y \mathbf{a}_I$$

(7.12)

where

$$\Psi_I = \begin{bmatrix} \Psi_I \mathbf{I} & \mathbf{0} \\ \mathbf{0} & \Psi_I \mathbf{I} \end{bmatrix}, \quad \mathbf{a}_I = \begin{bmatrix} a_{1I} \\ a_{2I} \end{bmatrix}, \quad a_{1I} = \begin{bmatrix} a_{111I} \\ a_{122I} \\ a_{112I} \end{bmatrix}, \quad a_{2I} = \begin{bmatrix} a_{211I} \\ a_{222I} \\ a_{212I} \end{bmatrix}$$

(7.13)

in which Ψ_I and $\mathbf{a}_I$ are the matrix and vector composed of the RK shape functions and the generalized coefficients, respectively.

The corresponding matrices in $\mathbf{A}$ and $\mathbf{b}$ for solving the χ-unit cell problem are given as

$$\mathbf{A}_{IJ}^1 = \mathbf{L}^1 \Psi_J^{x^{\mathrm{T}}}(\mathbf{p}_I) = \begin{bmatrix} a_1 & 0 & 0 & a_3 & 0 & 0 \\ 0 & a_1 & 0 & 0 & a_3 & 0 \\ 0 & 0 & a_1 & 0 & 0 & a_3 \\ a_4 & 0 & 0 & a_2 & 0 & 0 \\ 0 & a_4 & 0 & 0 & a_2 & 0 \\ 0 & 0 & a_4 & 0 & 0 & a_2 \end{bmatrix},$$

$$\mathbf{A}_{IJ}^2 = \mathbf{L}^2 \Psi_J^{y^{\mathrm{T}}}(\mathbf{p}_I) = \begin{bmatrix} a_5 & 0 & 0 & a_7 & 0 & 0 \\ 0 & a_5 & 0 & 0 & a_7 & 0 \\ 0 & 0 & a_5 & 0 & 0 & a_7 \\ a_8 & 0 & 0 & a_6 & 0 & 0 \\ 0 & a_8 & 0 & 0 & a_6 & 0 \\ 0 & 0 & a_8 & 0 & 0 & a_6 \end{bmatrix}$$

(7.14)

$$a_1 = (\lambda + 2\mu)\Psi^x_{J,x}(\mathbf{p}_J), \quad a_5 = \mu\Psi^y_{J,y}(\mathbf{p}_J),$$
$$a_2 = \mu\Psi^x_{J,x}(\mathbf{p}_J), \quad a_6 = (\lambda + 2\mu)\Psi^y_{J,y}(\mathbf{p}_J),$$
$$a_3 = \mu\Psi^x_{J,y}(\mathbf{p}_J), \quad a_7 = \lambda\Psi^y_{J,x}(\mathbf{p}_J),$$
$$a_4 = \lambda\Psi^x_{J,y}(\mathbf{p}_J), \quad a_8 = \mu\Psi^y_{J,x}(\mathbf{p}_J)$$

(7.15)

$$\mathbf{A}^3_{IJ} = \mathbf{B}^1_h \Psi^{x^{\mathrm{T}}}_J(\mathbf{q}_I) = \begin{bmatrix} a_9 & 0 & 0 & a_{11} & 0 & 0 \\ 0 & a_9 & 0 & 0 & a_{11} & 0 \\ 0 & 0 & a_9 & 0 & 0 & a_{11} \\ a_{12} & 0 & 0 & a_{10} & 0 & 0 \\ 0 & a_{12} & 0 & 0 & a_{10} & 0 \\ 0 & 0 & a_{12} & 0 & 0 & a_{10} \end{bmatrix}$$

(7.16)

$$\mathbf{A}^4_{IJ} = \mathbf{B}^2_h \Psi^{y^{\mathrm{T}}}_J(\mathbf{q}_I) = \begin{bmatrix} a_{13} & 0 & 0 & a_{15} & 0 & 0 \\ 0 & a_{13} & 0 & 0 & a_{15} & 0 \\ 0 & 0 & a_{13} & 0 & 0 & a_{15} \\ a_{16} & 0 & 0 & a_{14} & 0 & 0 \\ 0 & a_{16} & 0 & 0 & a_{14} & 0 \\ 0 & 0 & a_{16} & 0 & 0 & a_{14} \end{bmatrix}$$

$$a_9 = (\lambda + 2\mu)\Psi^x_J(\mathbf{q}_I)n^s_1, \quad a_{13} = \mu\Psi^y_J(\mathbf{q}_I)n^s_2,$$
$$a_{10} = \mu\Psi^x_J(\mathbf{q}_I)n^s_1, \quad a_{14} = (\lambda + 2\mu)\Psi^y_J(\mathbf{q}_I)n^s_2,$$
$$a_{11} = \mu\Psi^x_J(\mathbf{q}_I)n^s_2, \quad a_{15} = \lambda\Psi^y_J(\mathbf{q}_I)n^s_1,$$
$$a_{12} = \lambda\Psi^x_J(\mathbf{q}_I)n^s_2, \quad a_{16} = \mu\Psi^y_J(\mathbf{q}_I)n^s_1$$

(7.17)

and

$$\mathbf{b}^1 = \begin{bmatrix} 0 & 0 & 0 & 0 & 0 & 0 \end{bmatrix}^{\mathrm{T}},$$
$$\mathbf{b}^2 = \begin{bmatrix} (\lambda + 2\mu)n^s_1 & \lambda n^s_1 & \mu n^s_2 & \lambda n^s_2 & (\lambda + 2\mu)n^s_2 & \mu n^s_1 \end{bmatrix}^{\mathrm{T}}$$

(7.18)

Here we use the property $\chi_{kmn} = \chi_{knm}$, and λ and μ are Lame' constants.

For the $\boldsymbol{\eta}$-unit cell problem in two-dimension, consider

$$\boldsymbol{\eta} = \sum_{I=1}^{N_s} \boldsymbol{\Psi}_I \mathbf{a}_I \tag{7.19}$$

$$\boldsymbol{\eta}_{,x} = \sum_{I=1}^{N_s} \boldsymbol{\Psi}_I^x \mathbf{a}_I$$

$$\boldsymbol{\eta}_{,y} = \sum_{I=1}^{N_s} \boldsymbol{\Psi}_I^y \mathbf{a}_I \tag{7.20}$$

The corresponding matrices in $\mathbf{A}$ and $\mathbf{b}$ for solving the $\boldsymbol{\eta}$-unit cell problem are given as follows:

$$\mathbf{A}_{IJ}^1 = \mathbf{L}^1 \boldsymbol{\Psi}_J^{x^{\mathrm{T}}}(\mathbf{p}_I) = \begin{bmatrix} (\lambda+2\mu)\Psi_{J,x}^x(\mathbf{p}_I) & \mu\Psi_{J,y}^x(\mathbf{p}_I) \\ \lambda\Psi_{J,y}^x(\mathbf{p}_I) & \mu\Psi_{J,x}^x(\mathbf{p}_I) \end{bmatrix},$$

$$\mathbf{A}_{IJ}^2 = \mathbf{L}^2 \boldsymbol{\Psi}_J^{y^{\mathrm{T}}}(\mathbf{p}_I) = \begin{bmatrix} \mu\Psi_{J,y}^y(\mathbf{p}_I) & \lambda\Psi_{J,x}^y(\mathbf{p}_I) \\ \mu\Psi_{J,x}^y(\mathbf{p}_I) & (\lambda+2\mu)\Psi_{J,y}^y(\mathbf{p}_I) \end{bmatrix},$$

$$\mathbf{A}_{IJ}^3 = \mathbf{B}_h^1 \boldsymbol{\Psi}_J^{x^{\mathrm{T}}}(\mathbf{q}_I) = \begin{bmatrix} (\lambda+2\mu)\Psi_J^x(\mathbf{q}_I)n_1^s & \mu\Psi_J^x(\mathbf{q}_I)n_2^s \\ \lambda\Psi_J^x(\mathbf{q}_I)n_2^s & \mu\Psi_J^x(\mathbf{q}_I)n_1^s \end{bmatrix}, \tag{7.21}$$

$$\mathbf{A}_{IJ}^4 = \mathbf{B}_h^2 \boldsymbol{\Psi}_J^{y^{\mathrm{T}}}(\mathbf{q}_I) = \begin{bmatrix} \mu\Psi_J^y(\mathbf{q}_I)n_2^s & \lambda\Psi_J^y(\mathbf{q}_I)n_1^s \\ \mu\Psi_J^y(\mathbf{q}_I)n_1^s & (\lambda+2\mu)\Psi_J^y(\mathbf{q}_I)n_2^s \end{bmatrix}$$

$$\mathbf{b}^1 = \begin{bmatrix} 0 & 0 \end{bmatrix}^{\mathrm{T}}, \quad \mathbf{b}^2 = \begin{bmatrix} n_1^s & n_2^s \end{bmatrix}^{\mathrm{T}} \tag{7.22}$$

In a similar way, for the $\boldsymbol{\kappa}$-unit cell problem, we introduce the following approximation:

$$\boldsymbol{\kappa} = \sum_{I=1}^{N_s} \boldsymbol{\Psi}_I \mathbf{a}_I \tag{7.23}$$

$$\boldsymbol{\kappa}_{,x} = \sum_{I=1}^{N_s} \boldsymbol{\Psi}_I^x \mathbf{a}_I$$

$$\boldsymbol{\kappa}_{,y} = \sum_{I=1}^{N_s} \boldsymbol{\Psi}_I^y \mathbf{a}_I \tag{7.24}$$

The associated matrices in $\mathbf{A}$ and $\mathbf{b}$ are given by

$$\mathbf{A}_{IJ}^1 = \mathbf{L}^1 \boldsymbol{\Psi}_J^{x^{\mathrm{T}}}(\mathbf{p}_I) = 2\mu_v \begin{bmatrix} \Psi_{J,x}^x(\mathbf{p}_I) & 0 & 0 \\ 0 & \Psi_{J,x}^x(\mathbf{p}_I) & 0 \\ 0 & 0 & \Psi_{J,x}^x(\mathbf{p}_I) \end{bmatrix},$$

$$\mathbf{A}_{IJ}^2 = \mathbf{L}^2 \boldsymbol{\Psi}_J^{y^{\mathrm{T}}}(\mathbf{p}_I) = 2\mu_v \begin{bmatrix} \Psi_{J,y}^y(\mathbf{p}_I) & 0 & 0 \\ 0 & \Psi_{J,y}^y(\mathbf{p}_I) & 0 \\ 0 & 0 & \Psi_{J,y}^y(\mathbf{p}_I) \end{bmatrix}, \quad (7.25)$$

$$\mathbf{A}_{IJ}^3 = \mathbf{B}_g \boldsymbol{\Psi}_J^{\mathrm{T}}(\mathbf{q}_I) = \begin{bmatrix} \Psi_J(\mathbf{q}_I) & 0 & 0 \\ 0 & \Psi_J(\mathbf{q}_I) & 0 \\ 0 & 0 & \Psi_J(\mathbf{q}_I) \end{bmatrix},$$

$$\mathbf{b}^1 = \begin{bmatrix} -1 & 0 & -1 \end{bmatrix}^{\mathrm{T}}, \quad \mathbf{b}^3 = \begin{bmatrix} 0 & 0 & 0 \end{bmatrix}^{\mathrm{T}}$$

7.3 Image Based G-RKCM for Unit Cell Modeling

The accurate prediction of mechanical properties of materials with complex geometry relies largely on the numerical model's geometry representation ability. In microstructure modeling, how to locate and represent material interface configuration and construct discretization following the material heterogeneity is of critical importance in the image based modeling. In this section, we will investigate these numerical issues and verify the effectiveness of the proposed image based numerical methods for microstructure modeling.

7.3.1 Image Segmentation and Interface Points Generation

The proposed method constitutes three steps in the discretization of microstructures for solving unit cell problems using medical images: (1) the level set segmentation, (2) the interface points

generation, and (3) the interface reconstruction. To demonstrate the proposed image based discretization of microstructures for solving the unit cell problems, consider the microstructural image of trabecular bone shown in Figure 7-1 presented by 25×25 pixels. For the level set image segmentation, the parameters for the level set equation are chosen as follows: $\mu=\nu=0$, $\lambda_1=\lambda_2=10000$, $dt=0.1$, $\varepsilon=2a$, residual= 5×10^{-6}, and the gradient reproducing kernel collocation method (G-RKCM) is introduced for the discretization of level set equation ((6.17) in Chapter 6). The RK shape function is constructed by the quadratic bases with a quadratic kernel function using the support size $a=2.4$. With the level set segmentation technique, the interface is identified with residual 1.3494e-06 at the 15-th step, and the results are depicted in Figure 7-2 (a). Next, the interface points are constructed using the level set function values at the pixels. To proceed, we introduce linear interpolation of level set functions in both x and y directions in the neighboring points where the level set function changes sign. In other words, if two neighboring points contain opposite signs of level set function values, the interpolation is performed to locate the interface point with zero level set value. An example of x-direction interpolation of interface point is shown in Figure 7-3. The interface points obtained by the linear interpolation are shown in Figure 7-2 (b).
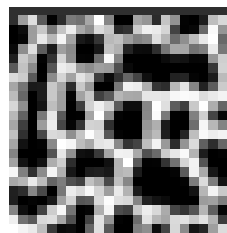

Figure 7-1 Microstructural image of trabecular bone presented by 25×25 pixels
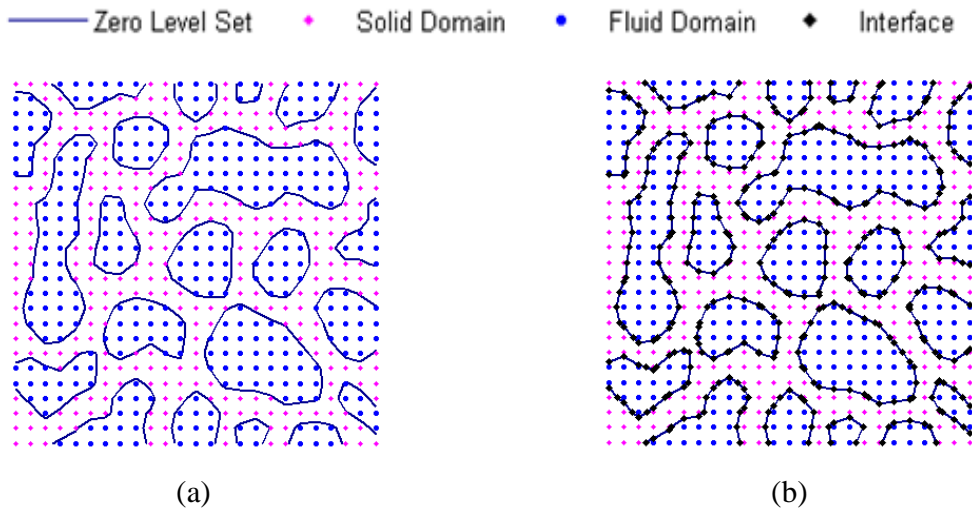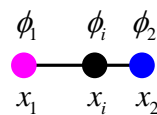
Figure 7-2 (a) Level set method for interface identification; and (b) Interface approximation at additional collocation points

$$x_i = x_1 + (x_2 - x_1)\frac{-\phi_1}{\phi_2 - \phi_1}$$

Figure 7-3 Illustration of linear interpolation in interface approximation

7.3.2 Interface Reconstruction

As shown in Figure 7-4, the domain points (blue points) and the interface points (black points) have been identified in Section 7.3.1. Based on the shortest distance between two adjacent interface points, the interface points can be connected in sequence to form a closed loop. To avoid identification of two adjacent points with the shortest distance while not belonging to the interface, we further identify the sign of inner product of the surface normals of the candidate interface points having shortest distance. In other words, when the inner product of surface

normals of the two interface points identified with shortest distance is less than zero, these two points are treated as interface points on different interfaces and will not be connected in the interface construction. As shown in Figure 7-4 (a) and (b) presented by 20×20 pixels and 25×25 pixels, respectively, it is expected that the results of interface reconstruction is resolution dependent as shown in Figure 7-5 and Figure 7-6, where the implicit representation is zero level set and the explicit representation is reconstructed interface. For the same microstructures with higher resolution such as 45×45 pixels shown in Figure 7-7 (a), the explicit representation of interface points agrees with the implicit representation in Figure 7-7 (b).

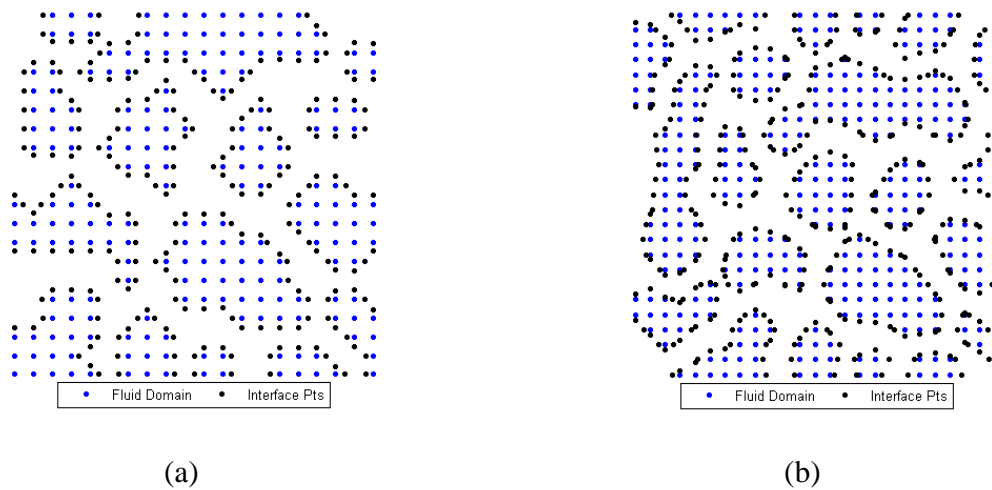(a)   (b)

Figure 7-4 Domain and interface points for unit cells presented by (a) 20×20 pixels; and (b) 25×25 pixels
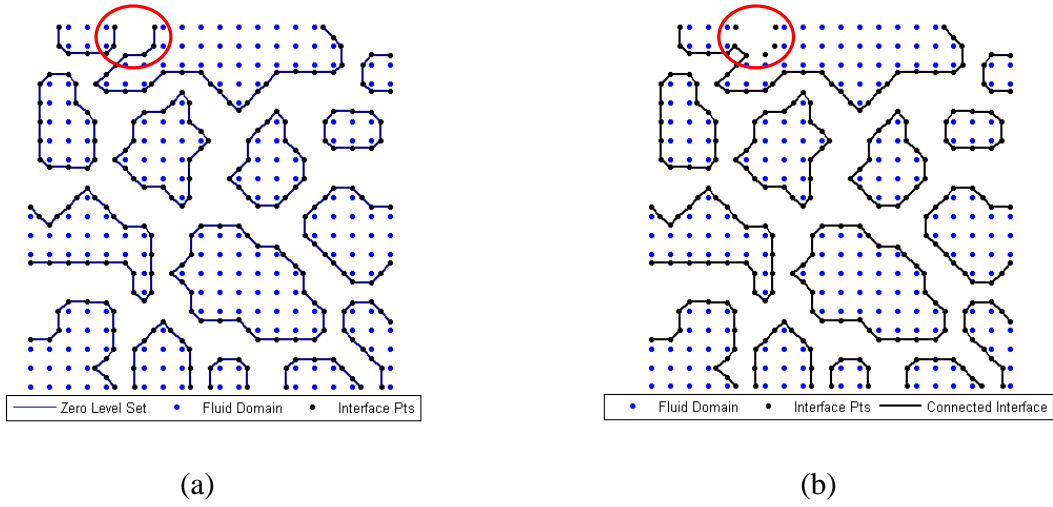
Figure 7-5 Microstructure with 20×20 pixels: (a) implicit representation; and (b) explicit representation
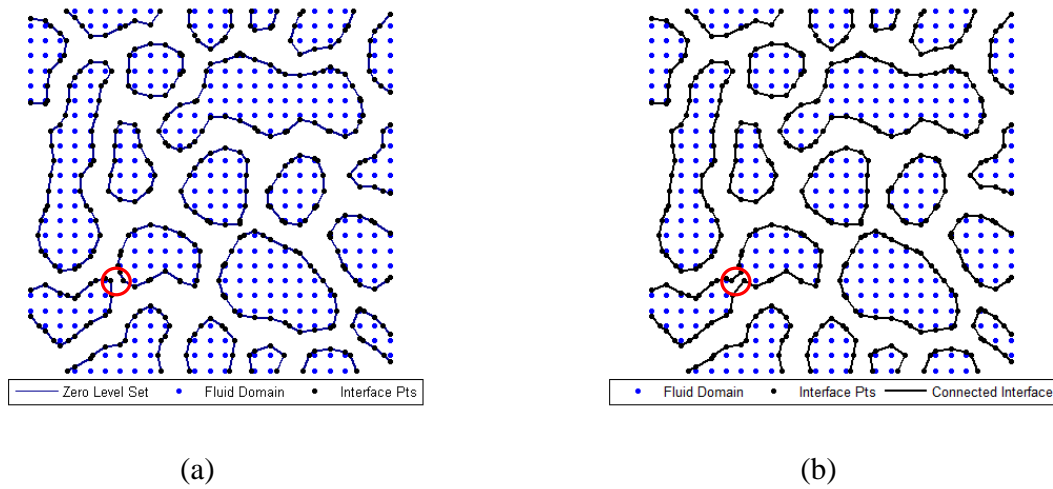

Figure 7-6 Microstructure with 25×25 pixels: (a) implicit representation; and (b) explicit representation
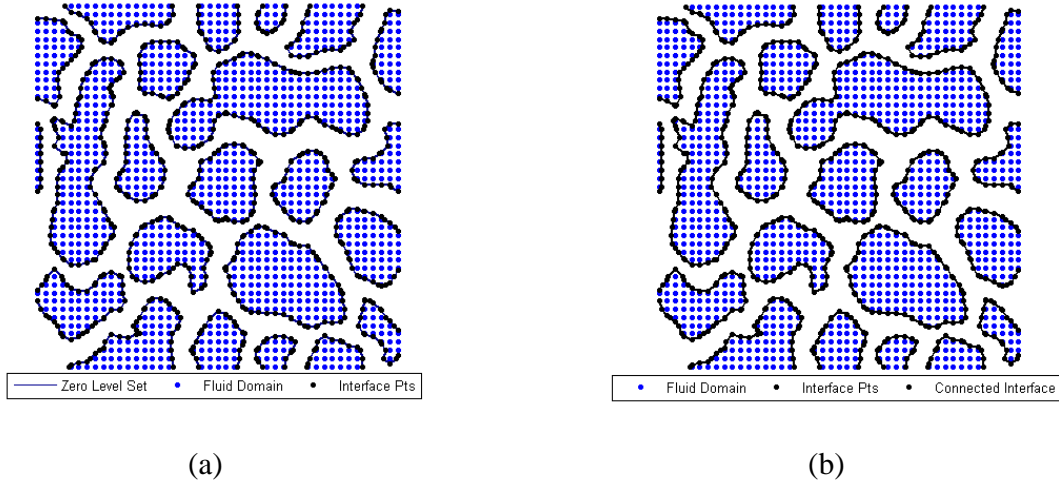
$$\text{(a)} \qquad\qquad\qquad\qquad\qquad\qquad \text{(b)}$$

Figure 7-7 Microstructure with 45×45 pixels: (a) implicit representation; and (b) explicit representation

The proposed algorithm for interface discretization and reconstruction is summarized as follows:

Algorithm 7.1

Given a set of N_{int} interface points $\mathbf{S} = \left\{\mathbf{x}_1, \mathbf{x}_2, ..., \mathbf{x}_{N_{\mathrm{int}}}\right\} \subseteq \mathbf{\Omega} \cup \partial\mathbf{\Omega}$ on the pixel based uniform xy grid with the corresponding set of unit normals $\mathbf{N} = \left\{\mathbf{n}_1, \mathbf{n}_2, ..., \mathbf{n}_{N_{\mathrm{int}}}\right\}$ in the domain $\mathbf{\Omega}$. Note that image pixels are uniformly distributed with constant nodal distances Δx and Δy in the x- and y- directions, respectively.

(1) Arbitrarily select the first point NGP=1 in the first interface point group NG=1. Set the initial shortest distance as $d_{\mathrm{short}} = \sqrt{2}\Delta x \Delta y$.

(2) For each point $\mathbf{x}_I$, find the interface candidate points $\mathbf{x}_{\mathrm{adj}}$ from $\mathbf{S}$ that are located inside the square with dimension $2\Delta x \times 2\Delta y$ and centered at $\mathbf{x}_I$ and is closest to $\mathbf{x}_I$.

144

(3) If $d_{\mathbf{x}_I, \mathbf{x}_{adj}} < d_{short}$, set $d_{short} = d_{\mathbf{x}_I, \mathbf{x}_{adj}}$ until the closest point $\mathbf{x}_{close} = \mathbf{x}_{adj}$ is found.

(4) If $\mathbf{n}_I \cdot \mathbf{n}_{close} < 0$, omit $\mathbf{x}_{close}$ and find the next closest interface point until $\mathbf{n}_I \cdot \mathbf{n}_{close} \geq 0$ and

$\mathbf{x}'_{close} = \mathbf{x}_{adj}$. Update NGP=NGP+1.

(5) If $\mathbf{x}_{adj} = \mathbf{x}_1$ or $\mathbf{x}_{adj} \in \partial\mathbf{\Omega}$, one connected interface is completed. Update NG=NG+1.

(6) Repeat (1) to (5) until all points in $\mathbf{S}$ are identified.

7.3.3 Interior Points Identification
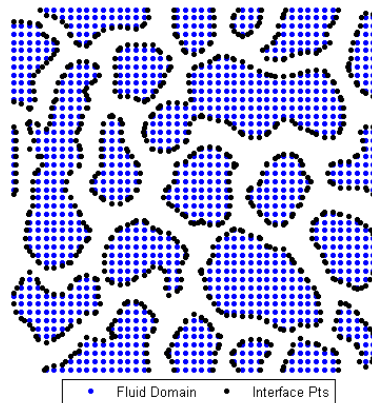
Figure 7-8 Illustration of partitioning points inside the interface

After explicitly connecting the interface points, identification of the points inside these loops leads to an inside-outside problem. For illustration purposes, here we show identification of the fluid points inside each interface loop as illustrated in Figure 7-8, in which the blue points denote the points needed to be partitioned while the black points denote the connected interface/boundary points obtained in Section 7.3.2. To find the uniformly distributed grid points

enclosed by the boundary, we begin with the two boundary points $\mathbf{x}_I$ in one interface group with the same minimum y coordinate while having the maximum distance in x coordinates. The inside points are found if they have the same y coordinate while having x coordinates in-between the two boundary points $\mathbf{x}_I$. The corresponding algorithm for interior points partitioning is given as follows:

Algorithm 7.2

Given a set of uniformly distributed N_d domain (grid) points $\mathbf{S}^d = \left\{ \mathbf{x}_1^d, \mathbf{x}_2^d, \ldots\ldots, \mathbf{x}_{N_d}^d \right\} \subseteq \mathbf{\Omega} \cup \partial\mathbf{\Omega}$ and a set of NG connected interface groups $\mathbf{S}^{\text{int}} = \left\{ \mathbf{s}_1^{\text{int}}, \mathbf{s}_2^{\text{int}}, \ldots\ldots, \mathbf{s}_{NG}^{\text{int}} \right\} \subseteq \mathbf{\Omega} \cup \partial\mathbf{\Omega}$, with each interface group $\mathbf{s}_I^{\text{int}}$ containing NGP points in I-th group $\mathbf{s}_I^{\text{int}} = \left\{ \mathbf{x}_{I1}^{\text{int}}, \mathbf{x}_{I2}^{\text{int}}, \ldots\ldots, \mathbf{x}_{INGP}^{\text{int}} \right\}$ in $\mathbf{\Omega}$.

(1) For a given interface group $NG = I$, find all interface points with the same y-coordinate and order their corresponding x-coordinates as $x_{I1}^{\text{int}} < x_{I2}^{\text{int}} < \ldots x_{I(2n-1)}^{\text{int}} < x_{I(2n)}^{\text{int}}$. Note that there are even number of interface points in each interface group that have the same y-coordinate. Group the pairs of the interface points $\left\{ \mathbf{x}_{I(2i-1)}^{\text{int}}, \mathbf{x}_{I(2i)}^{\text{int}} \right\}$, where $1 \le i \le n$.

(2) For each pair of interface points $\left\{ \mathbf{x}_{I(2i-1)}^{\text{int}}, \mathbf{x}_{I(2i)}^{\text{int}} \right\}$, find all domain point $\mathbf{x}_J^d$ such that $y_{I(2i-1)}^{\text{int}} = y_J^d = y_{I(2i)}^{\text{int}}$ and $x_{I(2i-1)}^{\text{int}} < x_J^d < x_{I(2i)}^{\text{int}}$, and assign these domain points $\mathbf{x}_J^d$ as the member of interior points associated with the interface group I.

(3) Repeat (1)-(2) for all interface pairs in $\mathbf{s}_I^s$. Advance to next group NG=NG+1.

(4) Remove identified interior points from the domain points. Repeat (1)-(3) for all interface groups in $\mathbf{S}^{\text{int}}$.

7.3.4 Verification Example

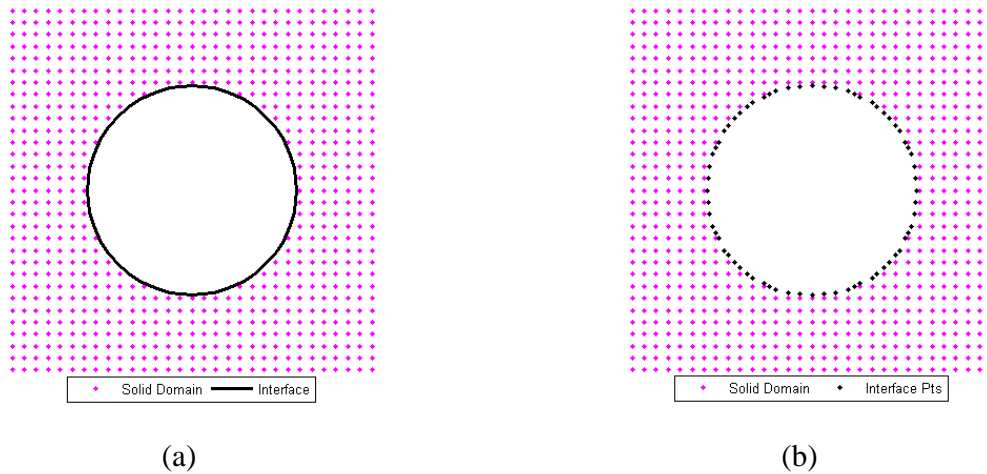(a)   (b)

Figure 7-9 Unit cell geometry for porosity $\phi = 0.25$: (a) Unit cell with interface; and (b) Unit cell with approximated interface points

For a porous elastic material described by an elastic body composed of periodically distributed voids, the analytical derivation of effective moduli was given by Nemat-Nasser et al. (1982) as the extension of Eshelby inclusion problems (1957). In this example, a unit cell with a circular void inclusion of varying porosity ϕ from 0.15 to 0.25 in plane strain condition is considered, where the material constants for the solid matrix are $E = 1000$ and $\nu = 0.3$. It is noted that the analytical estimates of effective moduli are derived for porosity up to $\phi = 0.5$, but the analytical estimates are reported to best fit experimental data for different materials when $\phi < 0.3$ as compared by Nemat-Nasser et al. (1982). In the study, the unit cell is discretized by 31×31 grid points, and the solid domain and interface location are depicted in Figure 7-9 (a), and the interface points construction based on the algorithms discussed in Section 7.3.1 are shown in Figure 7-9 (b). The geometry shown in Figure 7-9 is for the case of porosity $\phi = 0.25$. The G-

147

RKCM is employed with equal-order quadratic bases and a quintic B-spline kernel function. Based on the discretization, the numerical prediction of elastic moduli and material constants obtained by G-RKCM is compared with the analytical values in Table 7-1. As can be shown, the numerical prediction of the homogenized material properties converges to the analytical solutions as the porosity reduces.

Table 7-1 Effective moduli for the unit cell with different porosity ϕ

Porosity ϕ	0.15		0.20		0.25	
Material Constants	Analytical Estimates	Numerical Results	Analytical Estimates	Numerical Results	Analytical Estimates	Numerical Results
$\overline{C}_{1111}\left(\overline{C}_{2222}\right)$	875.0000	876.0423	771.3462	775.3003	678.4615	691.3444
$\overline{C}_{1122}\left(\overline{C}_{2211}\right)$	323.6538	323.5311	268.2692	265.0028	218.6538	218.9385
$\overline{E}$	700.2176	701.5263	632.8942	640.2887	571.8766	586.0275
$\overline{v}$	0.2700	0.2697	0.2580	0.2547	0.2437	0.2405

7.3.5 Influence of Basis Functions in G-RKCM

Due to the convergence requirement of the gradient RK approximation, G-RKCM with equal-order quadratic bases is adopted for solving unit cell problems. Nevertheless, the interface points can become non-uniformly distributed, and the selection of kernel support in the RK shape functions to be large enough to ensure a non-singular moment matrix and yet small enough to

properly represent the fine resolution of microstructures can be contradicting. To resolve this difficulty, we introduce Shepard functions (Appendix D) as the RK shape functions near the interface points to allow the use of small kernel support for proper discretization of microstructural heterogeneity. Note that the employment of Shepard function is equivalent to RK shape function with zero-th order basis. To understand the influence of Shepard functions on the solution accuracy in G-RKCM, consider a two-dimensional Poisson problem as follows:

$$\Delta u\left(x, y\right) = \left(x^2 + y^2\right)e^{xy} \quad \text{in } \Omega = \left(0,1\right) \times \left(0,1\right)$$
$$u\left(x, y\right) = e^{xy} \quad \text{on } \partial\Omega$$

(7.26)

Here, the domain is discretized by 25×25 source points while the boundary conditions are imposed at 51 collocation points per side as shown in Figure 7-10. The influence of the employment of Shepard functions on the L2 error norms of u and $u_{,\alpha}$ obtained by G-RKCM is presented in Figure 7-11. The results show that the employment of less than 10% Shepard functions at the source points would yield less than 0.1% error in L2 error norms of u and $u_{,\alpha}$ compared to the case without using any Shepard functions.
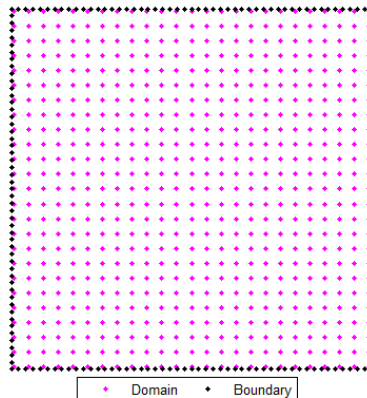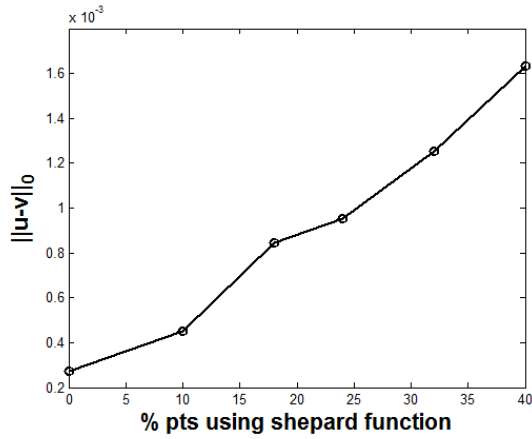

Figure 7-10 Discretization in Poisson problem

149
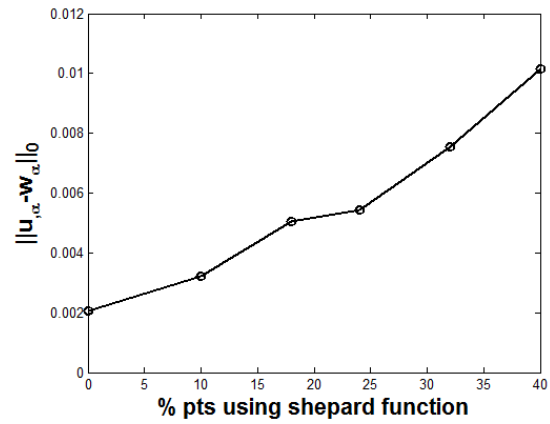
Figure 7-11 Convergence of L2 norms of u and $u_{,\alpha}$ in Poisson problem with respect to the % of Shepard functions used at source points

7.4 Investigation of Trabecular Bone Mechanical Properties

The accuracy of the homogenized material parameters depends greatly on the accuracy of the characteristic functions such as χ, η, and κ to be solved from the unit cell problems, the representative unit cell size, and the resolution of microstructural image. In this section, we will first investigate the size effect of the unit cell and image resolution on the reliability of the predicted mechanical properties. Then, the proposed numerical framework will be employed to investigate the human trabecular bone mechanical properties.

In the following numerical examples, G-RKCM with equal-order quadratic bases and a quintic B-spline kernel function is employed to solve unit cell problems, and the same source points and collocation points are adopted in strong form collocation, while the interface points are used as the boundary collocation points. The homogenized material constants are obtained by solving the

characteristic functions first and then by using Gauss quadrature with 4 integration points in each triangle to carry out the calculation of homogenized material properties. Due to the orthotropy in the trabecular bones, the homogenized elastic tensor is then transformed to the orthotropic direction (Appendix E) to obtain the effective Young's moduli and Poisson ratios.

7.4.1 Investigation of Unit Cell Dimension on Homogenized Mechanical Properties
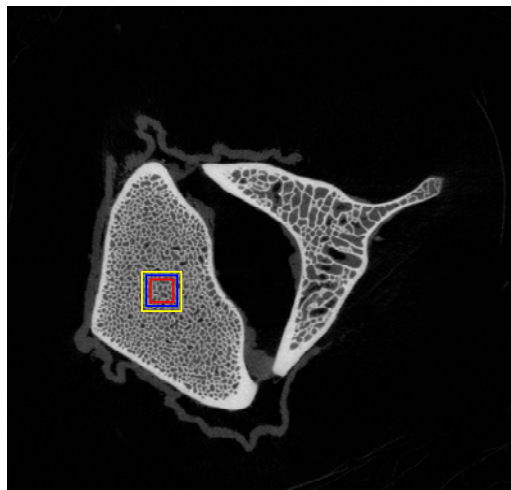
Figure 7-12 Images of a mammalian vertebra with specified unit cell locations: reference unit cell (depicted by a red square), unit cells with 120%, and 140% of the reference cell sizes (depicted by a blue square, and yellow square, respectively)

To investigate the dimension of unit cell and its influence on the mechanical properties, three unit cells with different representative unit cell dimensions are considered. As shown in Figure 7-12, the trabecular bone image of a sheep vertebra (1024×973 pixels), adopted from the website of SCANCO Medical (http://www.scanco.ch/), is obtained by Xtreme-CT (a high-

151

resolution peripheral quantitative-computed tomography, HR-pQCT) with nominal resolution of $41\,\mu m$ and a maximum scan size $126\,mm \times 150\,mm$ in the plane. In Figure 7-12, a reference unit cell is specified by a red square, with $10\,mm \times 10\,mm$. Based on this reference unit cell dimension, two unit cells with enlarged dimensions equivalent to 120% and 140% of the reference cell are extracted from the same location depicted by a blue square and yellow square in Figure 7-12, respectively. The microstructures of three unit cells are shown in Figure 7-13, and they are discretized by 25×25 pixels, 30×30 pixels, and 35×35 pixels.

The following parameters are adopted to solve the level set segmentation equation: $\mu = \nu = 0$, $\lambda_1 = \lambda_2 = 10000$, $dt = 0.1$, $\varepsilon = 2a$, with the residual 5×10^{-6}. In the interface identification process, the RK shape functions are constructed using a quadratic basis and a quadratic kernel function, and the RK support size is set as $a = 2.4$. The microstructures with reconstructed interfaces and partitioned domain are shown in Figure 7-14. The material properties of the trabecular ovine bone are given as follows: the Young's modulus is $1.192\,GPa$ (Nafei et al., 2000), the Poisson's ratio is 0.3 (Brown, 1988), and the blood viscosity in the adult sheep is $4.373\times10^{-3}\,Pa\cdot s\left(N\cdot\sec/m^2\right)$ (Windberger et al., 2003).
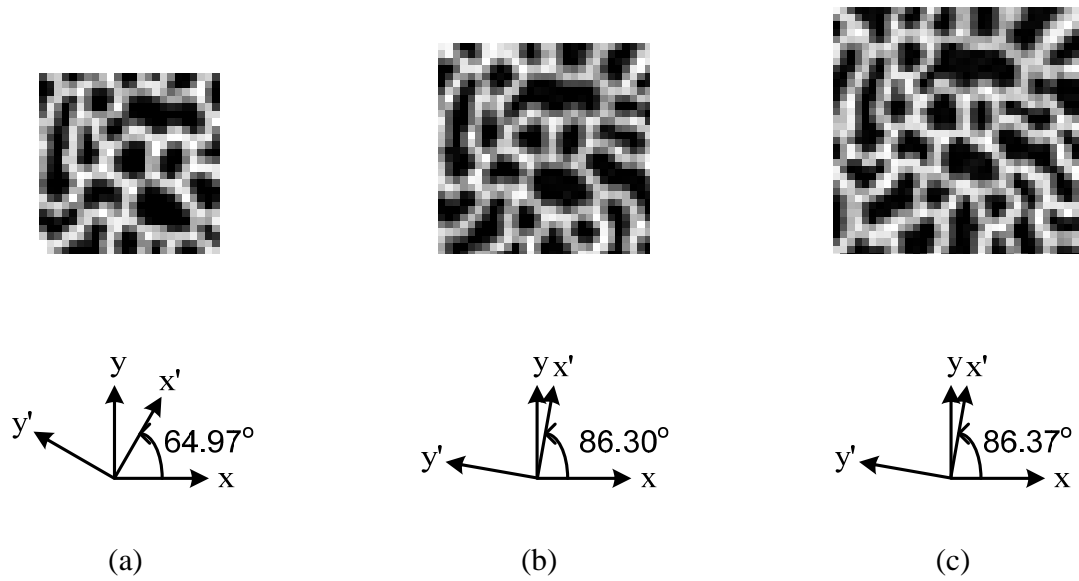
Figure 7-13 Images of unit cells: (a) Reference unit cell; (b) 120% of reference cell; (c) 140% of reference cell; and the corresponding principal direction of unit cells
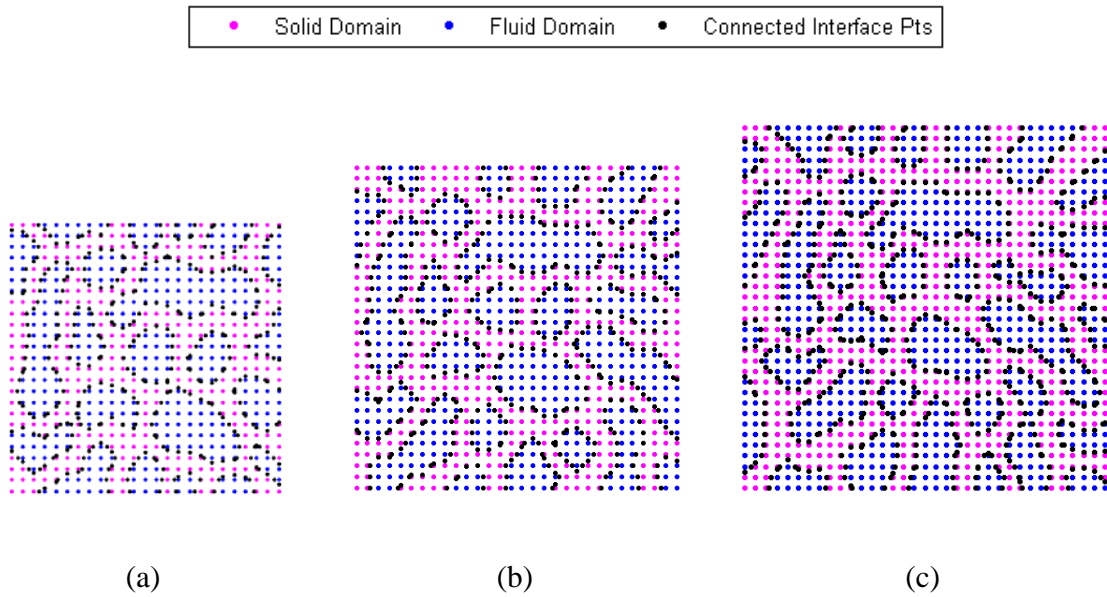

Figure 7-14 Connected interface and partitioned domain for unit cells with different sizes: (a) Reference unit cell; (b) 120% of reference cell; and (c) 140% of reference cell

The effective Young's moduli and Poisson ratio, the homogenized effective stress coefficient $\bar{\alpha}_{ij}$, and the homogenized permeability tensors $\bar{K}_{ij}$ for the three unit cells are summarized in Table 7-2, Table 7-3, and Table 7-4, respectively. The percentage of points using Shepard functions is less than 10%. It is observed that the homogenized material constants obtained from the unit cells with different representative sizes exhibit converging behavior as the dimension of the unit cell increases.

Recall that the effective stress coefficient α in Biot's theory accounts for the effective stress effect $\sigma_{ij}^{eff} = \sigma_{ij}^{t} - \alpha p \delta_{ij}$ as described in Chapter 3. The homogenized effective stress coefficient $\bar{\alpha}_{ij}$ plays a similar role in the homogenized macroscopic stress $\bar{\sigma}_{ij} = \bar{C}_{ijkl} \dfrac{\partial u_k^0}{\partial x_l} - \bar{\alpha}_{ij} p^0$ in poroelastic materials as presented in Chapter 4, which determines the influence of pore pressure on the effective stress. In addition, $\bar{\alpha}_{ij}$ indicates the degree of anisotropy. For anisotropic materials, $\bar{\alpha}_{11} \neq \bar{\alpha}_{22}$ in general, which is observed in Table 7-3. In particular, the angle between the principal direction of the trabecular bone and the global x direction varies from 64.97° to 86.37° as depicted in Figure 7-13, where only one angle is calculated for 2D images and the counterclockwise direction is defined as positive direction. For the selected microstructure of a trabecular bone, this numerical study suggests that representative cell dimension needs to be carefully selected for homogenization analysis to ensure that the microstructural feature is captured while the degrees of free representing the model size are not too big for computational efficiency.

Table 7-2 Effective Young's moduli and Poisson ratio obtained from unit cells with different sizes

Material Constants	Reference Unit Cell	120% of Reference Cell	140% of Reference Cell
$\bar{E}_{11}\left(MPa\right)$	281.5300	312.7431	317.3712
$\bar{E}_{22}\left(MPa\right)$	382.6884	370.3672	361.0187
$\bar{v}_{12}$	0.1487	0.1573	0.1615
$\bar{v}_{21}$	0.2021	0.1901	0.1837

Table 7-3 Components of homogenized effective stress coefficient tensor obtained from unit cells with different sizes

$\bar{\alpha}_{ij}$	Reference Unit Cell	120% of Reference Cell	140% of Reference Cell
$\bar{\alpha}_{11}$	0.2333	0.2425	0.2461
$\bar{\alpha}_{22}$	0.2240	0.2480	0.2596

Table 7-4 Components of homogenized permeability tensor obtained from unit cells with different sizes

$\bar{K}_{ij}\left(10^{-6}\,m^4\!\big/N\cdot s\right)$	Reference Unit Cell	120% of Reference Cell	140% of Reference Cell
$\bar{K}_{11}$	5.44	4.74	4.53
$\bar{K}_{22}$	4.55	4.20	4.09

155

7.4.2 Investigation of Image Resolution on Mechanical Properties

To study the influence of image resolution on the homogenized material parameters, the reference unit cell with 25×25 pixels is further presented by 35×35 pixels and 45×45 pixels as shown in Figure 7-15. The microstructures with connected interfaces and the corresponding segmented domains are shown in Figure 7-16.

(a)   (b)   (c)
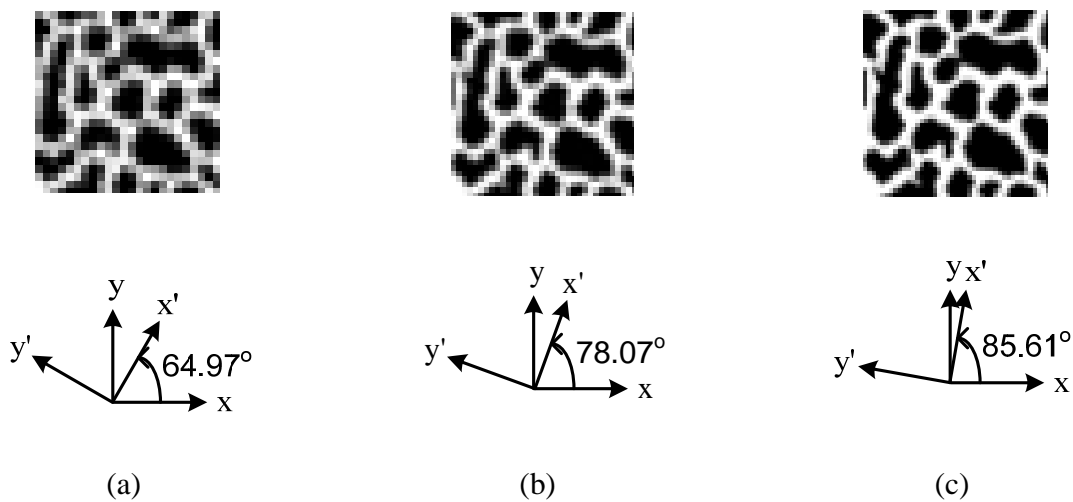
Figure 7-15 Images of the unit cell discretized by (a) 25×25 pixels; (b) 35×35 pixels; (c) 45×45 pixels; and the corresponding principal direction of unit cells

The homogenized material constants obtained by unit cells with different resolution are shown in Table 7-5, Table 7-6, and Table 7-7, which exhibit converging behavior as the resolution increases. In this study, the percentage of points using Shepard functions is within 10%. The porosity ϕ of the microstructure gradually increases from 0.5280 to 0.5620 in accord with the image resolution. For the homogenized permeability tensor $\bar{K}_{ij}$ given in Table 7-7, the permeability is converging as the resolution of image increases. For 2D images, the angle between the principal direction of the trabecular bone and the global x direction is observed to

be $64.97° \sim 85.61°$ with the counterclockwise direction defined as positive direction shown in Figure 7-15. This study shows that the resolution of the microstructure images needs to be properly selected for desired accuracy in homogenization analysis.
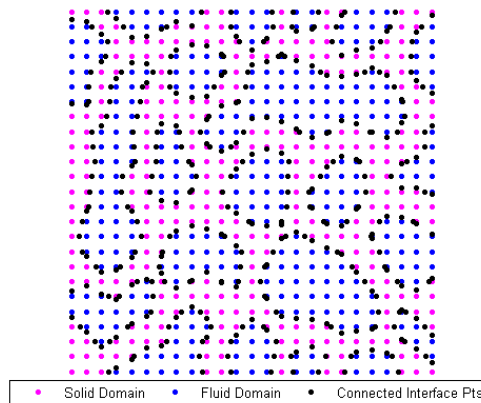
(a)
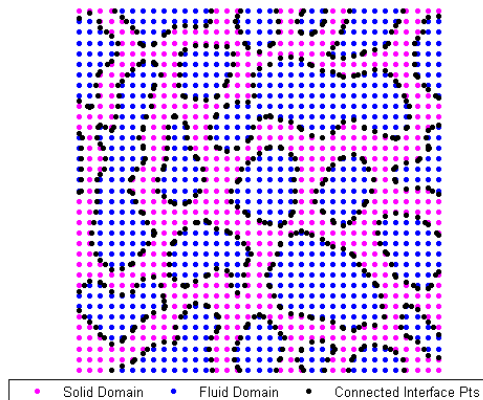
(b)
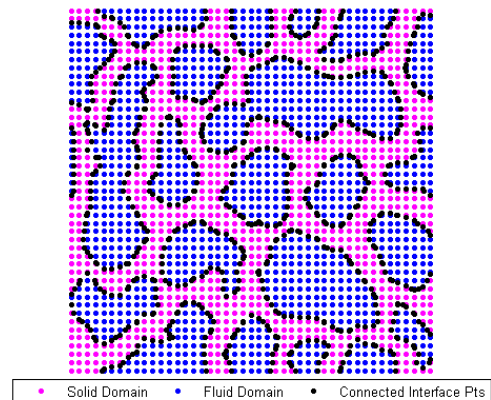
(c)

Figure 7-16 Connected interface and partitioned domain for unit cells with different resolution: (a) 25×25 pixels; (b) 35×35 pixels; and (c) 45×45 pixels

157

Table 7-5 Effective Young's moduli and Poisson ratio obtained from unit cells with different resolution

Material Constants	25×25 pixels	35×35 pixels	45×45 pixels
$\bar{E}_{11}(MPa)$	281.5300	316.6133	318.5854
$\bar{E}_{22}(MPa)$	382.6884	351.4823	342.7927
$\bar{v}_{12}$	0.1487	0.1625	0.1714
$\bar{v}_{21}$	0.2021	0.1907	0.1844

Table 7-6 Components of homogenized effective stress coefficient tensor obtained from unit cells with different resolution

$\bar{\alpha}_{ij}$	25×25 pixels	35×35 pixels	45×45 pixels
$\bar{\alpha}_{11}$	0.2333	0.2500	0.2571
$\bar{\alpha}_{22}$	0.2240	0.2471	0.2545

Table 7-7 Components of homogenized permeability tensor obtained from unit cells with different resolution

$\bar{K}_{ij}\left(10^{-6}\,m^4\!/N\cdot s\right)$	25×25 pixels	35×35 pixels	45×45 pixels
$\bar{K}_{11}$	5.44	6.07	6.41
$\bar{K}_{22}$	4.55	5.02	5.19

7.4.3 Investigation of Mechanical Properties in Human Trabecular Bones

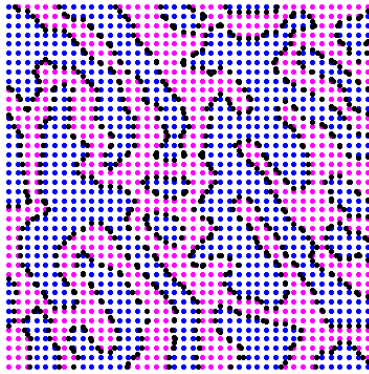In this section, the proposed numerical framework for interface identification and solution of microstructural problems will be employed to investigate the human trabecular bone mechanical properties. Unless otherwise mentioned, the G-RKCM is employed to solve unit cell problems, and the parameters for RK shape functions and for level set equation are adopted the same as those given in Section 7.4.1. In this study, the percentage of points using Shepard functions is within 15%.

The microstructural images of trabecular bone used herein are obtained from human femora, human tibias, and human vertebrae available in the literatures, from which the unit cells are extracted (Kuhn et al., 1990; Genant et al., 2000; Pothuaud et al., 2000; Kim and Al-Hassani, 2002; Kinney et al., 2005; Bauer et al., 2006; Bauer et al., 2007) as shown in Figure 7-17, where the unit cell length is taken as $5\,mm$ per side. Based on the investigation of image resolution in Section 7.4.2, the unit cells are presented by 40×40 pixels such that the distribution of solid skeleton and pores are captured properly. The material properties of human trabecular bone are given as follows. The Young's modulus and Poisson's ratio are $5\,GPa$ and 0.3, respectively (Mente and Lewis, 1989; Choi et al., 1990; Hollister et al., 1994). The viscosity of human bone marrow is taken as $0.04\,Pa \cdot s \left(N \cdot \sec / m^2 \right)$ at $37^{\circ}C$ (Bryant et al., 1989; Grimm and Williams, 1997).

(a) Femur
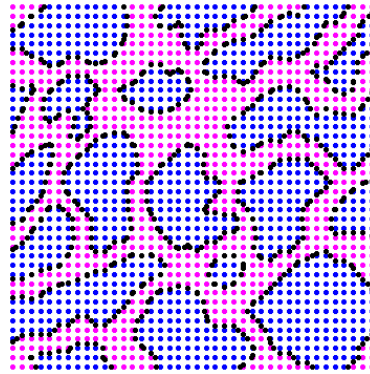
(b) Femur
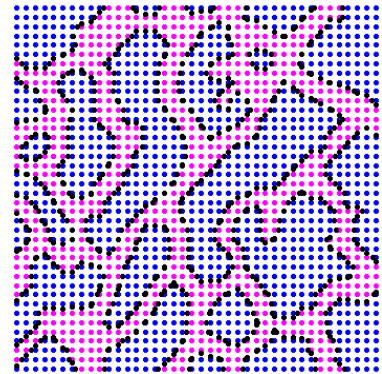
(c) Femur
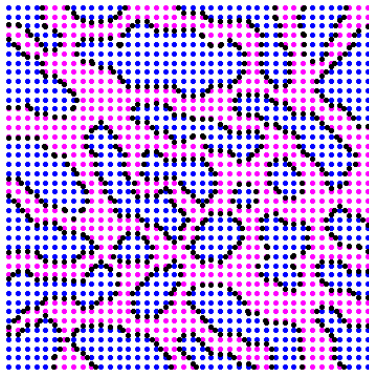
(d) Femur
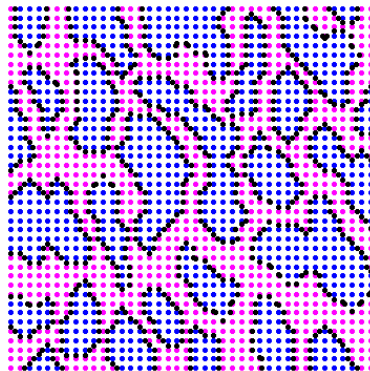
(e) Femur
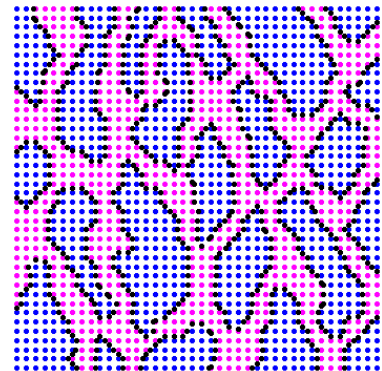
(f) Femur

(g) Femur

(h) Tibia

(i) Tibia

160

(j) Tibia　　　　　　　　(k) Vertebra　　　　　　　　(l) Vertebra

(m) Vertebra　　　　　　　　(n) Unknown
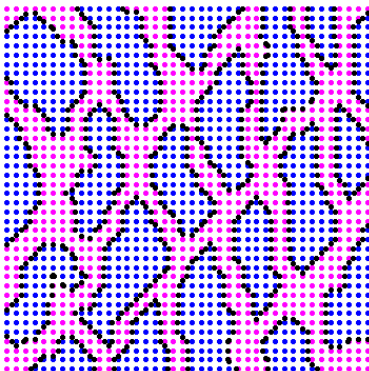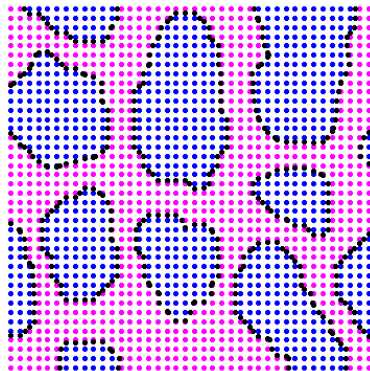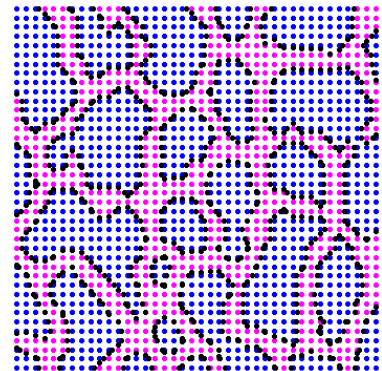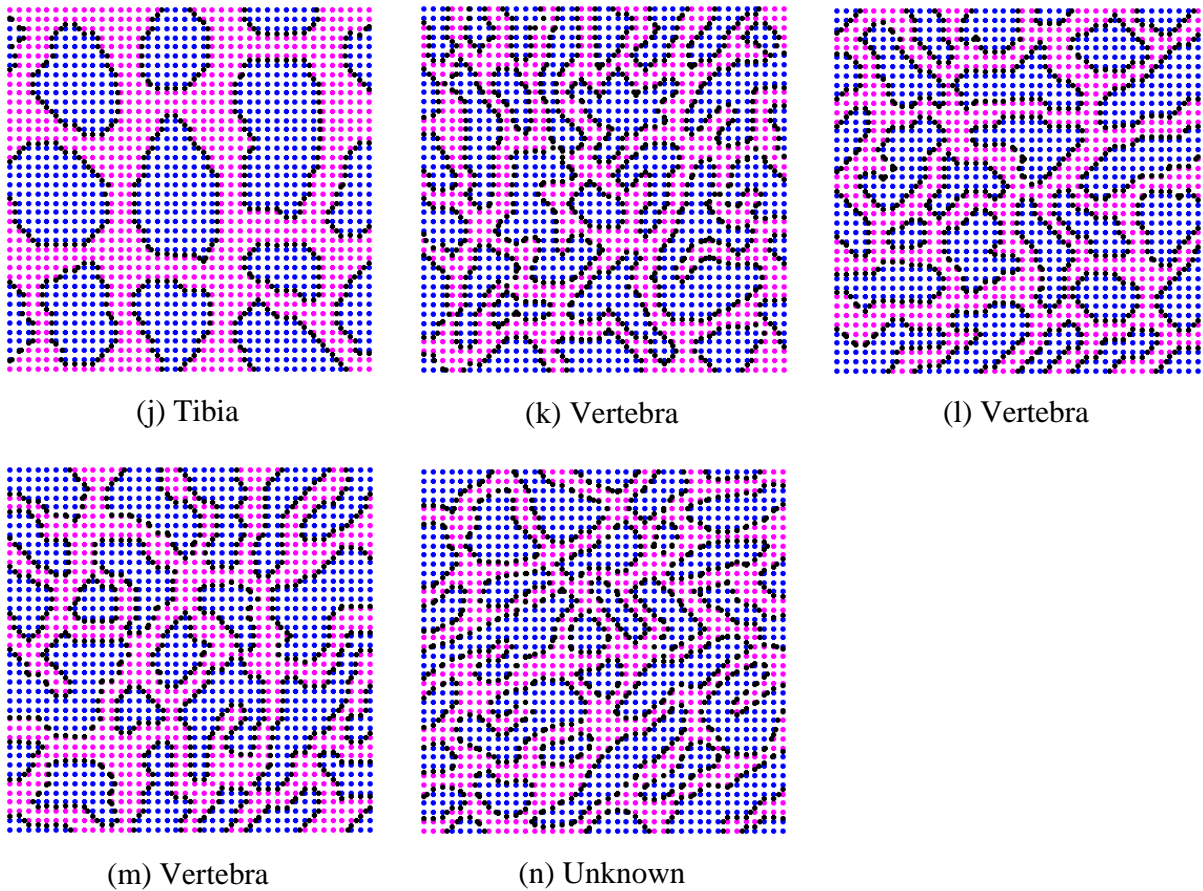
Figure 7-17 Microstructures of human trabecular bones segmented by the proposed image-based strong form collocation method

Since trabecular bones have been recognized as anisotropic materials, the homogenized elasticity tensor $\bar{C}_{ijkl}$ needs to be transformed to the symmetry coordinate system in order to compare with the experimental data (Cowin and Mehrabadi, 1987; Hollister et al., 1991; Podshivalov, 2011). Following the original work done by Cowin and Mehrabadi (1987), the homogenized elasticity tensor is transformed to the principal planes where trabecular bones exhibit orthotropy. The corresponding procedure adopted from Cowin and Mehrabadi (1987) for tensor transformation is given in Appendix E.

161

The reported experimental data for trabecular bone material properties such as modulus-density relations have shown substantial difference from different literatures (Keaveny et al., 2001; Zysset 2003; Hellmich et al., 2004; Helgason et al. 2008). It still remains unclear whether such difference can be entirely attributed to methodological discrepancy. For example, machine errors, specimen size and geometry, and anatomic site are all factors affecting the experimental results (Keaveny et al., 2001; Helgason et al., 2008).

For the effective Young's moduli obtained from the microstructures, the numerical experimentation is compared with the reported experimental data summarized by Helgason et al. (2008), in which the experiments were conducted on human trabecular bones with various anatomical sites including femur, tibia, and vertebra, etc. Further, only experimental results obtained from direct mechanical testing were adopted to exclude errors from different measuring techniques such as ultrasound or indentation, and only the highest values of moduli in principle direction were considered. Among these studies, two normalization criteria have been made for quantitative comparison, the different definitions of density have been unified as the apparent bone density, and the experimental data have been normalized with respect to the strain rate (Helgason et al., 2008). The original sources of data are referred to the following work: Carter and Hayes (1977), Lotz et al. (1990), Hodgskinson and Currey (1992), Dalstra et al. (1993), Keller (1994), and Li and Aspden (1997).

In this study, we also investigate the principal direction for human trabecular bones as given in Table 7-8. Based on these 2D images, the range of directional angle between the principal direction of the trabecular bone and the global x direction lies between $1.85°$ and $75.30°$, where the counterclockwise direction is defined as the positive direction. The wide span of principal

direction change suggests the anisotropic property of trabecular bone and the need of reliable

analysis to predict the associated mechanical behavior.

Table 7-8 Principal direction of human trabecular bones

Image Case	(a)	(b)	(c)	(d)	(e)	(f)	(g)
Direction (degree)	35.51	75.30	19.55	58.25	70.54	54.89	25.83
Image Case	(h)	(i)	(j)	(k)	(l)	(m)	(n)
Direction (degree)	1.85	49.70	14.35	8.63	62.40	51.18	45.99
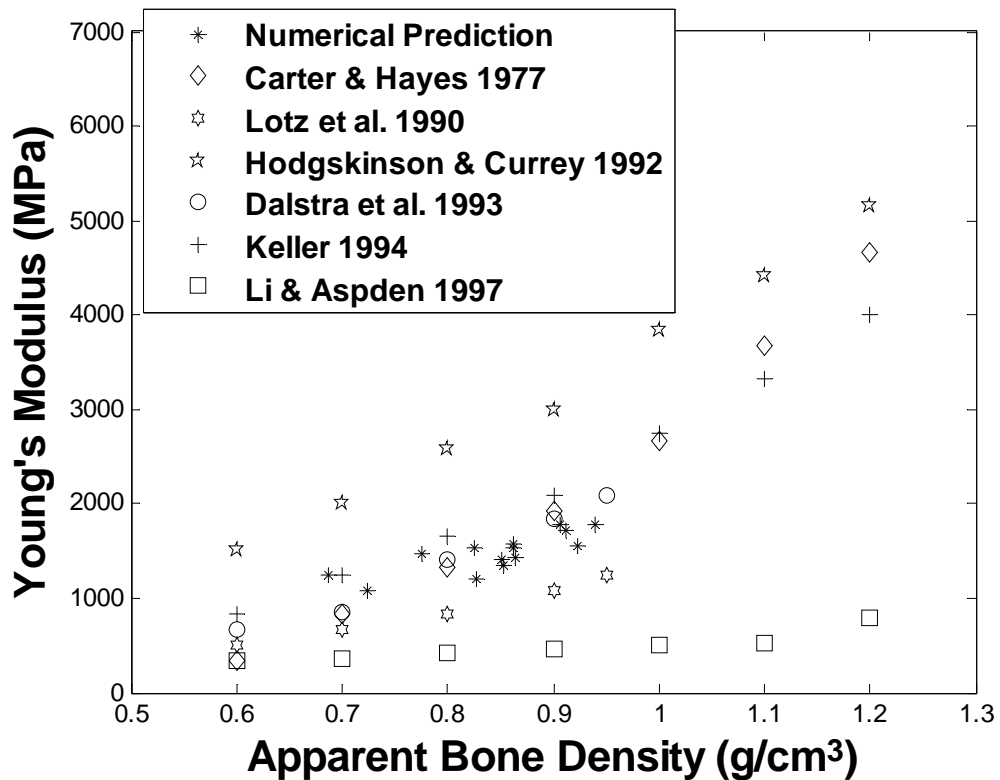
Figure 7-18 Comparison of effective Young's moduli with experimental data
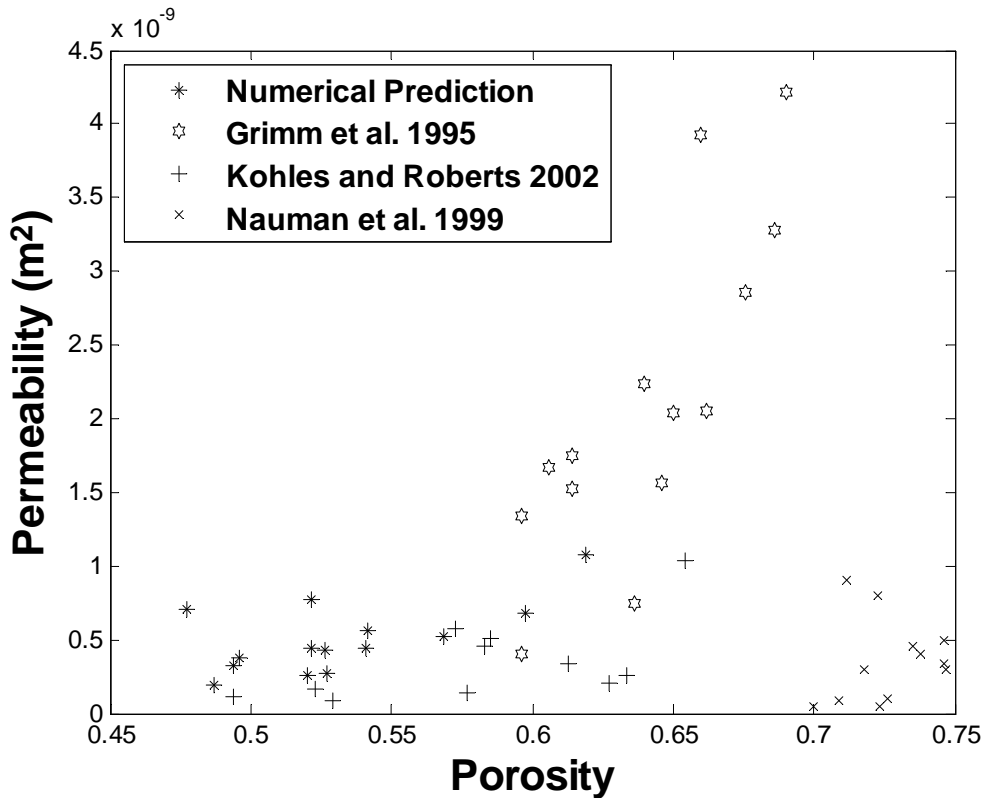
Figure 7-19 Comparison of homogenized permeability with experimental data

The elastic property of trabecular bones is primarily related to the apparent bone density. The apparent bone density ρ_{app} is defined as the product of volume fraction of bone and trabecular tissue density, in which the definition of volume fraction is bone volume divided by the total volume (BV/TV) of specimen, while the trabecular tissue density typically has a constant value around $2\,g/cm^3$ (Keaveny et al., 2001; Helgason et al., 2008). In this study, the trabecular tissue density is adopted as $2\,g/cm^3$, and the apparent bone density ρ_{app} is calculated by $\rho_{app} = 2(1-\phi)\,g/cm^3$, in which ϕ is the porosity. Figure 7-18 compares the numerical results of effective Young's moduli with experimental data. As observed, the numerical prediction lies in

the range where most experimental data are reported. This indicates that the proposed numerical framework is capable of predicting the bone tissue behavior through multiscale homogenization.

On the other hand, for the permeability measured in the trabecular bones, the reported range of bone permeability in literature has a wide span from 10^{-8} to $10^{-14}\left(m^2\right)$, in which the values of human trabecular bone are around 10^{-8} to $10^{-11}\left(m^2\right)$ (Grimm and Williams 1997; Nauman et al., 1999; Baroud et al., 2004). Based on the experimental results, the explanation for the variation may attribute to flow direction, bone porosity, and microstructural morphology such as trabecular architecture and separation for various anatomical sites. In addition, the measurement of permeability in mechanical tests still poses a technical challenge, which requires specimen control such as maintaining a constant pressure gradient and degassing the fluid (Nauman et al., 1999). From our multiscale numerical simulation, the predicted permeability is in agreement with the experimental data as shown in Figure 7-19, where the largest value of permeability component is used in the comparison. Nevertheless, it should be reminded that the porosity obtained from two-dimensional images might be underestimated since the inter connection of pores in three dimension is not modeled when a two-dimensional microstructure is considered.

7.4.4 Validation of Macroscopic Trabecular Bone Modeling

Consider a trabecular bone microstructural image presented by 45×45 pixels shown in Figure 7-20, with unit cell size $10\,mm\times10\,mm$. The parameters adopted to solve the level set equation are $\mu=\nu=0$, $\lambda_1=\lambda_2=10000$, $dt=0.1$, $\varepsilon=2a$, with the residual 5×10^{-6}. In the interface

identification process, the RK shape functions are constructed by a quadratic basis and a quadratic kernel function, and the RK support size is set as $a = 2.4$.
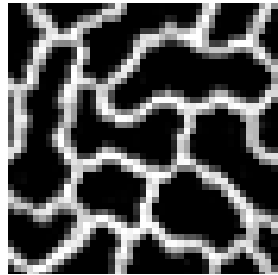
Figure 7-20 Images of the unit cell
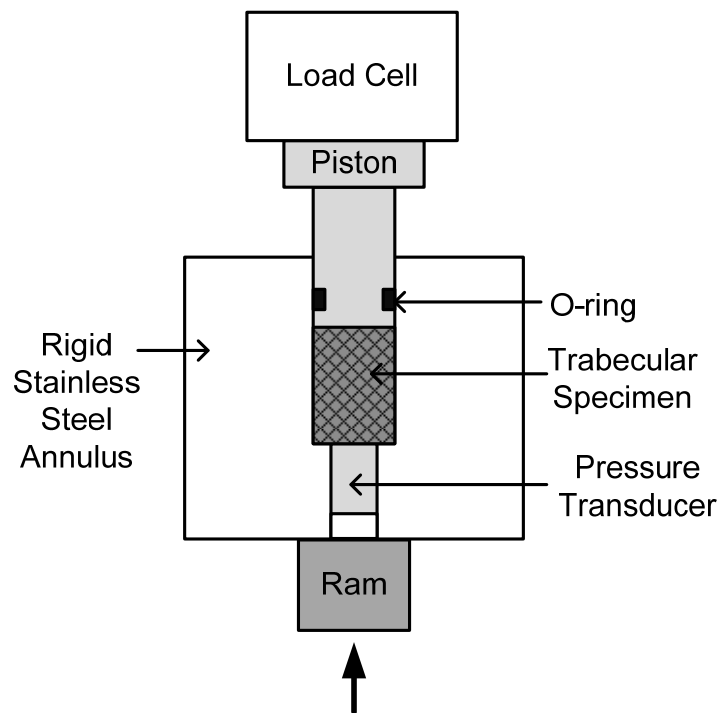
Figure 7-21 Undrained uniaxial strain testing
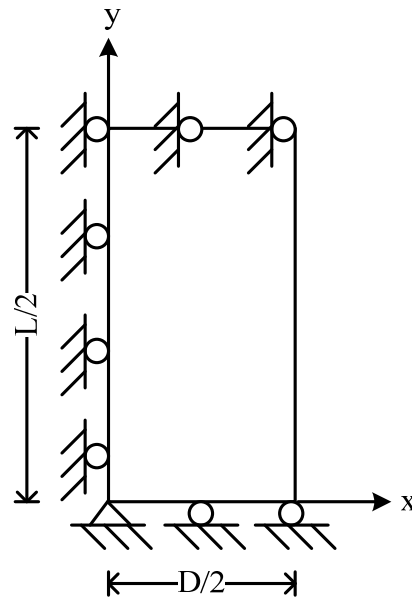
Figure 7-22 Two-dimensional poroelastic model of the cylindrical trabecular bone specimen

Table 7-9 Material properties for bovine trabecular bone (Lim and Hong, 2000)

$E\left(MPa\right)$	225.6714
ν	0.242
$\mu_v\left(Pa\cdot s\right)$	0.1

A material testing system designed for cylindrical specimens under uniaxial strain tests (Lim and Hong, 2000) is shown in Figure 7-21, where a compression force $2N$ was defined as zero load in the testing machine. The fluid pressure generated during deformation was recorded with a pressure transducer located below the specimen in the undraincd condition. The measured data

were recorded at $10Hz$. Since the stress-strain relation for the trabecular bone is limited within the elastic range, the numerical experimentation is conducted within the axial strain of 0.6% (Keaveny et aI., 1994; Hong et al., 2001). Therefore, the specimen is subjected to maximum strain 0.6% at a given strain rate 0.0001/sec under displacement control. The material properties of the bovine trabecular bone obtained from the experiment are summarized in Table 7-9, where E is Young's modulus, v is Poisson ratio of the solid skeleton, and μ_v is the viscosity. To numerically simulate a cylindrical specimen subjected to the uniaxial strain rate, a two-dimensional axisymmetric poroelastic model is developed for trabecular bone modeling as depicted in Figure 7-22, where the specimen has $D = 10mm$ in diameter and $L = 20mm$ in length (Hong et al., 2001). The corresponding boundary conditions and initial conditions for the axisymmetric specimen model are

$$
\begin{aligned}
&(1)\,\text{at } x = 0, \quad y = 0, \quad u_1^0 = u_2^0 = 0 \\
&(2)\,\text{on } x = 0, \quad u_1^0 = 0, \quad \overline{t}_2^{\,s} = 0, \quad \frac{\partial p^0}{\partial x} = 0 \\
&(3)\,\text{on } x = \frac{D}{2}, \quad \overline{t}_1^{\,s} = \overline{t}_2^{\,s} = 0, \quad p^0 = 0 \\
&(4)\,\text{on } y = 0, \quad u_2^0 = 0, \quad \overline{t}_1^{\,s} = 0, \quad \frac{\partial p^0}{\partial y} = 0 \\
&(5)\,\text{on } y = \frac{L}{2}, \quad u_1^0 = 0, \quad \frac{\partial p^0}{\partial y} = 0, \quad u_2^0(t) = 10\left(\frac{L}{2}\right)t
\end{aligned}
\tag{7.27}
$$

which are boundary conditions. The initial conditions are

$$
\begin{aligned}
&p^0\left(x, y, t = 0\right) = 0 \\
&u_1^0\left(x, y, t = 0\right) = u_2^0\left(x, y, t = 0\right) = 0
\end{aligned}
\tag{7.28}
$$

168

Recall the strong form of the homogenized macroscopic continuity and equilibrium equations derived in Chapter 4 are

$$
\begin{aligned}
&\frac{\partial u_{i,i}^{0}(\mathbf{x},t)}{\partial t} - \bar{K}_{ij} p_{,ij}^{0}(\mathbf{x},t) = 0 \quad \text{in } \Omega \\
&p^{0} = \bar{p}^{0} \quad \text{on } \Gamma_{p} \\
&-\bar{K}_{ij} p_{,j}^{0} = \bar{q}_{i} \quad \text{on } \Gamma_{q}
\end{aligned}
\tag{7.29}
$$

and

$$
\begin{aligned}
&\left(\bar{C}_{ijkl} u_{(k,l)}^{0} - \bar{\alpha}_{ij} p^{0} \right)_{,j} + \bar{f}_{i}^{S} = 0 \quad \text{in } \Omega \\
&u_{i}^{0} = \bar{u}_{i}^{0} \quad \text{on } \Gamma_{u} \\
&\left(\bar{C}_{ijkl} u_{(k,l)}^{0} - \bar{\alpha}_{ij} p^{0} \right) n_{j} = \bar{t}_{i}^{S} \quad \text{on } \Gamma_{t}
\end{aligned}
\tag{7.30}
$$

with the initial conditions given by

$$
\begin{aligned}
&p^{0}(\mathbf{x},t=0) = \bar{p}_{(t=0)}^{0} \quad \text{in } \Omega \\
&u_{i}^{0}(\mathbf{x},t=0) = \bar{u}_{i(t=0)}^{0} \quad \text{in } \Omega
\end{aligned}
\tag{7.31}
$$

In the numerical experimentation, the G-RKCM with equal-order quadratic bases and a quintic B-spline kernel function is employed. The domain is discretized by the same source and collocation points, i.e., 11×21 points. To solve the quasi-static system in (7.29)-(7.31), we employ the forward Euler scheme and have the following discretization:

$$
\begin{aligned}
&u_{i,i}^{0(n+1)} = u_{i,i}^{0(n)} + \Delta t \bar{K}_{ij} p_{,ij}^{0(n)} \\
&\bar{C}_{ijkl} \frac{\partial u_{(k,l)}^{0(n+1)}}{\partial x_{j}} - \bar{\alpha}_{ij} \frac{\partial p^{0(n+1)}}{\partial x_{j}} = -\bar{f}_{i}^{S(n+1)}
\end{aligned}
\tag{7.32}
$$

in which the superscript n denotes the time step at $t = t^n$.

The approximation for $\mathbf{u}^0$ and p^0 are given by

$$\mathbf{u}^0 = \sum_{I=1}^{N_s} \mathbf{\Psi}_I \mathbf{a}_I$$
$$p^0 = \sum_{I=1}^{N_s} \psi_I b_I$$

(7.33)

where the gradient reproducing kernel approximation is employed. Denote the general form for solving the quasi-static system by G-RKCM in (7.32) as

$$\mathbf{A}^{(n+1)}\mathbf{a}^{(n+1)} = \begin{bmatrix} \mathbf{A}^{1(n+1)} + \mathbf{A}^{2(n+1)} \\ \sqrt{\alpha_h}\left(\mathbf{A}^{3(n+1)} + \mathbf{A}^{4(n+1)}\right) \\ \sqrt{\alpha_g}\,\mathbf{A}^{5(n+1)} \end{bmatrix} \mathbf{a}^{(n+1)}$$

$$\equiv \begin{bmatrix} \mathbf{A}^{1(n)} + \mathbf{A}^{2(n)} \\ \sqrt{\alpha_h}\left(\mathbf{A}^{3(n)} + \mathbf{A}^{4(n)}\right) \\ \sqrt{\alpha_g}\,\mathbf{A}^{5(n)} \end{bmatrix} \mathbf{a}^{(n)} - \begin{bmatrix} \mathbf{b}^{1(n)} \\ \mathbf{b}^{2(n)} \\ \mathbf{b}^{3(n)} \end{bmatrix} + \begin{bmatrix} \mathbf{b}^{1(n+1)} \\ \mathbf{b}^{2(n+1)} \\ \mathbf{b}^{3(n+1)} \end{bmatrix} = \mathbf{A}^{(n)}\mathbf{a}^{(n)} - \mathbf{b}^{(n)} + \mathbf{b}^{(n+1)}$$

(7.34)

with

$$\mathbf{a}^{(n+1)} = \begin{bmatrix} a_{1I}^{(n+1)} & a_{2I}^{(n+1)} & b_I^{(n+1)} \end{bmatrix}^{\mathrm{T}}$$

(7.35)

where $\mathbf{A}^{(n+1)}$ and $\mathbf{A}^{(n)}$ constitute matrices associated with the differential operators and $\mathbf{b}^{(n+1)}$ and $\mathbf{b}^{(n)}$ constitute vectors related to the boundary operators at $t = t^{n+1}$ and $t = t^n$, respectively, and $\sqrt{\alpha_h}$ is the weight on $\partial\Omega^h$ and $\sqrt{\alpha_g}$ is the weight on $\partial\Omega^g$.

170

The corresponding operators in (7.34) are given as follows:

$$\mathbf{A}_{IJ}^{1(n+1)} = \mathbf{L}^1 \mathbf{\Psi}_J^{x^{\mathrm{T}}} \left(\mathbf{p}_I \right) = \begin{bmatrix} \overline{C}_{1111}\Psi_{J,x}^x + \overline{C}_{1111}\left(\dfrac{\Psi_J^x}{x} - \dfrac{\Psi_J}{x^2} \right) & \overline{C}_{1212}\Psi_{J,y}^x & -\overline{\alpha}_{11}\psi_J^x \\ \overline{C}_{2211}\Psi_{J,y}^x & \overline{C}_{1212}\Psi_{J,x}^x & -\overline{\alpha}_{12}\psi_J^x \end{bmatrix}$$

$$\mathbf{A}_{IJ}^{2(n+1)} = \mathbf{L}^2 \mathbf{\Psi}_J^{y^{\mathrm{T}}} \left(\mathbf{p}_I \right) = \begin{bmatrix} \overline{C}_{1212}\Psi_{J,y}^y & \overline{C}_{1122}\Psi_{J,x}^y & -\overline{\alpha}_{12}\psi_J^y \\ \overline{C}_{1212}\Psi_{J,x}^y + \overline{C}_{2211}\dfrac{\Psi_J^y}{x} & \overline{C}_{2222}\Psi_{J,y}^y & -\overline{\alpha}_{22}\psi_J^y \end{bmatrix}$$

(7.36)

$$\mathbf{A}_{IJ}^{3(n+1)} = \mathbf{B}_h^1 \mathbf{\Psi}_J^{x^{\mathrm{T}}} \left(\mathbf{q}_I \right) = \begin{bmatrix} \overline{C}_{1111}\Psi_J^x n_1 + \overline{C}_{1111}\dfrac{\Psi_J}{x}n_1 & \overline{C}_{1212}\Psi_J^x n_2 & -\overline{\alpha}_{11}\psi_J n_1 \\ \overline{C}_{2211}\Psi_J^x n_2 + \overline{C}_{2211}\dfrac{\Psi_J}{x}n_2 & \overline{C}_{1212}\Psi_J^x n_1 & -\overline{\alpha}_{12}\psi_J n_1 \end{bmatrix}$$

$$\mathbf{A}_{IJ}^{4(n+1)} = \mathbf{B}_h^2 \mathbf{\Psi}_J^{y^{\mathrm{T}}} \left(\mathbf{q}_I \right) = \begin{bmatrix} \overline{C}_{1212}\Psi_J^y n_2 & \overline{C}_{1122}\Psi_J^y n_1 & -\overline{\alpha}_{12}\psi_J n_2 \\ \overline{C}_{1212}\Psi_J^y n_1 & \overline{C}_{2222}\Psi_J^y n_2 & -\overline{\alpha}_{22}\psi_J n_2 \end{bmatrix}$$

(7.37)

$$\mathbf{A}^{5(n+1)} = \mathbf{B}_g \mathbf{\Psi}_J \left(\mathbf{r}_I \right) = \begin{bmatrix} \Psi_J & 0 & 0 \\ 0 & \Psi_J & 0 \end{bmatrix}$$

which are operators for solving the homogenized macroscopic equilibrium equation. Since trabecular bone is typically recognized as orthotropic or transversely isotropic materials, it is assumed that the material constant in circumferential direction is the same as the one in radial direction.

$$\mathbf{A}_{IJ}^{1(n+1)} + \mathbf{A}_{IJ}^{2(n+1)} = \begin{bmatrix} \Psi_J^x + \dfrac{\Psi_J}{x} & \Psi_J^y & 0 \end{bmatrix}$$

$$\mathbf{A}_{IJ}^{1(n)} + \mathbf{A}_{IJ}^{2(n)} = \begin{bmatrix} \Psi_J^x + \dfrac{\Psi_J}{x} & \Psi_J^y & \Delta t\left(\overline{K}_{11}\psi_{J,x}^x + \overline{K}_{12}\psi_{J,y}^x p_{,12}^0 + \overline{K}_{21}\psi_{J,x}^y + \overline{K}_{22}\psi_{J,y}^y + \overline{K}_{11}\dfrac{\psi_J^x}{x} \right) \end{bmatrix}$$

(7.38)

$$\mathbf{A}_{IJ}^{3(n+1)} = \mathbf{B}_h^1 \mathbf{\Psi}_J^{x^{\mathrm{T}}} \left(\mathbf{q}_I \right) = \begin{bmatrix} 0 & 0 & -\overline{K}_{11}\psi_J^x \\ 0 & 0 & -\overline{K}_{21}\psi_J^x \end{bmatrix}$$

$$\mathbf{A}_{IJ}^{4(n+1)} = \mathbf{B}_h^2 \mathbf{\Psi}_J^{y^{\mathrm{T}}} \left(\mathbf{q}_I \right) = \begin{bmatrix} 0 & 0 & -\overline{K}_{12}\psi_J^y \\ 0 & 0 & -\overline{K}_{22}\psi_J^y \end{bmatrix}$$

(7.39)

171

$$\mathbf{A}_{IJ}^{5(n+1)} = \mathbf{B}_g \mathbf{\Psi}_J^T (\mathbf{q}_I) = \begin{bmatrix} 0 & 0 & \psi_J \end{bmatrix}$$
$$\mathbf{b}^{2(n+1)} = \begin{bmatrix} \bar{q}_1 & \bar{q}_2 \end{bmatrix}^T, \quad \mathbf{b}^{3(n+1)} = \bar{p}^0 \tag{7.40}$$

which are the matrix operators for the homogenized macroscopic continuity equation.

We first compare out numerical prediction with the experimental result (Lim and Hong, 2000) as shown in Figure 7-23, which is performed under constant strain rate $0.0001/\text{sec}$. With the consideration of solid and fluid interaction in the microstructure, the predicted pressure-strain relation shows lower pressure prediction in comparison with the experimental result, where the average pressure is averaged over the whole domain in the numerical simulation. The reduction of pore pressure reflects the material anisotropy resulting from the microstructure. Nevertheless, it should mention that the reported material properties are measured based on the assumption of uniformly distributed pores in the trabecular bone. The lack of consideration of solid-fluid variation in the trabecular bone specimens is the limitation of the experiments as pointed out by Lim and Hong (2000). Therefore, the employment of multiscale modeling considering microstructural geometry, solid and fluid interaction, and material anisotropy provides a chance to investigate the trabecular bone behavior precisely.

To understand the influence of viscosity on the variation of fluid pressure, we conduct numerical experimentation by varying the order of viscosity from $1.0 Pa \cdot s$ to $0.01 Pa \cdot s$ to consider the common range of viscosity for trabecular bones. Table 7-10 and Table 7-11 summarize the effective Young's moduli and the components of the homogenized permeability tensor obtained from our numerical framework for multiscale modeling. Figure 7-24 predicts the pore pressure-

axial strain relation for trabecular bones under constant strain rate 0.0001/sec with different

viscosity of fluid. For the given trabecular bone image, it is observed that the nonlinear behavior

of fluid pressure becomes obvious as the viscosity increases. Especially, among the predicted

pore pressure-axial strain curves, the lowest value of viscosity exhibits the most linear relation.

The decrease of fluid pressure in accordance with the increase of viscosity is observed, which is

the consequence of the increase of permeability induced by the microstructural geometry.
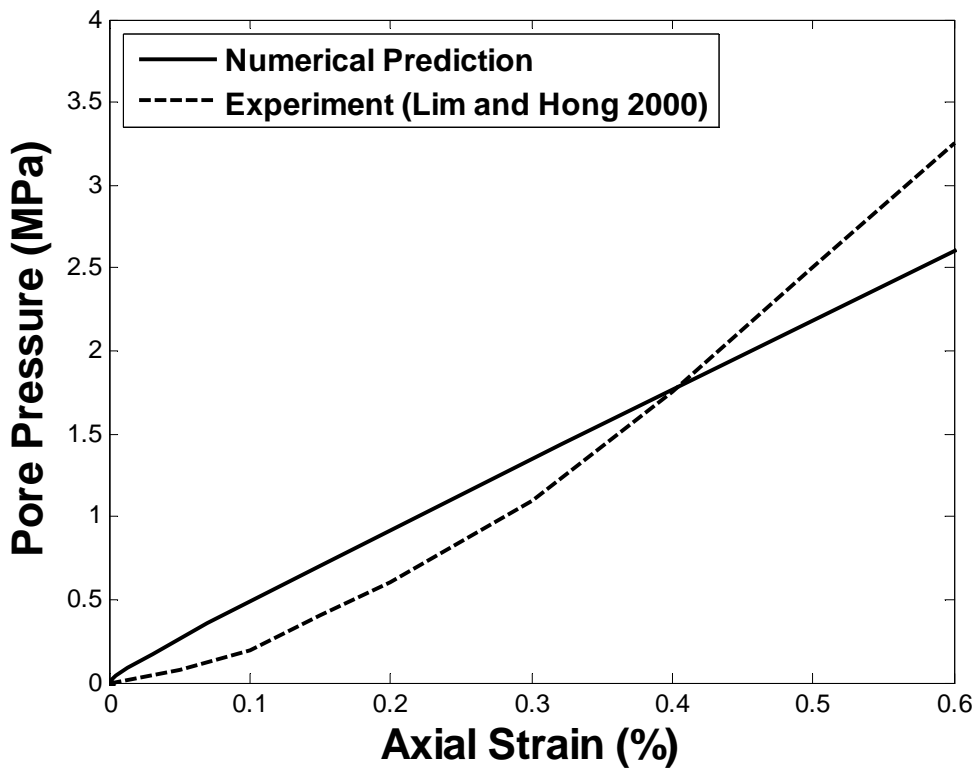
Figure 7-23 Pore pressure-axial strain relation

Table 7-10 Effective Young's moduli

$\bar{E}_{11}\left(MPa\right)$	33.7797
$\bar{E}_{22}\left(MPa\right)$	38.8259

Table 7-11 Components of homogenized permeability tensor obtained by different viscosity

Viscosity $(Pa \cdot s)$	1.0	0.1	0.01
$\overline{K}_{11}\left(m^2/(Pa \cdot s)\right)$	1.3391×10^{-7}	1.0131×10^{-7}	5.6485×10^{-8}
$\overline{K}_{22}\left(m^2/(Pa \cdot s)\right)$	1.2679×10^{-7}	1.0098×10^{-7}	5.4502×10^{-8}
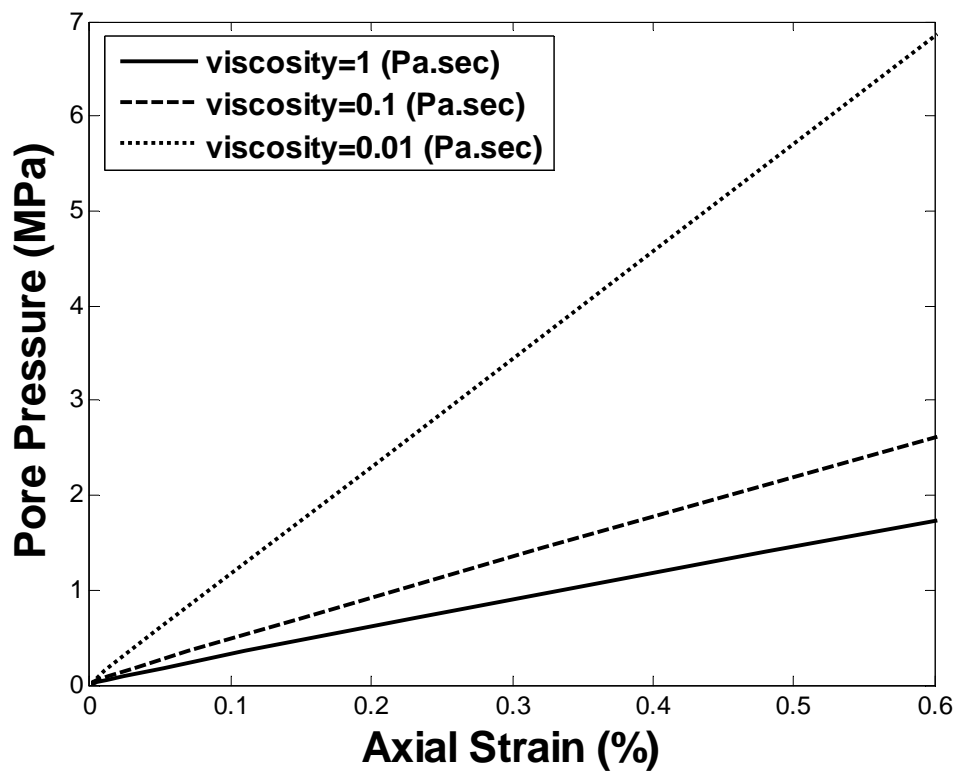
Figure 7-24 Pore pressure and axial strain relation under constant strain rate with different viscosity of fluid

7.5 Summary

To model poroelastic bone materials having high degree of material heterogeneity, we introduced the asymptotic-based multiscale homogenization method to retrieve the microstructural response. To employ the microstructural images for construction of the unit cell model directly, we introduced the strong form collocation method for image segmentation based on level set method. With the proposed image-based strong form collocation method for the level set interface and boundary identification, the threshold in the process of phase segmentation in several commonly used methods such as FEMs is unnecessary, even for dissimilar phases with jagged edges and blurry boundaries. Once the solid and fluid phases are segmented, the microstructural models can be constructed directly from the image pixels and consequently solved by the strong form collocation methods. In contrast to the finite element modeling, there is no issue about mesh quality and mesh reconstruction in the proposed strong form collocation methods.

In this chapter, we showed that in the proposed G-RKCM for solving unit cell problems, the same collocation points and source points can be used while the interface condition is imposed by the collocation points. For non-uniform geometry of microstructures, where the employment of small kernel support to properly represent microstructural heterogeneity could lead to singularity in the moment matrix of RK shape functions, the Shepard functions were introduced to some source points, and the influence of this approach on the solution accuracy was investigated. In the unit cell study, the influences of microstructural dimension and image resolution on the accuracy of the predicted homogenized material properties were investigated through the real trabecular bone images. A numerical experimentation using human trabecular

bone images gave good agreement with experimental data. The numerical studies show that the proposed image-based multiscale computational framework demonstrated the capability of predicting the trabecular bone tissue macroscopic behavior using microstructural information.

Chapter 8 Conclusions and Future Work

This dissertation aims for the development of effective and robust computational methods for modeling poroelastic biological materials with high degree of material heterogeneity and complicated geometry. The efforts are motivated by two unresolved fundamental issues in bio-material modeling: (1) a computational model that is capable of discretizing the geometric configuration of biological materials and the associated microstructures based on medical images, and (2) a numerical method that is effective in modeling microstructures and predicting the macroscopic behavior of poroelastic bone materials.

8.1 Summary of Developments

The Biot's theory has been commonly used as the classic description of poroelasticity, in which a fluid-saturated porous medium is assumed and composed of the solid skeleton and fluid. In the quasi-static Biot's theory, two governing equations are considered, the equilibrium equation based on the effective stress and the continuity equation described by Darcy's law. This work investigates how the microstructures and material properties of porous materials constitute the macroscopic poroelastic material behavior described by the classical Biot's theory. We introduced an asymptotic based multiscale homogenization method to correlate the macro- and micro-mechanical behaviors of poroelastic materials, where an elastic solid and Newtonian fluid of low viscosity are considered. Through this homogenization process, the generalized Darcy's

177

law, homogenized macroscopic continuity equation, and homogenized macroscopic equilibrium equation were obtained, where the homogenized macroscopic continuity and equilibrium equations reassemble the governing equations in the Biot's theory.

The earlier work in the development of direct strong form collocation methods, such as the reproducing kernel collocation method (RKCM), addressed the domain integration issue in the Galerkin type meshfree method, such as the reproducing kernel particle method (RKPM), but with increased computational complexity due to taking higher order derivatives of the approximation functions and the need of using large number of collocation points for optimal convergence. In this work, we intended to address the computational complexity in RKCM while achieving optimal convergence by introducing a gradient reproduction kernel approximation. The proposed gradient reproducing kernel collocation method (G-RKCM) reduces the order of differentiation to the first order for solving second order PDEs with strong form collocation. We also showed that, different from the typical strong form collocation method where a significant large number of collocation points than the number of source points is needed for optimal convergence, the same number of collocation points and source points can be used in G-RKCM. We also showed that the same order of convergence rates in the primary unknown and its first order derivative is achieved, owing to the imposition of gradient reproducing conditions. The numerical examples were given to verify the analytical prediction.

To effectively construct microstructures with multiple phases from medical images, we introduced the active contour model based on variational level set formulation for interface identification and boundary segmentation. Inspired by the images with pixel point discretization, we introduced the RKCM and G-RKCM to solve the level set equation. In particular, the G-

RKCM has been shown effective since the second derivatives of the level set function involved in the regularization term are approximated by the first order differentiations of the gradient RK shape functions. By introducing the active contour model, the proposed G-RKCM was employed to solve the level set equation by direct collocation. For images with two-color data, an investigation on the continuity of the kernel function showed that a B-spline kernel function with lower continuity can be preferably used to avoid the oscillation of level set functions.

When using RKCM to solve the level set equation in the image segmentation, it is shown that the consistency conditions imposed in construction of the RK shape function can be relaxed. Specifically, the kernel function can be directly used as the shape function in the strong form collocation method for computational efficiency. For images with two colors, the direct collocation method has been introduced to solve the degenerated level set equation without regularization term, and the transformation matrix is no longer needed in RKCM for solving the active contour model, thereby making the numerical algorithm very efficient.

To deal with medical images obtained from CT scan or MRI, we introduced the proposed G-RKCM to solve the unit cell problems, where the microstructures were first segmented by the level set method and then discretized directly using image pixels without the need of CAD procedures in mesh based methods. The associated discretization of governing equations for unit cell problems have been performed based on G-RKCM. Furthermore, some numerical issues related to microstructure modeling such as the interface discretization and influence of basis functions were investigated.

To validate the developed image-based multiscale computational framework for biological materials such as bone tissue, we first verified the proposed G-RKCM for solving unit cell

problems. Then, we investigated the size effect and image resolution of the unit cells for trabecular bone modeling. Further, we conducted numerical experimentation based on medical images available from literature to compute the macroscopic mechanical properties of a trabecular bone, and made a comparison of the predicted macroscopic material properties with experimental data. We demonstrated that the developed computational framework is capable of modeling microstructures with complicated configurations and predicting the associated macroscopic mechanical behavior accurately.

8.2 Suggestions for Future Research

We conclude this research by suggesting future directions for the image-based computational framework in bio-material modeling as follows:

(1) Extension of the image-based multiscale computational framework in three-dimension

The developed image-based bio-material modeling framework can be directly extended to three-dimensional modeling. With a series of image scans available elsewhere, a three-dimensional computational model can be constructed to simulate the bio-material behavior and predict the associated mechanical properties more accurately.

(2) Strong form collocation method for incompressible problems

In this study, we have shown that the proposed strong form collocation method, G-RKCM, for solving boundary value problems efficiently. Due to assumed strain nature and least-squares formulation, it is worth of further theoretical investigation of incompressibility.

(3) Investigation trabecular bone mechanical properties in different anatomical sites

Since the homogenized material properties of the trabecular bone obtained from the microstructures are representative near the location of the real bone where the samples are extracted, the homogenized material parameters are applicable to the bone model with similar geometric composition. As such, the mechanical properties of human trabecular bones can be better understood when different portions of bones such as femora, tibias, and vertebrae are investigated individually. Furthermore, a comparison of trabecular bone material properties with associated experimental data in the same anatomical site will help to accurately predict bone tissue behavior. Thus, the extension of the validity of the homogenized material properties can be done by sampling more areas of the bony microstructures obtained from CT or MRI.

(4) Extension of Image-based modeling in biomechanics

The multiscale homogenization of poroelastic materials provides a way to investigate the two-phase phenomenon such as solid and fluid. For bone materials, the investigation of the relationship between the increase of porosity in bones and bone mass density (BMD) in humans, in particular, requires nondestructive and non-invasive experiments and modeling techniques for clinical research. The developed computational framework will offer further assistance to the research in the bio-medical related fields.

Appendix A

Gradient Reproducing Kernel Approximation in Two-Dimension

Consider the approximation of $\mathbf{u}_{,x}$ and $\mathbf{u}_{,y}$ in two-dimension as follows:

$$\mathbf{u}_{,x} \approx \mathbf{w}_x = \sum_{I=1}^{N_s} \Psi_I^x(\mathbf{x}) \mathbf{a}_I$$
$$\mathbf{u}_{,y} \approx \mathbf{w}_y = \sum_{I=1}^{N_s} \Psi_I^y(\mathbf{x}) \mathbf{a}_I$$

(A1)

where

$$\Psi_I^x(\mathbf{x}) = C^1(\mathbf{x}; \mathbf{x} - \mathbf{x}_I) \varphi_a(\mathbf{x} - \mathbf{x}_I)$$
$$\Psi_I^y(\mathbf{x}) = C^2(\mathbf{x}; \mathbf{x} - \mathbf{x}_I) \varphi_a(\mathbf{x} - \mathbf{x}_I)$$

(A2)

For demonstration purposes, consider a case with linear bases $q = 1$ in two-dimension:

$$C^i(\mathbf{x}; \mathbf{x} - \mathbf{x}_I) = b_{00}^i(\mathbf{x}) + b_{10}^i(\mathbf{x})(x - x_I) + b_{01}^i(\mathbf{x})(y - y_I) =: \mathbf{H}^{\mathrm{T}}(\mathbf{x} - \mathbf{x}_I) \mathbf{b}^i(\mathbf{x}), \quad i = 1, 2 \quad \text{(A3)}$$

where the coefficients $b_{\alpha_1 \alpha_2}^i(\mathbf{x})$ are determined by satisfying the partition of nullity and first order derivative reproducing conditions shown below:

$$\sum_{I=1}^{N_s} \Psi_I^x(\mathbf{x}) = 0, \quad \sum_{I=1}^{N_s} \Psi_I^x(\mathbf{x}) x_I = 1, \quad \sum_{I=1}^{N_s} \Psi_I^x(\mathbf{x}) y_I = 0 \qquad \text{(A4a,b,c)}$$

$$\sum_{I=1}^{N_s} \Psi_I^y(\mathbf{x}) = 0, \quad \sum_{I=1}^{N_s} \Psi_I^y(\mathbf{x}) x_I = 0, \quad \sum_{I=1}^{N_s} \Psi_I^y(\mathbf{x}) y_I = 1 \qquad \text{(A5a,b,c)}$$

From (A4), multiplying (A4a) by x and subtracting (A4b) leads to

$$\sum_{I=1}^{N_s} \Psi_I^x(\mathbf{x})(x - x_I) = -1 \tag{A6}$$

Similarly, multiplying (A5a) by y and subtracting (A5c) yields

$$\sum_{I=1}^{N_s} \Psi_I^x(\mathbf{x})(y - y_I) = 0 \tag{A7}$$

Applying the same procedures to (A7), we have

$$\sum_{I=1}^{N_s} \Psi_I^y(\mathbf{x})(x - x_I) = 0 \tag{A8}$$

$$\sum_{I=1}^{N_s} \Psi_I^y(\mathbf{x})(y - y_I) = -1 \tag{A9}$$

The first order derivative reproducing conditions in (A6) and (A7) can be equivalently written as

$$\sum_{I=1}^{N_s} \Psi_I^x(\mathbf{x}) = 0, \quad \sum_{I=1}^{N_s} \Psi_I^x(\mathbf{x})(x - x_I) = -1, \quad \sum_{I=1}^{N_s} \Psi_I^x(\mathbf{x})(y - y_I) = 0 \tag{A10}$$

$$\sum_{I=1}^{N_s} \Psi_I^y(\mathbf{x}) = 0, \quad \sum_{I=1}^{N_s} \Psi_I^y(\mathbf{x})(x - x_I) = 0, \quad \sum_{I=1}^{N_s} \Psi_I^y(\mathbf{x})(y - y_I) = -1 \tag{A11}$$

From which we can express the first order derivative reproducing conditions (A10) and (A11) as:

$$\sum_{I=1}^{N_s} \Psi_I^x(\mathbf{x}) \mathbf{H}(\mathbf{x} - \mathbf{x}_I) = -\mathbf{H}_{,x}(\mathbf{0}) \tag{A12}$$

$$\sum_{I=1}^{N_s} \Psi_I^y(\mathbf{x}) \mathbf{H}(\mathbf{x} - \mathbf{x}_I) = -\mathbf{H}_{,y}(\mathbf{0}) \tag{A13}$$

Substituting (A2) and (A3) into (A12) and (A13) give rise to

$$\mathbf{M}(\mathbf{x})\mathbf{b}^1(\mathbf{x}) = -\mathbf{H}_{,x}(\mathbf{0}) \tag{A14}$$

183

$$\mathbf{M}(\mathbf{x})\mathbf{b}^2(\mathbf{x}) = -\mathbf{H}_{,y}(\mathbf{0}) \tag{A15}$$

where $\mathbf{M}(\mathbf{x})$ is the moment matrix given in Chapter 5. Consequently the gradient RK shape functions are obtained as

$$\Psi_I^x(\mathbf{x}) = -\mathbf{H}_{,x}^{\mathrm{T}}(\mathbf{0})\mathbf{M}^{-1}(\mathbf{x})\mathbf{H}(\mathbf{x}-\mathbf{x}_I)\varphi_a(\mathbf{x}-\mathbf{x}_I)$$
$$\Psi_I^y(\mathbf{x}) = -\mathbf{H}_{,y}^{\mathrm{T}}(\mathbf{0})\mathbf{M}^{-1}(\mathbf{x})\mathbf{H}(\mathbf{x}-\mathbf{x}_I)\varphi_a(\mathbf{x}-\mathbf{x}_I) \tag{A16}$$

Appendix B

Derivation of the Numerical Algorithm for the Reinitialization

Recall the reinitialization equation:

$$\frac{\partial \psi(\mathbf{x},t)}{\partial t} + sign(\phi(\mathbf{x},\tau))|\nabla \psi(\mathbf{x},t)| = sign(\phi(\mathbf{x},\tau)) \tag{B.1}$$

which can be written as

$$\frac{\partial \psi(\mathbf{x},t)}{\partial t} + \mathbf{w} \cdot \nabla \psi(\mathbf{x},t) = sign(\phi(\mathbf{x},\tau)) \tag{B.2}$$

where

$$\mathbf{w} = sign(\phi)\frac{\nabla \psi}{|\nabla \psi|} \tag{B.3}$$

By using the iterative method, (B.2) can be updated as follows:

$$\psi_{i,j}^{n+1} = \psi_{i,j}^{n} - dt S_{\varepsilon}\left(\phi_{i,j}\right) G\left(\psi_{i,j}^{n}\right) \tag{B.4}$$

where $S_{\varepsilon}\left(\phi_{i,j}\right)$ is the signed function defined as

$$S_{\varepsilon}\left(\phi_{i,j}\right) = \frac{\phi_{i,j}}{\sqrt{\phi_{i,j}^{2} + \varepsilon^{2}}} \tag{B.5}$$

and

$$
G\left(\psi_{i,j}\right) = \begin{cases}
\sqrt{\max\left(\left(a^+\right)^2,\left(b^-\right)^2\right) + \max\left(\left(c^+\right)^2,\left(d^-\right)^2\right)} - 1, & \text{if } \phi_{i,j} > 0 \\
\sqrt{\max\left(\left(a^-\right)^2,\left(b^+\right)^2\right) + \max\left(\left(c^-\right)^2,\left(d^+\right)^2\right)} - 1, & \text{if } \phi_{i,j} < 0 \\
0, & \text{otherwise}
\end{cases}
\tag{B.6}
$$

where the superscripts "+" and "–" denote the positive and negative parts in a, b, c, and d, which are expressed as

$$
\begin{aligned}
a &= \left(\psi_{i,j} - \psi_{i-1,j}\right)/h \\
b &= \left(\psi_{i+1,j} - \psi_{i,j}\right)/h \\
c &= \left(\psi_{i,j} - \psi_{i,j-1}\right)/h \\
d &= \left(\psi_{i,j+1} - \psi_{i,j}\right)/h
\end{aligned}
\tag{B.7}
$$

where h is the nodal distance.

The stopping criterion is

$$
error = \left|\psi_{i,j}^{n+1} - \psi_{i,j}^{n}\right| < dt \cdot h^2
\tag{B.8}
$$

with $dt = h/10$ and $\varepsilon = h$ in S_ε suggested by Sussman et al. (1994).

Appendix C

Derivation of the Bound on the Homogenized Effective Stress Tensor

The weak form of the unit cell problems for $\boldsymbol{\chi}$ and $\boldsymbol{\eta}$ are

$$\int_{Y_s} \frac{\partial v_i}{\partial y_j} C_{ijmn} \frac{\partial \chi_m^{kl}}{\partial y_n} dY = \int_{Y_s} \frac{\partial v_i}{\partial y_j} C_{ijkl} dY \tag{C.1}$$

$$\int_{Y_s} \frac{\partial v_i}{\partial y_j} C_{ijkl} \frac{\partial \eta_k}{\partial y_l} dY = \int_{Y_s} \frac{\partial v_i}{\partial y_j} \delta_{ij} dY \tag{C.2}$$

The bilinear form of the variational formulation can be expressed as

$$B(w_i, v_i) = \int_{Y_s} \frac{\partial v_i}{\partial y_j} C_{ijkl} \frac{\partial w_k}{\partial y_l} dY \tag{C.3}$$

The corresponding bilinear expressions for χ_i^{kl} and η_i are

$$B(\chi_i^{kl}, v_i) = \int_{Y_s} \frac{\partial v_i}{\partial y_j} C_{ijkl} dY \tag{C.4}$$

$$B(\eta_i, v_i) = \int_{Y_s} \frac{\partial v_i}{\partial y_i} dY \tag{C.5}$$

Recall the homogenized effective stress tensor:

$$\bar{\alpha}_{ij} = \frac{1}{|Y|} \int_{Y_s} C_{ijkl} \frac{\partial \eta_k}{\partial y_l} dY \tag{C.6}$$

For linear elastic materials of solid skeleton, the constitutive law is

$$C_{ijkl} = \lambda \delta_{ij} \delta_{kl} + \mu \left(\delta_{ik} \delta_{jl} + \delta_{il} \delta_{jk} \right) \tag{C.7}$$

Substituting (C.7) into (C.6) and taking summation on i lead to

$$\bar{\alpha}_{ii} = \frac{E}{(1-2\nu)(1+\nu)} \frac{1}{|Y|} \int_{Y_s} \frac{\partial \eta_i}{\partial y_i} dY \tag{C.8}$$

which is valid for 2D unit cell problems. Based on (C.5), consider the following bilinear form:

$$B\left(\eta_i, \eta_i \right) = \int_{Y_s} \frac{\partial \eta_i}{\partial y_i} dY \geq 0 \tag{C.9}$$

From (C.8) and (C.9), we have

$$\bar{\alpha}_{ii} \geq 0 \tag{C.10}$$

Similarly, substituting (C.7) into (C.4) and taking summation on k yield

$$B\left(\chi_i^{kk}, v_i \right) = \frac{E}{(1-2\nu)(1+\nu)} \int_{Y_s} \frac{\partial v_i}{\partial y_i} dY \tag{C.11}$$

Considering the bilinear form of $B\left(\eta_i, v_i \right)$ in (C.5), (C.11) can be written as

$$B\left(\chi_i^{kk}, v_i \right) = B\left(\frac{E}{(1-2\nu)(1+\nu)} \eta_i, v_i \right) \tag{C.12}$$

which implies

$$\chi_i^{kk} = \frac{E}{(1-2\nu)(1+\nu)} \eta_i \tag{C.13}$$

Recall the homogenized elasticity tensor:

$$\overline{C}_{ijkl} = (1-\phi)C_{ijkl} - \frac{1}{|Y|}\int_{Y_S} C_{ijmn}\frac{\partial \chi_m^{kl}}{\partial y_n}dY \qquad\qquad (C.14)$$

Introducing (C.7) to (C.14) and taking summation on k lead to

$$\overline{C}_{ijkk} = \frac{E}{(1-2\nu)(1+\nu)}\left[(1-\phi)\delta_{ij} - \frac{1}{|Y|}\int_{Y_S} C_{ijmn}\frac{\partial \eta_m}{\partial y_n}dY\right] \qquad\qquad (C.15)$$

Taking summation on i and substituting (C.6) into (C.15) give rise to

$$\overline{C}_{iikk} = \frac{E}{(1-2\nu)(1+\nu)}\left[2(1-\phi) - \overline{\alpha}_{ii}\right] \qquad\qquad (C.16)$$

From (C.16), the upper bound for $\overline{\alpha}_{ii}$ is

$$\overline{\alpha}_{ii} \le 2(1-\phi) \qquad\qquad (C.17)$$

By combining (C.10) and (C.17), the bound for $\overline{\alpha}_{ii}$ in 2D is

$$0 \le \overline{\alpha}_{ii} \le 2(1-\phi) \qquad\qquad (C.18)$$

Appendix D

Shepard Function

In the numerical examples, the G-RKCM is adopted with equal-order quadratic bases for construction of RK shape functions and gradient RK shape functions. Nevertheless, for microstructures with irregular configuration, a shepard function is employed whenever the singularity of the moment matrix is encountered at a point, which is given by

$$\Psi_I(\mathbf{x}) = \frac{\varphi_a(\mathbf{x} - \mathbf{x}_I)}{\sum_{J=1}^{N_s} \varphi_a(\mathbf{x} - \mathbf{x}_J)} \tag{D.1}$$

where it satisfies the zero-th consistency condition or the partition of unity. The associated correction function and moment matrix are defined as

$$C(\mathbf{x}; \mathbf{x} - \mathbf{x}_I) = \mathbf{M}^{-1}(\mathbf{x}) \tag{D.2}$$

$$\mathbf{M}(\mathbf{x}) = \sum_{I=1}^{N_s} \varphi_a(\mathbf{x} - \mathbf{x}_I) \tag{D.3}$$

When a shepard function is used, the corresponding support size is reduced to the distance h between two grid points, i.e., $a = 1.001h$.

Appendix E

Tensor Transformation

Consider the general form of the homogenized elasticity tensor representing an anisotropic material:

$$\overline{C} = \begin{bmatrix} C_{11} & C_{12} & C_{13} & C_{14} & C_{15} & C_{16} \\ C_{12} & C_{22} & C_{23} & C_{24} & C_{25} & C_{26} \\ C_{13} & C_{23} & C_{33} & C_{34} & C_{35} & C_{36} \\ C_{14} & C_{24} & C_{34} & C_{44} & C_{45} & C_{46} \\ C_{15} & C_{25} & C_{35} & C_{45} & C_{55} & C_{56} \\ C_{16} & C_{26} & C_{36} & C_{46} & C_{56} & C_{66} \end{bmatrix} \tag{E.1}$$

To find the planes of symmetry, the following two matrices are defined:

$$\overline{C}_{ijkk} = \begin{bmatrix} C_{11} + C_{12} + C_{13} & C_{16} + C_{26} + C_{36} & C_{15} + C_{25} + C_{35} \\ C_{16} + C_{26} + C_{36} & C_{12} + C_{22} + C_{23} & C_{14} + C_{24} + C_{34} \\ C_{15} + C_{25} + C_{35} & C_{14} + C_{24} + C_{34} & C_{13} + C_{23} + C_{33} \end{bmatrix} \tag{E.2}$$

$$\overline{C}_{ikkj} = \begin{bmatrix} C_{11} + C_{55} + C_{66} & C_{16} + C_{26} + C_{45} & C_{15} + C_{46} + C_{35} \\ C_{16} + C_{26} + C_{45} & C_{22} + C_{44} + C_{66} & C_{24} + C_{34} + C_{56} \\ C_{15} + C_{46} + C_{35} & C_{24} + C_{34} + C_{56} & C_{33} + C_{44} + C_{55} \end{bmatrix} \tag{E.3}$$

If the eigenvectors of these two matrices are the same and the eigenvalues are different, then the orthotropic planes of symmetry exist as shown by Cowin and Mehrabadi (1987). With the transformation matrix $\mathbf{Q}$ formed by the eigenvectors, the orthotropic elasticity tensor can be determined by

$$\overline{C}'_{pqrs} = Q_{pi} Q_{qj} Q_{rk} Q_{sl} \overline{C}_{ijkl} \tag{E.4}$$

where

$$\overline{C}'_{ijkl} = \begin{bmatrix} C'_{11} & C'_{12} & C'_{13} & 0 & 0 & 0 \\ C'_{12} & C'_{22} & C'_{23} & 0 & 0 & 0 \\ C'_{13} & C'_{23} & C'_{33} & 0 & 0 & 0 \\ 0 & 0 & 0 & C'_{44} & 0 & 0 \\ 0 & 0 & 0 & 0 & C'_{55} & 0 \\ 0 & 0 & 0 & 0 & 0 & C'_{66} \end{bmatrix} \tag{E.5}$$

References

(1) P. Fillunger, Der Auftrieb von Talsperren, and Teil I-III. Österr. Wochenschrift für den öffentlichen Baudienst 7 (1913), 532-510.

(2) K. Terzaghi, Erdbaumechanic auf bodenphysikalischer grundlage, Franz Deuticke, Leipzig, (1925) 399.

(3) M.A. Biot, General theory of three-dimensional consolidation, J Appl Phys 12 (1941), 155-164.

(4) M.A. Biot, Theory of elasticity and consolidation for a porous anisotropic solid, J Appl Phys 26 (1955), 182-185.

(5) M.A. Biot, Theory of propagation of elastic waves in a fluid-saturated porous solid, J Acoust Soc Am 28 (1956), 168-191.

(6) M.A. Biot, Mechanics of deformation and acoustic propagation in porous media, J Appl Phys 33 (4) (1961), 1483-1498.

(7) L.E. Malvern, Introduction to the mechanics of a continuous medium, Prentice-Hall, Englewood Cliffs, New Jersey, 1969.

(8) R.I. Borja, Finite element formulation for transient pore pressure dissipation: A variational approach, Int J Solids Struct 22 (11) (1986), 1201-1211.

(9) T. Bourbié, O. Coussy, and B. Zinszner, Acoustics of porous media, Gulf Pub Co, Houston, 1987.

(10) R. de Boer and W. Ehlers, A historical review of the formulation of porous media theories, Acta Mech 74 (1988), 1-8.

(11) Y.C. Fung, In: Biomechanics, mechanical properties of living tissues (2nd ed.), Springer-Verlag, New York, 1993.

(12) E. Detournay and A. H.-D. Cheng, Fundamentals of poroelasticity, Comprehensive rock engineering: Principles, practice and projects, Pergamon, New York, 1993, 113-171.

(13) B.R. Simon, J.P. Liable, D. Pflaster, Y. Yuan, and M. H. Krag, A poroelastic finite element formulation including transport and swelling in soft tissue structures, J Biomech Eng 118 (1996), 1-9.

(14) J.M. Huyghe and J.D. Janssen, Quadriphasic mechanics of swelling incompressible porous media, Int J Eng Sci 35 (1997), 793-802.

(15) M. Schanz, Poroelastodynamics: linear models, analytical solutions, and numerical methods, Appl Mech Rev 62 (2009), 28-42.

(16) I. Babuska, Homogenization approach in engineering, in: J.L. Lions and R. Glowinski eds., Computing methods in applied sciences and engineering, lecture note in economics and mathematical systems, Springer-Verlag, Berlin, 134 (1976), 137-153.

(17) A. Bensousson, J.L. Lions, and G. Papanicolaou, Asymptotic analysis for periodic structures, North-Holland, Amsterdam, 1978.

(18) E. Sanchez-Palencia, Non-homogeneous media and vibration theory, in: lecture notes in physics, 127, Springer-Verlag, Berlin, 1980.

(19) J.L. Lions, Some methods in the mathematical analyses of systems and their control, Science press, Beijing, and Gordon and Breach, New York, 1981.

(20) N. Bakhvalov and G. Panasenko, Homogenisation: averaging processes in periodic media: mathematical problems in the mechanics of composite materials, Kluwer Academic Publishers, Boston, 1989.

(21) J.M. Guedes and N. Kikuchi, Preprocessing and postprocessing for materials based on the homogenization method with adaptive finite element methods, Comp Meth Appl Mech Engng 83 (1990), 143-198.

(22) U. Hornung, Homogenization and porous media, Springer, New York, 1997.

(23) K. Terada, T. Ito, and N. Kikuchi, Characterization of the mechanical behaviors of solid-fluid mixture by the homogenization method, Comput Meth Appl Mech Engng 153 (1998), 223-257.

(24) N. Takano, Y. Ohnishi, M. Zako, K. Nishiyabu, The formulation of homogenization method applied to large deformation problem for composite materials. Int J Solids Struct 37 (2000) 6517-6535.

(25) K. Terada, T. Kyoya, M. Kazama, K. Lee, and L. Oyang, Image-based modeling and analysis of microstructures for two-scale problems in geomechanics, Int J Numer Anal Methods Geomech 26 (2002), 273-297.

(26) N. Takano, M. Zako, T. Okazaki, and K. Terada, Microstructure-based evaluation of the influence of woven architecture on permeability by asymptotic homogenization theory, Compos Sci Technol 62 (2002), 1347-1356.

(27) J.S. Chen and S. Mehraeen, Variationally consistent multi-scale modeling and homogenization of stressed grain growth, Comput Methods Appl Mech Eng 193 (2004), 1825-1848.

(28) J.S. Chen and S. Mehraeen, Multi-scale modeling of heterogeneous materials with fixed and evolving microstructures, Model Simul Mater Sci Eng 13 (2005), 95-121.

(29) X. Zhang, S. Mehraeen, J.S. Chen, and N. Ghoniem, Multiscale total Lagrangian formulation for modeling dislocation-induced plastic deformation in polycrystalline materials, Int J Multisc Comput Eng 4 (2006), 29-46.

(30) R. L. Hardy, Multiquadric equations of topography and other irregular surfaces, J Geophys Res 176 (1971), 1905-1915.

(31) P. Lancuster and K. Salkauskas, Surface generated by moving least squares methods, Math Comput 37 (1981), 141-158.

(32) R. Franke, Scattered data interpolation: tests of some methods, Math Comput 98 (1982), 181-200.

(33) O.C. Zienkiewicz, S. Qu, R.L. Taylor, and S. Nakazawa, The patch test for mixed formulations, Int J Numer Meth Engng 23 (1986), 1873-1883.

(34) R. L. Hardy, Theory and applications of the multiquadric-biharmonic method: 20 years of discovery, Comput Math Appl 19 (1990), 163-208.

(35) B. Nayroles, G. Touzot, and P. Villon, Generalizing the finite element method: diffuse approximation and diffuse elements, Comput Mech 10 (1992), 307-318.

(36) E.J. Kansa, Multiqudrics—a scattered data approximation scheme with applications to computational fluiddynamics. I. Surface approximations and partial derivatives, Comput Math Appl 19 (1992), 127-145.

(37) E.J. Kansa, Multiqudrics—a scattered data approximation scheme with applications to computational fluiddynamics. II. Solutions to parabolic, hyperbolic and elliptic partial differential equations, Comput Math Appl 19 (1992), 147-161.

(38) W.R. Madych, Miscellaneous error bounds for multiquadric and related interpolatory. Comput Math Appl 24 (1992), 121-138.

(39) W.R. Madych and S.A. Nelson, Bounds on multivariate polynomials and exponential error estimates for multiquadric interpolation, J Approx Theory 70 (1992), 94-114.

(40) T. Belytschko, Y. Y. Lu, and L. Gu, Element-free Galerkin methods, Int J Numer Methods Eng 37 (1994), 229-256.

(41)   D. Sulsky, Z. Chen, and H. L. Schreyer, A particle method for history-independent materials, Comput Methods Appl Mech Eng 118 (1994), 179-196.

(42) I. Babuska, F. Ihlenburg, E. Paik, and S. Sauter, A generalized finite element method for solving the Helmholtz equation in two dimensions with minimal pollution, Comput Methods Appl Mech 128 (1995), 325-359.

(43)   W.K. Liu, S. Jun, and Y.F. Zhang, Reproducing kernel particle methods, Int J Numer Methods Fluids 20 (1995), 1081-1106.

(44) T. Belytschko, Y. Krongauz, D. Organ, M. Fleming, and P. Krysl, Meshless methods: an overview and recent development, Comput Methods Appl Mech Eng 139 (1996), 3-49.

(45)   S. Beissel and T. Belytschko, Nodal integration of the element-free Galerkin method, Comput Methods Appl Mech Engrg 139 (1996), 49-74.

(46) J.S. Chen, C. Pan, C.T. Wu, and W.K. Liu, Reproducing kernel particle methods for large deformation analysis of nonlinear structures, Comput Meth Appl Mech Eng 139 (1996), 195-227.

(47)   E. Onate, S. Idelsohn, O.C. Zienkiewicz, and R.L. Taylor, A finite point method in computational mechanics. Application to convective transport and fluid flow, Int J Numer Meth Eng 39 (1996), 3839-3866.

(48) J. M. Melenk and I. Babuska, The partition of unity finite element method: basic theory and applications, Comput Methods Appl Mech Eng 139 (1996), 289-314.

197

(49) I. Babuska and J.M. Melenk, The partition of unity method, Int J Numer Methods Eng 40 (1997), 727-758.

(50) R. Franke and R. Schaback, Solving partial differential equations by collocation using radial functions, Appl Math Comput 93 (1998), 73-82.

(51) S. Li and W.K. Liu, Synchronized reproducing kernel interpolant via multiple wavelet expansion, Comput Mech 21 (1998), 28-47.

(52) N.R. Aluru, A point collocation method based on reproducing kernel approximation, Int J Numer Methods Eng 47 (2000), 1083-1121.

(53) J. Bonet and S. Kulasegaram, Correction and stabilization of smooth particle hydrodynamics methods with applications in metal forming simulations, Int J Numer Meth Engng 47 (2000), 1189-1214.

(54) H. Wendland, Meshless Galerkin methods using radial basis functions, Math Comput 68 (1999), 1521-1531.

(55) E.J. Kansa and Y.C. Hon, Circumventing the ill-conditioning problem with multiquadric radial basis functions: applications to elliptic partial differential equations, Comput Math Appli 4 (2000), 123-137.

(56) W. Han and X. Meng, Error analysis of the reproducing kernel particle method, Comput Methods Appl Mech Eng 190 (2001), 6157-6181.

(57) Y. C. Hon and R. Schaback, On unsymmetric collocation by radial basis functions, Appl Math Comput 119 (2001), 177-186.

(58) X. Zhang, X. H. Liu, K. Z. Song, and M. W. Lu, Least-squares collocation meshless method, Int J Numer Meth Eng 51 (2001), 1089-1100.

(59) J.S. Chen, C.T. Wu, S. Yoon, and Y. You, A stabilized conforming nodal integration for Galerkin mesh-free methods, Int J Numer Methods Eng 50 (2001), 435-466.

(60) D.W. Kim and Y. Kim, Point collocation methods using the fast moving least-square reproducing kernel approximation, Int J Numer Meth Eng 56 (2003), 1445-1464.

(61) J.S. Chen, X. Zhang, and T. Belytschko, An Implicit Gradient Model by a Reproducing Kernel Strain Regularization in Strain Localization Problems, Comput Methods Appl Mech Eng 193 (2004), 2827-2844.

(62) H.Y. Hu, J.S. Chen, and W. Hu, Weighted radial basis collocation method for boundary value problems, Int J Numer Methods Eng 69 (2007), 2736-2757.

(63) J.S. Chen, W. Hu, and H.Y. Hu, Reproducing kernel enhanced local radial basis collocation method, Int J Numer Meth Eng 75 (2008), 600-627.

(64) M.A. Puso, J.S. Chen, E. Zywicz, and W. Elmer, Meshfree and finite element nodal integration methods, Int J Numer Meth Engng 74 (2008), 416-446.

(65) I. Babuska, U. Banerjee, J.E. Osborn, and Q. Zhang, Effect of numerical integration on meshless methods, Comput Methods Appl Mech Engrg 198 (2009), 2886-2897.

(66) J.S. Chen, L. Wang, H.Y. Hu, S.W. Chi, Subdomain radial basis collocation method for heterogeneous media, Int J Numer Meth Eng 80 (2009), 163-190.

(67) H.Y. Hu and C.K. Lai, A study on convergence and complexity of reproducing kernel collocation method, Interaction Multiscale Mech 2 (2009), 295-319.

(68) L. Wang, J. S. Chen, and H. Y. Hu, Subdomain Radial Basis Collocation Method for Fracture Mechanics, Int J Numer Meth Eng 83 (2010), 851-876.

(69) H.Y. Hu, J.S. Chen, and W. Hu, Error analysis of collocation method based on reproducing kernel approximation, Numer Meth Part D E 27 (2011), 554-580.

199

(70) http://academic.kellogg.edu/herbrandsonc/bio201_mckinley/skele tal.htm

(71) SCANCO Medical, http://www.scanco.ch/

(72) M. Kass, A. Witkin, and D. Terzopoulos, Snakes: Active Contour Models. Intl J Computer Vision, 1 (1988), 321-331.

(73) S. Osher and J.A. Sethain, Fronts propagation with curvature-dependent speed: Algorithms based on Hamilton-Jacobi Formulation, J Comput Phys 79 (1988), 12-49.

(74) D. Mumford and J. Shah, Optimal approximation by piecewise smooth functions and associated variational problems, Commun Pure Appl Math 42 (1989), 577-685.

(75) M. Sussman, P. Smereka, and S. Osher, A level set approach for computing solutions to incompressible two-phase flow, J Comput Phys 119 (1994), 146-159.

(76) D. Adalsteinsson and J. A. Sethian, A fast level set method for propagating interfaces, J Comput Phys, 118 (1995), 269-277.

(77) T. Chan and L. Vese, An active contour model without edges, In Lecture Notes in Comp Sci 1687, eds. M. Neilsen, P. Johansen, O.F. Olsen and J. Weickert, (1999), 141-151.

(78) D. Peng, B. Merriman, S. Osher, H.-K. Zhao, and M. Kang, A PDE-Based Fast Local Level Set Method, J Comput Phys 155 (1999), 410-438.

(79) T. Chan, B.Y. Sandberg, and L. Vese, Active contours without edges for vector-valued images, JVCIR 11 (2000), 130-141.

(80) T. Chan and L. Vese, Active Contours without Edges, IEEE Trans Image Process 10 (2) (2001), 266-277.

(81) S. Osher and R.P. Fedkiw, Level set methods: An overview and some recent results, J Comput Phys 169 (2) (2001), 463-502.

(82) S.J. Osher and R.P. Fedkiw, Level Set Methods and Dynamic Implicit Surfaces, Springer Verlag, New York, 2002.

(83) T.F. Chan and L.A. Vese. Active contour and segmentation models using geometric PDE's for medical imaging. Malladi, R. (Ed.), Geometric Methods in Bio-Medical Image Processing, Series: Mathematics and Visualization, Springer, 2002.

(84) B. Song and T. Chan, A fast algorithm for level set based optimization, UCLA Cam Report, 2002.

(85) L.A. Vese and T.F. Chan, A multiphase level set framework for image segmentation using the Mumford and Shah model, Intl J Computer Vision, 50(3) (2002), 271-293.

(86) F. Gibou and R. Fedkiw, A fast hybrid k-means level set algorithm for segmentation, In 4th Annual Hawaii International Conference on Statistics and Mathematics (2005), 281-291.

(87) J.L. Williams and J.L. Lewis, Properties and an anisotropic model of cancellous bone from the proximal tibia epiphysis, J Biomech Eng 104 (1982), 50-56.

(88) J.D. Eshelby, The determination of the elastic field of an ellipsoidai inclusion, and related problems, Proc Roy Soc Lond, A241 (1957) 376-396.

(89) S. Nemat-Nasser, T. Iwakuma, and M. Hejazi, On composites with periodic structure, Mech Matl, 1 (1982) 239-267.

(90) L.J. Gibson, The mechanical behavior of cancellous bone, J Biomech 18 (1985), 317-28.

(91) S.C. Cowin and M.M. Mehrabadi, On the identification of material symmetry for anisotropic elastic materials, Quart J Mech Appl Math 40 (1987), 451-476.

(92) J.D. Bryant, T. David, P.H. Gaskell, S. King, G. Lond, Rheology of bovine bone marrow, Proc Insrn Mech Engrs, H 203 (1989), 71-75.

(93) P.L. Mente and J.L. Lewis, Experimental method for the measurement of the elastic modulus of trabecular bone tissue, J Orthop Res 7 (1989), 456-461.

(94) K. Choi, J.L. Kuhn, M.J. Ciarelli, and S.A. Goldstein, The elastic modulus of trabccular, subchondral, and cortical bone tissue and the size-dependency of cortical bone modulus, J Biomech 23 (1990), 1103-1113.

(95) S.J. Hollister, D.P. Fyhrie, K.J. Jepsen, and S.A. Goldstein, Application of homogenization theory to the study of trabecular bone mechanics, J Biomech 24 (1991), 825-839.

(96) S.J. Hollister and B.A. Riemer, Digital-image-based finite element analysis for bone microstructure using conjugate gradient and Gaussian filter techniques, Mathematical Methods in Medical Imaging 11, Proceedings SPIE-The International Society for Optical Engineering (1993), 95-106. Society of Photo-Optical Instrumentation Engineers, Bellingham, WA.

(97) H. Hoppe, T. DeRose, T. Duchamp, J. McDonald, and W. Stuetzle, Mesh optimization, Proceedings of the 20th Annual Conference on Computer Graphics and Interactive Techniques (1993), 19-26. ACM, Anaheim, CA.

(98) S.J. Hollister, J.M. Brennan and N. Kikuchi, A homogenization procedure for calculating trabecular bone effective stiffness and tissue level stress, J Biomech 27 (1994), 433-444.

(99) S.J. Hollister and N. Kikuchi, Homogenization theory and digital imaging: a basis for studying the mechanics and design principles of bone tissue, Biotech Bioeng 43 (1994), 586-596.

(100) K. Najarian, Notes of introduction to biomedical engineering, 1995.

(101) D. Ulrich, B. van Rietbergen, H. Weinans, and P. Ruegsegger, Finite element analysis of trabecular bone structure: A comparison of image-based meshing techniques, J Biomech 31 (1998), 1187-1192.

(102) J.L. Kuhn, S.A. Goldstein, L.A. Feldkamp, R.W. Goulet, and G. Jesion, Evaluation of a microcomouted tomography system to study trabecular bone structure, J Orthop Res 8 (1990), 833-842.

(103) S.C. Cowin, Bone poroelasticity, J Biomech 32 (1999), 217-238.

(104) G.T. Charras and R.E. Guldberg, Improving the local solution accuracyof large-scale digital image-based finite element analyses, J Biomech 33 (2000), 255-259.

(105) T.M. Keaveny, E.F. Morgan, G.L. Niebur, and O.C.Yeh, Biomechanics of trabecular bone, Annu Rev Biomed Eng 3 (2001), 307-333.

(106) T. Hara, E. Tanck, J. Homminga, and R. Huiskes, The influence of microcomputed tomography threshold variations on the assessment of structural and mechanical trabecular bone properties, Bone 31 (2002), 107-109.

(107) L. Podshivalov, Y. Holdstein, A. Fischer, and P.Z. Bar-Yoseph, Towards a multi-scale computerized bone diagnostic system: 2D micro-scale finite element analysis, Commun Numer Meth Engng 25 (2009), 733-749.

(108) L. Podshivalov, A. Fischer, and P.Z. Bar-Yoseph, Multiscale FE method for analysis of bone micro-structures, J Mech Behav Biomed (2011), 888-899.

(109) P. Gonçalves Coelho, P. Rui Fernandes, and H. Carriço Rodrigues, Multiscale Modeling of Bone Tissue with Surface and Permeability Control, J Biomech 44(2) (2011), 321-329.

(110) H.K. Genant, C. Gordon, Y. Jiang, T.M. Link, D. Hans, S. Majumdar, and T.F. Lang, Advanced imaging of the macrostructure and microstructure of bone, Horm Res 54 (2000), 24-30.

(111) L. Pothuaud, P. Porion, E. Lespessailles, C.L. Benhamou, and P. Levitz, A new method for three-dimensional skeleton graph analysis of porous media: Application to trabecular bone microarchitecture, J Microsc 199 (2000), 149-161.

(112) H.S. Kim and S.T. Al-Hassani, A morphological model of vertebral trabecular bone, J Biomech 35 (2002), 1101-1114.

(113) J.H. Kinney, J.S. Stolken, T.S. Smith, J.T. Ryaby, and N.E. Lane, An orientation distribution function for trabecular bone, Bone 36 (2005), 193-201.

(114) J.S. Bauer, S. Kohlmann, F. Eckstein, D. Mueller, E.-M. Lochmüller, and T.M. Link, Structural analysis of trabecular bone of the proximal femur using multislice computed tomography: a comparison with dual X-ray absorptiometry for predicting biomechanical strength in vitro, Calcif Tissue Int 78 (2006), 78-89.

(115) J.S. Bauer, T.M. Link, A. Burghardt, T.D. Henning, D. Mueller, S. Majumdar, and S. Prevrhal, Analysis of trabecular bone structure with multidetector spiral computed tomography in a simulated soft-tissue environment, Calcif Tissue Int 80 (2007), 366-373.

(116) D.R. Carter and W.C. Hayes, The compressive behavior of bone as a two-phase porous structure, J Bone Joint Surg Am 59 (1977), 954-962.

(117) J.C. Lotz, T.N. Gerhart, and W.C. Hayes, Mechanical properties of trabecular bone from the proximal femur: a quantitative CT study, J Comput Assist Tomogr 14 (1990), 107-114.

(118) R. Hodgskinson and J.D. Currey, Young's modulus, density and material properties in cancellous bone over a large density range, J Mater Sci: Mater Med 3 (1992), 377-381.

(119) M. Dalstra, R. Huiskes, A. Odgaard, and L. van Erning, Mechanical and textural properties of pelvic trabecular bone, J Biomech 26 (1993), 523-535.

(120) T. M. Keaveny, X. E. Guo, E. F. Wachtel, T. A. McMahon, and W. C. Hayes, Trabecular Bone Exhibits Fully Linear Elastic Behavior and Yields at Low Strains, J Biomech, 27 (1994), 1127-1136.

(121) T.S. Keller, Predicting the compressive mechanical behavior of bone, J Biomech 27 (1994), 1159-1168.

(122) M.J. Grimm, K.R. Foster, J.L. Williams, Measurements of permeability and tortuosity in caleaneal bone. M.L. Hull (Ed.), ASME Advances in Bioengineering, BED-31 ASME, New York (1995), 155-156.

(123) M.J. Grimm and J.L.Williams, Measurements of permeability in human calcaneal trabecular bone, J Biomech 30 (1997), 743-745.

(124) A. Hosokawa and T. Otani, Ultrasonic wave propagation in bovine cancellous bone, J Acoust Soc Am, 101 (1997), 558-562.

(125) B. Li and R.M. Aspden, Composition and mechanical properties of cancellous bone from the femoral head of patients with osteoporosis or osteoarthritis, J Bone Miner Res 12 (1997), 641-651.

(126) T.H. Lim and J.H. Hong, Poroelastic properties of bovine vertebral trabecular bone, J Orthop Res, 18 (2000), 671-677.

(127) J.H. Hong, M.S. Mun, and T.H. Lim, Strain Rate Dependent Poroelastic Properties of Bovine Vertebral Trabecular Bone, KSME Int J, 15 (2001), 1032-1040.

(128) S.S. Kohles and J.B. Roberts, Linear Poroelastic Cancellous Bone Anisotropy: Trabecular Solid Elastic and Fuild Transport Properties, J Biomech Eng 124 (2002), 521-526.

(129) P.K. Zysset, A review of morphology—elasticity relationships in human trabecular bone: theories and experiments, J Biomech 36 (2003), 1469-1485.

(130) C. Hellmich, F.J. Ulm, and L. Dormieux, Can the diverse elastic properties of trabecular and cortical bone be attributed to only a few tissue-independent phase properties and their interactions? Arguments from a multiscale approach, Biomech Model Mechanobiol 2 (2004b), 219-238.

(131) B. Helgason, E. Perilli, E. Schileo, F. Taddei, S. Brynjolfsson, and M. Viceconti, Mathematical relationships between bone density and mechanical properties: A literature review, Clin Biomech 23 (2) (2008a), 135-146.